

AFOSR-TR- 91 09 29

(2)

AD-A244 131



DTIC

S C D

ATP

and is

Best Available Copy

91-19201



91 1227 078

REPORT DOCUMENTATION PAGE

Form Approved
OMB No. 0704-0188

1a. REPORT SECURITY CLASSIFICATION Unclassified			1b. RESTRICTIVE MARKINGS			
2a. SECURITY CLASSIFICATION AUTHORITY			3. DISTRIBUTION / AVAILABILITY OF REPORT Approved for public release, distribution unlimited			
2b. DECLASSIFICATION / DOWNGRADING SCHEDULE			4. PERFORMING ORGANIZATION REPORT NUMBER(S)			
6a. NAME OF PERFORMING ORGANIZATION University of Colorado at Boulder			6b. OFFICE SYMBOL (If applicable) CEAE Dept.		7a. NAME OF MONITORING ORGANIZATION Air Force Office of Scientific Research AFOSR/NA	
6c. ADDRESS (City, State, and ZIP Code) Dept. Civil, Env., and Arch. Engineering Boulder, Colorado 80309-0428			7b. ADDRESS (City, State, and ZIP Code) Building 410 Bolling Air Force Base, DC 20332-6448			
8a. NAME OF FUNDING / SPONSORING ORGANIZATION ZS-AF Office of Scientific Research		8b. OFFICE SYMBOL (If applicable) AFOSR/NA		9. PROCUREMENT INSTRUMENT IDENTIFICATION NUMBER AFOSR-89-0289		
8c. ADDRESS (City, State, and ZIP Code) Bolling Air Force Base Washington, D.C. 20332-6448			10. SOURCE OF FUNDING NUMBERS			
			PROGRAM ELEMENT NO. 61102 F	PROJECT NO. 2302	TASK NO. C2	WORK UNIT ACCESSION NO.
11. TITLE (Include Security Classification) Brittle Ductile Failure Mechanics of Mortar and Concrete						
12. PERSONAL AUTHOR(S) Sture, Stein, Willam Kaspar J., and Saouma, V.						
13a. TYPE OF REPORT Final		13b. TIME COVERED FROM 89/4/15 TO 91/9/30		14. DATE OF REPORT (Year, Month, Day) 1991, September 30		15. PAGE COUNT 135
16. SUPPLEMENTARY NOTATION						
17. COSATI CODES			18. SUBJECT TERMS (Continue on reverse if necessary and identify by block number) cementitious composites, fracture, slip, plasticity, integration, work-softening, stability, tension-shear and compression-shear experiments, polygonization.			
FIELD	GROUP	SUB-GROUP				
19. ABSTRACT (Continue on reverse if necessary and identify by block number) The final technical report summarizes analysis and results comprising both theory and experiments related to modeling of interfaces between cement matrix and aggregate. The model simulates accurately behavior under complex two and three-dimensional states of stress and deformation, where tension-shear and compression-shear conditions occur. The constitutive theory describes fracture and slip of the interface, and adhesion, debonding, and mobilized friction mechanisms are modeled. Fracture energy release is used to control softening. Analytical predictions of experiments compare well, and the model has been implemented in nonlinear finite element analysis codes. Two theses (Ph.D., Thomas Stankowski; MS, Philippe Menetrey) and eight scientific papers have been prepared under the auspices of the project.						
20. DISTRIBUTION / AVAILABILITY OF ABSTRACT <input checked="" type="checkbox"/> UNCLASSIFIED/UNLIMITED <input type="checkbox"/> SAME AS RPT. <input type="checkbox"/> DTIC USERS				21. ABSTRACT SECURITY CLASSIFICATION Unclassified		
22a. NAME OF RESPONSIBLE INDIVIDUAL Dr. Spencer T. Wu			22b. TELEPHONE (Include Area Code) (202) 767-6962		22c. OFFICE SYMBOL AFOSR/NA	

REPORT DOCUMENTATION PAGE

Form Approved
GSA No. 347-108

30 Sept., 1991

Final, April 1989 - Sept. 1991

Brittle ductile failure mechanics of mortar and concrete

AFOSR-89-0289 G

Stein Sture, Kaspar Willam, and Victor Saouma

Department of Civil, Environmental, and Architectural
Engineering
University of Colorado at Boulder
Colorado 80309-0428

Air Force Office of Scientific Research, AFOSR/NA
Building 410
Bolling Air Force Base
Washington, DC 20332-6448

11. SUPPLEMENTARY NOTES

12a. DISTRIBUTION AVAILABILITY STATEMENT

12b. DISTRIBUTION STATEMENT

13. ABSTRACT (Maximum 200 words)

The final report summarizes analysis and results comprising both theory and experiments related to modeling of interfaces between cement matrix and aggregate. The model simulates accurately behavior under complex two- and three-dimensional states of stress and deformation, where tension-shear and compression-shear conditions occur. The constitutive theory describes fracture and slip of the interface, and adhesion, debonding, and mobilized friction mechanisms are modeled. Fracture energy release is used to control softening. Analytical predictions of experiments compare well, and the model has been implemented in nonlinear finite element analysis codes.

Two theses (Ph.D.; Thomas Stankowski, MS; Philippe Menetrey) and eight scientific papers have been prepared under the auspices of the project.

14. SUBJECT TERMS

cementitious composites; fracture; slip; plasticity; integration; work-softening; stability; tension-shear and compression-shear experiments; polygonization.

15. NUMBER OF

135

16. PRICE CODE

17. SECURITY CLASSIFICATION OF REPORT

Unclassified

18. SECURITY CLASSIFICATION OF THIS PAGE

Unclassified

19. SECURITY CLASSIFICATION OF ABSTRACT

Unclassified

20. LIMITATION

UL

TABLE OF CONTENTS

	Page
1. Executive Summary	2
2. List of Publications in the Project	3
<u>PART 1</u> FRACTURE AND SLIP OF INTERFACES IN CEMENTITIOUS COMPOSITES, MODEL CHARACTERISTICS	1
Abstract.	2
Contents.	3
1. Introduction	4
2. Concepts of Fracturing and Slip	5
3. Fracture/Slip Criterion	7
4. Postfailure Behavior	8
5. Uniqueness of Response - Brittle Behavior	12
6. Calibration	17
7. Application	17
8. Appendix I: References	19
9. Appendix II: Notation	21
10. Appendix III: The Construction of Voronoi Polyhedra in Three Dimensions.	23
<u>PART 2</u> MODEL IMPLEMENTATION	1
1. Introduction	3
2. Incremental Relations	3
2.1 Implicit Integration	3
2.2 Newton Iteration	5
2.3 Interpolation/Iteration Scheme	6
2.4 Iterative Procedure for Mixed Control	8

3.	Finite Element Modeling with Interfaces	8
3.1	Basic Equations	8
3.2	Iterative Scheme - Numerical Performance . . .	10
4.	Numerical Results	12
5.	Summary and Conclusions	13
6.	Appendix I: Algorithmic Tangent Stiffness . . .	15
7.	Appendix II: Extension of the Model to Three Dimensions	17
8.	Appendix III: References	18
9.	Appendix IV: Notation.	19
 PART 3 INTERFACE EXPERIMENTS		1
1.	Introduction	1
2.	Apparatus	1
3.	Experiments	2
4.	Experimental Data	3
5.	List of Figures	5



Accession For	
NTIS GRA&I	<input checked="" type="checkbox"/>
DTIC TAB	<input type="checkbox"/>
Unannounced	<input type="checkbox"/>
Justification	
By	
Distribution/	
Availability Codes	
Dist	Avail and/or Special
A-1	

1. EXECUTIVE SUMMARY

This is the final technical report in the AFOSR supported project entitled, Brittle Ductile Failure Mechanics of Mortar and Concrete. The report summarizes theory, analysis, and experimental results obtained in model studies on cement matrix (mortar) and aggregate (stone).

This report describes the theory, implementation, and predictive capabilities of a new and relatively straightforward constitutive theory for interfaces, that describes fracture, slip and post-peak and residual behavior for mortar-aggregate composites (concrete). Adhesion, debonding and mobilized friction are accounted for in the characterization of interface behavior, and the debonding is controlled through a work-softening rule, that incorporates tensile crack opening as well as tangential slip. The material parameters have clear physical meaning and can be calibrated from conventional and special interface experiments. The predictive performance of the model is tested on both large and small composite structures, and the results compare well to those obtained in laboratory experiments.

The last part of the report contains data from mortar-aggregate interface experiments, where small specimens were subjected to combinations of tensile and shear or compression and shear loading. Experimental technique and apparatus are also described.

The report comprises three parts, which are organized as follows: Part 1; Modeling of fracture and slip of interfaces in cementitious composites (model characteristics), Part 2; Model implementation, and Part 3; Interface experiments.

Several publications have been prepared in the project, and the bibliography is attached on the next page. Additional journal and conference papers will also be prepared based on the contents of this report.

LIST OF PUBLICATIONS PREPARED IN THE PROJECT

"Simulation of Failure Processes in Cementitious Particle Composites," by T. Stankowski, S. Sture, K. Runesson, and K. Willam, in Proc. ASCE Engineering Mechanics Division, Specialty Conference, May 19-22, 1991, Columbus, Ohio, pp. 1102-1107.

"Simulation of Failure Processes in Cementitious Composites - Concrete," by T. Stankowski, S. Sture, K.J. Willam, and K. Runesson, Proc. Int. Conf. Fracture Processes in Brittle Disordered Materials, June 19-21, 1991, Noordwijk, The Netherlands.

"Progressive Failure Analysis of Cementitious Composites," by T. Stankowski, S. Sture, and K. Runesson, in Proc. Int. Conf. Constitutive Laws for Engineering Materials, Recent Advances and Industrial and Infrastructure Applications, Univ. of Arizona, Tucson, Jan. 1991, pp. 627-632.

"Numerical Simulation of Failure in Particle Composites," by T. Stankowski, Proc. World Conf. Computational Mechanics, Stuttgart, August, 1990.

"Theory and Basic Concepts for Modelling Concrete Behavior," K.J. Willam, T. Stankowski, and S. Sture, Comite Euro-International du Beton (CEB) Bulletin 194, Modelling of Structural Reinforced and Prestressed Concrete in Computer Programs, May, 1990, pp. 15-43.

"Numerical Simulation of Progressive Failure in Particle Composites", T. Stankowski, Ph.D. Thesis, Department of Civil, Env., and Arch. Engineering, University of Colorado at Boulder, 1990, 118 pp.

A Three-Dimensional Model Based on the Finite Element Method and Plasticity Theory to Analyze Plain Concrete Structures," P. Menetrey, MS Thesis, Department of Civil, Env., and Arch. Engineering, University of Colorado at Boulder, August, 1991, 128 pp.

"Simulation Issues of Distributed and Localized Failure Computations," by K.J. Willam, T. Stankowski, K. Runesson, and S. Sture, Proc. Cracking and Damage- Strain Localization and Size Effects, Eds. J. Mazars and Z.P. Bazant, Elsevier Appl. Sci., London, 1989, pp. 363-378.

"Combined Compression-Shear Experiments on Mortar-Aggregate Interfaces," by T. Stankowski, S. Sture, and K. Runesson, Proc. ASCE, Materials Eng. Div. Congress, Denver, Colorado, August, 1990, Vol. I, pp. 350-359.

FRACTURE AND SLIP OF INTERFACES IN CEMENTITIOUS COMPOSITES

Part I: Model Characteristics

by

T. Stankowski¹, K. Runesson², S. Sture³

¹Res. Assoc., Dept. of Civil, Environmental, and Architectural Engrg., University of Colorado, Boulder, CO 80309.

²Visit.Prof., Dept. of Civil, Environmental, and Architectural Engrg., University of Colorado, Boulder, CO 80309.

³Prof., Dept. of Civil, Environmental, and Architectural Engrg., University of Colorado, Boulder, CO 80309.

Abstract:

A new and relatively simple constitutive theory that describes fracture and slip of an interface in cementitious composites such as concrete is presented. Adhesion, debonding and mobilized friction mechanisms are considered in the characterization of the interface behavior. The debonding mechanism in a state of combined normal and shear stress, i.e. the degradation of tensile and shear strengths, is monitored via a *work-softening* rule which entails tensile crack opening as well as tangential slip. As a result, a fracture energy release based plasticity model is obtained. The material parameters are physically transparent and are conveniently calibrated from characteristic response functions that can be observed experimentally in pure tension and in pure shear. Analytical predictions are compared with experimental results for the case when constant normal traction is applied while the slip displacement is monitored.

Contents

1 INTRODUCTION	4
2 CONCEPTS OF FRACTURING AND SLIP	5
3 FRACTURE/SLIP CRITERION	7
4 POSTFAILURE BEHAVIOR	8
5 UNIQUENESS OF RESPONSE - BRITTLE BEHAVIOR	12
6 CALIBRATION	17
7 APPLICATION	17
8 APPENDIX I: REFERENCES	19
9 APPENDIX II: NOTATION	21
10 APPENDIX III: THE CONSTRUCTION OF VORONOI POLYHEDRA IN THREE DIMENSIONS	23

1 INTRODUCTION

Degradation of macroscopic strength and stiffness properties during progressive failure of cementitious materials such as concrete, are closely tied to degradation mechanisms in the internal structure of the highly heterogeneous material. In order to quantitatively describe these mechanisms, the cementitious material is considered as a two-phase composite consisting of aggregates and mortar, and the interaction between these two constituents is modelled with an interface.

The constitutive behavior of this interface is considered as a most significant feature of the internal structure that often determines the overall response. Only few experimental investigations confirming this principal belief have been carried out by Chandra (1969). Numerical studies have been undertaken previously on highly idealized as well as on fairly realistic layouts of the internal structure involving aggregate and mortar interaction, Stankowski (1990), Willam et al. (1988), Roelfstra et al. (1985). Related studies on frictional interface behavior have been carried out by van Mier et al. (1988), Shah et al. (1987) and Atkinson et al. (1989) and on geomaterials by Goodmann (1980), Plesha et al. (1988,1989) and Gilette et al. (1983).

In this paper a relatively simple constitutive model, which reproduces the principal features of the interface behavior, will be developed and formulated in analogy to incremental plasticity for a continuum. This model is able to describe fracture and slip of the interface for an arbitrary combination of the normal and tangential tractions. A fracture criterion that defines the onset of tensile and/or shear debonding is suggested. This fracture criterion is of curvilinear extension of the Mohr-Coulomb with smooth transition between failure in tension and shear. Cohesive softening of the bond due to fracturing occurs for an arbitrary mode of loading whenever the fracture criterion is satisfied. In particular, a stress state comprising shear and compression will also induce degradation of the bond similar to bedonding in excessive tension. In the residual state only frictional resistance will be available in the presence of compressive stresses. Cases of particular interest are clearly direct tension, pure shear and

direct compression. The constitutive relations are regularized by the introduction of a recoverable adhesion component in the tangential as well as the normal directions. A non-associated slip rule is used in order to account for dilatancy effect in a realistic manner.

In Part II of this paper we discuss the numerical technique that is used to integrate the constitutive relations in a step-by-step fashion. A robust incremental solution technique is essential for the successful application of the constitutive model to solve boundary value problems.

2 CONCEPTS OF FRACTURING AND SLIP

In the proposed constitutive theory it is assumed that the relative displacement \mathbf{u} between the aggregates and the matrix can be decomposed into reversible and irreversible (elastic and plastic) parts that are denoted \mathbf{u}^e and \mathbf{u}^p respectively. In analogy to the static and dynamic components of dry friction, the elastic component \mathbf{u}^e will be referred to as *adherence*, whereas the normal and tangential components of \mathbf{u}^p will be called *slip* irrespective of the direction of relative motion. In the following derivations we will attempt to provide a formal structure to the two interfacial processes of tensile debonding and tangential slip. The relative displacement is thus decomposed in

$$\mathbf{u} = u_n \mathbf{e}_n + u_t \mathbf{e}_t \quad (1)$$

and

$$\dot{\mathbf{u}} = \dot{\mathbf{u}}^e + \dot{\mathbf{u}}^p \quad (2)$$

The unit base vectors \mathbf{e}_n and \mathbf{e}_t in the normal and tangential directions of the interface are attached to the matrix surface as indicated in Fig. 1. We shall now introduce the contact traction \mathbf{t} , which is further defined in terms of normal (t_n) and tangential (t_t) components

$$\mathbf{t} = t_n \mathbf{e}_n + t_t \mathbf{e}_t \quad (3)$$

The adhesion between the binder and the substrate may be expressed by means of a simple analogy to elasticity

$$\dot{\mathbf{u}}^e = \mathbf{C}^e \dot{\mathbf{t}}$$

or

$$\begin{bmatrix} \dot{u}_n^e \\ \dot{u}_t^e \end{bmatrix} = \begin{bmatrix} K_n^{-1} & 0 \\ 0 & K_t^{-1} \end{bmatrix} \begin{bmatrix} \dot{t}_n \\ \dot{t}_t \end{bmatrix} \quad (4)$$

where \mathbf{C}^e is the elastic compliance matrix that is defined by the incremental (tangent) normal and tangential stiffness moduli K_n and K_t . Typically, K_n is significantly larger in compression than in tension. A simple assumption that will be adopted here is that the stiffness property in the normal direction as expressed in Eq. 4 is bilinear, as shown in Fig. 2,

$$K_n = \begin{cases} K_n^+, & \text{if } t_n > 0 \text{ or } t_n = 0, \dot{t}_n > 0 \\ K_n^-, & \text{if } t_n < 0 \text{ or } t_n = 0, \dot{t}_n < 0 \end{cases} \quad (5)$$

where K_n^+ and K_n^- are material parameters with $K_n^- \gg K_n^+$ and compression being negative. These elastic stiffness parameters differ from the traditional concept of elastic moduli, as they denote the tangential stiffness in terms of force per length to the third power. In Eq. 5 it was assumed that there is no coupling between the normal and the tangential components, which can be viewed as zero dilatancy in the elastic range.

The interface properties can be attributed partly to the presence of asperities, voids, incomplete contacts, etc. within a thin layer. However, the width of this layer is negligible in comparison to the characteristic size of the 'microstructural elements'. The roughness, or 'wavyness', of the contacting surfaces will also influence the plastic properties. Although the introduction of reversible deformations in the interface is physically justified, the elastic moduli may be considered merely as numerical artifacts in order to regularize the resulting boundary value problem. In other words, the conventional unilateral contact condition $u_n \geq 0$ is abandoned in favor of the more versatile concept of a finite elastic stiffness in compression.

3 FRACTURE/SLIP CRITERION

In pure tension the strength is characterized by the tensile peak (or ultimate) strength $f_{n,u}$. In combined normal and shear loading, however, the strength comprises the adhesion $f_{t,u}$ between the different materials and the mobilized friction due to the presence of a normal traction $t_n \neq 0$. This friction is considered to be a consequence of the mineral to mineral surface friction and geometric roughness between the contacting surfaces. The adhesion, which is the equivalent of the cohesion within a continuous material, is sometimes called the slip limit.

Clearly, the two mechanisms of tensile debonding in the normal direction e_n and slip in the tangential direction e_t are physically connected in the sense that slip may be viewed as a consequence of a crack that develops along the interface, whereby the bond strength is degraded further. In the event that one or both mechanisms are activated it seems appropriate to introduce the notation *Fracture Criterion* for the surface in (t_n, t_t) -space that represents the onset of inelastic displacements. A simple *Fracture Criterion* can be expressed as

$$F = |t_t|^a - \frac{(f_{t,u})^a}{f_{n,u}}(f_n - t_n) = 0 \quad (6)$$

where f_n denotes the current value of the normal strength. The current value of the shear strength is denoted by f_t (and is used later). The peak, or initial, strength values are denoted $f_{n,u}$ and $f_{t,u}$ respectively, and it follows that

$$t_n \leq f_n, \quad 0 \leq f_n \leq f_{n,u} \quad (7)$$

$$|t_t| \leq f_t \quad (8)$$

The shape of the slip surface is such that the normal is horizontal at the tensile apex $(t_n, t_t) = (f_n, 0)$. Furthermore, a constant exponent $a > 1$, that determines the shape of the surface, is defined in terms of the coefficient of friction μ when $t_n = 0$ according to the expression

$$a = \frac{1}{\mu} \frac{f_{n,u}}{f_{t,u}} \quad (9)$$

as shown in Fig. 3. The current slip surface is obtained from the initial slip surface, defined by $f_n = f_{n,u}$, simply by translating the initial surface along the t_n -axis to the left, as illustrated in Fig. 4.

In order to obtain realistic dilatancy characteristics it is necessary to employ a non-associated slip rule. This is accomplished in the most straightforward way by assuming that the flow direction corresponds to the gradient of a plastic potential defined by the coefficient of dilatancy $\nu \leq \mu$ rather than the coefficient of friction μ . This can be expressed via a transformation matrix \mathbf{A} in the flow rule

$$\dot{\mathbf{u}}^p = \dot{\lambda} \mathbf{m}, \quad \mathbf{m} = \mathbf{A} \mathbf{n}, \quad \mathbf{n} = \partial F / \partial \mathbf{t} \quad (10)$$

where $\dot{\lambda} \geq 0$ is a plastic multiplier and

$$\mathbf{A} = \begin{bmatrix} 1 & 0 \\ 0 & \mu/\nu \end{bmatrix}, \quad \mathbf{n} = \begin{bmatrix} (f_{t,u})^a / f_{n,u} \\ a |t_t|^{a-1} \text{sign}(t_t) \end{bmatrix} \quad (11)$$

For large compressive stresses, the dilatancy should be small and may eventually vanish for large amounts of slip due to frictional wear of the surface asperities. Although an associated slip rule would display vanishing dilatancy when $t_n = -\infty$, the nonassociated rule offers the possibility to modulate normality and further suppress undesired dilatancy.

4 POSTFAILURE BEHAVIOR

In the present model we adopt the hypothesis that continued deformation after the onset of fracture/slip is accompanied by softening for any loading path. The debonding process will be therefore described via a *work-softening* hypothesis in the form of a suitable weighted fracture energy release measure κ , which is chosen (as the softening variable) according to the rate law

$$\dot{\kappa} = \langle t_n \rangle \dot{u}_n^p + t_{t,eff} \dot{u}_t^p \quad (12)$$

where $t_{t,eff}$ is the effective shear traction contributing to the debonding process during shearing and $\langle \cdot \rangle$ is the McAuley bracket defined as $\langle t_n \rangle = \frac{1}{2}(t_n + |t_n|)$,

extracting the tensile normal traction contributing to the softening. Assuming that $t_n = t_n(u_n^p)$ and $t_t = t_t(u_t^p)$ for any load path, we may define the fracture energies G_f^I and G_f^{II} as

$$G_f^I = \int_0^\infty f_n(u_n^p) du_n^p = \int_0^\infty t_n(u_n^p) du_n^p \quad \text{when } t_t = 0 \quad (13)$$

$$G_f^{II} = \int_0^\infty f_t(u_t^p) du_t^p = \int_0^\infty t_{t,eff}(u_t^p) du_t^p \quad \text{when } t_n = 0 \quad (14)$$

It should be noted at this point that the constants G_f^I and G_f^{II} are pertinent to the *interface* behavior and do not necessarily relate to those of the constituents of the cementitious composite. In fact, they are quite different. The hypothesis represented by Eq. 12 determines the behavior of the interface in the various modes of loading via the fracture energy release G_f^I and G_f^{II} in pure tension as well as in pure shear.

Following the assumption stated by Nilsson et al. (1984), Glemberg (1984) and Willam et al. (1984), we shall assume that the tensile strength is degrading exponentially from the peak value $f_{n,u}$ as

$$f_n(u_n^p) = f_{n,u} e^{-\alpha u_n^p}, \quad \alpha = f_{n,u} / G_f^I \quad (15)$$

The current amount of released energy κ in pure tension is defined as

$$\kappa(u_n^p) = \int_0^{u_n^p} f_n(v) dv = G_f^I \left(1 - \frac{f_n(u_n^p)}{f_{n,u}} \right) \quad (16)$$

where the last expression is obtained upon invoking Eq. 15. Alternatively, the relation in Eq. 16 can be inverted to yield

$$f_n(\kappa) = f_{n,u} \left(1 - \frac{\kappa}{G_f^I} \right) \quad (17)$$

The relations (15) and (17) are depicted in Fig. 5. It is noted that Eq. 16 gives $f_n(G_f^I) = 0$ as expected, although f_n vanishes asymptotically when it is expressed as a function of normal deformation u_n^p .

Defining the effective shear traction as

$$t_{t,eff} = k(t_t - f_{t,r}) \quad (18)$$

where k is the ratio of the fracture energy release in tension and shear, typically in the range $k \sim 0.01 - 0.1$

$$k = G_f^I / G_f^{II} \quad (19)$$

and $f_{t,r}$ is the residual shear strength that remains after maximum degradation has occurred

$$f_{t,r} = \begin{cases} 0 & , f_n \geq 0 \\ f_{t,u}(-t_n/f_{n,u})^{\frac{1}{a}} & , t_n \leq 0 \end{cases} \quad (20)$$

we now can integrate Eq. 12 in pure shear, where $t_n = 0$ and $t_t = f_t(u_t^p)$

$$\kappa(\infty) = k \int_0^\infty f_t(u_t^p) du_t^p = k G_f^{II} = G_f^I \quad (21)$$

where Eqs. 14 and 19 were used. In other words, when the interface has fractured completely in pure tension, then the shear resistance is also exhausted corresponding to the fact that the amount G_f^{II} of (shear) energy has dissipated and vice versa. From these assumptions it is apparent that the characteristics of the relation between f_n and u_n^p will strongly determine the behavior in combined fracture and slip, since $f_n(u_n^p)$ is taken as the universal relationship to describe the material response.

By invoking the yield criterion in order to express f_t in terms of f_n when $t_n = 0$ and by using Eq. 17, it is possible to integrate Eq. 12. This leads to a simple explicit expression of the relation $f_t(u_t^p)$:

$$f_t = f_{t,u} \left(1 - \frac{u_t^p}{\bar{u}_t} \right)^{\frac{1}{a-1}} \quad (22)$$

where \bar{u}_t is the finite value of u_t^p

$$\bar{u}_t = \frac{a}{a-1} \frac{G_f^{II}}{f_{t,u}} \quad (23)$$

that is obtained when $\kappa = G_f^H$. From Eq. 22 it is concluded that this value corresponds to the vanishing of the shear strength f_t , which means that $u_t = u_t^p = \bar{u}_t$ when $f_t = 0$ since $u_t^e = 0$ at this stage. By augmenting the relation (22) with the elastic component of u_t , we may derive the relation between u_t and f_t as

$$\frac{u_t}{\bar{u}_t} = 1 + \frac{f_t}{f_{t,u}} \left(\frac{f_{t,u}}{K_t \bar{u}_t} - \left(\frac{f_t}{f_{t,u}} \right)^{a-2} \right) \quad (24)$$

This relation is shown in Fig. 7 as the special case of $t_t(u_t)$ when $t_n = 0$. Since it is not possible to find a simple explicit expression for $t_t(u_t)$ when $t_n > 0$, all curves in Fig. 7 are obtained by numerical integration as will be discussed in a subsequent section of this paper. All response curves were obtained using the following material data:

$$f_{n,u} = 1 \quad f_{t,u} = 2 \quad \text{and} \quad k = 0.1$$

while the values of the exponent a and the normal traction t_n were varied.

It can be readily checked in Fig. 7 that the theoretical values of \bar{u}_t , as given by Eq. 23, is also obtained numerically. Furthermore, Fig. 7 also shows the interesting phenomenon that totally brittle behavior is obtained before the shear strength has completely degraded. From the results it seems that the value of a as well as t_n play a significant role for the brittleness. This behavior is of considerable concern for the numerical treatment, since it may cause premature breakdown of the integration algorithm due to the use of finite increments. An analysis of the spectral properties of the appropriate tangent matrix that aims at finding the stress level t_t when this 'snap-back' behavior occurs is carried out in the next subsection.

Fig. 8 shows the corresponding dilatancy in pure shear as well as for $t_n > 0$. For pure shear it is straightforward to find explicitly the relationship between u_t^p and $u_n = u_n^p$ when $t_n = 0$. Using the flow rule expressed by Eq. 10 and the expression for t_t in Eq.(22), we obtain

$$u_n = -\frac{\nu}{\mu} a \frac{f_{t,u}}{f_{n,u}} \ln \left(1 - \frac{u_t^p}{\bar{u}_t} \right) \bar{u}_t \quad (25)$$

It is seen that $u_n = \infty$ when $u_t = u_t^p = \bar{u}_t$ as shown also in Fig. 8.

Figs. 9 and 10 show the behavior for compressive contact stress, $t_n \leq 0$. While t_t approaches $f_{t,r}$ asymptotically for large amounts of slip (except in the special case when $t_n = 0$), the dilatancy displacement u_n^p is finite at the residual load level (except when $t_n = 0$) as shown in Fig. 10.

A final comment on the (in-) validity of the assumption that μ is constant may be appropriate. There seems to be experimental evidence that the behavior in shear depends on the two competing processes that may be described as adhesional softening and frictional hardening. The former process is treated in the theory described previously, while it would be possible to simulate frictional hardening by assuming that the internal friction μ is an increasing function of κ , i.e. $d\mu(\kappa)/d\kappa > 0$. The explicit choice of this functional relationship depends on the roughness of the contact surfaces. For successively increasing t_n the released energy is expected to decrease until a transition point is reached after which the response will be entirely hardening.

5 UNIQUENESS OF RESPONSE - BRITTLE BEHAVIOR

It is shown in Fig. 7 that totally brittle behavior was obtained before the shear strength was completely exhausted for constant $t_n > 0$, while this phenomenon seems not to occur in pure shear (when $t_n = 0$). It is possible to obtain completely brittle response also in pure tension depending on the *assumed* shape of the relation between f_n and u_n^p and provided that either K_n or G_f^I is sufficiently small. However, such brittleness would occur immediately post peak. Subsequently, we shall investigate the possibility that the response becomes non-unique under mixed control of displacements and tractions within the framework of elastic-plastic behavior.

It will be assumed that t_1 and u_2 are the control variables, where t_1 may be either t_n or t_t , whereas u_2 plays the role of either u_t or u_n . The relationship in Eq. 5 may

then be rearranged as

$$\begin{bmatrix} \dot{u}_1^e \\ \dot{t}_2 \end{bmatrix} = \begin{bmatrix} K_1^{-1} & 0 \\ 0 & K_2 \end{bmatrix} \begin{bmatrix} \dot{t}_1 \\ \dot{u}_2^e \end{bmatrix} \quad (26)$$

The consistency condition $\dot{F} \leq 0$ can be written explicitly as

$$\dot{F} = n_1 \dot{t}_1 + n_2 \dot{t}_2 + \frac{\partial F}{\partial \kappa} \dot{\kappa} \leq 0 \quad (27)$$

where

$$n_i = \frac{\partial F}{\partial t_i}, \quad i = 1, 2 \quad (28)$$

From the work-softening hypothesis 12 and the flow rule 11 we obtain

$$\dot{\kappa} = \dot{\lambda} \mathbf{s}^T \mathbf{m} \quad (29)$$

where

$$\mathbf{s} = [\langle t_n \rangle, k(t_t - f_{t,r})]^T \quad (30)$$

and where the flow direction \mathbf{m} is given by Eq. 11. Inserting the expression (29) into the condition (26), we can rewrite the condition (27) in terms of the control variables t_1 and u_2

$$\dot{F} = n_1 \dot{t}_1 + n_2 K_2 \dot{u}_2 - \dot{\lambda} (H + n_2 K_2 m_2) \leq 0 \quad (31)$$

where H is the generalized hardening modulus

$$\begin{aligned} H &= -\frac{\partial F}{\partial \kappa} \mathbf{s}^T \mathbf{m} \\ &= -\frac{(f_{t,u})^a}{G_f^I} \left[\frac{\langle t_n \rangle}{f_{n,u}} (f_{t,u})^a + k (|t_t| - |f_{t,r}|) \frac{\mu}{\nu} a |t_t|^{a-1} \right] \end{aligned} \quad (32)$$

It is noted that the expression (32) is independent of the particular choice of control variables.

Introducing the 'plastic modulus' K under mixed control

$$K = H + n_2 K_2 m_2 \quad (33)$$

and the 'loading function' ϕ

$$\phi = n_1 \dot{t}_1 + n_2 K_2 \dot{u}_2 \quad (34)$$

we may rewrite the condition 31 as

$$\dot{F} = \phi - \dot{\lambda} K \leq 0 \quad (35)$$

The general loading criterion for elastic-plastic behavior is conveniently given in terms of the Kuhn - Tucker conditions

$$\dot{\lambda} \geq 0, \quad \dot{F} \leq 0, \quad \dot{\lambda} \dot{F} = 0 \quad (36)$$

and, consequently, from these criteria and 34 we obtain

$$\dot{\lambda} = \phi/K > 0 \quad (P), \quad \phi \leq 0 \quad (N, E) \quad (37)$$

where P stands for plastic loading, while N and E denote neutral loading and elastic unloading respectively. The requirement for a non-ambiguous loading criterion, i.e. that the loading cases (P) and (E) are mutually exclusive in terms of the value of ϕ , is that $K > 0$. This requirement is necessary and sufficient to assure a unique response for the chosen mixed mode of control.

From Eqs. 26 and (37) the tangent relationship in plastic loading can now be established in the form

$$\begin{bmatrix} \dot{u}_1 \\ \dot{t}_2 \end{bmatrix} = \left(\begin{bmatrix} K_1^{-1} & 0 \\ 0 & K_2 \end{bmatrix} + \frac{1}{K} \begin{bmatrix} m_1 n_1 & m_1 K_2 n_2 \\ -m_2 K_2 n_1 & -m_2 K_2^2 n_2 \end{bmatrix} \right) \begin{bmatrix} \dot{t}_1 \\ \dot{u}_2 \end{bmatrix} \quad (38)$$

or, in compact form,

$$\dot{y} = \mathbf{E} \dot{x}, \quad \mathbf{E} = \mathbf{E}^e + \frac{1}{K} \mathbf{m}^* \mathbf{n}^{*T} \quad (39)$$

where

$$\mathbf{x} = \begin{bmatrix} t_1 \\ u_2 \end{bmatrix}, \quad \mathbf{y} = \begin{bmatrix} u_1 \\ t_2 \end{bmatrix}, \quad \mathbf{m}^* = \begin{bmatrix} m_1 \\ -K_2 m_2 \end{bmatrix}, \quad \mathbf{n}^* = \begin{bmatrix} n_1 \\ K_2 n_2 \end{bmatrix} \quad (40)$$

In order to investigate the characteristics of the constitutive relation (39), especially with regard to the possibility of completely brittle behavior, it is illuminating

to first establish the spectral properties of \mathbf{E} . In fact, brittle behavior corresponds to (at least) one eigenvalue of \mathbf{E} being infinitely large. It is then convenient to consider the special eigenvalue problem

$$\mathbf{E} \mathbf{x}^{(i)} = \lambda^{(i)} \mathbf{E}^e \mathbf{x}^{(i)} \quad (41)$$

It can be shown easily, c.f. Runesson et al. (1989), that one eigenvalue is

$$\lambda^{(1)} = 1 + \frac{1}{K} \mathbf{n}^{*T} (\mathbf{E}^e)^{-1} \mathbf{m}^* = \frac{H + n_1 K_1 m_1}{H + n_2 K_2 m_2} \quad (42)$$

corresponding to the eigenmode

$$\mathbf{x}^{(1)} = \alpha (\mathbf{E}^e)^{-1} \mathbf{m}^* = \alpha \begin{bmatrix} K_1 m_1 \\ -m_2 \end{bmatrix}, \quad \alpha = \text{scalar} \quad (43)$$

The second eigenmode $\mathbf{x}^{(2)}$ is orthogonal to \mathbf{n}^* corresponding to the unit eigenvalue $\lambda^{(2)} = 1$. In fact, $\mathbf{x}^{(2)}$ defines neutral loading since we have

$$\mathbf{n}^{*T} \mathbf{x}^{(2)} = n_1 \dot{t}_1^{(2)} + n_2 K_2 \dot{u}_2^{(2)} = \phi = 0 \quad (44)$$

In order to avoid brittle behavior, i.e. $\lambda^{(1)} \neq -\infty$, for arbitrary mixed control, it follows from Eq. 42 that we must require $K > 0$. This condition was established previously as the condition for non-ambiguous plastic loading.

Consider first the case of pure tension, i.e. $t_n (= u_2)$ changes while $t_t (= t_1) = 0$. Since $t_n \geq 0$, we obtain $f_{t,r} = 0$ from Eq. 20, and H becomes

$$H = -\frac{(f_{t,u})^{2a}}{G_j^l} \frac{t_n}{f_{n,u}} \quad (45)$$

and, so, the condition $K > 0$ becomes

$$K_n - \frac{t_n f_{n,u}}{G_j^l} > 0 \quad (46)$$

The most critical situation occurs when $t_n = f_{n,u}$, i.e. at the onset of tensile debonding, which implies that the criterion for unconditional uniqueness of the entire re-

sponse function in pure tension is

$$K_n > \frac{(f_{n,u})^2}{G_f^I} \quad (47)$$

This condition can also be obtained in a more direct fashion by differentiating the basic relation (15), invoking the elastic portion and imposing the condition that the total compliance relating \dot{u}_n and \dot{t}_n does not vanish. Clearly, the condition (47) corresponds entirely to the one associated with the "smeared fictitious crack" model for an equivalent continuum; see Ottosen (1986) and Willam et al. (1985).

Consider next the case that $t_n (= t_1) \geq 0$ is fixed while $u_t (= u_2)$ is assumed to vary in a prescribed fashion. In this case, since $t_n \geq 0$, it follows that

$$H = -\frac{(f_{t,u})^a}{G_f^I} \left(\frac{t_n}{f_{n,u}} (f_{t,u})^a + \frac{ka\mu}{\nu} |q_t|^a \right) \quad (48)$$

and, so, the condition $K > 0$ becomes

$$|t_t|^{2a-2} - \frac{(f_{t,u})^a}{aK_t G_f^{II}} |q_t|^a - \frac{\nu t_n (f_{t,u})^{2a}}{\mu a^2 f_{n,u} K_t G_f^I} > 0 \quad (49)$$

In the special case of pure shear, $t_n = 0$, we obtain the condition

$$|t_t|^{a-2} - \frac{(f_{t,u})^a}{a K_t G_f^{II}} > 0 \quad (50)$$

If $1 \leq a \leq 2$ the most critical situation appears for $|t_t| = f_{t,u}$, which gives the condition for a unique response curve

$$K_t > \frac{(f_{t,u})^2}{a G_f^{II}} \quad (51)$$

If $a > 2$ the condition 51 can never be satisfied for the entire response curve whatever parameter values are chosen. Completely brittle behavior is obtained when

$$\frac{|t_t|}{f_{t,u}} = \left(\frac{(f_{t,u})^2}{a K_t G_f^{II}} \right)^{\frac{1}{a-2}} \quad (52)$$

It is interesting to note that the condition (52) can also be obtained from the relation in Eq.24, when it is required that the compliance vanishes. Furthermore, it follows from Eq.24 that the corresponding value of u_t is

$$\frac{u_t}{\bar{u}_t} = 1 + (a - 2) \left(\frac{(f_{t,u})^2}{a K_t G_f^{II}} \right)^{\frac{a-1}{a-2}} \quad (53)$$

It is noted that $u_t/\bar{u}_t > 1$ when $a > 2$. Consequently, a 'snap-back' behavior would be observed at further reduction of the shear strength f_t .

The anticipated behavior is confirmed in the Figs. 7 and 11 for the values $a = 1.5$ and $a = 2.5$. In the latter case, brittle behavior is obtained for $t_t/f_{t,u} = 0.102$ and $u_t/\bar{u}_t = 1.076$ when the value $G_f^{II} = 0.005???$ was chosen corresponding to $\bar{u}_t = 0.0041667$.

6 CALIBRATION

Except for the elastic moduli K_n and K_t , the suggested model involves the parameters G_f^I , G_f^{II} (or k), $f_{n,u}$, $f_{t,u}$, μ , ν . The parameters G_f^I and $f_{n,u}$ are determined from a uniaxial tension test, while G_f^{II} and $f_{t,u}$ are obtained in pure shear. At least one more shear test is needed, say for $t_n < 0$, where values $t_t = \bar{t}_t$ at the onset of fracturing/slip are recorded. At this stage we have $f_n = f_{n,u}$ and Eq. 6 gives

$$a = \frac{\ln(1 - \frac{t_n}{f_{n,u}})}{\ln(|\bar{t}_t| / f_{t,u})} \quad (54)$$

and μ is obtained with Eq. 9. A least squares fit for several experiments (for different t_n) will provide a rational calibration.

The only remaining task is to determine the dilatation parameter ν . Rewriting Eq. 25 in terms of u_n/\bar{u}_t versus u_t^p/\bar{u}_t , we may solve for ν when all other parameter values have been determined.

7 APPLICATION

The predictive capabilities of the proposed constitutive theory are compared to two kinds of experiments. In the first category, the interface is physically represented by a mortar joint between two masonry bricks, which are displaced relative to one another. Details of the experiment are described by Attkinson (1989) and the setup is schematically illustrated in Fig. 11. In this form of experimental arrangement it is reasonable to assume that the observed deformations are confined to the mortar layer since the bricks are superior in strength and stiffness by at least one order of magnitude compared to the masonry mortar. Fig. 12 shows the analytical load-displacement predictions of the constitutive model and the experimental results for three levels of constant normal compressive load. In these particular experiments the normal stress was maintained at a constant level while the shear was applied by controlled tangential displacement.

The second set of experimental results were obtained from pilot studies currently performed at the University of Colorado, in which mortar-aggregate interface characteristics are investigated. In these experiments, the mortar is represented by a concrete mix in which particles with a diameter larger than 2.8 mm have been omitted. The aggregate is represented by a 6.0 mm thick granite plate or disk whose surfaces have been carefully treated by sandblasting to ensure uniform and competent bonds with the adjacent mortar. A mortar disk having 50 mm diameter and a uniform thickness of 25 mm is cast directly on this granite plate, which have been glued to a base aluminum plate with structural epoxy. Several granite disk - aluminum base assemblies have been manufactured to test various series of mortar-granite interfaces. After curing, the specimen is placed into a direct simple shear apparatus, and a aluminum top plate that is mounted in a loading frame, is glued in situ to the top surface of the mortar disk. The vertical loading frame allows the application of normal compressive or tensile loads. Shearing is applied by controlled displacement of the base assembly sledge system on which the base aluminum plate has been mounted. A previously

mentioned the vertical load was kept constant during the experiments. However, due to inadequate stiffness of the test apparatus, a stable post-peak response was not obtained, and clearly, the degree of instability increases as the normal compression increased.

Fig. 13 shows the obtained results along with the analytical predictions of the proposed model at the constitutive level. The displayed horizontal displacements are relative displacements between the top and base aluminum plates. Since the granite plates are far stiffer than the mortar, the measured displacements reflect essentially the deformation of the interface and the mortar, except at the residual strength after the interface has failed. From these considerations, it has to be concluded, that the interface properties during loading and softening have to be determined from an inverse identification procedure, in which the entire specimen is modeled as a miniature structure and realistic boundary condition are applied, as illustrated in Fig. 14.

ACKNOWLEDGEMENTS

The authors gratefully acknowledge the financial assistance provided by Grant AFOSR-89-0289 and the support of Dr. Spencer Wu.

8 APPENDIX I: REFERENCES

- Atkinson, R.H., Saeb, S., Amadei, B., Sture, S. (1989), "Response of Masonary Bed Joints in Direct Shear", *ASCE J. Struct. Eng.*, Vol. 115, No. 9, pp. 2276-2296
- Chandra, S. (1969), "Fracture of Concrete under Monotonically Increasing, Cyclic and Sustained Loading", *Ph.D. Thesis, Dept. CEAE, University of Colorado, Boulder, Colorado*
- Gillette, D., Sture, S., Ko, H.-Y., Gould, M.C., Scott, G.A. (1983), "Dynamic Behavior of Rock Joints", *Proc. 24th U.S. Symposium on Rock Mechanics, Texas A & M Univ., 1983* pp. 163-179.

- Glemberg,R. (1984), "Dynamic Analysis of Concrete Structures", *Dept. of Struct. Mech.*, Publ. 84:1, Chalmers University of Technology, Gothenburg, Sweden
- Goodman, R.E. (1980), "Introduction to Rock Mechanics", *John Wiley & Sons*, New York, N.Y.
- Nilsson,L., Oldenburg,M. (1984), "Nonlinear Wave Propagation in Plastic Fracturing Materials - A Constitutive Modelling and Finite Element Analysis", *IUTAM Symposium: Nonlinear Deformation Waves*, Tallin 1982, Springer Verlag, Berlin 1982, pp. 209-217
- van Mier,J.G.M, Nooru-Mohamed,M.B. (1988), "Failure of Concrete under Tensile and Shear Like Loadings", *Int. Workshop on Fracture Toughness and Fracture Energy-Test Methods for Concrete and Rock*, Oct.12-14,1988, Tohoku University, Sendai, Japan
- Ottosen,N.S. (1986), "Thermodynamical Consequences of Strain-Softening in Tension", *J. Eng. Mech.*, ASCE, Vol. 112, No. 11, pp. 1152-1164
- Plesha,M.E., Haimson,B.C. (1988), "An Advanced Model for Rock Joint Behavior: Analytical, Experimental and Implementational Considerations", *Proc. 29th Symp. on Rock Mechanics*
- Plesha,M.E., Ballarini,R., Parulekar,A., (1989), "Constitutive Model and Finite Element Procedure for Dilatant Contact Problems", *ASCE J. Eng. Mech.*, Vol. 115, No. 12, pp. 2649-2668
- Roelfstra,P.E., Sadouki,H., Wittmann,F.H. (1985), "Le Béton Numérique", *Materials and Structures*, RILEM, Vol. 118, No. 107, pp. 309-317
- Runesson,K., Mroz,Z. (1989), "A Note on Non-Associated Plastic Flow Rules", *Int. J. Plasticity*, Vol. 5, pp. 639-658
- Shah,S.P., Sankar,R. (1987), "Internal Cracking and Strain Softening Response of Concrete under Uniaxial Compression", *Report Center of Concrete and Geomaterials, Technological Institute, Northwestern University, Evanstone, Il.*
- Stankowski,T. (1990) Numerical Simulation of Progressive Failure in Particle Composites, *Ph.D. Thesis, C.E.A.E. Department, University of Colorado, Boulder, Col-*

orado Willam,K., Bicanic,N., Sture,S. (1984),”Constitutive and Computational Aspects of Strain-Softening And Localization in Solids”, *ASME/WAM 1984 Symposium on Constitutive Equations, Macro and Computational Aspects*, (Ed. K. Willam), ASME Vol G00274, New York, N.Y., pp 233-252

Willam,K., Pramono,E., Sture,S. (1985),”Stability and Uniqueness of Strain-Softening Computations”,*Europe - U.S. Symposium on Finite Element Methods for Non-linear Problems*, (Eds. Bergan, Bathe, Wunderlich), Springer Verlag, Berlin, pp. 119-142

Willam,K.J., Stankowski,T., Runesson,K., Sture,S. (1988),” Simulation Issues of Distributed and Localized Failure Computations”, *France - U.S. Workshop on Strain Localization and Size Effect Due to Cracking and Damage*, ENS Cachan, France, (Eds Mazars and Bažant, Elsevier Appl. Science, pp. 363-378

9 APPENDIX II: NOTATION

A = transformation matrix

a = exponent of fracture/slip function

C = compliance matrix

F = fracture/slip function

f = tensile/shear strength

G_f^I, G_f^{II} = energy release in tension and shear (material constants)

H = hardening modulus

k = material constant

K_n, K_t = elastic normal and tangential stiffness moduli

K = plastic modulus

e_n, e_t = normal and tangential base vectors

m = gradient of plastic potential

n = gradient of fracture function

t = vector of contact traction

\mathbf{s} = vector of effective traction

\mathbf{u} = vector of relative displacements

\mathbf{x} = eigenmode

α = coefficient

κ = measure of released fracture energy

λ = plastic multiplier; eigenvalue (with superscript)

ϕ = loading function

μ = coefficient of friction

ν = coefficient of dilatancy

Subscripts

n = normal direction

r = residual strength

t = tangential direction

n, u = initial (ultimate) tensile strength

t, u = initial (ultimate) shear strength

Superscripts

$(\dot{\cdot})$ = rate, differentiation with respect to (pseudo)time

e = elastic

p = plastic

The Construction of Voronoi Polyhedra in Three Dimensions

In this section, we describe the construction of Voronoi polyhedra in three dimensions. The procedure is an extension of the algorithm that we employed in two dimensions, and which we used to generate the topology of the complete composite body comprising aggregate and matrix.

We recall that a Voronoi polyhedron with a given center (or pole) in an assembly of n centers is defined as the volume of the space that contains all points closer to this center than to any other center in the assembly. The vertices of these polyhedra are those points which are equidistant to four adjacent centers. The bounding surfaces or limiting boundaries of a polyhedron around a center i are established by vectors pointing from this center to adjacent centers j , and the origin of planes are the midpoints of these vectors. Clearly, due to the definition, the Voronoi polyhedra are convex.

The algorithm that we use to construct polyhedra employs these properties. In order to compute the (Cartesian) coordinates of each vertex, we have to solve the following set of four simultaneous quadratic equations

$$(x_p - x)^2 + (y_p - y)^2 + (z_p - z)^2 = r^2, \quad p = i, j, k, l \quad (1)$$

Again, we emphasize that the vertex is the location which is equidistant to the subset of four centers i, j, k, l of the assembly of n centers. Clearly, the set of quadratic equations can be reduced to three linear equations, which can readily be solved. In order to be a valid vertex, the definition of the polyhedra requires that this particular vertex is closer to the centers of the subset i, j, k, l that we are considering than any other center, and this test is used to accept or reject a vertex.

Once the vertex is accepted, it has to be labeled such that it is easily retrieved for

the construction of the bounding surfaces of the polyhedra. This is done efficiently by defining a three-dimensional array of the size $n_c \times n_f \times n_p$, where n_c is the total number of centers, n_f is the maximum number of faces in the polyhedron, and n_p is the maximum number of vertices defining the polygonal circumference of a polyhedron face. The last two numbers have to be estimated and depend on the distribution pattern of the centers. For the most regular and simple pattern which generates cubical or prismatic Voronoi polyhedra, n_f is equal to six (6) and n_p is equal to four (4). Highly irregular patterns require significantly larger n_f and n_p , e. g. $n_f > 15$ and $n_p = 10$. Each valid vertex is now consecutively numbered and stored in the array according to the indices i, j, v_p where $v_p = 1, \dots, n_p$ and i, j are the two centers on opposite sides of the polyhedron face. Since the vertex is related or connected to at least three faces, it will be recorded at least three times in the array. Cases involving more than three planes intersecting in one point are rare for irregular patterns of centers. For example consider the following case: Vertex no. 10 has been computed as being equidistant to centers 1, 2, 3, 4 and has been found to be valid. The vertex is part of the planes intersecting the line between the centers (1,2), (1,3) and (1,4). Thus, information pertaining to this vertex will be stored three times with these particular entries in the three-dimensional array.

This procedure has to be repeated for all possible subsets of centers i, j, k, l and the number of loops will be $\binom{n_c}{4}$. The number of loops can be reduced by defining a neighborhood for each center. For this purpose, the distances R between all centers are computed. A sphere with radius of approximately $R_{max} + R_{min} = R_n$ defines a neighborhood for each center i , which contains all adjacent centers j, k, l , which are of interest for constructing a polyhedron around center i . The size of the radius R_n of the sphere depends on the distribution pattern of centers, however, in the two dimensional

case it has been found to be sufficiently large.

When all vertices are computed, the bounding surfaces or limiting boundaries of the polyhedra are readily established. The polygon drawn in the surface plane between centers i and j are the vertices stored in the array $i, j, n, n = 1, \dots, n_p$.

The remaining consists of constructing the exterior surfaces of the domain subdivided into Voronoi polyhedra. This is achieved by first identifying all centers in the vicinity of the exterior surfaces, e. g. in a distance less than approximately $2 \times R_{max}$. In this second step we consider these centers i and only two other sets of centers j and k in their neighborhoods. The center(s) i is reflected on the exterior surface defining a point i' outside of the material. Three centers i, j, k form now together with point i' a subset from which a vertex can be computed as described above. Since this vertex is on the plane intersecting i and i' , it will be on the exterior surface. This vertex is stored only once in the three-dimensional array with the entry i, i' . Again, this loop has to be repeated for all centers in the vicinity of the material surfaces.

The algorithm can be summarized as follows:

1. Compute the distances between all centers, n , of the assembly and define the size of the neighborhood.
2. Identify for each center, i , those centers that are in the neighborhood, and which are relevant for the construction of the polyhedron around the center i .
3. Compute the vertices around each center, and check the validity of using the centers in the neighborhood and store them in a three-dimensional array.
4. Identify those centers which are close to the bounding surface of the domain considered.

5. Compute the vertices on the bounding surface, test them for their validity, and store the relevant information.

After completing the computations of the vertices, the topology of the polyhedra is completely defined within a three-dimensional array. The index i defines the polyhedron and together with index j the bounding surfaces of the polyhedron are labeled. The points with indices $i, j, k, l = 1, \dots, n_p$ define a polygon enclosing in the bounding surface i, j . In the event these polygons do not close, the size of the neighborhood has to be increased.

Reference

Finney, J. L. "A Procedure for the Construction of Voronoi Polyhedra", *J. Comp. Physics*, 1979, Vol. 32, pp. 137-143.

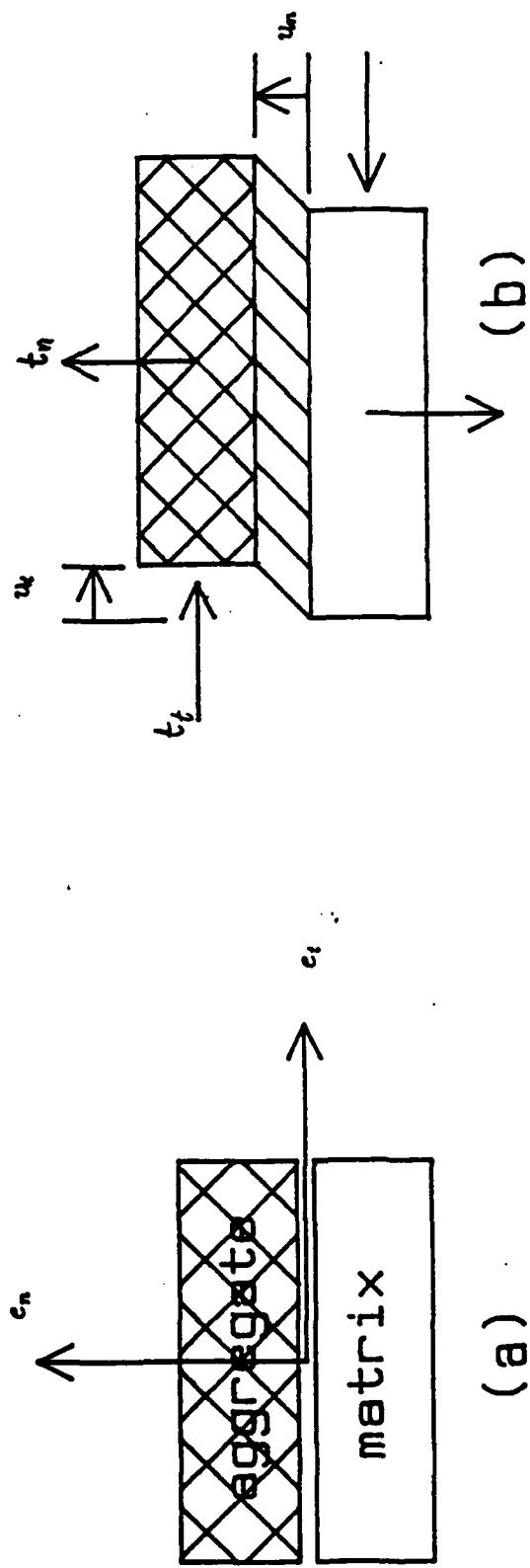


Figure 1: Definition of Forces and Relative Displacements

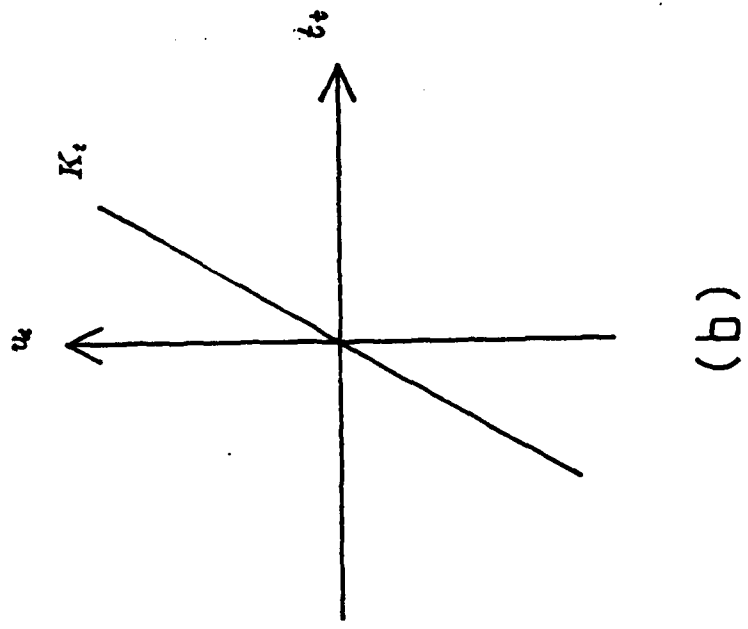
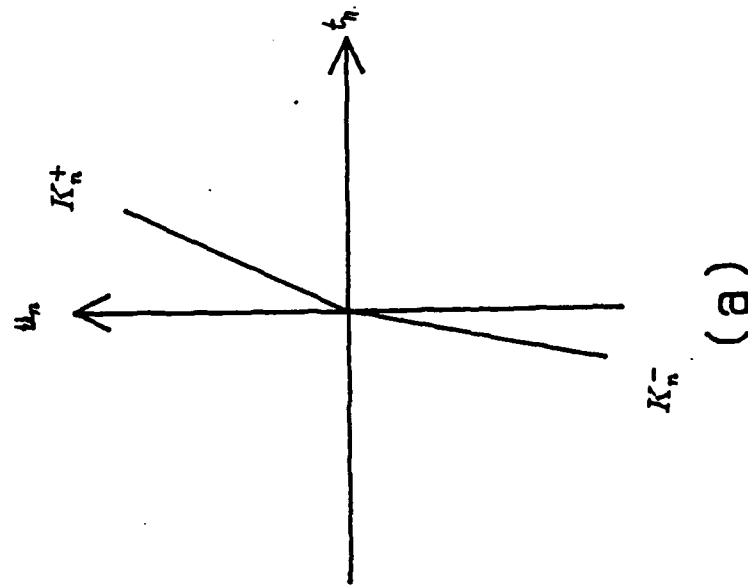


Figure 2: (a) Normal and (b) Tangential Elastic Stiffness

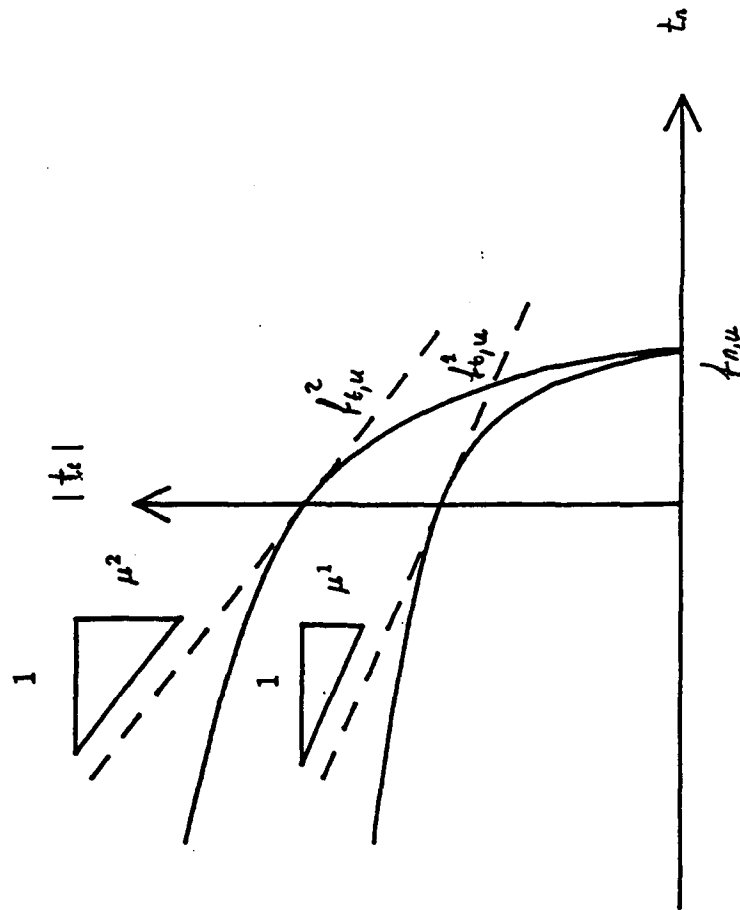
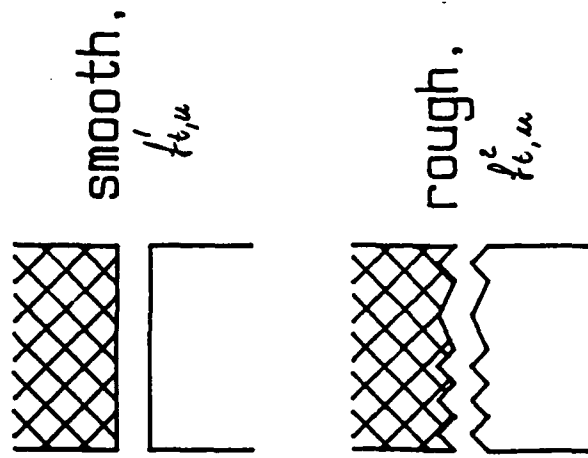


Figure 3: Fracture/Slip Criterion

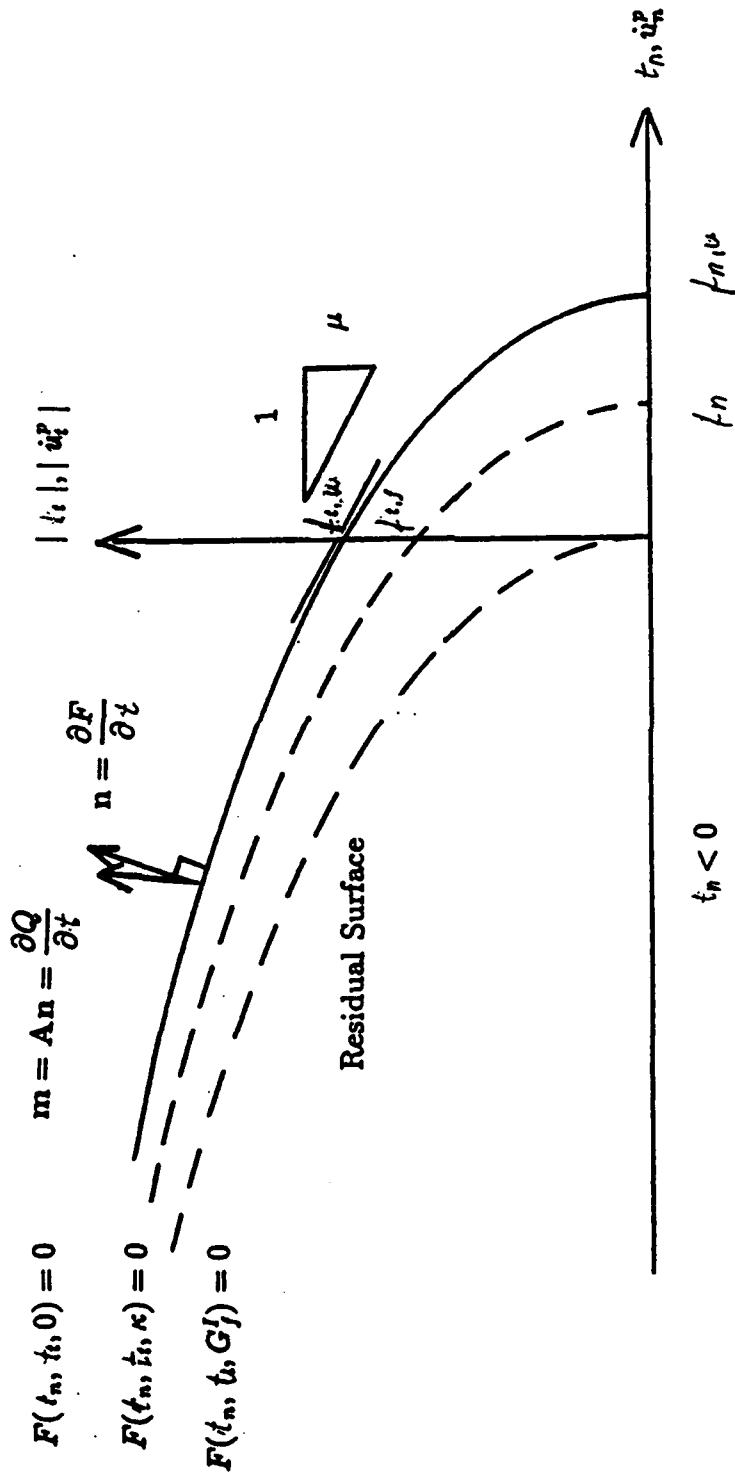
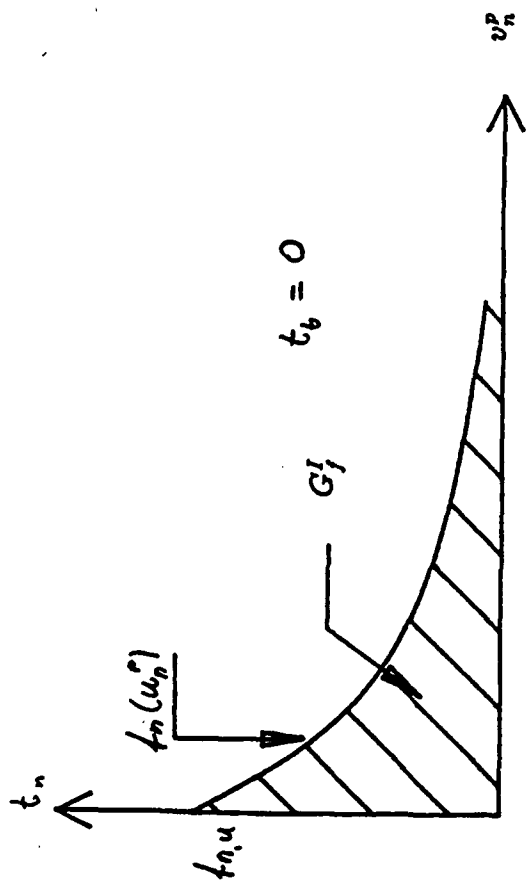
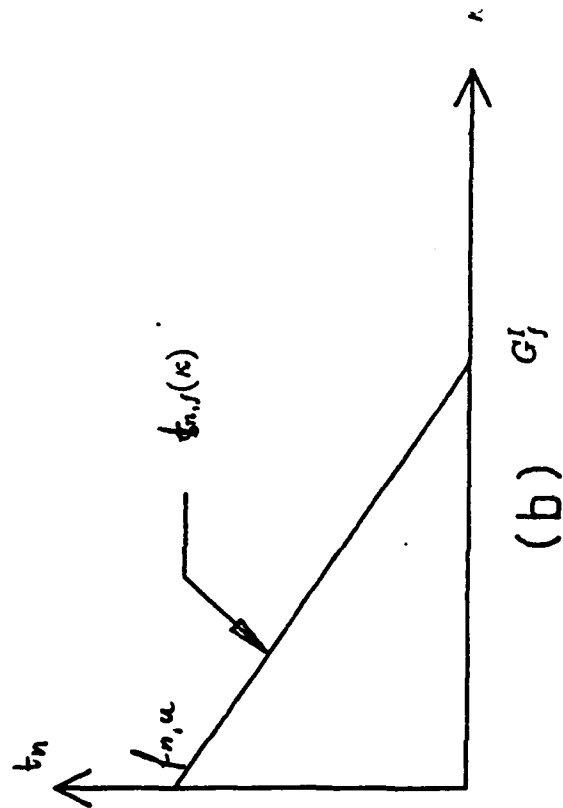


Figure 4: Softening Mechanism of Fracture/Slip Surface



(a)



(b)

Figure 5: (a) Energy Release and (b) Energy Release Rate in Pure Tension

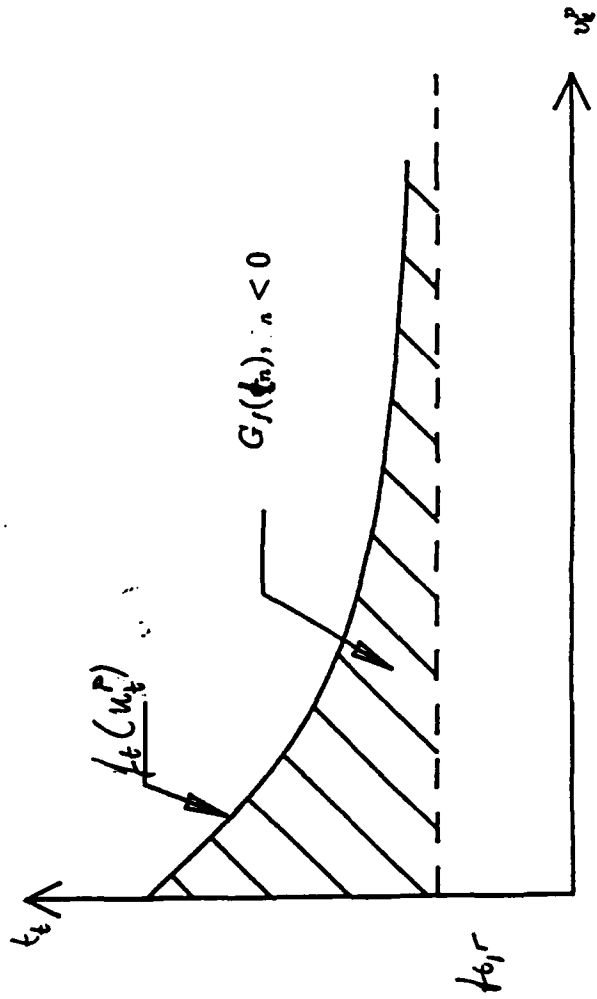
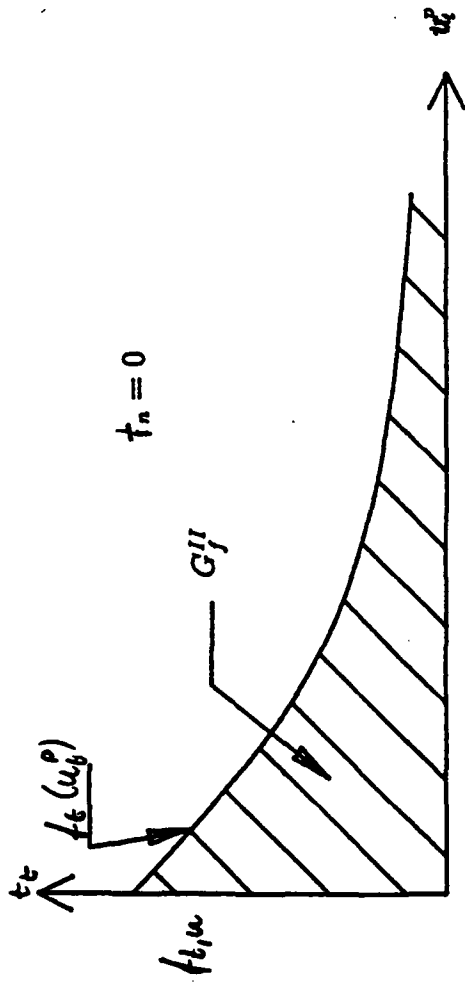


Figure 6: (a) Energy Release in Pure Shear and (b) Combined Shear and Compression

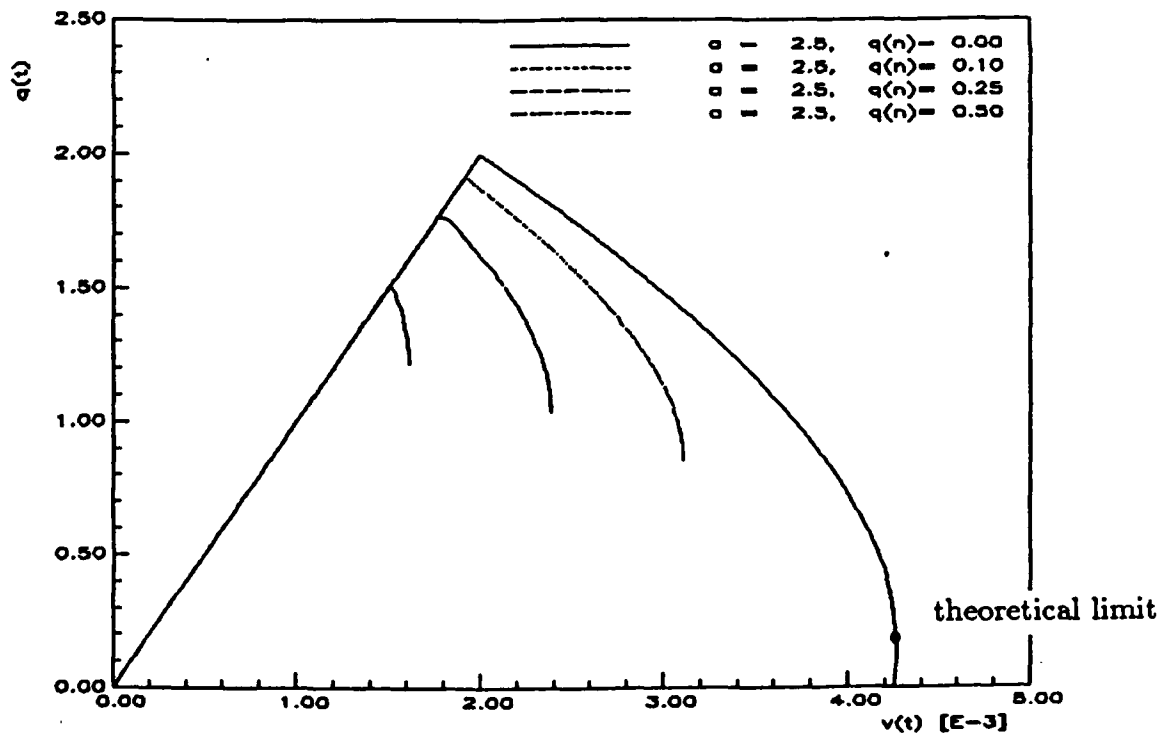
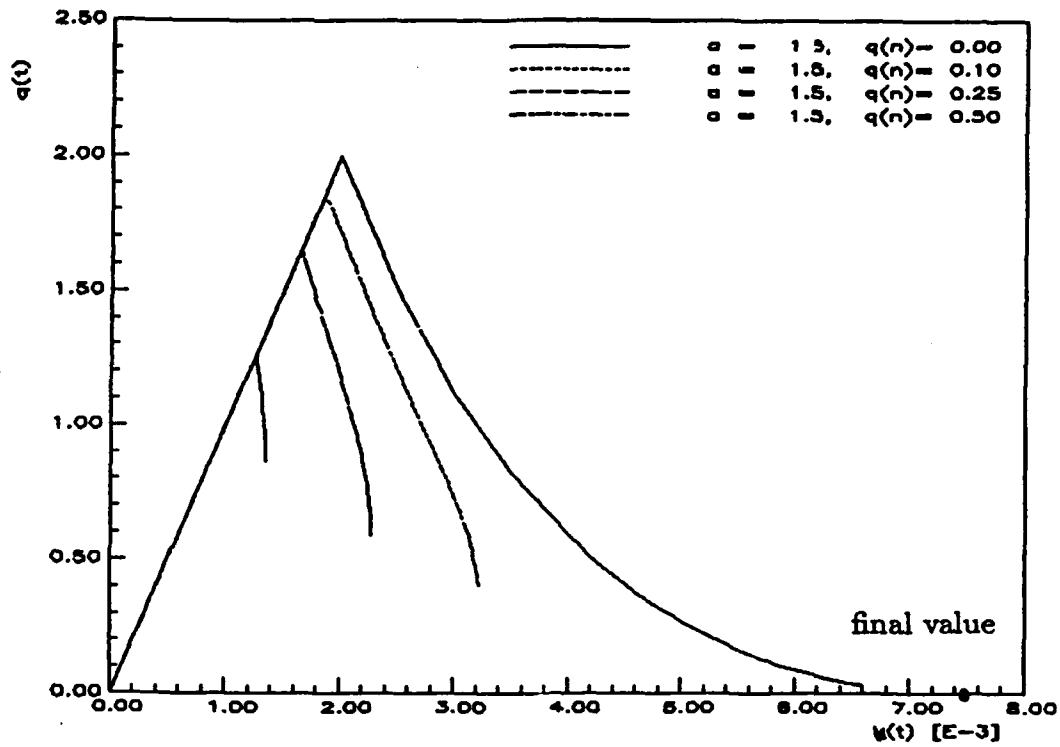


Figure 7: Shearing under Constant Tension for Two Values of Exponent α

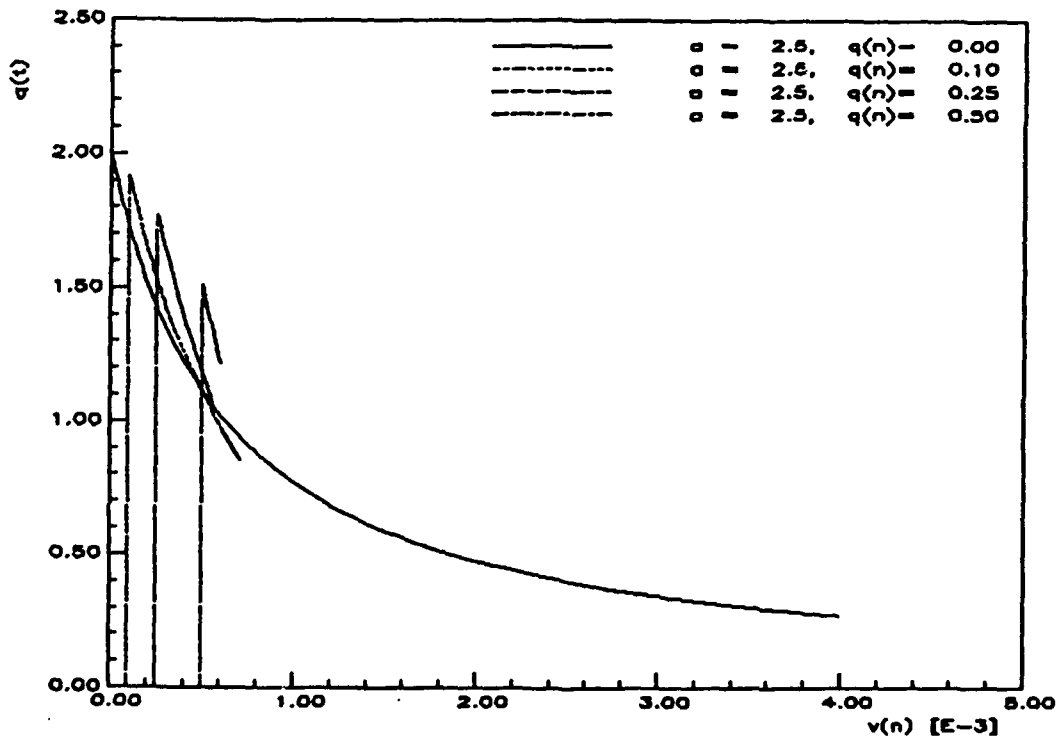
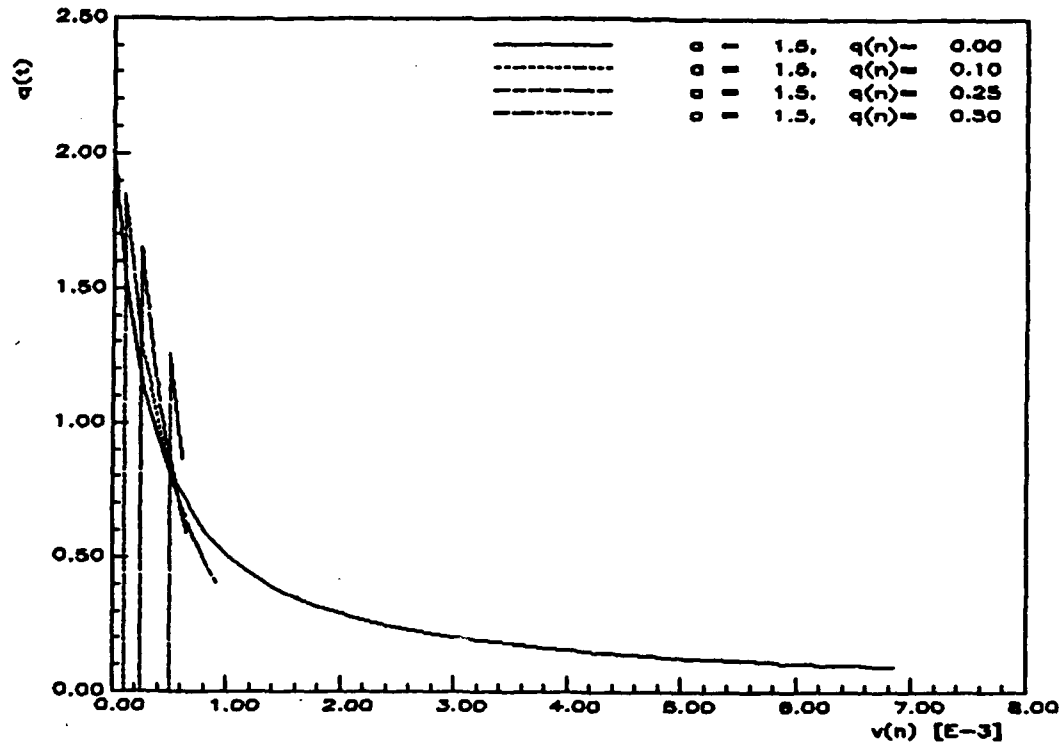


Figure 8: Shearing under Constant Tension for Two Values of Exponent α

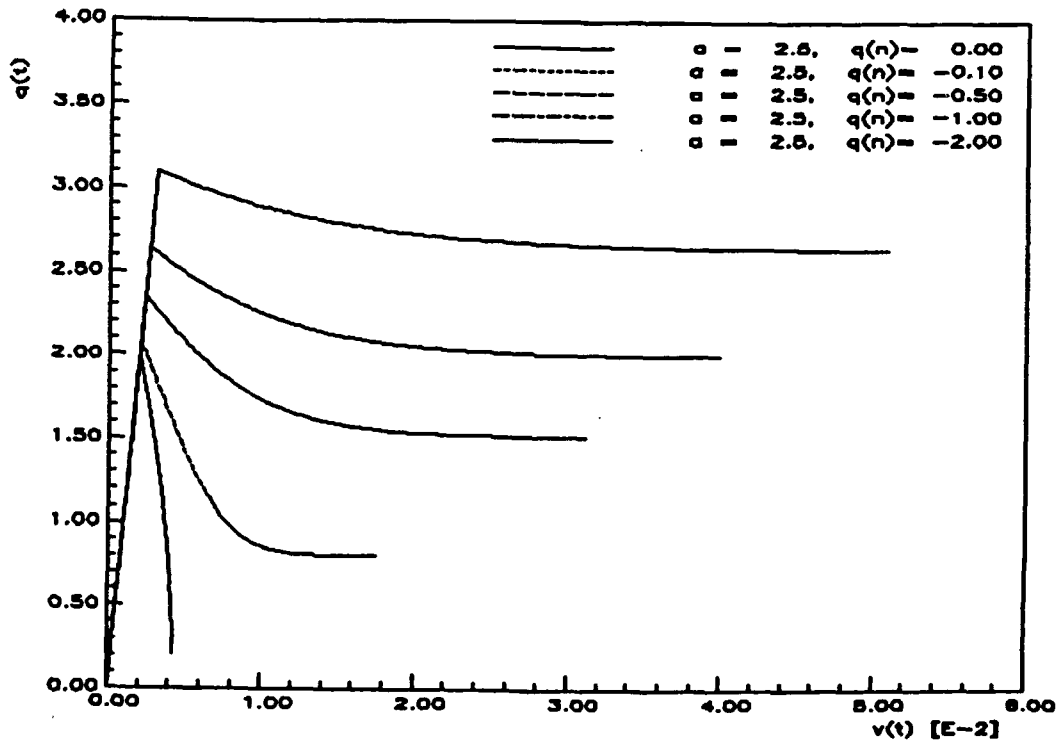
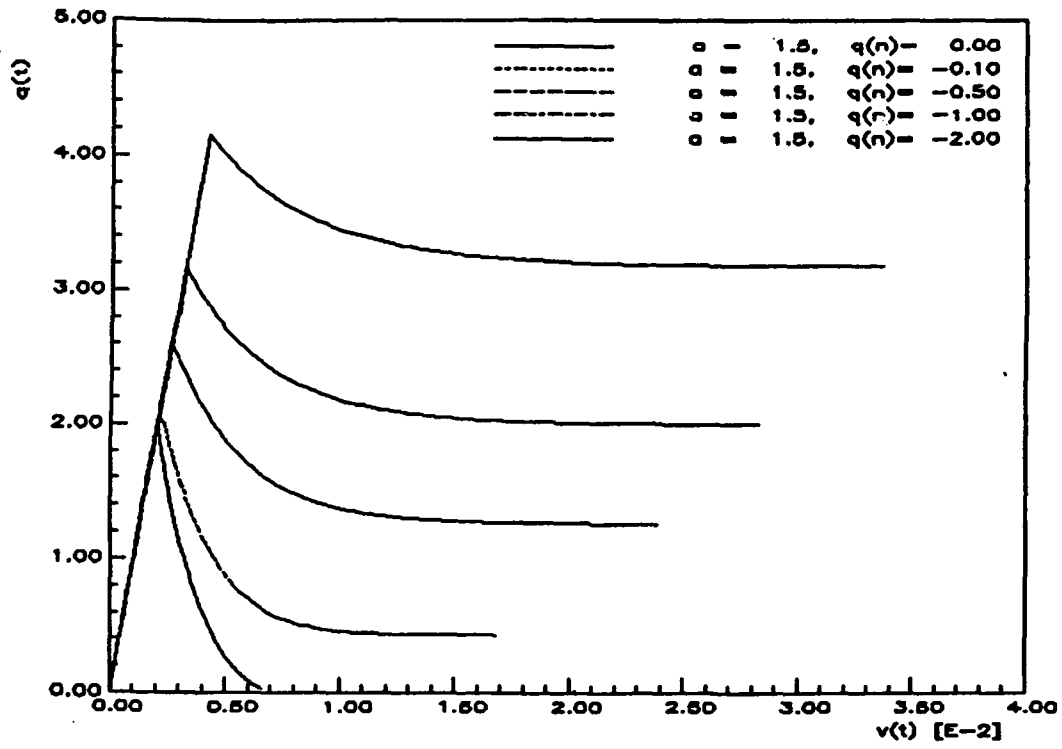


Figure 9: Shearing under Constant Compression For Two Values of Exponent α

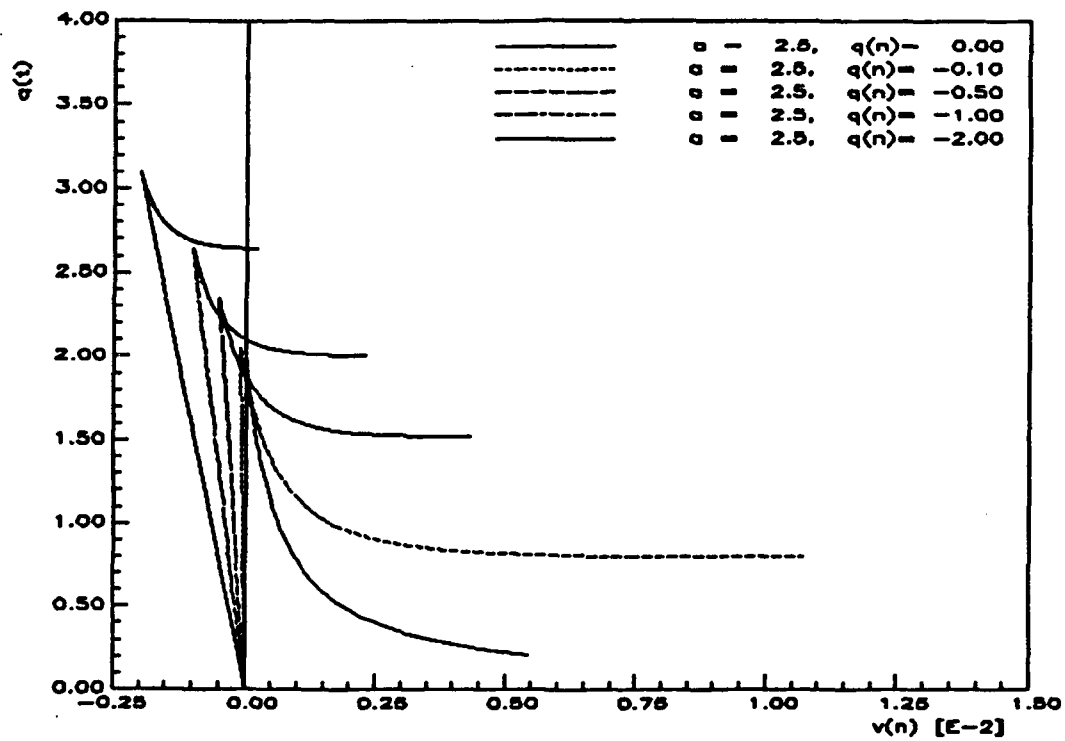
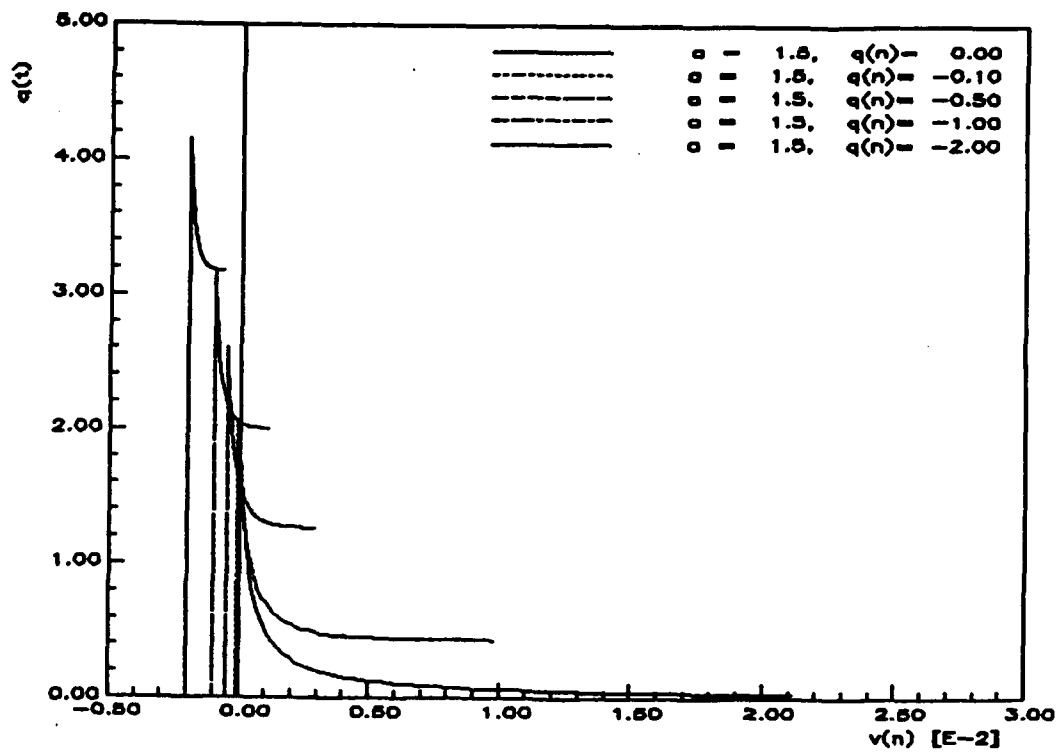


Figure 10: Shearing under Constant Compression For Two Values of Exponent α

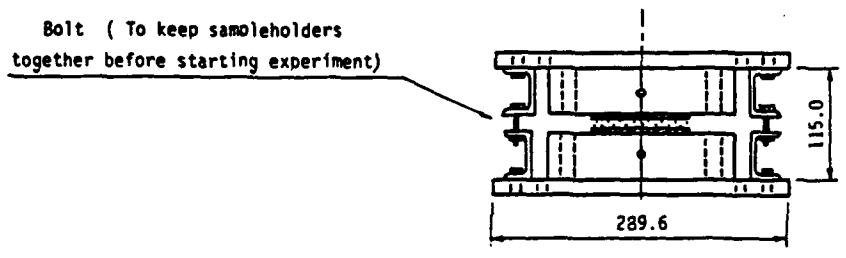
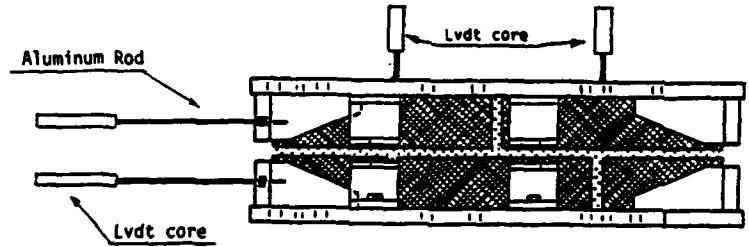
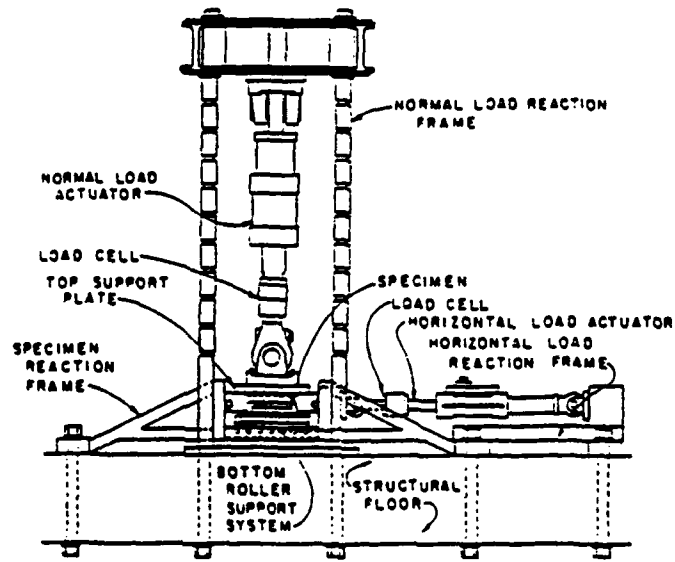
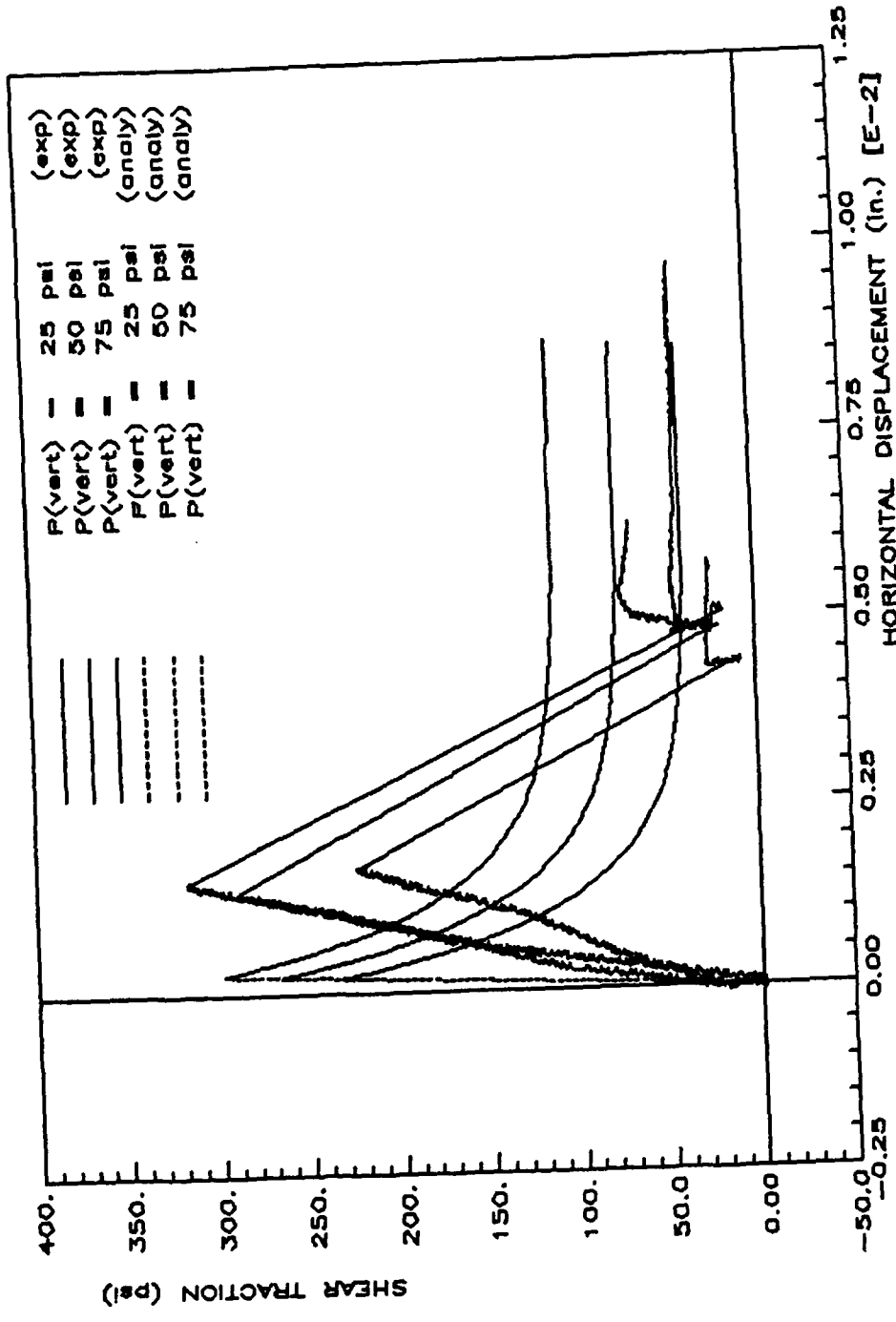
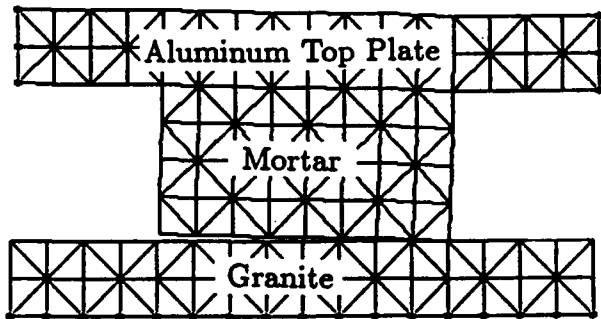
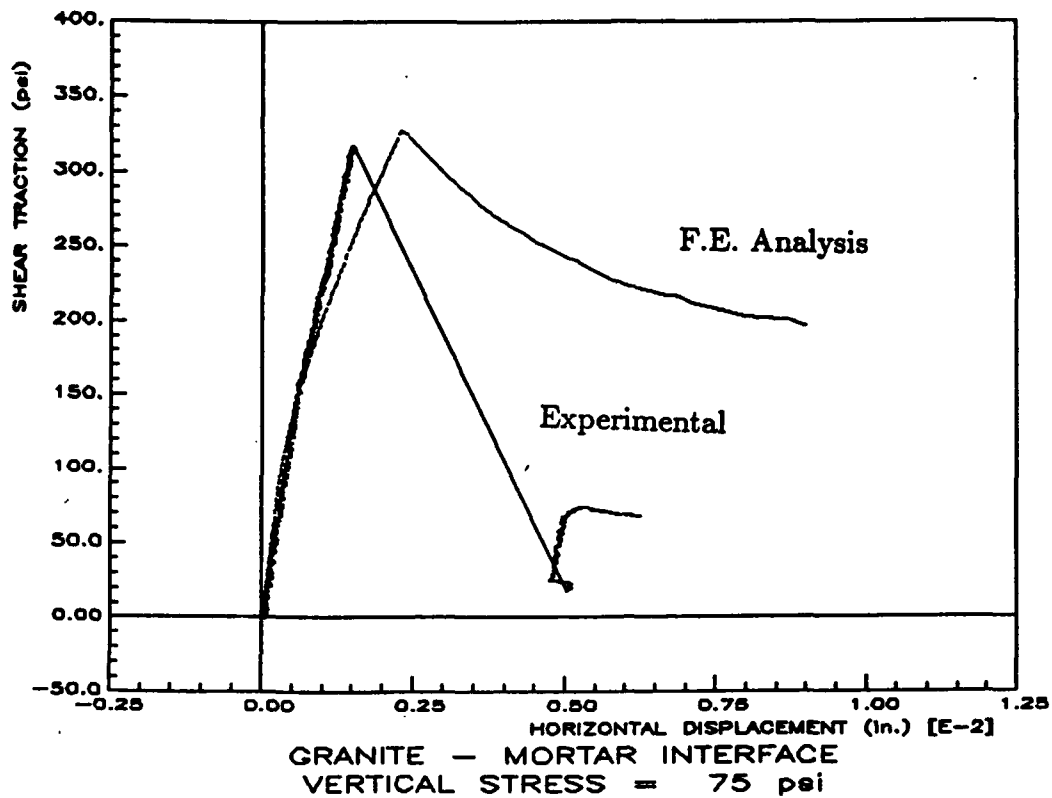


Figure 11: Direct Shear Apparatus

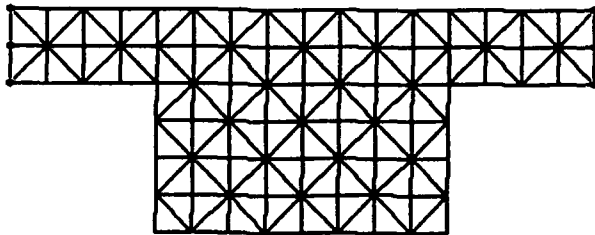


GRANITE - MORTAR INTERFACE
 VERTICAL STRESS = 25, 50, 75 psi

Figure 13: Shear Force - Displacement Response of Granite-Mortar Interfaces



Deformation at Peak



Deformation at Residual Strength



Figure 14: Structural Simulation of Granite-Mortar Interface

FRACTURE AND SLIP OF INTERFACES IN CEMENTITIOUS COMPOSITES

Part II: Model Implementation

by

T. Stankowski¹, K. Runesson², S. Sture³

¹Res. Assoc., Dept. of Civil, Environmental, and Architectural Engrg., University of Colorado, Boulder, CO 80309.

²Visit.Prof., Dept. of Civil, Environmental, and Architectural Engrg., University of Colorado, Boulder, CO 80309.

³Prof., Dept. of Civil, Environmental, and Architectural Engrg., University of Colorado, Boulder, CO 80309.

Contents

1	INTRODUCTION	3
2	INCREMENTAL RELATIONS	3
2.1	Implicit Integration	3
2.2	Newton Iteration	5
2.3	Interpolation/Iteration Scheme	6
2.4	Iterative Procedure for Mixed Control	8
3	FINITE ELEMENT MODELLING WITH INTERFACES	8
3.1	Basic Equations	8
3.2	Iterative Scheme - Numerical Performance	10
4	NUMERICAL RESULTS	12
5	SUMMARY AND CONCLUSIONS	13
6	APPENDIX I: ALGORITHMIC TANGENT STIFFNESS	15
7	APPENDIX II: EXTENSION OF THE MODEL TO THREE DI- MENSIONS	17
8	APPENDIX III: REFERENCES	18
9	APPENDIX IV: NOTATION	19

1 INTRODUCTION

In Part I of this paper we developed a constitutive theory for fracture and slip of interfaces in cementitious composites. The characteristic behavior that can be predicted with this constitutive theory was analyzed, and limited comparisons with experimental results obtained from shear tests under constant normal load were presented. In the present Part II we discuss the numerical techniques that are employed for integrating the constitutive relations of the interface. The fully implicit method, or *Closest Point Projection Method* (CPPM) is chosen as the 'core-algorithm' that employs a displacement-driven scheme. A robust iterative technique is devised for solving the nonlinear incremental problem of calculating the contact stresses or tractions in the interface, which is essential for the successful implementation in a finite element analysis code. We also use a scaled gradient iteration technique for the solution of the incremental finite element problem, which requires the development of the appropriate Algorithmic Tangent Stiffness matrix. This matrix can, in fact, be used to assess the stability of the actual incremental solution. Finally, finite element results are presented for pertinent boundary value problems.

2 INCREMENTAL RELATIONS

2.1 Implicit Integration

By combining Eqs. 2, 4 and 10 of Part I, Stankowski et al., we obtain the constitutive relationship between the interface tractions and relative displacements. These relations define together with the hardening rule in Eq. 29 and the fracture/slip criterion in Eq. 6, Part I, the complete set of constitutive relations for the behavior of the interface:

$$\dot{\mathbf{u}} = \mathbf{C}^e \dot{\mathbf{t}} + \dot{\lambda} \mathbf{m}(\mathbf{t}) \quad (1)$$

$$\dot{\kappa} = \dot{\lambda} \mathbf{s}^T(\mathbf{t}) \mathbf{m}(\mathbf{t}) \quad (2)$$

$$F(\mathbf{t}, \kappa) = 0 \quad (3)$$

A number of different techniques for integrating these relations are available. The *Generalized Trapezoidal Rule* (GTR) has been evaluated by Stankowski (1990), and it was concluded that the most robust scheme should be based on a fully implicit integration scheme, which is a special case of the GTR-method. In this paper we employ a slightly modified version of the implicit method (CPPM), which has been developed by Runesson et al.(1988), whereby the modification concerns the integration of the softening variable in Eq. 2. Since the current yield surface $F = 0$ is always convex for a given value of κ , integration according to the CPPM guarantees the existence of a stress solution in terms of a projection property.

Using the modified CPPM we may integrate Eqs. 1 and 2 to obtain, for $0 \leq \beta \leq 1$,

$${}^{n+1}\mathbf{t} = {}^{n+1}\mathbf{t}^e - \lambda \mathbf{D}^e {}^{n+1}\mathbf{m} \quad (4)$$

$${}^{n+1}\kappa = {}^n\kappa + \lambda {}^{n+1-\beta}\mathbf{s}^T {}^{n+1}\mathbf{m} \quad (5)$$

$${}^{n+1}F = 0 \quad (6)$$

where ${}^n(\cdot)$ denotes the current state at time $t = {}^nt$, whereas ${}^{n+1}(\cdot)$ denotes the updated or unknown state. The trial (elastic) traction ${}^{n+1}\mathbf{q}^e$ is defined as

$${}^{n+1}\mathbf{t}^e = {}^n\mathbf{t} + \mathbf{D}^e \Delta \mathbf{u}, \quad \mathbf{D}^e = (\mathbf{C}^e)^{-1} \quad (7)$$

Furthermore, we have used the notation

$${}^{n+1}\mathbf{m} = \mathbf{m}({}^{n+1}\mathbf{t}), \quad {}^{n+1}F = F({}^{n+1}\mathbf{t}, {}^{n+1}\kappa) \quad (8)$$

$${}^{n+\gamma}\mathbf{s} = \mathbf{s}({}^{n+\gamma}\mathbf{t}), \quad {}^{n+\gamma}\mathbf{t} = (1 - \gamma) {}^n\mathbf{t} + \gamma {}^{n+1}\mathbf{t} \quad (9)$$

A variety of different techniques is available for the solution of Eqs. 9 for a given trial stress ${}^{n+1}\mathbf{t}^e$, either by a pure iteration scheme or a combined iteration/interpolation technique.

2.2 Newton Iteration

The most 'direct' approach is to use a Newton Iteration Scheme in order to calculate ${}^{n+1}\mathbf{q}$ and ${}^{n+1}\kappa$ simultaneously from Eqs. 9, whereby the current fracture/slip surface is updated at each iteration. It was shown by Stankowski (1990) that for this scheme to converge requires that the initial values are carefully chosen. Moreover, it is increasingly difficult to choose the initial values as the size of the load increments Δu increase, i.e. when ${}^{n+1}\mathbf{t}^e$ is far away from the initial fracture/slip surface nF . The performance of the iteration scheme is significantly improved, if the stress projection inferred by Eq. 4 is performed for a fixed surface, whereby ${}^{n+1}\mathbf{t}$ and λ are simultaneously calculated from the following equations:

$$\mathbf{g}({}^{n+1}\mathbf{t}, \lambda) = \hat{\mathbf{C}}^e ({}^{n+1}\mathbf{t} - {}^{n+1}\mathbf{t}^e) + \lambda \mathbf{n} ({}^{n+1}\mathbf{q}) = 0 \quad (10)$$

$$f({}^{n+1}\mathbf{t}) \equiv F({}^{n+1}\mathbf{t}, {}^{n+1}\kappa) = 0 \quad (11)$$

where $\hat{\mathbf{C}}^e = \mathbf{A}^{-1} \mathbf{C}^e$ and \mathbf{A} is the transformation matrix in Eq.(11) of Part I accounting for non-associated flow due to dilatancy properties of the interface. The structure of Eq. 11 is simple since, in fact, $\hat{\mathbf{C}}^e$ is diagonal.

Newton iterations to solve for ${}^{n+1}\mathbf{t}$ and λ from Eqs. 11 and (10) give for the iteration step $(.)^{i+1}$:

$${}^{n+1}\mathbf{t}^{(i+1)} = {}^{n+1}\mathbf{t}^{(i)} + d\mathbf{t}, \quad \lambda^{(i+1)} = \lambda^{(i)} + d\lambda \quad (12)$$

where the improved values $d\mathbf{t}$ and $d\lambda$ are calculated from the set of equations

$$\begin{bmatrix} \hat{\mathbf{C}}^e + \lambda \mathbf{N} & \mathbf{n} \\ \mathbf{n}^T & 0 \end{bmatrix}^{(i)} \begin{bmatrix} d\mathbf{t} \\ d\lambda \end{bmatrix} = - \begin{bmatrix} \mathbf{g}^{(i)} \\ f^{(i)} \end{bmatrix} \quad (13)$$

The matrix \mathbf{N} is the Hessian of f , i.e. $\mathbf{N} = \partial^2 f / \partial \mathbf{t} \partial \mathbf{t}$.

As indicated earlier, it seems to be essential to use good initial solutions ${}^{n+1}\mathbf{t}^{(0)}$ and $\lambda^{(0)}$ in order to ascertain that the scheme has efficient and reliable iteration

properties. For relatively small steps, it has proved efficient to calculate the predictor from forward extrapolations in Eq. 9 with $\beta = 0$. The solution is conveniently found by calculating $\lambda^{(0)}$ from

$$f(\lambda^{(0)}) = F({}^{n+1}\mathbf{t}^{(0)}, {}^{n+1}\kappa^{(0)}) \quad (14)$$

where

$${}^{n+1}\mathbf{t}^{(0)} = {}^{n+1}\mathbf{t}^e - \lambda^{(0)} \mathbf{D}^e \mathbf{n}_m \quad (15)$$

$${}^{n+1}\kappa^{(0)} = {}^n\kappa + \lambda^{(0)} \mathbf{n}_s^T \mathbf{n}_m \quad (16)$$

Since only an initial solution is sought, it is sufficient to find only an approximate solution of Eq. 14 with a limited number of iterations.

2.3 Interpolation/Iteration Scheme

For increasingly larger increments the quality of the predictor becomes a crucial issue for the success in efficiently solving the set of constitutive equations given in Eqs. 10 and (11). This is in particular the case, when the stress is projected onto a region of the fracture surface $F = 0$ with strong curvature, and when a significant change in the softening variable κ is encountered. In fact, the predictor obtained from a forward extrapolation outlined in the previous section, proved to be sufficient only when the magnitude of the elastic traction ${}^{n+1}\mathbf{t}^e$, which reflects the increment size, was of the same order as the elastic limit $f_{n,u}$. However, since it can be anticipated that slip and debonding occur in a rather brittle fashion close to structural failure with significant relative motion in the interface, it is essential to deal with elastic trial stresses ${}^{n+1}\mathbf{t}^e$ whose magnitudes are several orders larger than $f_{n,u}$. In order to find a solution of Eqs. 10 and (11) for these cases, an alternative technique was developed that employs a quadratic interpolation scheme for the calculation of ${}^{n+1}\mathbf{t}$ when $F = 0$ is maintained constant.

The projection of the elastic trial stress ${}^{n+1}\mathbf{t}^e$ onto the current slip surface $F^{(j)} = 0$ is carried out by solving the orthogonality condition

$$\mathbf{d}^T \mathbf{t}_F = 0 \quad (17)$$

where

$$\mathbf{d} = \mathbf{C}^e (\mathbf{t}^e - \mathbf{t}^{(i)}) \quad (18)$$

and \mathbf{t}_F is the tangent to the plastic potential in $\mathbf{t}^{(i)}$. This condition is equivalent to finding the minimum distance \mathbf{d} in strain space for the case of associated flow. For non-associated flow \mathbf{C}^e in Eq. 18 has to be transformed. The orthogonality condition in Eq. 17 has been chosen, since it is more suitable for the interpolation scheme employed. Alternatively, the stress projection could be carried out by minimizing $\|\mathbf{d}\|$. An initial interpolation interval is readily established for example by the projections of ${}^{n+1}\mathbf{t}^e$ parallel to the tangential and normal directions on $F^{(j)}$ and $t_n \leq f_n$. If $q_n > q_{n,f}$, then the initial interpolation interval is established by the projection of ${}^{n+1}\mathbf{t}_t$ in the normal direction on $F^{(j)}$ and by f_n . The intermediate pivot is taken at the midstep. Subsequent surface updates have to be monitored very carefully, since initial updates may result in

$${}^{n+1}\kappa^{(i+1)} > G_f^I \quad (19)$$

In this case, the motion of the surface has to be restricted by assuming

$${}^{n+1}\kappa^{(i+1)} = \alpha^* (G_f^I - {}^n\kappa) \quad (20)$$

where α^* is a factor, e.g. 0.5. As the iterations proceed, $\Delta\kappa$ decreases and will eventually become

$${}^{n+1}\kappa^{(i+1)} < {}^{n+1}\kappa^{(i)} \quad (21)$$

i.e. ${}^{n+1}\mathbf{t}^{(i+1)}$ is inside F such that $F({}^{n+1}\mathbf{t}^{(i+1)}, {}^{n+1}\kappa^{(i+1)}) < 0$. At this stage, the values ${}^{n+1}\kappa^{(i+1)}$ and ${}^{n+1}\kappa^{(i)}$ are used in an interpolation scheme to obtain new values for ${}^{n+1}\kappa$. During the surface updates the new interpolation intervals have to

be established carefully depending on the motion of the surface. The non-monotonic behavior arises from the *worksoftening* assumption and explains the limitation of a Newton iteration scheme to small step sizes, when the surface is updated at each iteration level.

2.4 Iterative Procedure for Mixed Control

Mixed control of one traction and one relative displacement component is readily dealt with within the framework of the outlined integration-iteration procedures. If for example, ${}^{n+1}t_n = {}^{n+1}\bar{t}_n$ is prescribed, then because of the elastic decoupling of ${}^{n+1}t_n^e$ and ${}^{n+1}t_t^e$, the first row in Eq. 4 can simply be deleted, and ${}^{n+1}t_n = {}^{n+1}\bar{t}_n$ is inserted in the other equations. When ${}^{n+1}t_t$ and λ have been calculated (after convergence of the chosen iteration algorithm), it is a relatively simple matter to calculate the remaining unknown displacement component Δu_n (and ${}^{n+1}u_n$) from the first row in Eq. 6.

3 FINITE ELEMENT MODELLING WITH INTERFACES

3.1 Basic Equations

In order to describe the interaction of two constituents across the interface we consider the common boundary Γ_c (interface) that separates the regions $\Omega^{(1)}$ and $\Omega^{(2)}$ as shown in Fig.(1). Apart from the common portion Γ_c , the boundary of each region is composed of a part with prescribed displacements and another part with prescribed applied tractions. For simplicity, we assume henceforth that the boundary tractions as well as the body forces are absent.

Vector components are normally referred to global Cartesian coordinates. However, along the interface it is convenient to resort to normal and tangential components. The relative displacement $\mathbf{v} = \mathbf{u}^{(2)} - \mathbf{u}^{(1)}$ and the contact traction $\mathbf{q} = \mathbf{q}^{(1)} = -\mathbf{q}^{(2)}$ at each point along the interface Γ_c may then be decomposed as in Eqs. 1 and

(3) of Part I, where the base vectors \mathbf{e}_n and \mathbf{e}_t are attached to the region $\Omega^{(1)}$.

At each instant the stresses must satisfy the equilibrium equations in the regions $\Omega^{(1)}$ and $\Omega^{(2)}$. The appropriate virtual work equation at time $t = t_{n+1}$ may be written as

$$\int_{\Omega^{(i)}} (\bar{\boldsymbol{\epsilon}}^{(i)})^T {}^{n+1}\boldsymbol{\sigma}^{(i)} d\Omega - \int_{\Gamma_c} (\bar{\mathbf{u}}^{(i)})^T {}^{n+1}\mathbf{t}^{(i)} d\Gamma = 0, \quad i = 1, 2 \quad (22)$$

for all (virtual) kinematically admissible displacements $\bar{\mathbf{u}}^{(i)}$. By adding, formally, the two equations in (22) we obtain

$$\sum_{i=1,2} \int_{\Omega^{(i)}} (\bar{\boldsymbol{\epsilon}}^{(i)})^T {}^{n+1}\boldsymbol{\sigma}^{(i)} d\Omega + \int_{\Gamma_c} \bar{\mathbf{u}}^T {}^{n+1}\mathbf{t} d\Gamma = 0 \quad (23)$$

where $\bar{\mathbf{u}} = \bar{\mathbf{u}}^{(2)} - \bar{\mathbf{u}}^{(1)}$.

The term of interest for interface modelling is the boundary term in in Eq.(23)

$$I = \int_{\Gamma_c} \bar{\mathbf{u}}^T {}^{n+1}\mathbf{t} d\Gamma = \int_{\Gamma_c} (\bar{u}_n {}^{n+1}t_n + \bar{u}_t {}^{n+1}t_t) d\Gamma \quad (24)$$

Since a constitutive relation is available for ${}^{n+1}t_n$ and ${}^{n+1}t_t$ in terms of Δu_n and Δu_t , i.e.

$${}^{n+1}\mathbf{t} = \mathbf{t}(\Delta \mathbf{u}) \quad (25)$$

or, explicitly

$${}^{n+1}t_n = t_n(\Delta u_n, \Delta u_t), \quad {}^{n+1}t_t = t_t(\Delta u_n, \Delta u_t)$$

the boundary integral in Eq.(24) contributes to the global stiffness of the jointed regions $\Omega^{(1)}$ and $\Omega^{(2)}$.

Discrete (= finite element) equations corresponding to the virtual work expression in Eq.(23) are obtained in the usual way via appropriate shape functions, where we expand the displacement field $\mathbf{u}^{(i)}$, $i = 1, 2$, and the relative displacements \mathbf{u} as

$$\mathbf{u}^{(i)} = \Phi^{(i)} \mathbf{p}^{(i)} + \Phi_c^{(i)} \mathbf{p}_c^{(i)}, \quad \mathbf{u} = \Phi_c (\mathbf{p}_c^{(2)} - \mathbf{p}_c^{(1)}) \quad (26)$$

Here, we have introduced Φ_c as the restriction of $\Phi_c^{(i)}$, $i = 1, 2$ to the interface Γ_c .

Inserting Eq.(26) into Eq.(23) gives rise to the set of equations

$$\begin{aligned}
 \mathbf{s}^{(1)}(\mathbf{p}^{(1)}, \mathbf{p}_c^{(1)}) &= 0 \\
 \mathbf{s}_c^{(1)}(\mathbf{p}^{(1)}, \mathbf{p}_c^{(1)}) - \mathbf{r}_c(\mathbf{p}_c^{(1)}, \mathbf{p}_c^{(2)}) &= 0 \\
 \mathbf{s}_c^{(2)}(\mathbf{p}^{(2)}, \mathbf{p}_c^{(2)}) - \mathbf{r}_c(\mathbf{p}_c^{(1)}, \mathbf{p}_c^{(2)}) &= 0 \\
 \mathbf{s}^{(2)}(\mathbf{p}^{(2)}, \mathbf{p}_c^{(2)}) &= 0
 \end{aligned} \tag{27}$$

where we have introduced the nodal forces

$$\begin{aligned}
 \mathbf{s}^{(i)} &= \int_{\Omega^{(i)}} (\mathbf{B}^{(i)})^T \boldsymbol{\sigma}(\boldsymbol{\epsilon}(\mathbf{p}^{(i)}, \mathbf{p}_c^{(i)})) d\Omega \\
 \mathbf{s}_c^{(i)} &= \int_{\Omega^{(i)}} (\mathbf{B}_c^{(i)})^T \boldsymbol{\sigma}(\boldsymbol{\epsilon}(\mathbf{p}^{(i)}, \mathbf{p}_c^{(i)})) d\Omega \\
 \mathbf{r}_c &= \int_{\Gamma_c} \boldsymbol{\Phi}_c^T \mathbf{t}(\mathbf{v}(\mathbf{p}_c^{(1)}, \mathbf{p}_c^{(2)})) d\Gamma
 \end{aligned} \tag{28}$$

with the common definition given to the strain-displacement matrices $\mathbf{B}^{(i)}$ and $\mathbf{B}_c^{(i)}$, $i = 1, 2$.

3.2 Iterative Scheme - Numerical Performance

For each time step the incrementally non-linear finite element problem in the set of equations Eq.(27) involving the interface model is solved by scaled gradient (or modified Newton) iterations. In the special case of true Newton iterations the *Algorithmic Tangent Stiffness* matrix for the composite is used. The contribution relating to the contact force \mathbf{r}_c is given as

$$\mathbf{s}_c = \int_{\Gamma_c} \boldsymbol{\Phi}_c^T \mathbf{D}_c(\mathbf{v}) \boldsymbol{\Phi}_c d\Gamma \tag{29}$$

where the appropriate formulation of the constitutive matrix of the algorithmic tangent moduli \mathbf{D}_c is given in the appendix. In the case there exists a unique solution to the incremental finite element problem defined by the equations Eq.(27) that corresponds to their minimum of an incremental potential as discussed by Runesson et al.

(1990), Newton iterations will converge to this solution (except in some pathological cases). However, for softening materials one may encounter unstable solutions that correspond to insufficiently localized deformation modes, and the solution turns out to be non-unique. In such a case, the Newton technique fails in general (depending on the choice of the start solution). A modified stiffness matrix, which is positive definite, must be adopted in order to ensure convergence to a local minimum, so that at the very least, an unstable solution can be avoided. (We note that there is still the inherent difficulty of finding the most stable solution.)

The crudest choice of an iteration matrix in this case, when the Hessian ceases to be positive definite, is the elastic stiffness matrix corresponding to the initial stress iteration method. In order to establish a modified stiffness that is closer to the Hessian, the negative eigenvalues are modified on the constitutive level as explained in the following.

Consider the eigenvalue problem for the Algorithmic Tangent Operator that is pertaining to the interface behavior

$$\mathbf{D}_c \mathbf{x}_i = \gamma_i \mathbf{D}_c^e \mathbf{x}_i, \quad i = 1, 2 \quad (30)$$

where \mathbf{x}_i are the \mathbf{D}_c^e -normalized eigenvectors. It follows that \mathbf{D}_c can be represented in terms of its spectral properties as (for the 2D-case)

$$\mathbf{D}_c = \sum_{i=1,2} \lambda_i \mathbf{x}_i \mathbf{x}_i^T \quad (31)$$

Whenever $\lambda_1 < 0$, we replace \mathbf{D}_c by \mathbf{D}_c^* defined as

$$\mathbf{D}_c^* = \sum_{i=1,2} \lambda_i \mathbf{x}_i \mathbf{x}_i^T \quad (32)$$

This choice representing zero stiffness associated with a (local) failure mode resembles the fully fractured behavior.

The situation that $\lambda_1 < 0$ was indeed encountered in the calculated examples. With the suggested modified stiffness, the resulting iteration procedure turned out to be quite efficient.

4 NUMERICAL RESULTS

In order to examine the ability of the interface model to mimic the separation of a single inclusion embedded in a matrix, a panel with a circular inclusion is subjected to uniaxial tension. Fig. 1 shows the deformed mesh (for a quarter panel, since symmetry can be exploited) and the load-displacement relation for this structure. The tensile strength of the mortar matrix was taken to be 20% higher than the one of the interface ($q_{n, fu}$). In order to assure that the post-peak load-displacement relation represents stable behavior under displacement control, i.e. to avoid snap-back behavior, we must choose the energy release G_f^I large enough. This may, in fact, correspond to a rather ductile post-peak response (on the constitutive level). It was concluded that the interface model can be utilized to capture the progressive failure from initial debonding to complete separation.

The previous (and original) application of the interface model was to mimic interaction and debonding of dissimilar materials of a composite. However, it is clearly possible to use this model in order to describe crack development in an initially homogeneous material. This application seems particularly attractive since problems deriving from smeared crack analysis, such as the proper definition of internal length, see e.g. Willam et al. (1986), is effectively avoided. The interface thus serves as a generalization of the *Fictitious Crack Model* by Hillerborg (1976), who took only tensile debonding into account.

In order to illustrate this application of the interface, the previous model problem will be reanalyzed. However, in contrast to the previous analysis, linear elastic material properties are assigned to the mortar matrix without any strength limitation. All mortar elements are surrounded by interface elements having the same tensile strength as the mortar matrix in the previous example. Fig. 2 shows the nominal stress-strain response for the panel with a single inclusion together with the deformed mesh shortly before the crack penetrates the cross section. The stages of progressive failure are easily identified as brittle aggregate-mortar interface failure, followed by

stress redistribution and stable crack propagation through the mortar-mortar interface until a crack develops. Subsequent crack opening results in an exponentially softening stress-strain response.

In this particular example, the mesh is fairly well aligned with the tensile failure mode, however, in a more general case, the failure mode had to be determined from a bifurcation analysis of the elastoplastic constitutive relation, cf. Sobh (1987), Ottosen et al. (1989), and the mesh had to be aligned subsequently with the crack direction.

5 SUMMARY AND CONCLUSIONS

In Part I, [1] a realistic interface model that comprises normal-shear stress coupling, dilatancy as well as elastic pre-peak adhesion was suggested. The constitutive relations were developed in analogy to plasticity theory. A thorough analysis of the constitutive relations was performed in terms of spectral properties of the tangent constitutive relations for displacement as well as for mixed mode of control. The predictive performance was assessed and compared favorably with experimental results.

This paper focusses on the numerical treatment of the interface model. In order to integrate the stresses, the generalized trapezoidal rule was used, whereas a hybrid integration scheme was employed for the integration of the single softening variable. Newton iterations were adopted for simultaneous calculation of updated stress and the current fracture/slip surface. However, This technique turned out to be reliable and stable only for small load steps. Modification of the iteration procedure by decoupling stress projection and surface update, i.e invoking the Newton iteration only for the stress projection on a fixed surface, which was updated subsequently employing an interpolation technique, improved the convergence behavior only partly. It was found that the most reliable technique in conjunction with the *Backward Euler Method* has to employ interpolation of the projected stresses in the iterative process.

The implementation of the interface model into a Finite Element Program includes the formulation of an Algorithmic Tangent Stiffness for the interface, which is used in a

true Newton iteration procedure to solve the incrementally non-linear problem in each load step. In order to ensure convergence to the physically feasible solution, it was found necessary to enforce positive definiteness of the tangent stiffness by suppressing possible 'unstable' eigenmodes corresponding to negative eigenvalues in the spectrally decomposed constitutive stiffness matrix. The resulting 'adjusted' Newton technique was found to perform well in terms of reliability and efficiency compared to the Modified Newton and the Initial Load Method. Especially for large load steps, the Newton technique was very competitive.

The analysis of a simple composite model configuration demonstrates the ability of the model to predict interface failure. The participation of the interface in the failure process results in a decreased composite strength and in a more localized failure with stages of brittle interface failure and stages of ductile crack propagation across the composite matrix.

The paper concludes with the application of the interface model as a *Generalized Fictitious Crack Model (GFCM)*. This application appears to be a natural extension of the interface concept to overcome problems deriving from smeared crack analysis, in particular in its ability to account for displacement discontinuities and stress-free crack boundaries. It is anticipated, that such a GFCM will be useful in conjunction with a suitable criterion to detect failure and the related crack direction, which may be determined via a bifurcation analysis of the elastic-plastic constitutive relations for the uncracked material. After the onset of cracking, the crack is modeled as an internal discontinuity with using the proposed interface model. The analyzed numerical example shows that the crack pattern extends from the mortar itself due to the introduction of the GFCM along predefined inter-element boundaries in the mortar.

6 APPENDIX I: ALGORITHMIC TANGENT STIFFNESS

The tangential behavior of ${}^{n+1}\mathbf{q}(\Delta\mathbf{v})$ for a change of $\Delta\mathbf{v}$ is defined by the matrix of Algorithmic Tangent Stiffness moduli $\hat{\mathbf{D}}$ defined by

$$\hat{\mathbf{D}}^e(\Delta\mathbf{u}) = \frac{\partial(\Delta\mathbf{t})}{\partial(\Delta\mathbf{u})} \quad (33)$$

This matrix has been derived elsewhere in conjunction with elastic-plastic continua. Firstly, let us define the matrix of the Algorithmic Elastic Stiffness moduli $\hat{\mathbf{D}}^e$

$$\hat{\mathbf{D}}^e(\Delta\mathbf{u}) = (\mathbf{C}^e + \lambda\hat{\mathbf{N}})^{-1} \quad (34)$$

where $\hat{\mathbf{N}} = \mathbf{A}\mathbf{N}$ and \mathbf{N} is the Hessian matrix of F , i.e. with the expressions for \mathbf{n} in Eq.(11) of Part I [1] we obtain

$$\mathbf{N} = \frac{\partial^2 F}{\partial \mathbf{t} \partial \mathbf{t}} = \frac{\partial \mathbf{n}^T}{\partial \mathbf{t}} = \begin{bmatrix} 0 & 0 \\ 0 & a(a-1) |t_t|^{a-2} \end{bmatrix} \quad (35)$$

$$\hat{\mathbf{N}} = \mathbf{A}\mathbf{N} = \begin{bmatrix} 0 & 0 \\ 0 & (\mu/\nu) a(a-1) |t_t|^{a-2} \end{bmatrix} \quad (36)$$

and, consequently,

$$\hat{\mathbf{D}}^e = \begin{bmatrix} K_n^{-1} & 0 \\ 0 & K_t^{-1} + \lambda(\mu/\nu) a(a-1) |t_t|^{a-2} \end{bmatrix}^{-1} \quad (37)$$

which is, of course, a symmetrical matrix since it is diagonal. It is noted, that the trivial situation $\hat{\mathbf{D}}^e = \mathbf{D}^e$ is obtained when (a) $t_t = 0$ (pure tension), (b) $a = 1$ (classical Coulomb Friction Model, however, here $a > 1$ was assumed), and (c) $\lambda = 0$ (continuum tangent stiffness).

We may now define

$$\hat{\mathbf{D}}(\Delta\mathbf{u}) = \hat{\mathbf{D}}^e - \frac{1}{K} \hat{\mathbf{D}}^e \mathbf{m} \hat{\mathbf{n}} \hat{\mathbf{D}}^e \quad (38)$$

where \hat{n} is an algorithmic gradient defined as

$$\hat{n} = n + \lambda \frac{\partial F}{\partial \kappa} \left(\frac{\partial \mathbf{s}^T}{\partial t} \mathbf{m} + \hat{N}t \right) \quad (39)$$

Moreover,

$$\hat{K} = \hat{H} + \hat{n}^T \hat{D}^e \mathbf{m}, \quad \hat{H} = -\frac{\partial F}{\partial \kappa} \mathbf{s}^T \mathbf{m} \quad (40)$$

The explicit expressions for n and m are given in Eqs.(10) and (11) of Part I [1].

With \mathbf{s} according to Eq.(29) in Part I, we obtain

$$\frac{\partial \mathbf{s}^T}{\partial t} \mathbf{m} = \left[\begin{array}{c} (f_{t,u})^3 < \text{sign}(t_n) > \\ (\mu/\nu) ka |t_i|^{a-1} \text{sign}(t_i) \end{array} \right] \quad (41)$$

Moreover, we obtain simply

$$\frac{\partial F}{\partial \kappa} = \frac{(f_{t,u})^a}{G_f^I} \quad (42)$$

$$\hat{N}q = \left[\begin{array}{c} 0 \\ (\mu/\nu) a (a-1) |t_i|^{a-1} \text{sign}(t_i) \end{array} \right] \quad (43)$$

by which \hat{n} can be calculated. Finally, \hat{H} was expressed explicitly in Eq.(31) of Part I [1].

7 APPENDIX II: EXTENSION OF THE MODEL TO THREE DIMENSIONS

This section describes briefly the extension of the constitutive model discussed in Part I [1] for the planar case to a 3D interface model. This model may be called isotropic in the sense that the tangential response is independent of the choice of the tangential cartesian coordinates e_x and e_y . The relative displacements may be defined by

$$\mathbf{u} = u_n \mathbf{e}_n + u_{tx} \mathbf{e}_x + u_{ty} \mathbf{e}_y \quad (44)$$

and the tractions are

$$\mathbf{t} = t_n \mathbf{e}_n + t_{tx} \mathbf{e}_x + t_{ty} \mathbf{e}_y \quad (45)$$

where e_{tx} and e_{ty} are two mutually orthogonal base vectors in the tangential plane. The decomposition of the relative displacement rates into an elastic part and an plastic part, Eq.(2), Part [1], is also assumed to be valid with the same assumptions as indicated in Section 2, Part [1]. The elastic compliance matrix becomes therefore

$$\dot{\mathbf{u}}^e = \mathbf{C}^e \dot{\mathbf{t}}$$

or

$$\begin{bmatrix} \dot{u}_n^e \\ \dot{u}_{tx}^e \\ \dot{u}_{ty}^e \end{bmatrix} = \begin{bmatrix} K_n^{-1} & 0 & 0 \\ 0 & K_{tx}^{-1} & 0 \\ 0 & 0 & K_{ty}^{-1} \end{bmatrix} \begin{bmatrix} \dot{t}_n \\ \dot{t}_{tx} \\ \dot{t}_{ty} \end{bmatrix} \quad (46)$$

and, in view of the assumed isotropy in shear, we have $K_{tx}^{-1} = K_{ty}^{-1}$.

The *Fracture Criterion* is formally identical to the one adopted previously, i.e.

$$F = |t_t|^a - \frac{(f_{t,u})^a}{f_{n,u}} (f_{n,f} - f_n) = 0 \quad (47)$$

however, t_t is now the norm of the shear tractions such that

$$t_t^2 = t_{tx}^2 + t_{ty}^2 \quad (48)$$

and the corresponding inelastic deformation rates are

$$\dot{\mathbf{u}}^p = \dot{\lambda} \mathbf{m}, \quad \mathbf{m} = \mathbf{A} \mathbf{n}, \quad \mathbf{n} = \partial F / \partial \mathbf{t} \quad (49)$$

and

$$\mathbf{A} = \begin{bmatrix} 1 & 0 & 0 \\ 0 & \mu/\nu & 0 \\ 0 & 0 & \mu/\nu \end{bmatrix}, \quad \mathbf{n} = \begin{bmatrix} (f_{t,u})^2/f_{n,u} \\ a (t_{tx}^2 + t_{ty}^2)^{(\frac{q}{2}-1)} |t_{tx}| \text{sign}(t_{tx}) \\ a (t_{tx}^2 + t_{ty}^2)^{(\frac{q}{2}-1)} |t_{ty}| \text{sign}(t_{ty}) \end{bmatrix} \quad (50)$$

The generalization of the work-softening hypothesis to three dimensions is incorporated in the new definition of the tangential shear tractions and the tangential inelastic deformation. The rate law for the fracture energy release κ is again formally identical with Eq.(18),

$$\dot{\kappa} = \langle t_n \rangle \dot{u}_n^p + k(t_t - f_{t,r})\dot{u}_t^p \quad (51)$$

however, \dot{u}_t^p is now defined by

$$(\dot{u}_t^p)^2 = (\dot{u}_{tx}^p)^2 + (\dot{u}_{ty}^p)^2 \quad (52)$$

and t_t and $f_{t,r}$ have been defined in Eq.(48) and Eq.(19), Part I,[1] respectively.

8 APPENDIX III: REFERENCES

Ottosen, N., Runesson, K. (1989), "Properties in Bifurcation Solution in Elasto-Plasticity", accepted for Publication in *Int. J. Solids and Structures*

Runesson, K., Sure, S. and Willam, K.J. (1988), "Integration in Computational Plasticity", *Computers and Structures*, 30, pp. 119-130

Sobh, N. (1987), "Bifurcation Analysis of Tangential Operators", *Ph.D. Thesis Dept. CEAE, University of Colorado, Boulder, Colorado*

Stankowski, T. (1990), "Numerical Simulation of Progressive Failure in Particle Composites", *Ph.D. Thesis Dept. CEAE, University of Colorado, Boulder, Colorado*

Stankowski, T., Runesson, R. and Sture, S. (1991), "Fracture and Slip of Interfaces in Cementitious Composites", *ASCE J. Eng. Mech.*, submitted for publication

Willam, K. J., Bicanic, N., Pramono, E. and Sture, S., "Composite Fracture Model for Strain Softening Computations of Concrete", *Fracture Mechanics of Concrete - Fundamentals and Applications*, Ed. Wittman, I, pp. 221-235

9 APPENDIX IV: NOTATION

C = compliance

D = stiffness

f = strength values

F = fracture function

m = gradient of plastic potential

n = gradient of fracture function

r = contact nodal forces

t = vector of contact traction

u = vector of relative displacements

p = vector of nodal displacements

x = eigenvectors

α = coefficient

β = coefficient

λ = plastic multiplier

κ = measure of released fracture energy

Φ = finite element shape functions

σ = stresses

ϵ = strains

Superscripts

$(\dot{\cdot})$ = rate, differentiation with respect to (pseudo) time

e = elastic

p = plastic

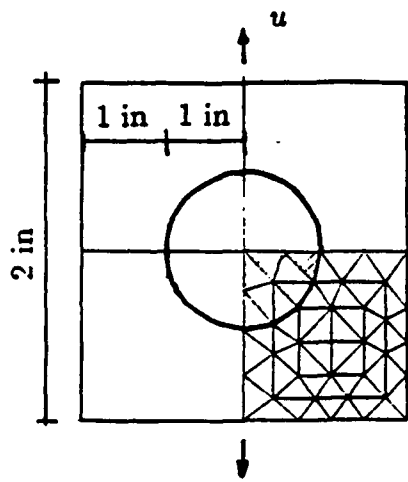
Subscripts

n = normal direction

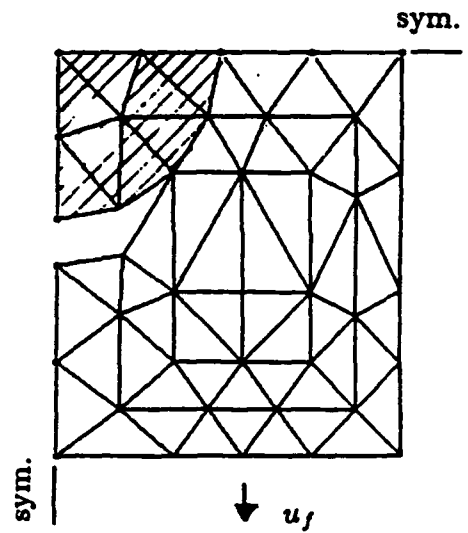
r = residual values

t = tangential direction

u = ultimate (peak) values



Geometry and Meshlayout



Deformed Mesh (1:50)

Fig. 1

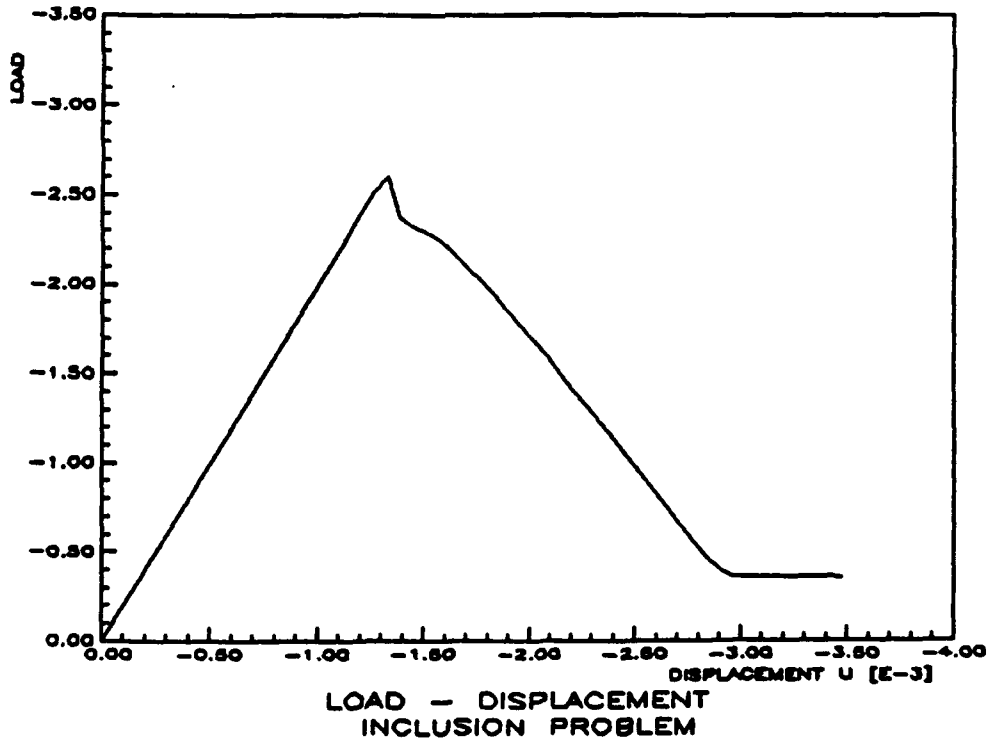


Fig. 2 Tensile Failure of Composite with Circular Inclusion

PART 3 INTERFACE EXPERIMENTS

1. INTRODUCTION

Interface experiments were conducted to investigate the mode of debonding, de-cohesion, fracture and slip of the mortar-aggregate composite, and an experimental apparatus was manufactured to achieve these objectives. The apparatus is capable of loading the interface specimens in combined tension-shear or compression shear modes, and it is sufficiently stiff to maintain overall specimen-loading apparatus stability throughout the debonding, fracture, and slip process.

This section describes experimental technique, apparatus, and results. A total of 52 experiments were conducted of which 32 were successful.

2. APPARATUS

The combined tension-shear and compression-shear interface experimental apparatus consists of two components, in that a general purpose MTS (Minnesota Testing Systems) 490 kN (110 kips) universal servo-controlled loading frame, that was operated in displacement control, is used as the external loading agency and provides the normal load to the interfaces in the smaller tangential interface loading apparatus, which is also operated in displacement control by means of a stiff constant speed screw-actuator. The apparatus is furnished with several linear variable differential transformers (LVDTs), which records absolute and relative tangential and vertical (normal) displacements in the matrix (mortar)-aggregate (granite) interface specimens. Load cells in the MTS and interface apparatus were used to record global loads or reactions. The interface apparatus is relatively compact and structurally stiff, and fits between the reaction frame of the MTS testing machine as seen in Figs. 1 and 2. Figures 3 and 4 show the LVDT placements, which show the measurement gage-points close to the interface itself.

The apparatus has a normal load capacity of nearly 50 kN in compression or tension (normal load over the interface), and a shear load capacity of also 50 kN. The resolution and accuracy of the system is relatively high, and loads as small as 0.05 N can be recorded. The precision gageheads (LVDTs) can measure displacements as small as 0.01 mm, with an accuracy of 0.005 mm. Since the stiffness of the apparatus is finite the relative displacements of the interface in both the tangential and normal directions are recorded as well as the total displacement measurement. This ensures accurate control and recording of the various motions. In most of the experiments described in the following the max.

compressive load was 5,590 N (400 psi; 2,760 kPa over the specimen), and tensile load 1,400 N (100 psi; 690 kPa over the specimen).

During the course of experimentation it was discovered that the tangential stiffness of the apparatus-specimen system was too flexible, since it was difficult to maintain control near peak and in the post-peak strength regimes. Additional stiffening was achieved by attaching structurally stiff brackets and tie-bars between the base assembly and the top support plate. The last portion of the experimental program benefited from this enhancement, and it was possible to maintain adequate stability in most tension-combined shear experiments.

3. EXPERIMENTS

A total of 32 successful experiments were conducted in the range -400 psi (compression) to 100 psi (tension). The initial stages of specimen preparation were conducted outside the apparatus, and preparation consisted of cleaning and sand-blasting an oversize and plane piece of granite, so that it had a rough but yet nominally smooth surface, that was representative of aggregate used in construction. A small (2.5 cm tall and 5.0 cm diameter) piece of aggregate-cement paste (mortar) composite with aggregate size smaller than 3 mm, was cast directly on top of the granite piece, and was let cure. Small pieces of stiff aluminum plate with bolt holes in the periphery, were subsequently glued to the top and bottom ends of the mortar-aggregate interface element, by means of Sika/Sikadur structural epoxy. Great care was exercised to make sure the two plates were aligned in parallel fashion.

While the epoxy was curing (24 hrs.) the specimen was inserted into the interface test apparatus, and the final stages of curing took place under a small normal load in the range of 5 to 10 psi (34.5 to 69 kPa), which ensured excellent bond. No failures were observed in the two epoxy-aluminum granite or mortar interfaces. Most experiments were conducted with granite aggregate, while some initial tests were also carried out with limestone. The cement used in all tests was Type III. Several specimen fixtures were made so that a series of tests could be performed after one another. Curing of the specimens typically took 10 to 14 days.

Although the experiments were designed and carried out with great care, it was difficult to align the plane of the specimens' interfaces within +/- 0.002 m of the level of the tangential loading actuator, which resulted in nonuniform stress distributions over the interface due to reactive moments. Also, in some tests it was decided to reduce the

area of the interface by reducing the diameter of the mortar phase's contact diameter by 0.75 cm. This helped stabilize the low normal (confining) stress experiments.

Nonlinear finite element analyses of the specimen-apparatus system were also conducted to help analyze and characterize the interface properties. These analyses have been described earlier by Stankowski (1990 a and b) and Stankowski et al. (1990 and 1991). It was established that the nominal or average properties for the interfaces were quite close to what was developed during the course of the numerical analysis-and-experiment inverse identification studies. The last figure in this report (Fig. 21) clearly shows that the interface properties (curved ultimate strength envelope, residual strength envelope, and various constants) match the data closely.

4. EXPERIMENTAL DATA

Figures 6 (a) - (e) through 20 (a) - (f) show load-displacement response diagrams for typical successful experiments conducted in the range -400 psi (-2,760 kPa) compressive normal stress to 100 psi (690 kPa) tensile normal stress. The diagrams (a) through (e) in each case show: (a) shear stress vs. normal displacement; (b) shear stress vs. shear (horizontal) displacement (total); (c) shear stress vs. shear (horizontal) displacement (bottom relative gage point location); (d) shear stress vs. shear (horizontal) displacement (top relative gage point location); and, (e) normal displacement vs. shear (horizontal) displacement, which is an indication of dilatancy of the interface during shearing. The "noise" seen in many of the response diagrams are due to characteristics of the signal processing and data acquisition units, and it is not connected to the nature of the experiments themselves. Further smoothing of the data will be conducted in subsequent paper preparation efforts.

It is noted that the experiments conducted at higher stress levels remained stable for longer periods than the low normal stress tests, which at times became quite unstable. The rate of dilatancy of the interfaces increases with lower normal stress ranges, and tends to diminish with higher stresses that suppress dilatancy. In the tensile loading cases where global instabilities often followed peak strength, it seems that the post-peak slopes for stable paths were an order of magnitude steeper than the ones observed. When comparing the experimental data with model performance, it seems that the model simulates behavior at all normal stress levels quite well. Also the normal displacement (dilatancy) response appears quite realistic. Peak and residual strength data for all tests are presented in Fig. 21. The open "squares" represent peak strength information,

and the "crosses" represent residual strength data. The model parameters that were obtained from this information are also shown in the figure.

(Please note that the following pages with figures and diagrams have not been paginated)

LIST OF FIGURES

- Fig. 1 Combined tension-shear or compression-shear mortar-aggregate experimental apparatus
- Fig. 2 (a) Apparatus mounted in MTS (490 kN) servo-controlled load frame. (b) Experimental apparatus with tangential displacement controlled screw-actuator.
- (a) (b)
- Fig. 3 (a) and (b) Experimental apparatus with LVDTs used for measurement of relative tangential and normal displacements
- (a) (b)
- Fig. 4 (a) Experimental apparatus with relative motion displacement transducers and mortar-aggregate interface specimen. (b) Mortar-aggregate (granite) specimen with attached aluminum base plates
- (a) (b)
- Fig. 5 (a) Top view, and (b) side view of mortar-aggregate (granite) specimen with bottom aluminum base plate
- (a) (b)
- Fig. 6 (a) - (e) Load-displacement response diagrams for test series 1
- Fig. 7 (a) - (e) Load-displacement response diagrams for test series 7
- Fig. 8 (a) - (e) Load-displacement response diagrams for test series 11
- Fig. 9 (a) - (e) Load-displacement response diagrams for test series 12
- Fig. 10 (a) - (e) Load-displacement response diagrams for test series 13
- Fig. 11 (a) - (e) Load-displacement response diagrams for test series 14
- Fig. 12 (a) - (e) Load-displacement response diagrams for test series 15

- Fig. 13 (a) - (e) Load-displacement response diagrams for test series 21
- Fig. 14 (a) - (e) Load-displacement response diagrams for test series 22
- Fig. 15 (a) - (f) Load-displacement response diagrams for test series 23
- Fig. 16 (a) - (e) Load-displacement response diagrams for test series 24
- Fig. 17 (a) - (f) Load-displacement response diagrams for test series 28
- Fig. 18 (a) - (f) Load-displacement response diagrams for test series 29
- Fig. 19 (a) - (f) Load-displacement response diagrams for test series 30
- Fig. 20 (a) - (f) Load-displacement response diagrams for test series 31
- Fig. 21 Ultimate (Peak) and residual strength envelopes for mortar-aggregate (granite) interfaces and calibrated model parameters

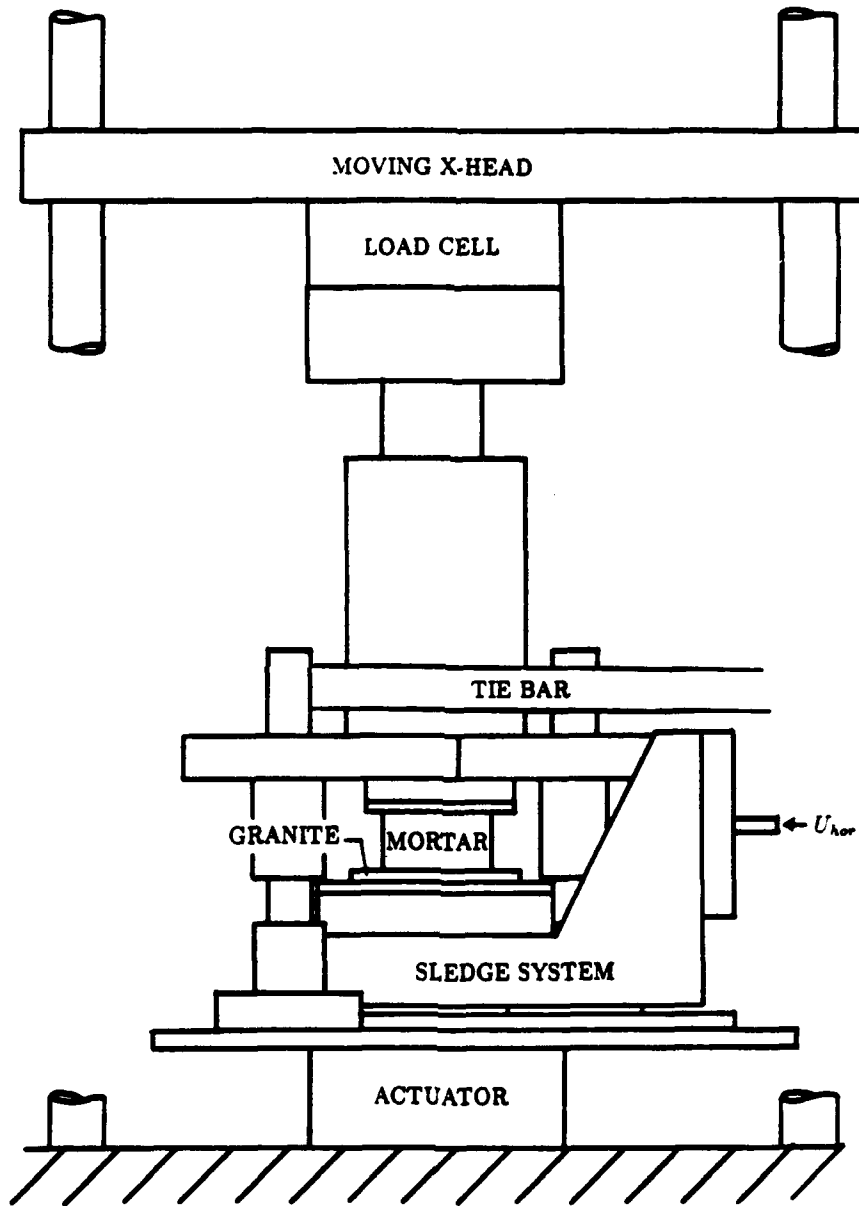
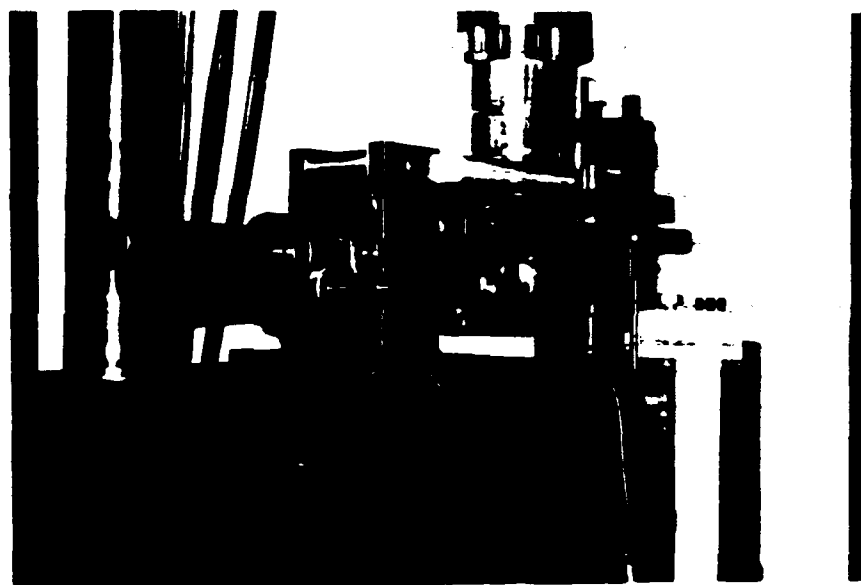


Fig. 1 Combined tension-shear or compression-shear mortar-aggregate experimental apparatus

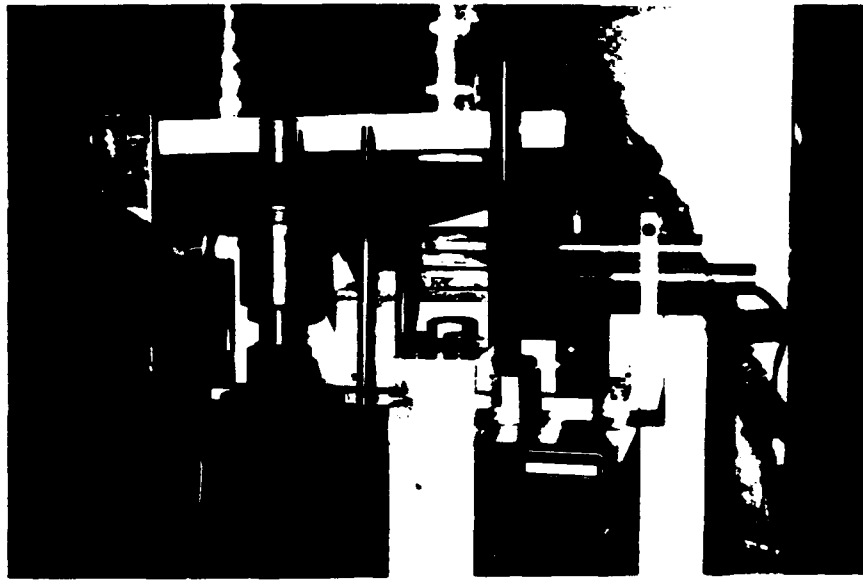


(a)

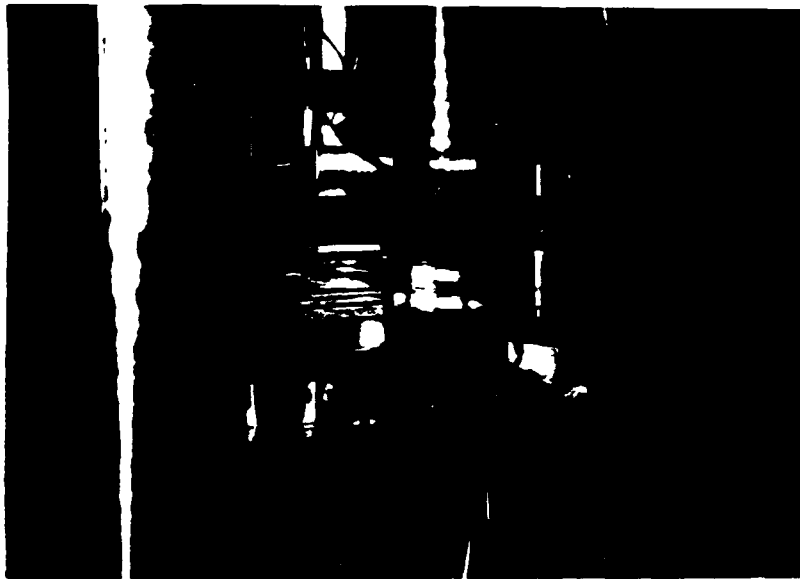


(b)

Fig. 2 (a) Apparatus mounted in MTS (490 kN) servo-controlled load frame. (b) Experimental apparatus with tangential displacement controlled screw-actuator.

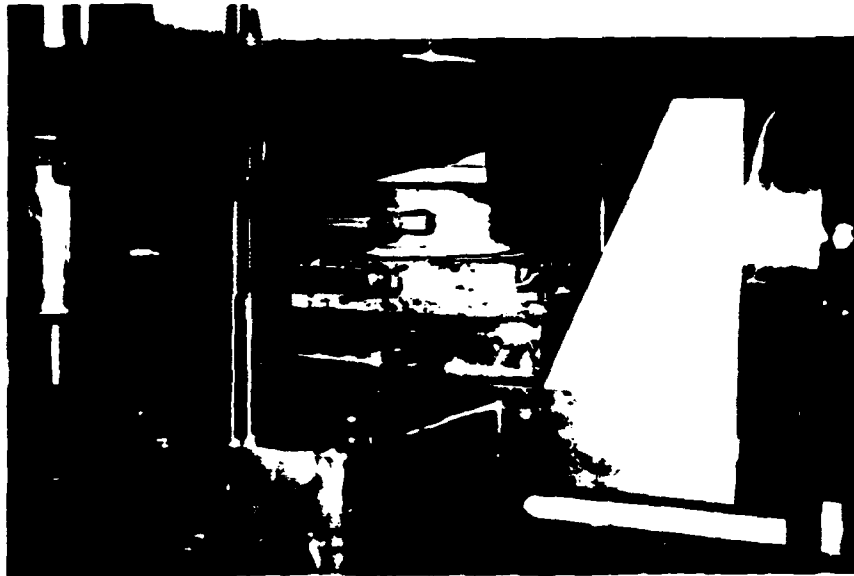


(a)

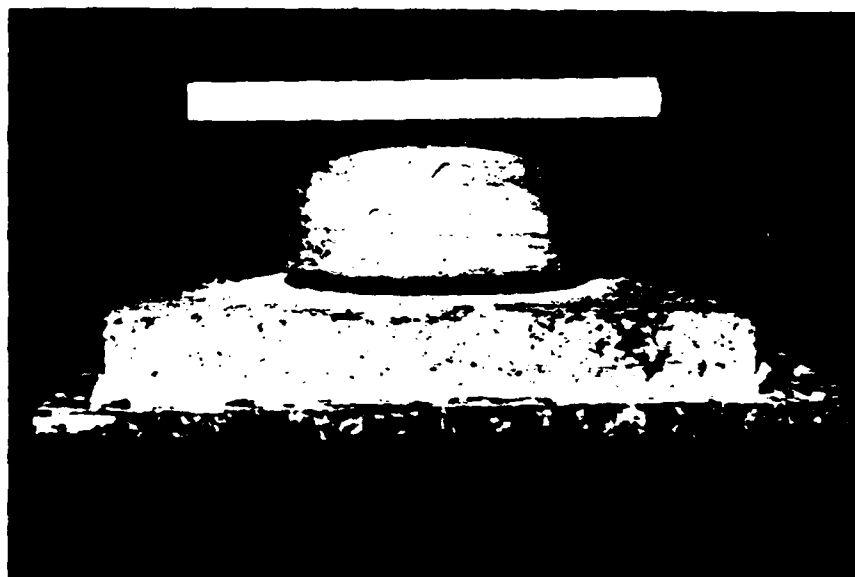


(b)

Fig. 3 (a) and (b) Experimental apparatus with LVDTs used for measurement of relative tangential and normal displacements

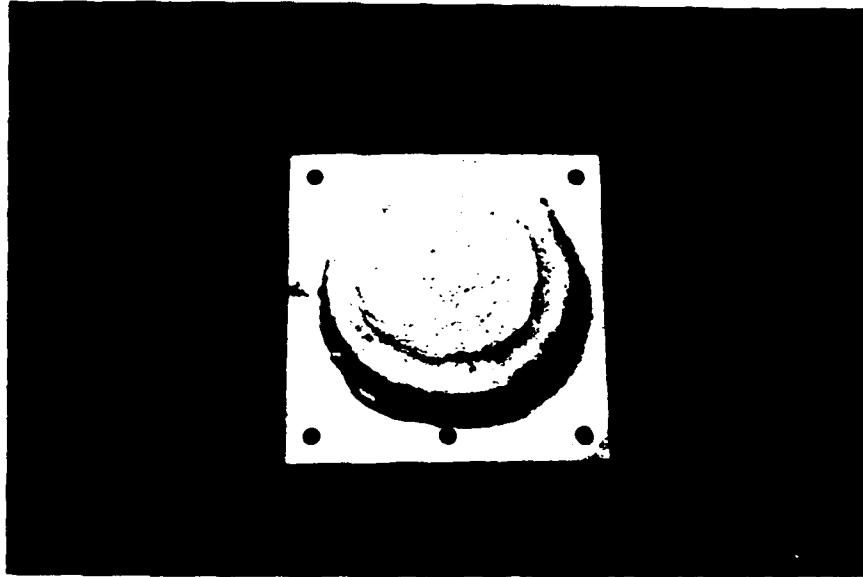


(a)



(b)

Fig. 4 (a) Experimental apparatus with relative motion displacement transducers and mortar-aggregate interface specimen. (b) Mortar-aggregate (granite) specimen with attached aluminum base plates



(a)



(b)

Fig. 5 (a) Top view, and (b) side view of mortar-aggregate (granite) specimen with bottom aluminum base plate

Normal Displacement - Shear Stress

Normal Stress = -100 psi, Htest1a

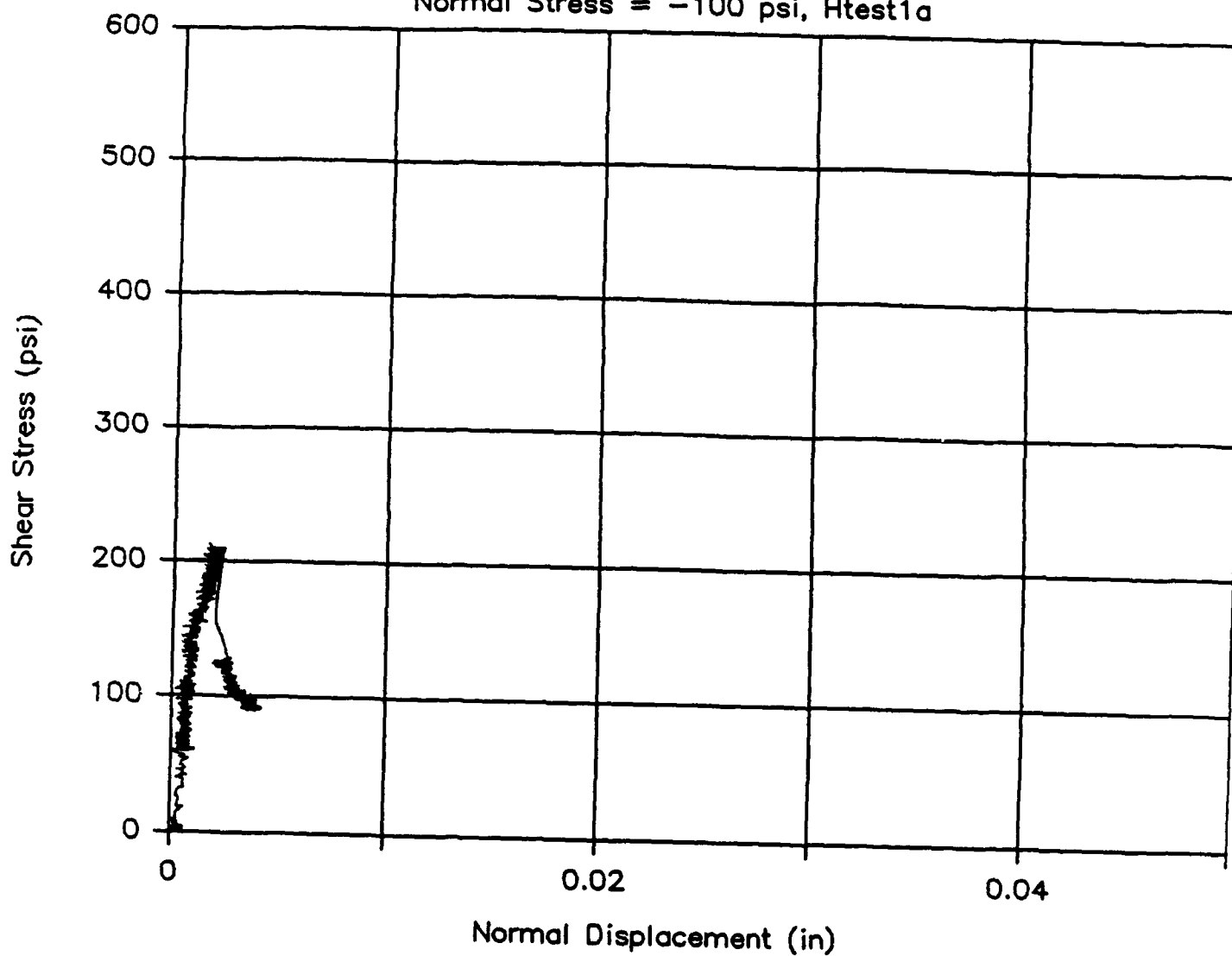
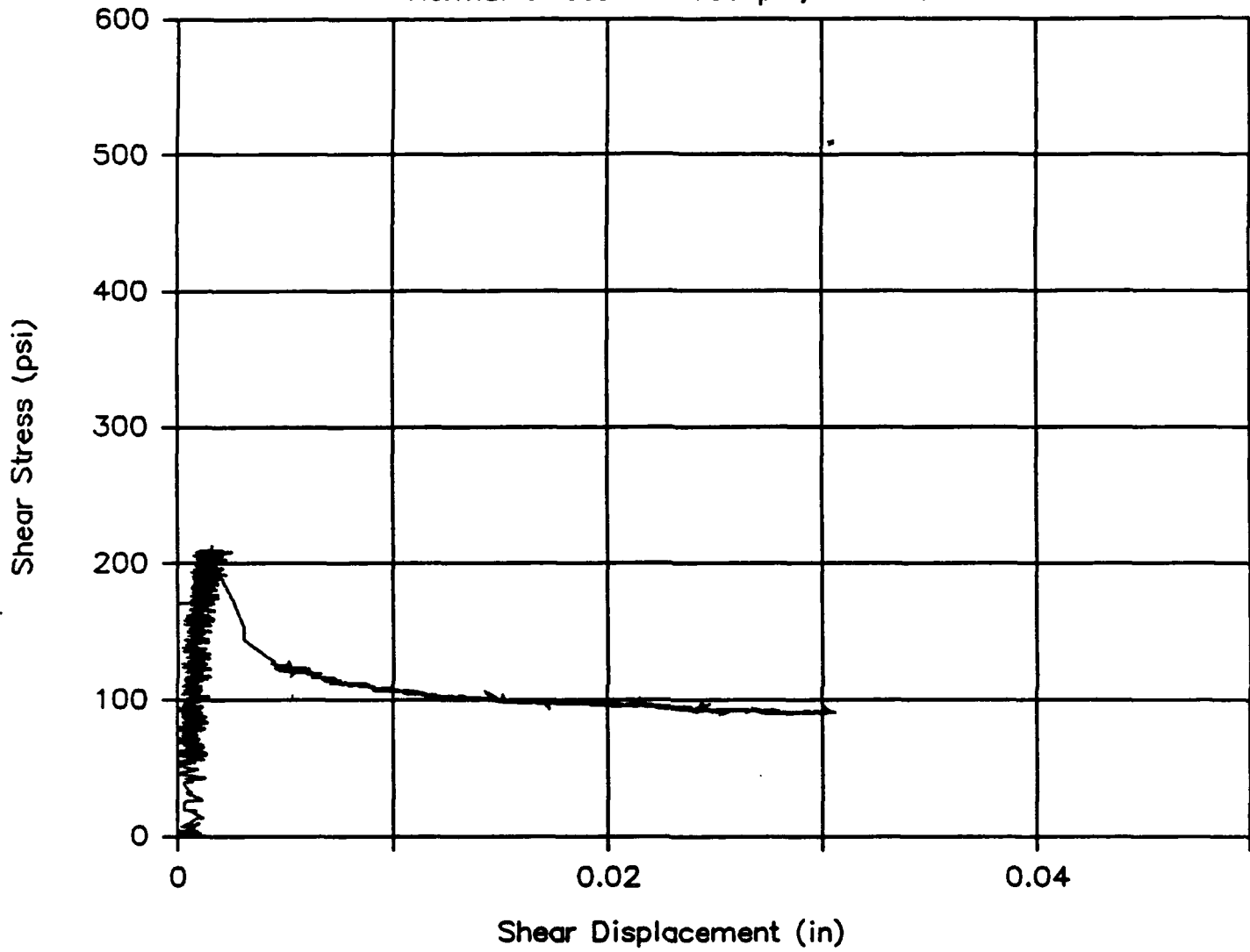


Fig. 6 (a) - (e) Load-displacement response diagrams for test series 1

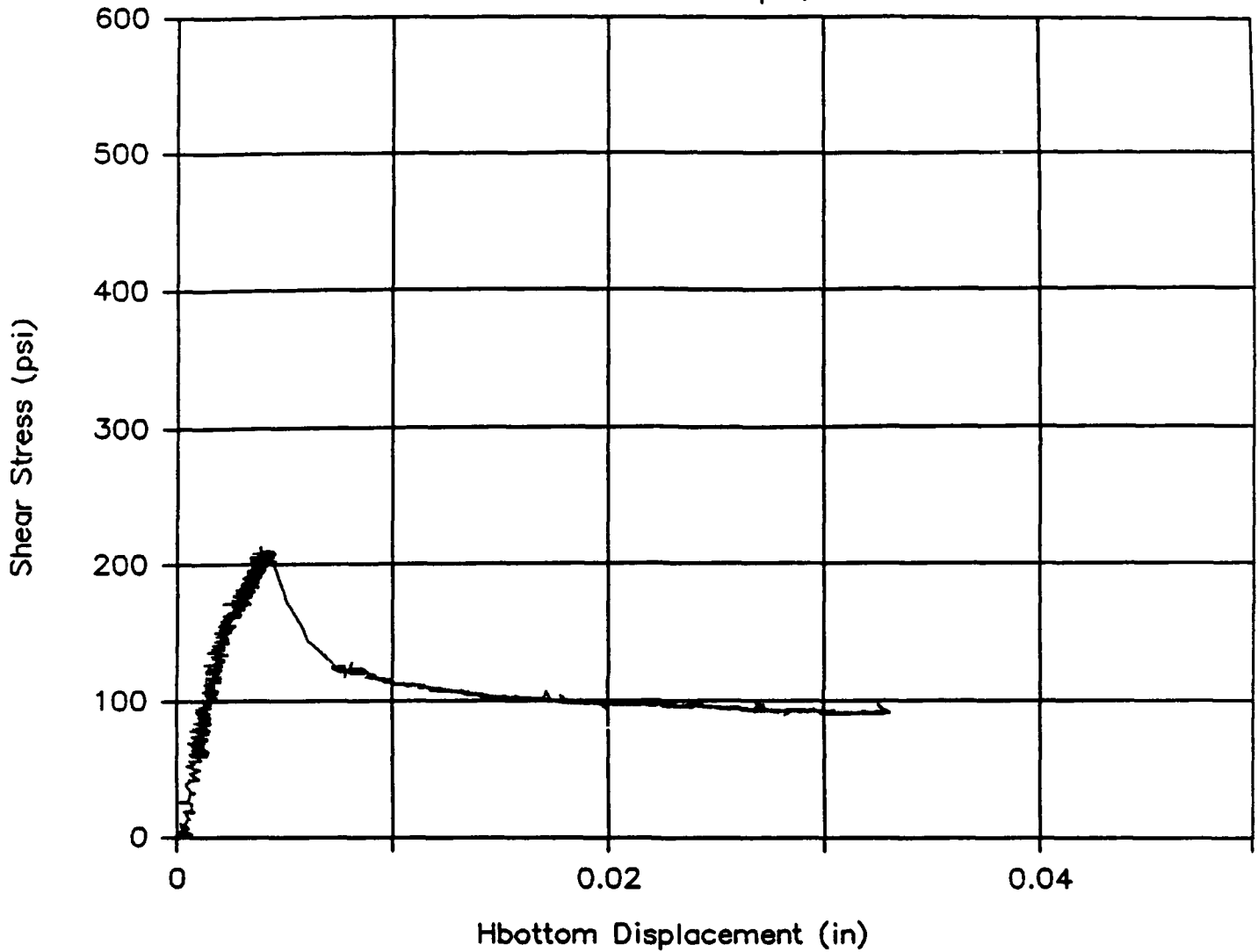
Shear Displacement – Shear Stress

Normal Stress = -100 psi, Htest1b



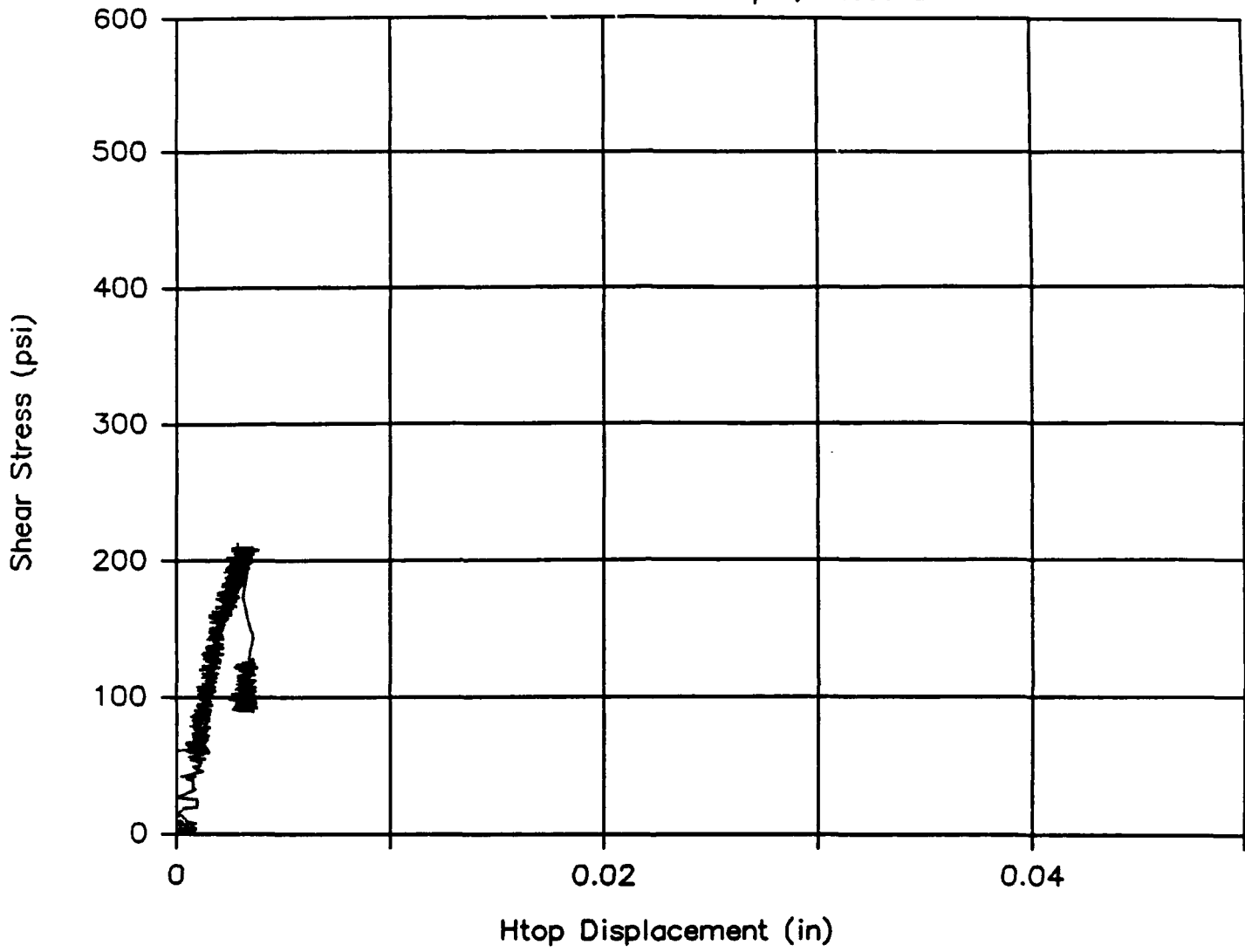
Hbottom Displacement – Shear Stress

Normal Stress = -100 psi, Htest1c



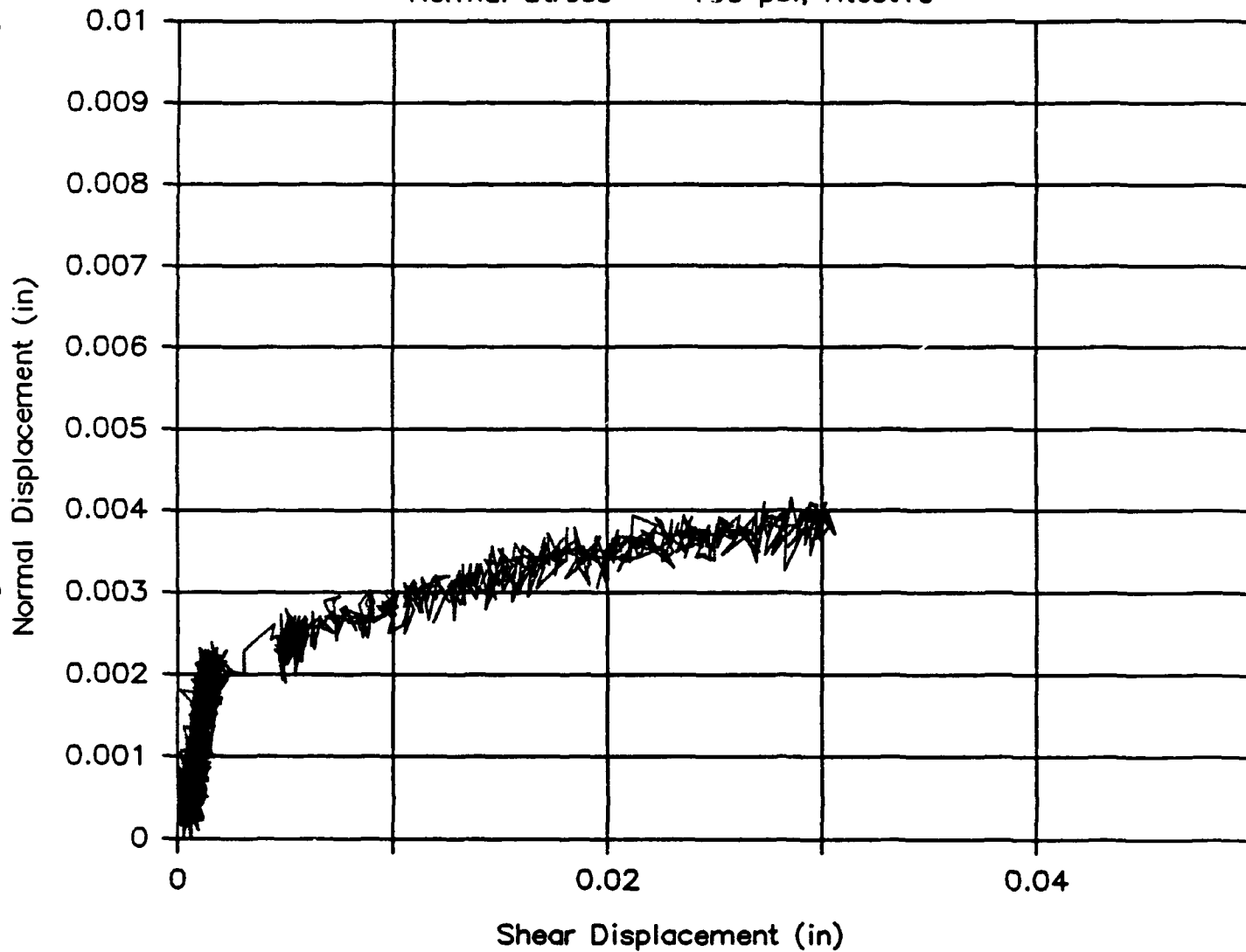
Htop Displacement – Shear Stress

Normal Stress = -100 psi, Htest1d



Shear Displacement—Normal Displacement

Normal Stress = -100 psi, Htest1e



Normal Displacement — Shear Stress

Normal Stress = -200 psi, Htest7a

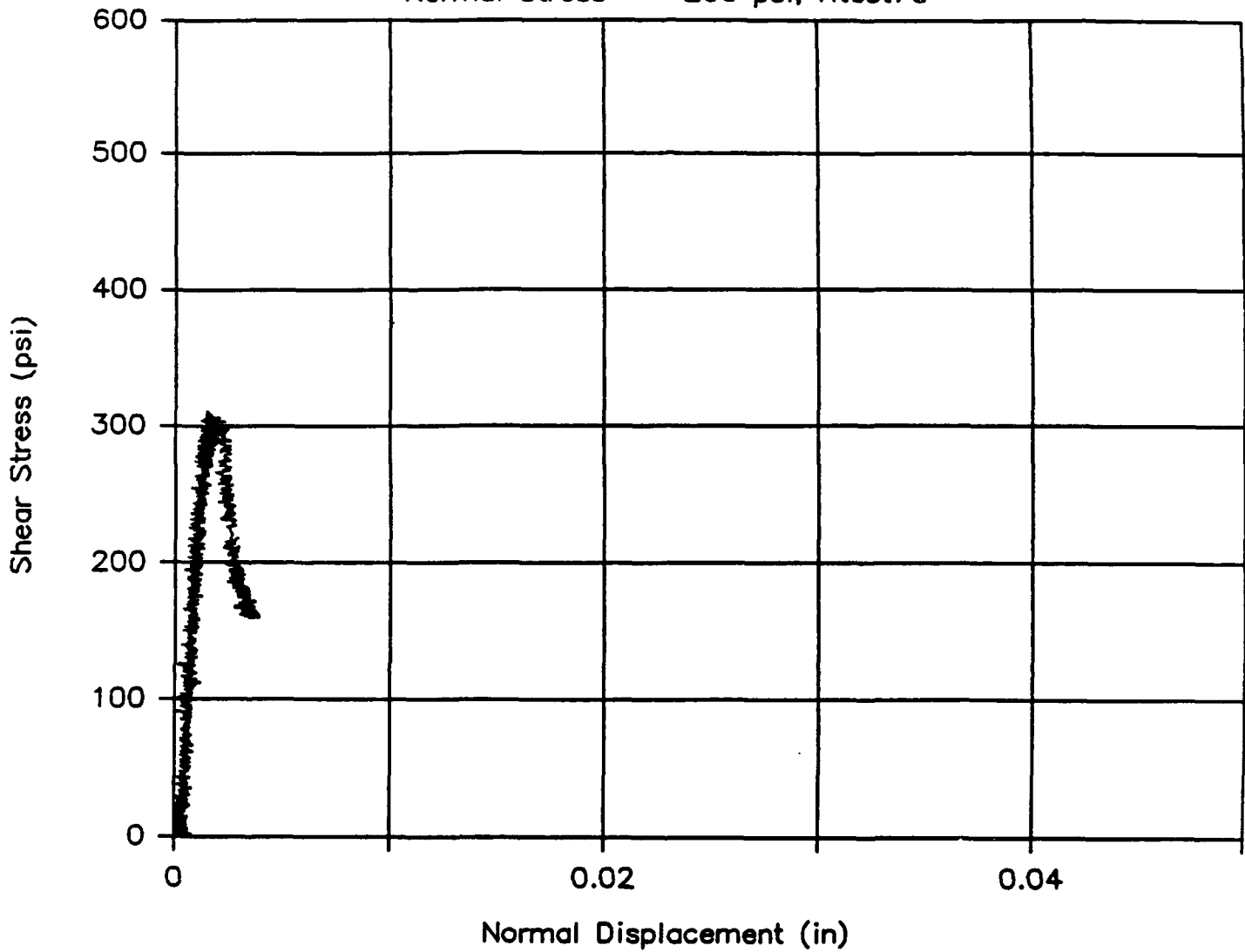
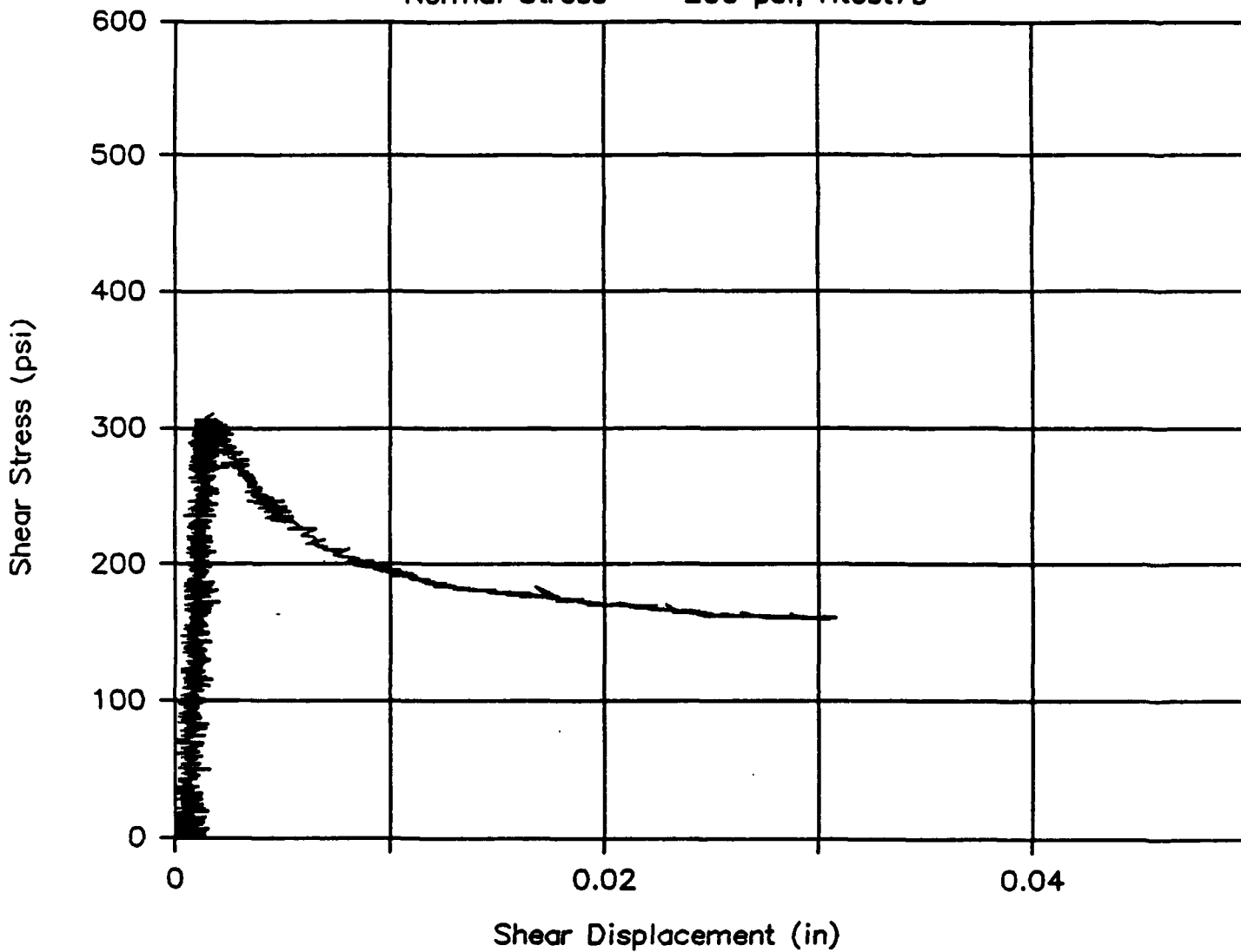


Fig. 7 (a) - (e) Load-displacement response diagrams for test series 7

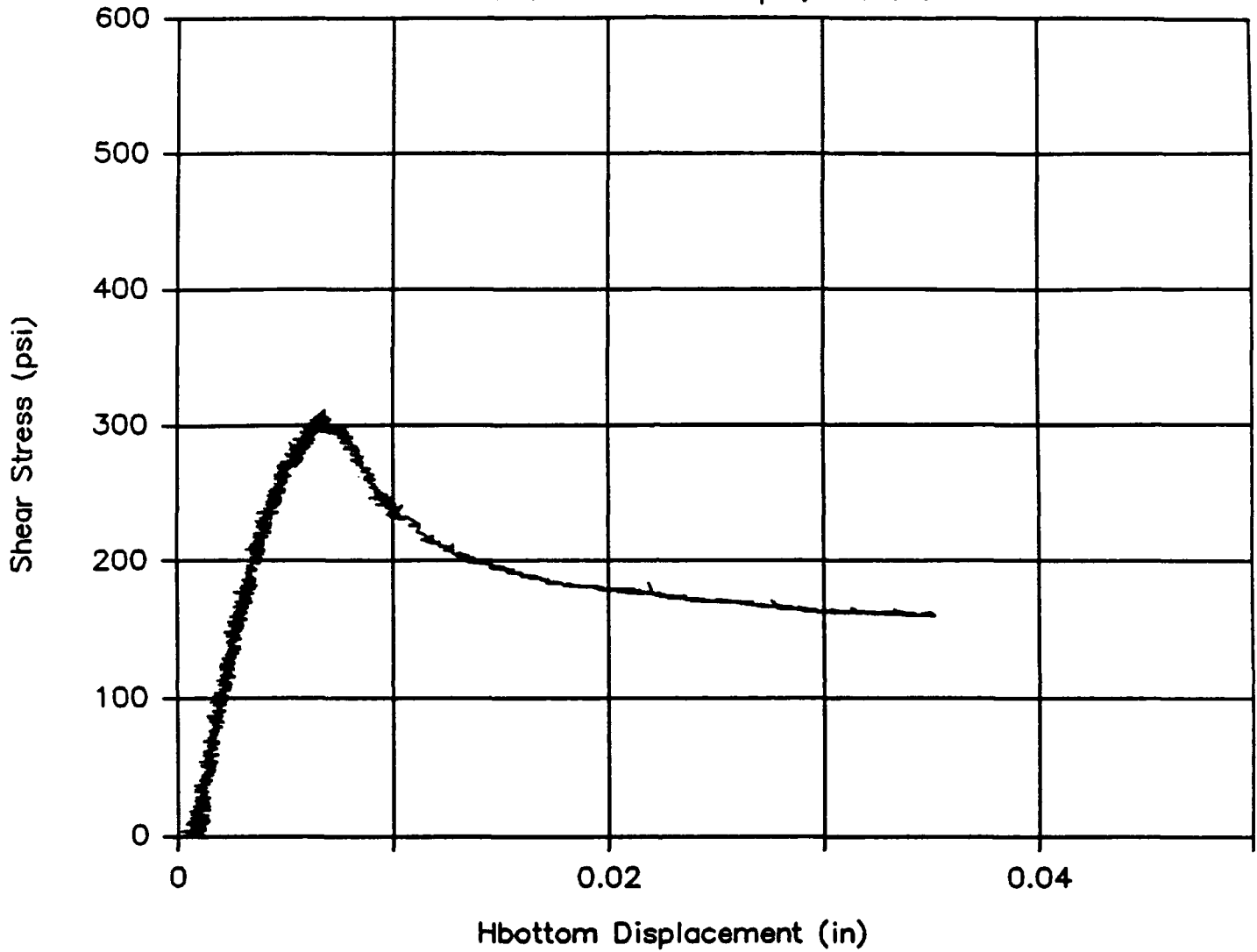
Shear Displacement — Shear Stress

Normal Stress = -200 psi, Htest7b



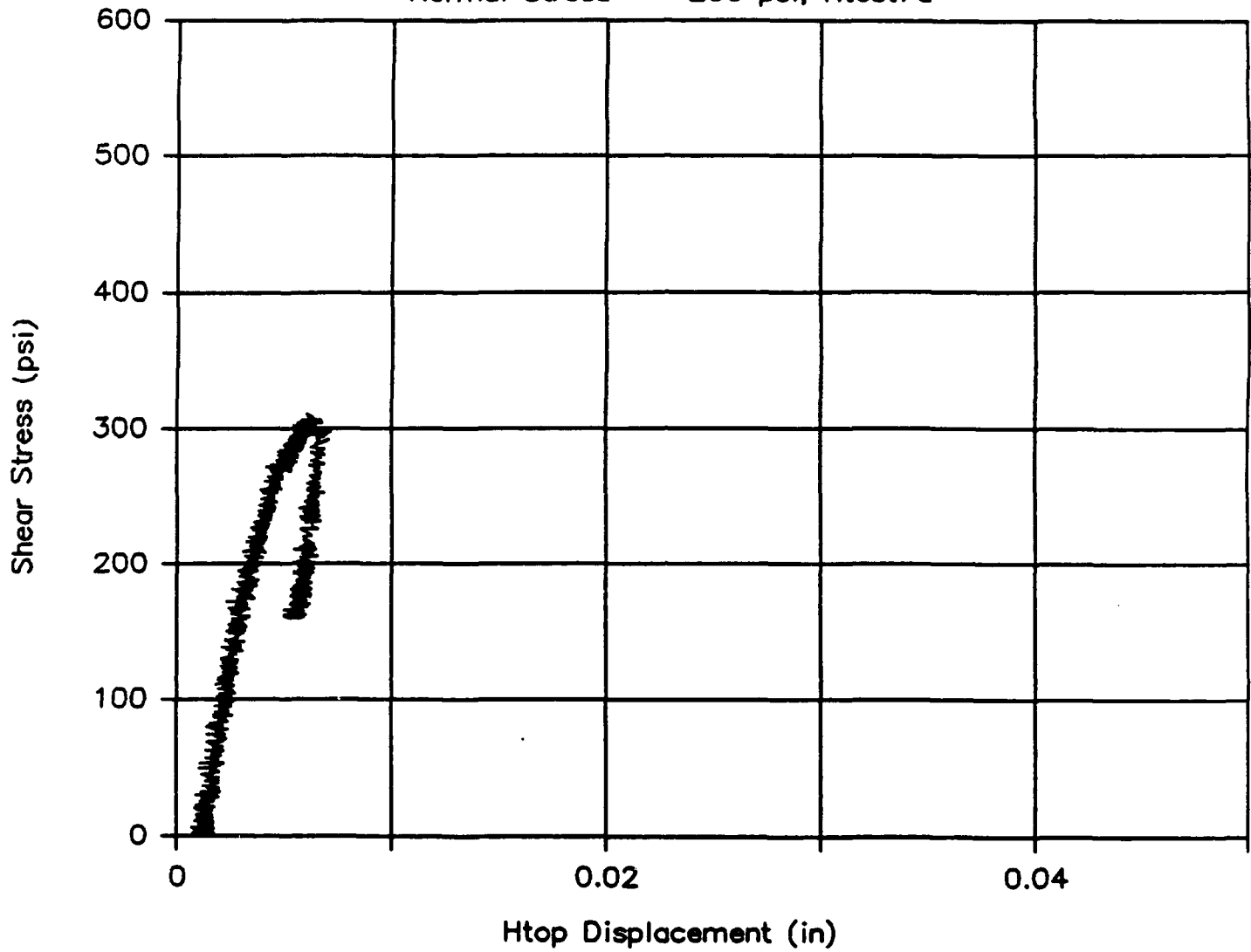
Hbottom Displacement – Shear Stress

Normal Stress = -200 psi, Htest7c



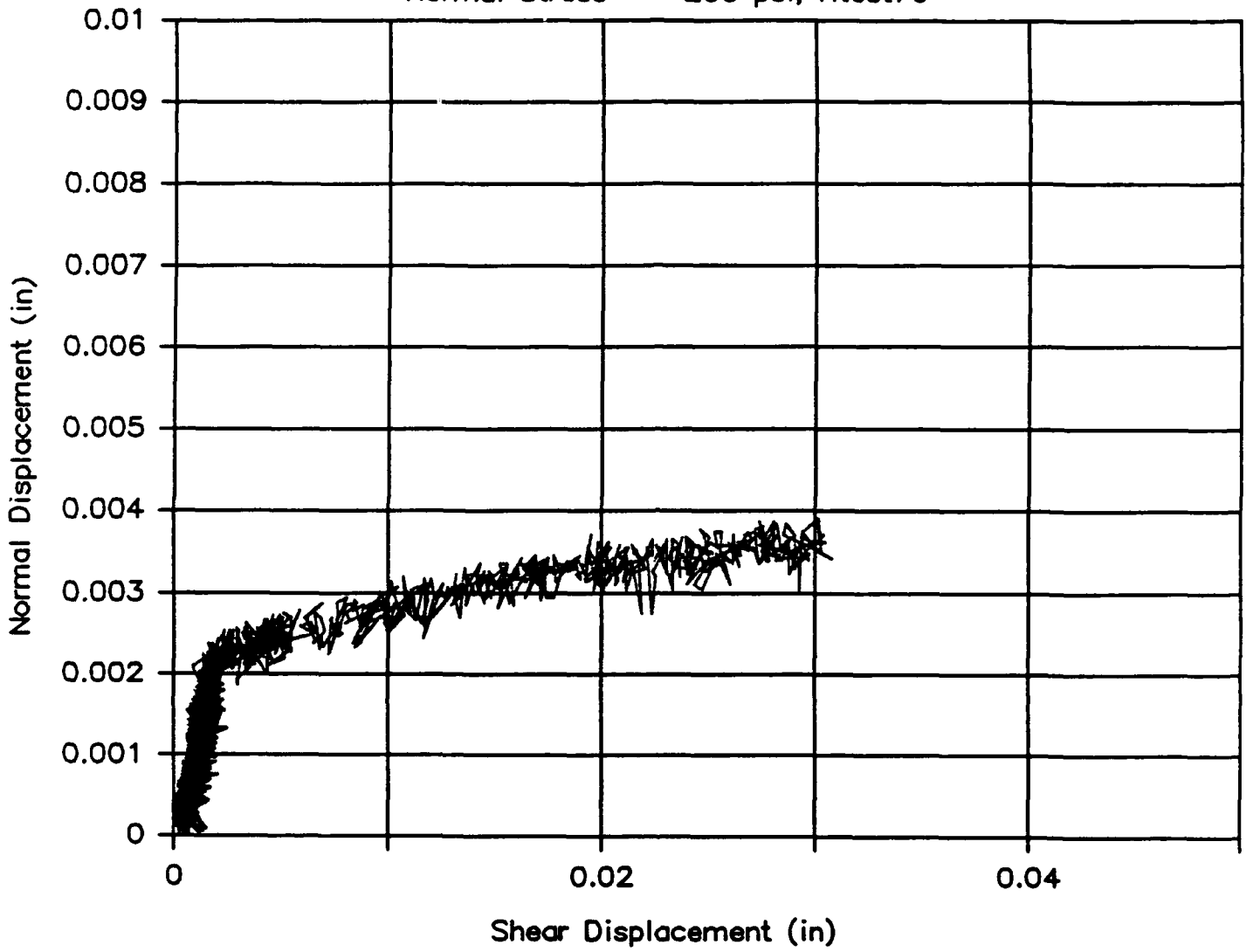
Htop Displacement – Shear Stress

Normal Stress = -200 psi, Htest7d



Shear Displacement—Normal Displacement

Normal Stress = -200 psi, Htest7e



Normal Displacement - Shear Stress

Normal Stress = -12.5 psi, Htest11a

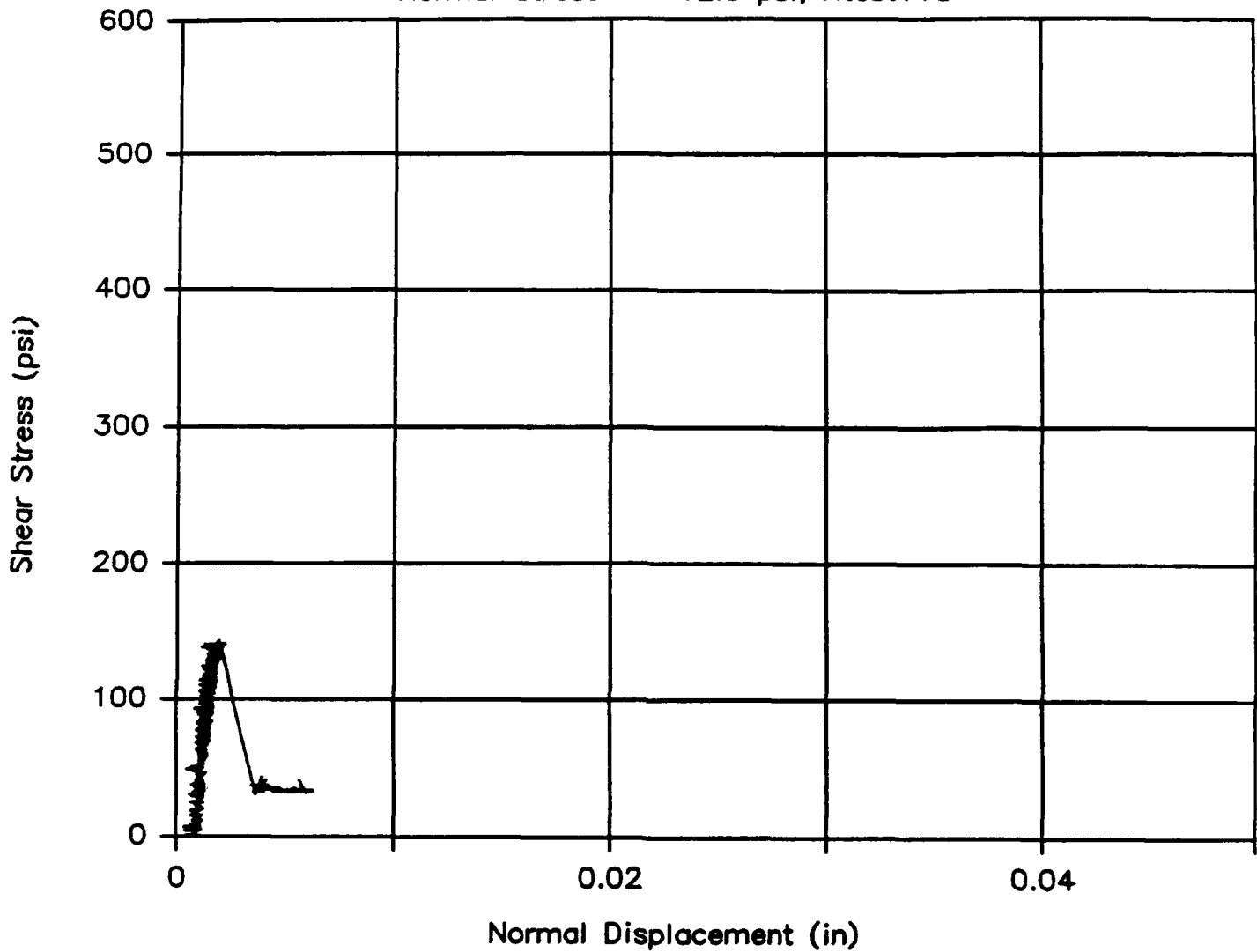
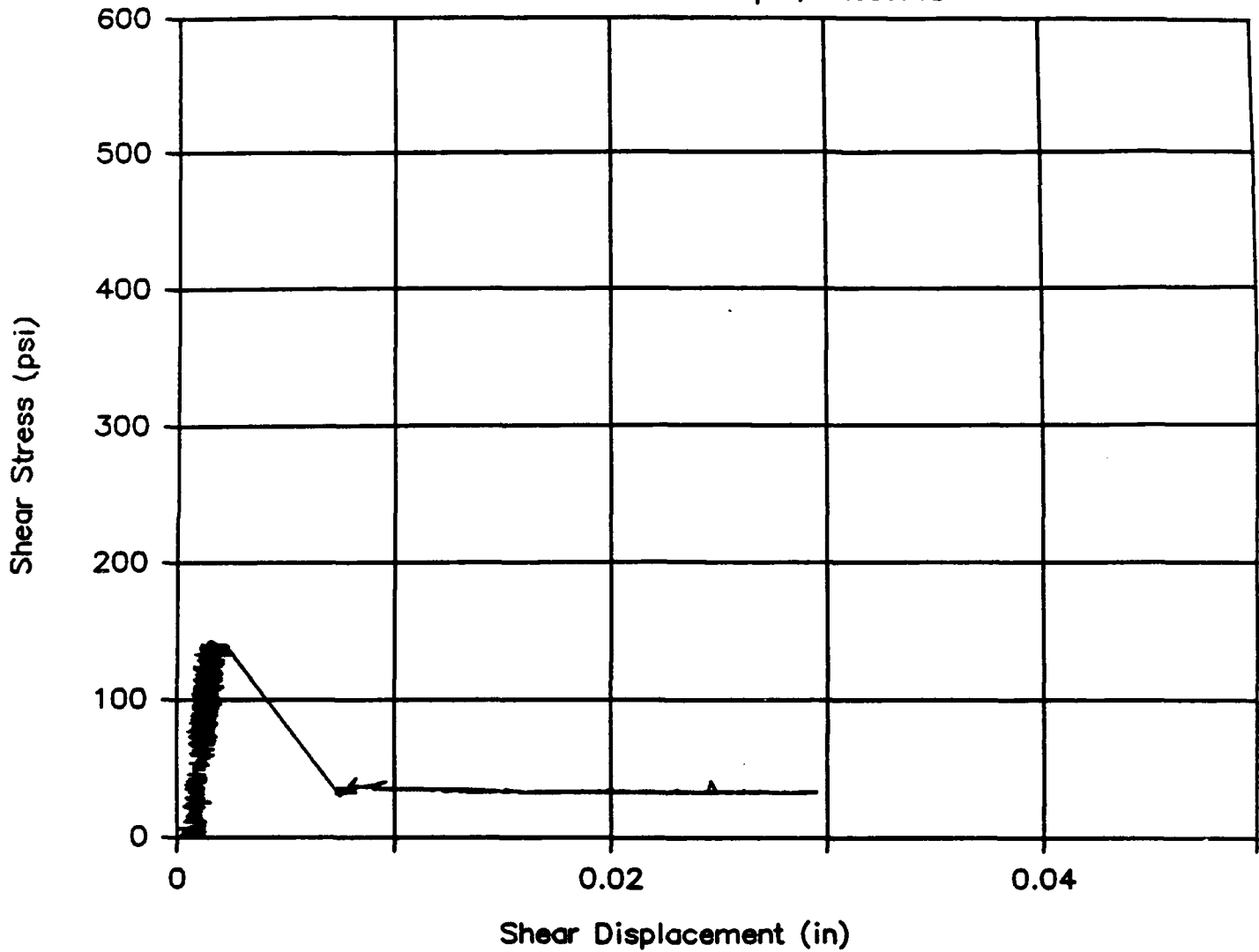


Fig. 8 (a) - (e) Load-displacement response diagrams for test series 11

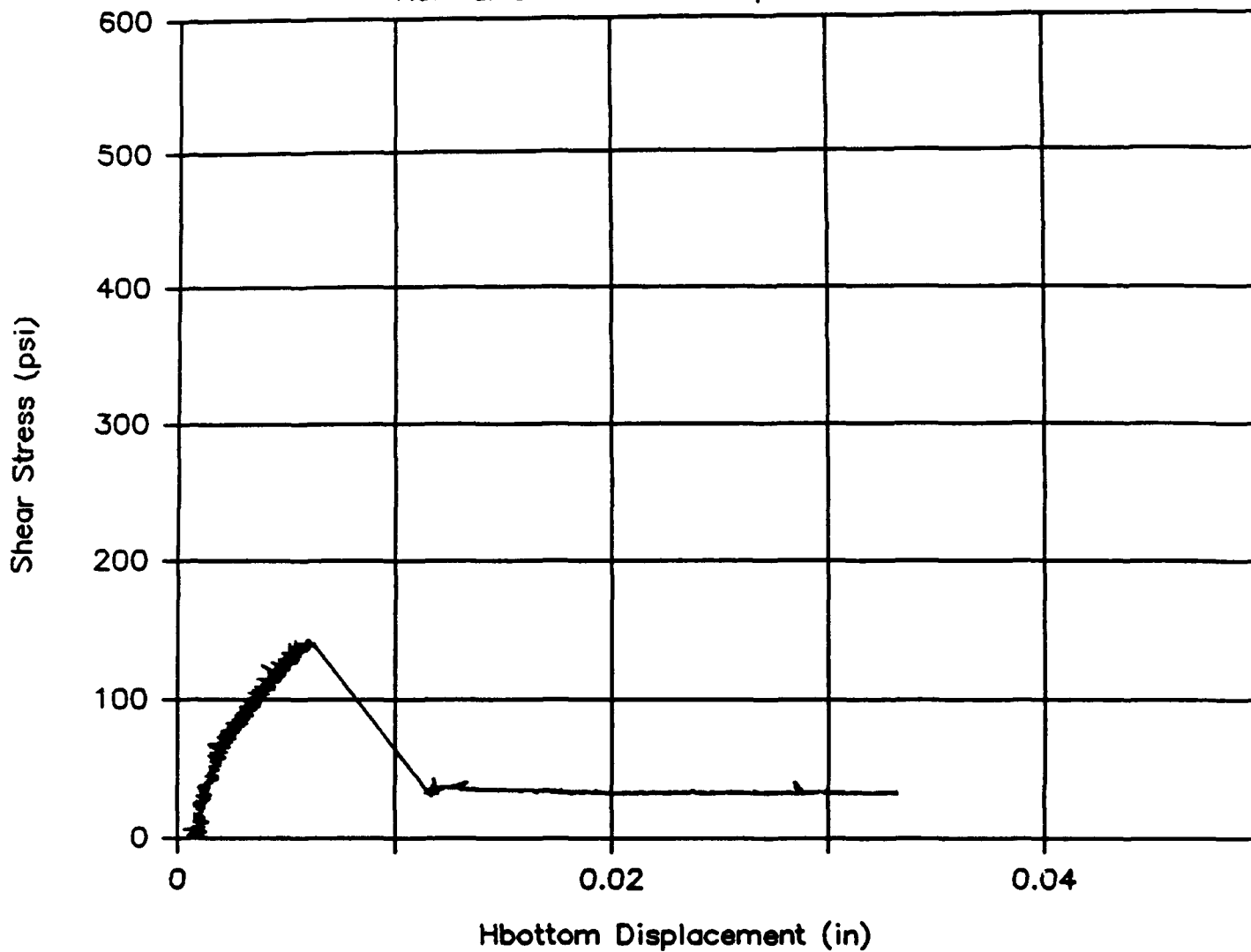
Shear Displacement – Shear Stress

Normal Stress = -12.5 psi, Htest11b



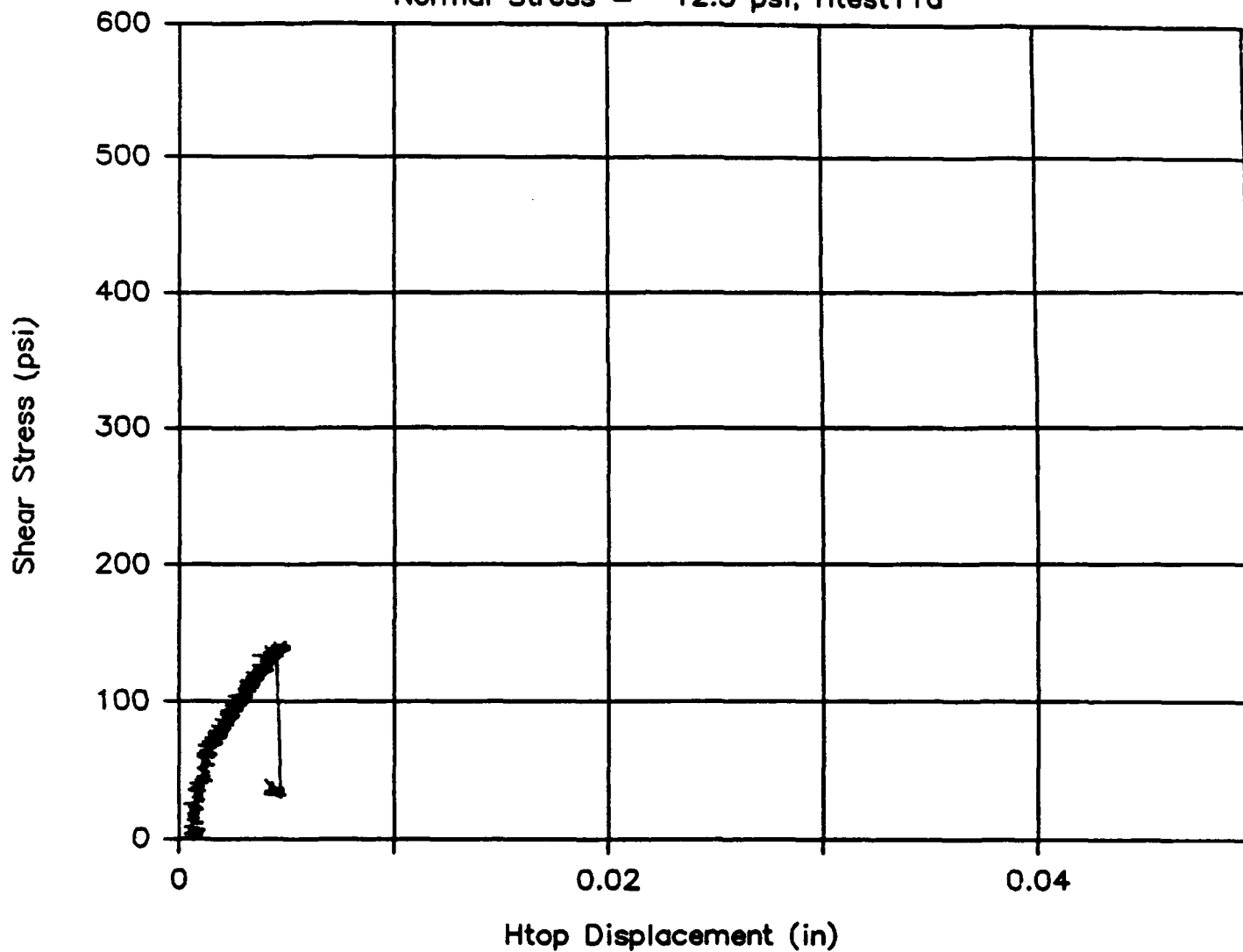
Hbottom Displacement – Shear Stress

Normal Stress = -12.5 psi, Htest11c



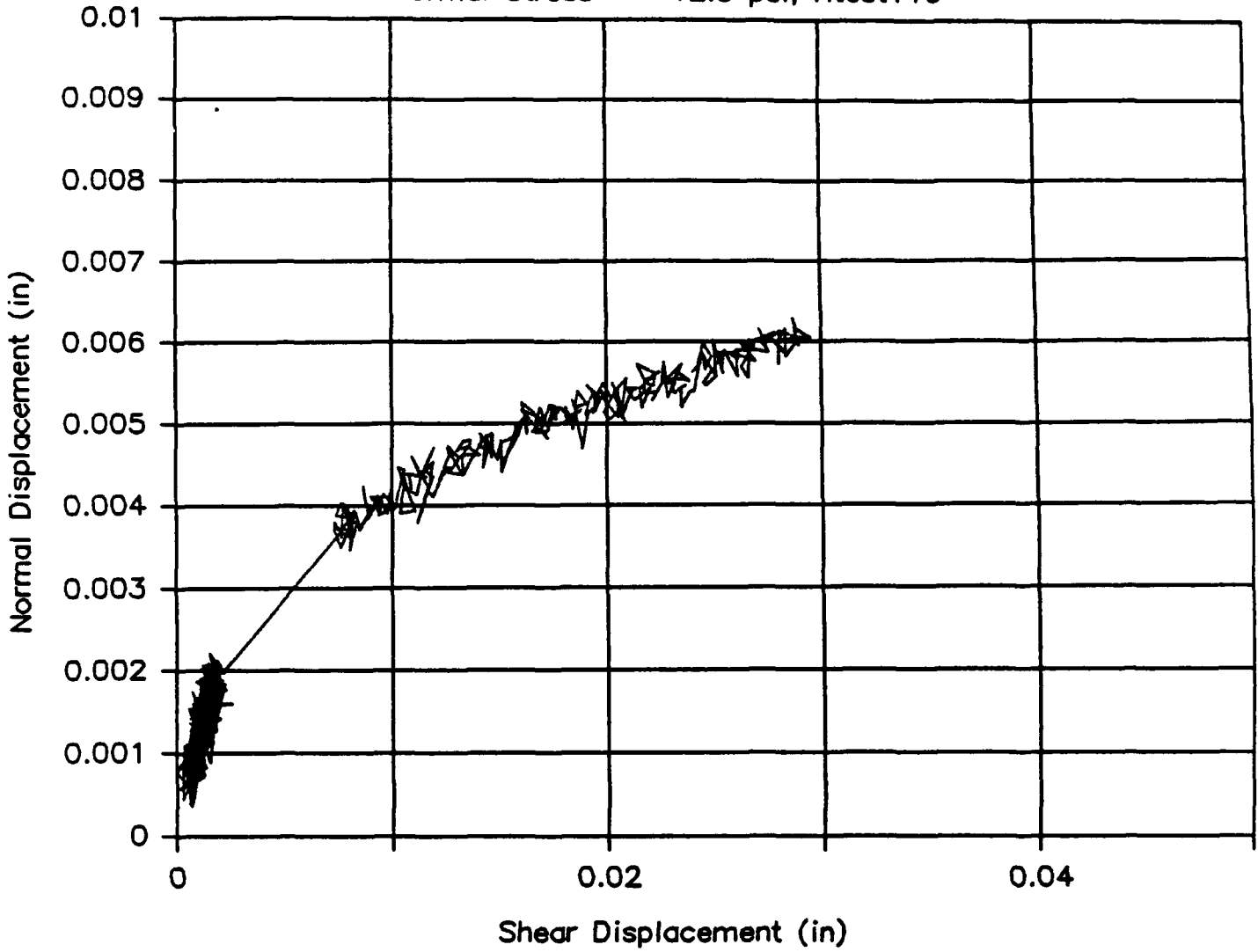
Htop Displacement – Shear Stress

Normal Stress = -12.5 psi, Htest11d



Shear Displacement—Normal Displacement

Normal Stress = -12.5 psi, Htest11e



Normal Displacement – Shear Stress

Normal Stress = -12.5 psi, Htest12a

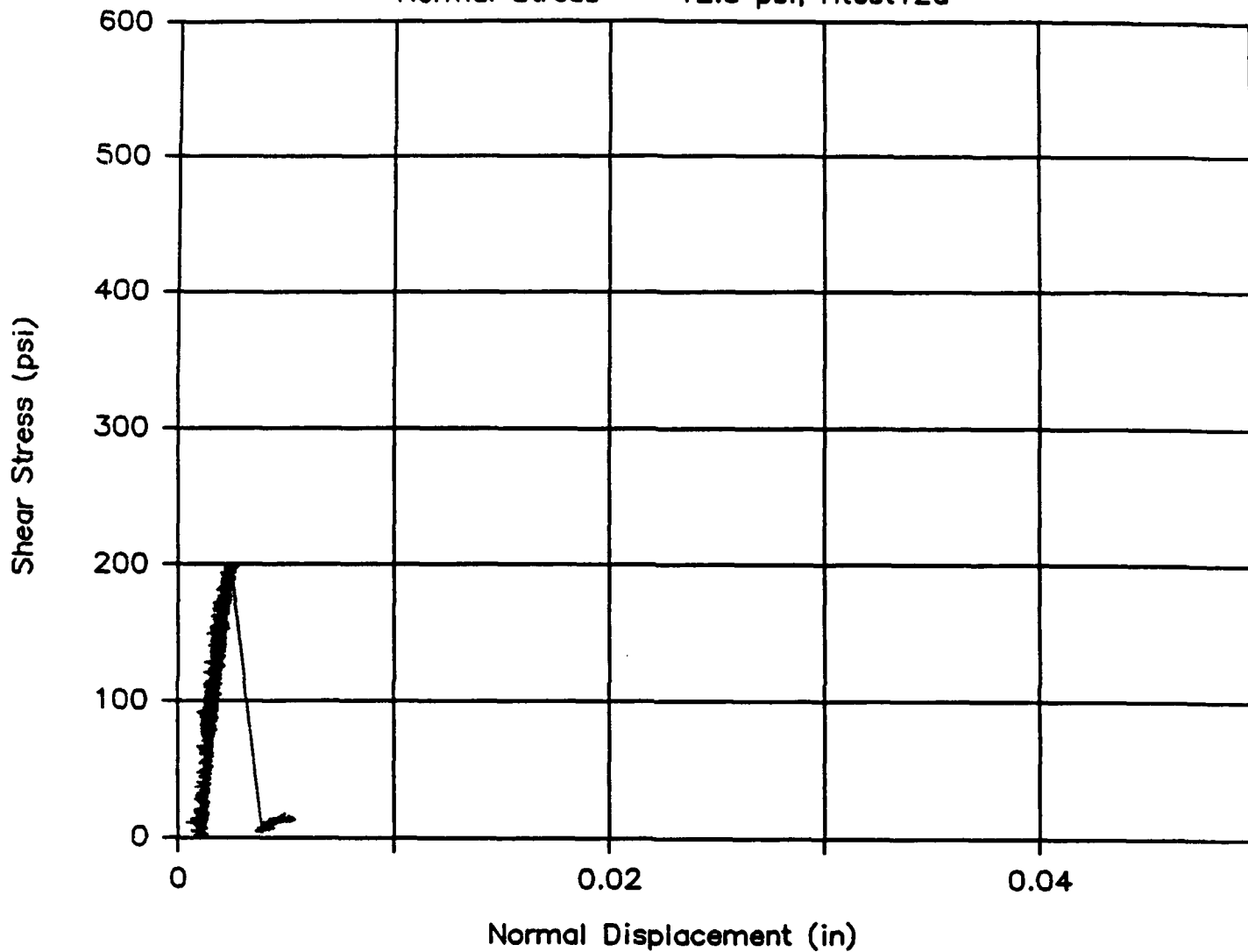
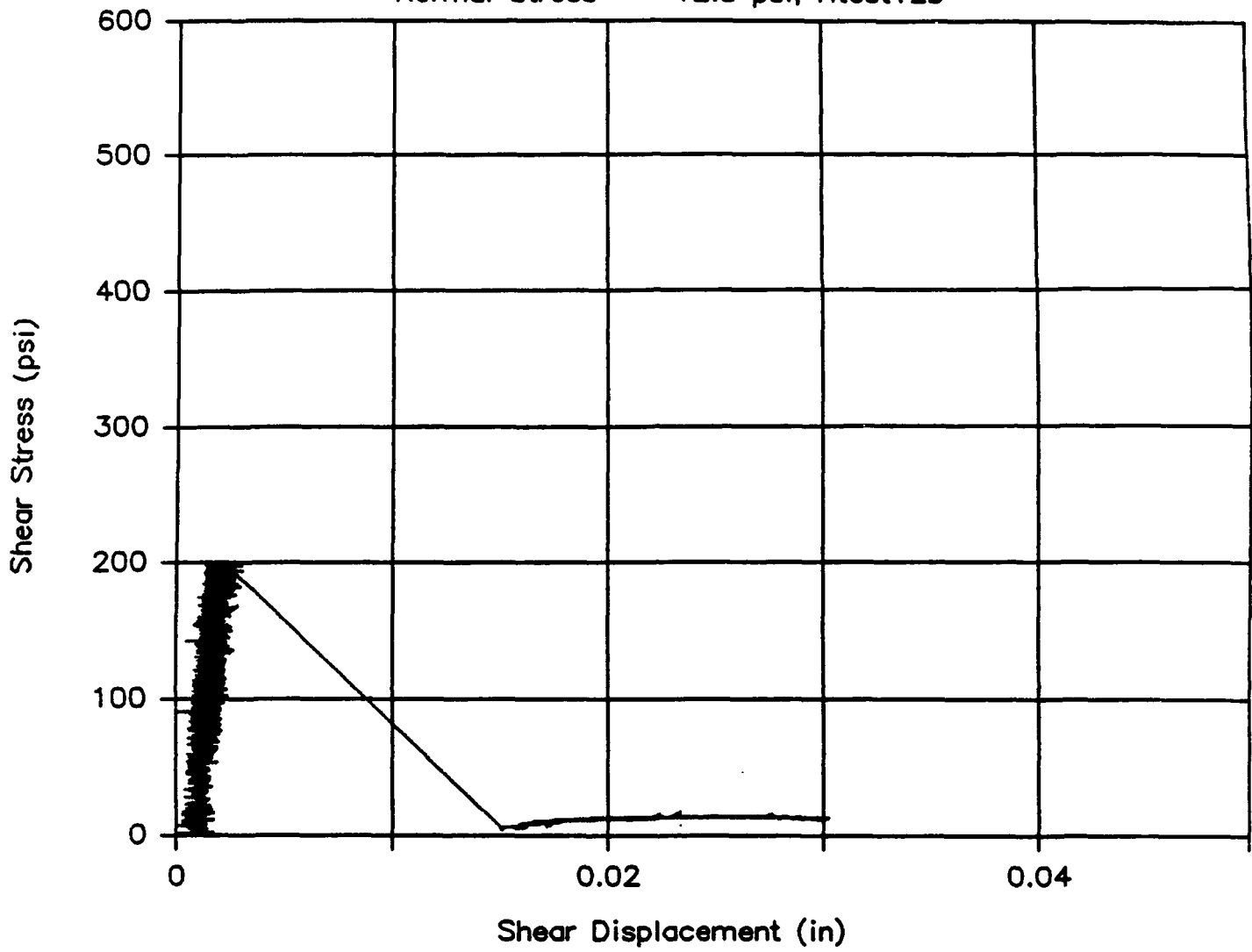


Fig. 9 (a) - (e) Load-displacement response diagrams for test series 12

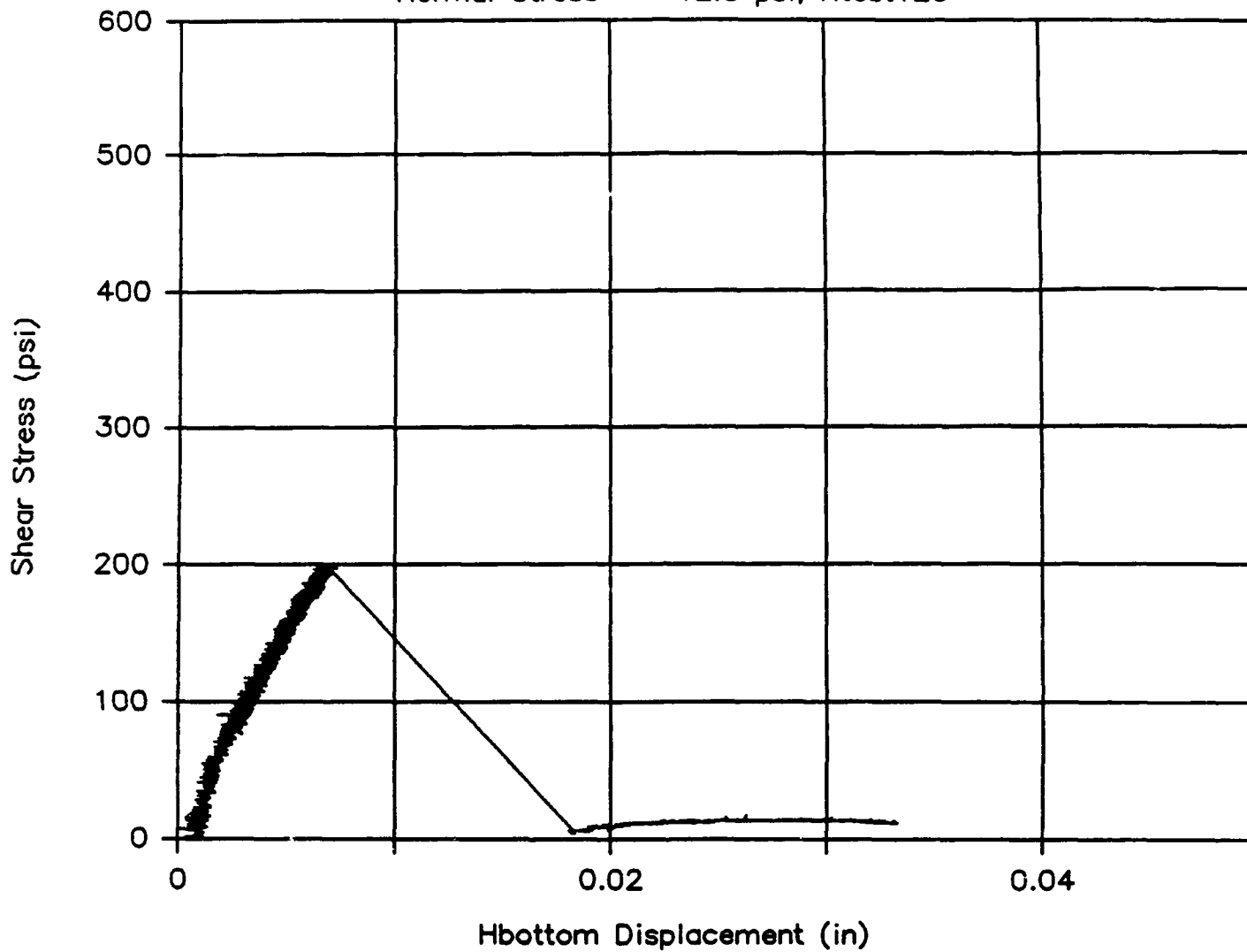
Shear Displacement – Shear Stress

Normal Stress = -12.5 psi, Htest12b



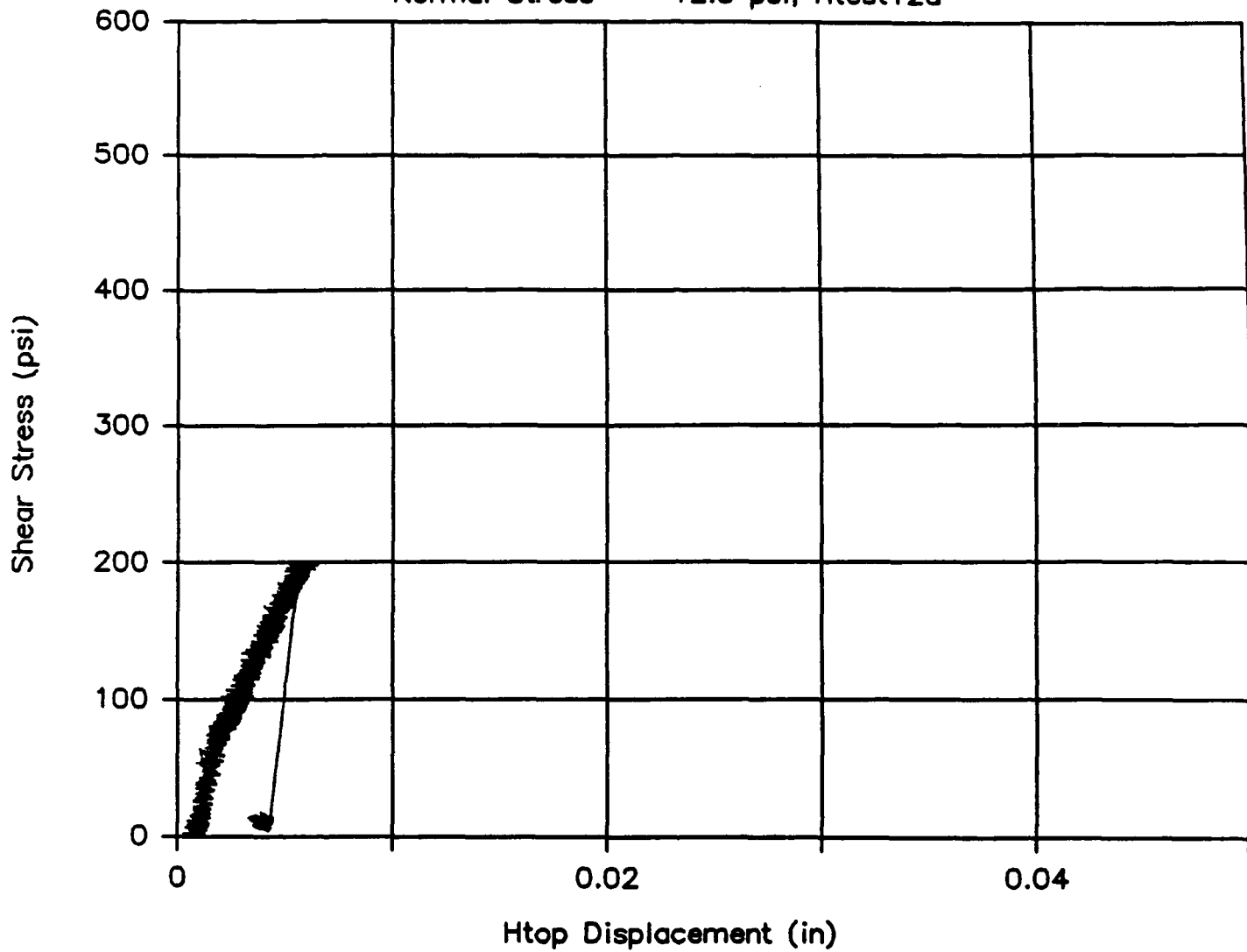
Hbottom Displacement – Shear Stress

Normal Stress = -12.5 psi, Htest12c



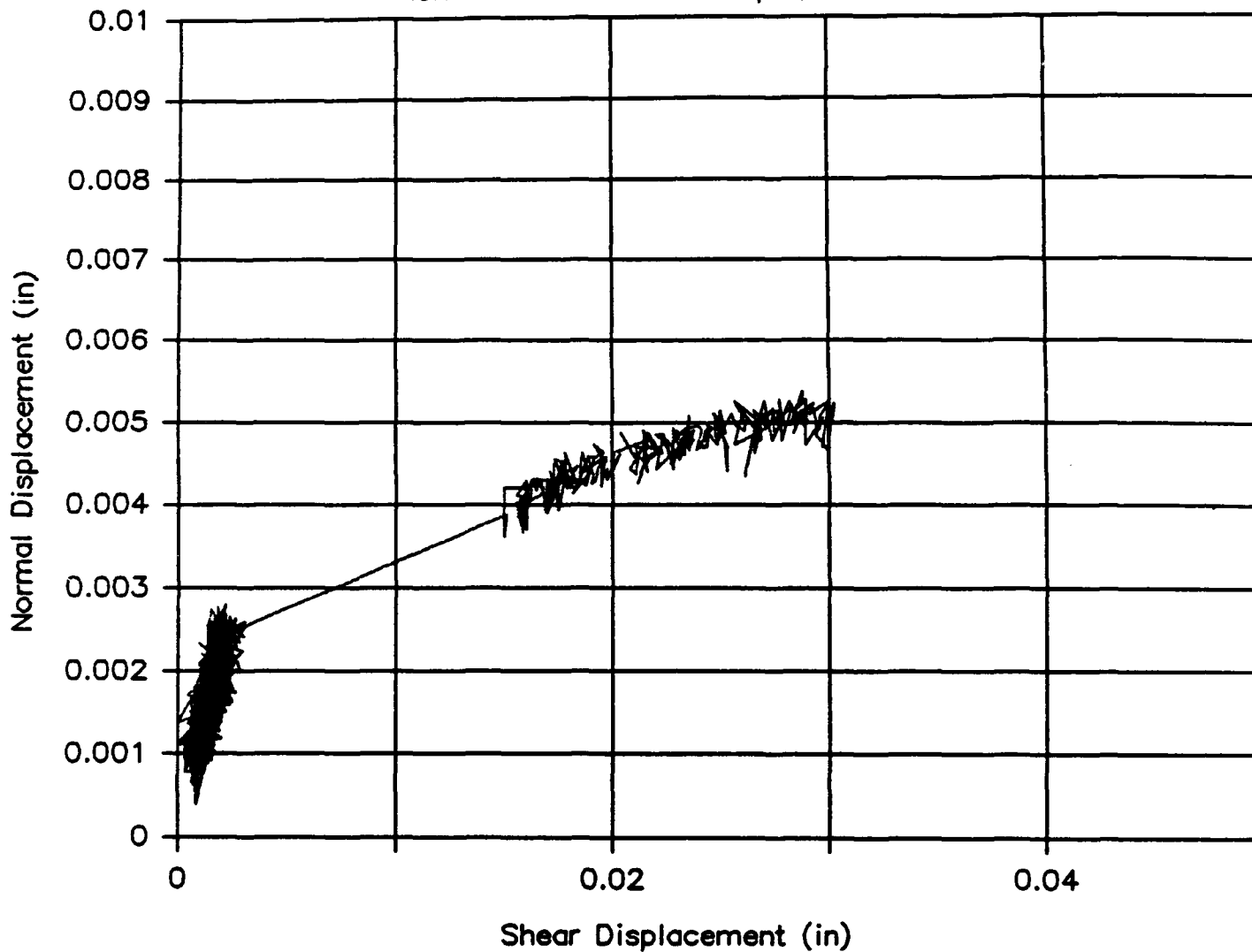
Htop Displacement – Shear Stress

Normal Stress = -12.5 psi, Htest12d



Shear Displacement—Normal Displacement

Normal Stress = -12.5 psi, Htest12e



Normal Displacement – Shear Stress

Normal Stress = -12.5 psi, Htest13a

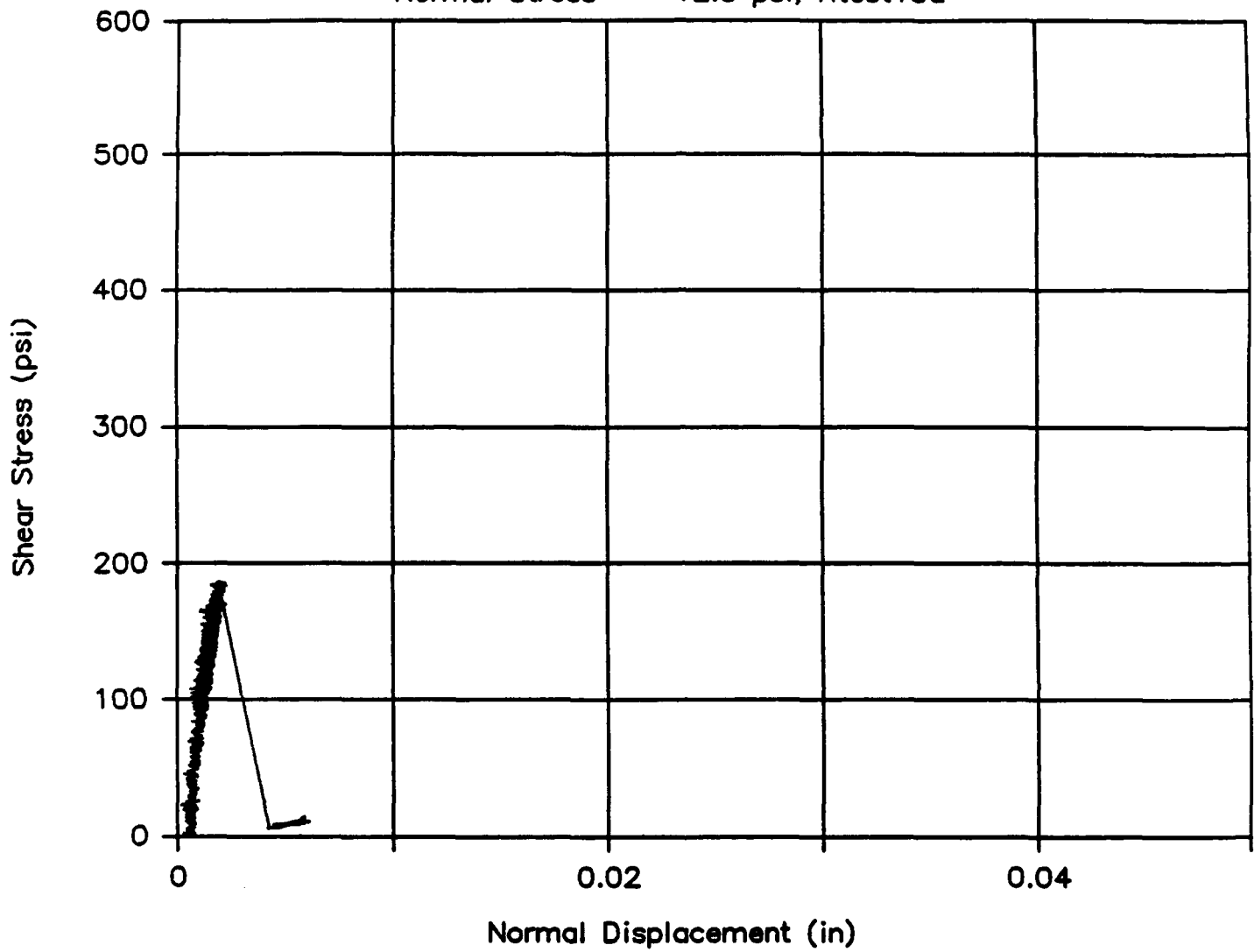
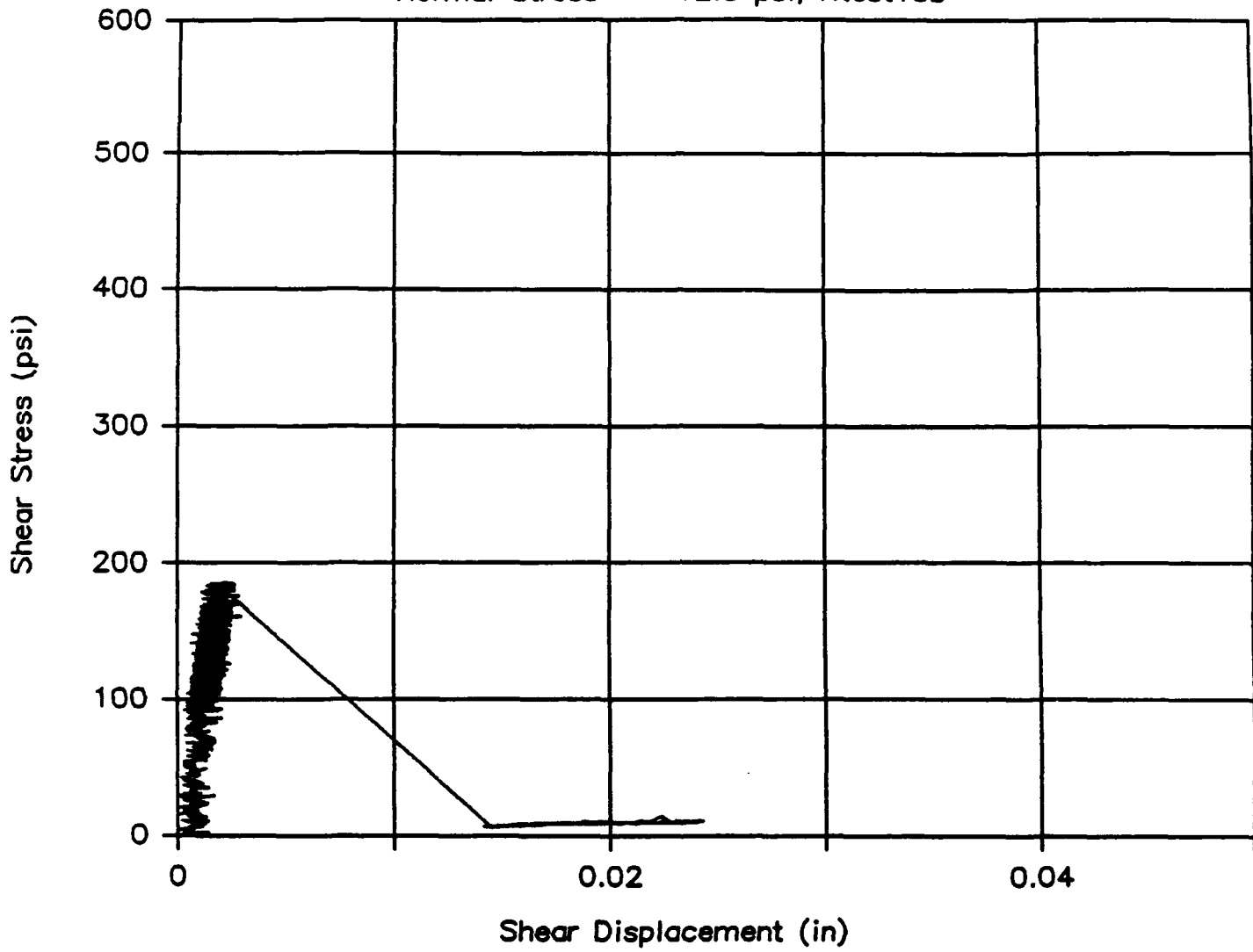


Fig. 10 (a) - (e) Load-displacement response diagrams for test series 13

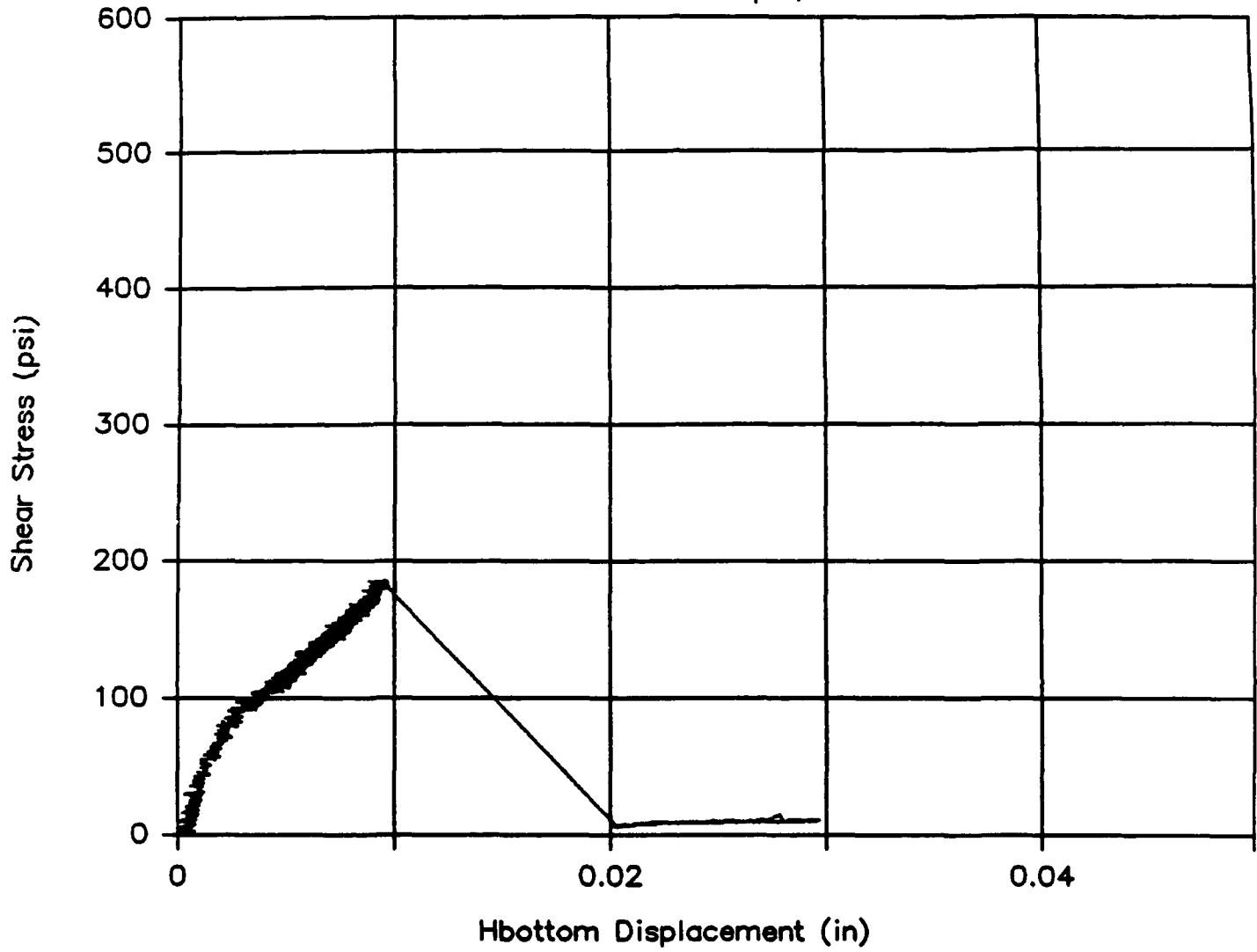
Shear Displacement – Shear Stress

Normal Stress = -12.5 psi, Htest13b



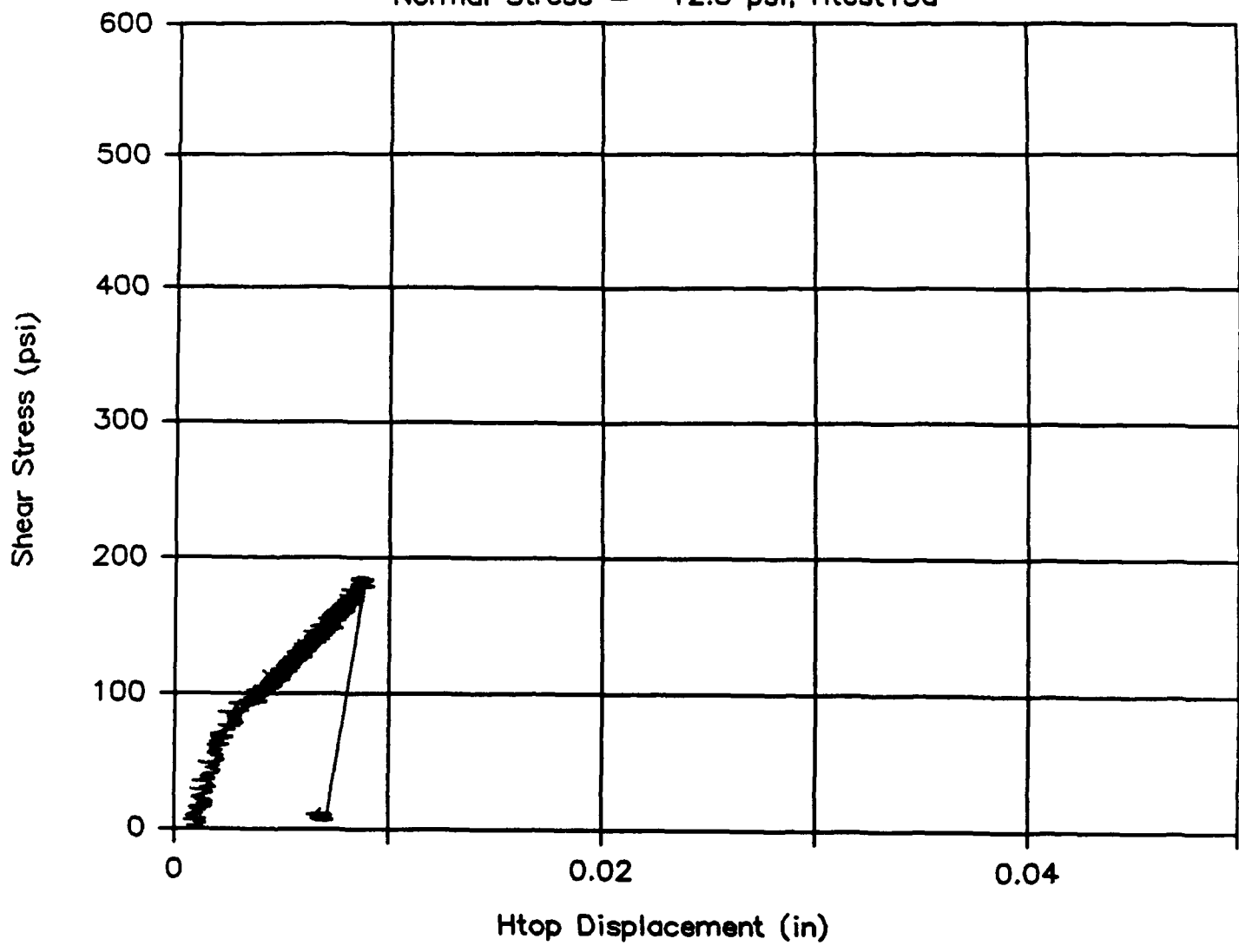
Hbottom Displacement – Shear Stress

Normal Stress = -12.5 psi, Htest13c



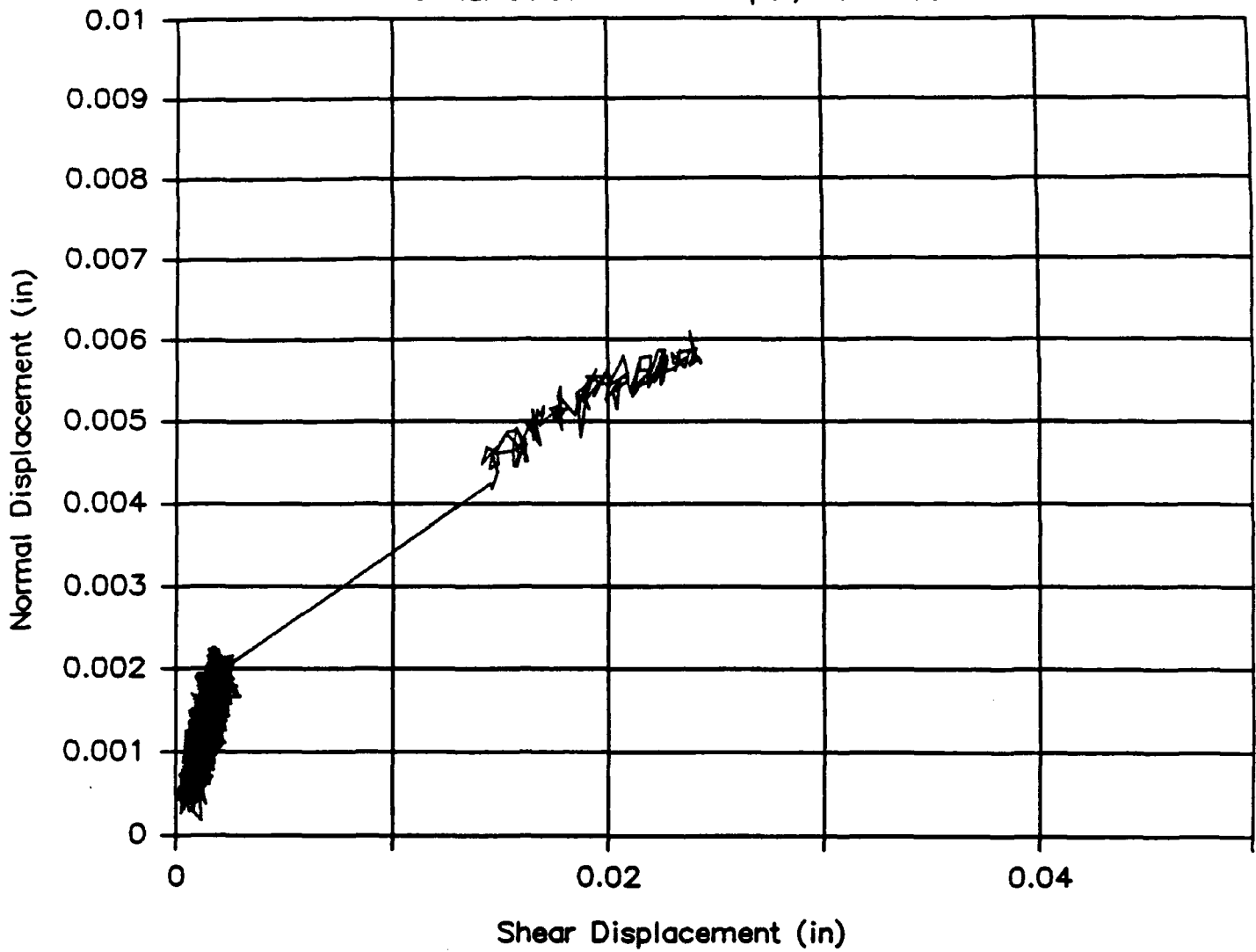
Htop Displacement – Shear Stress

Normal Stress = -12.5 psi, Htest13d



Shear Displacement—Normal Displacement

Normal Stress = -12.5 psi, Htest13e



Normal Displacement – Shear Stress

Normal Stress = -12.5 psi, Htest14a

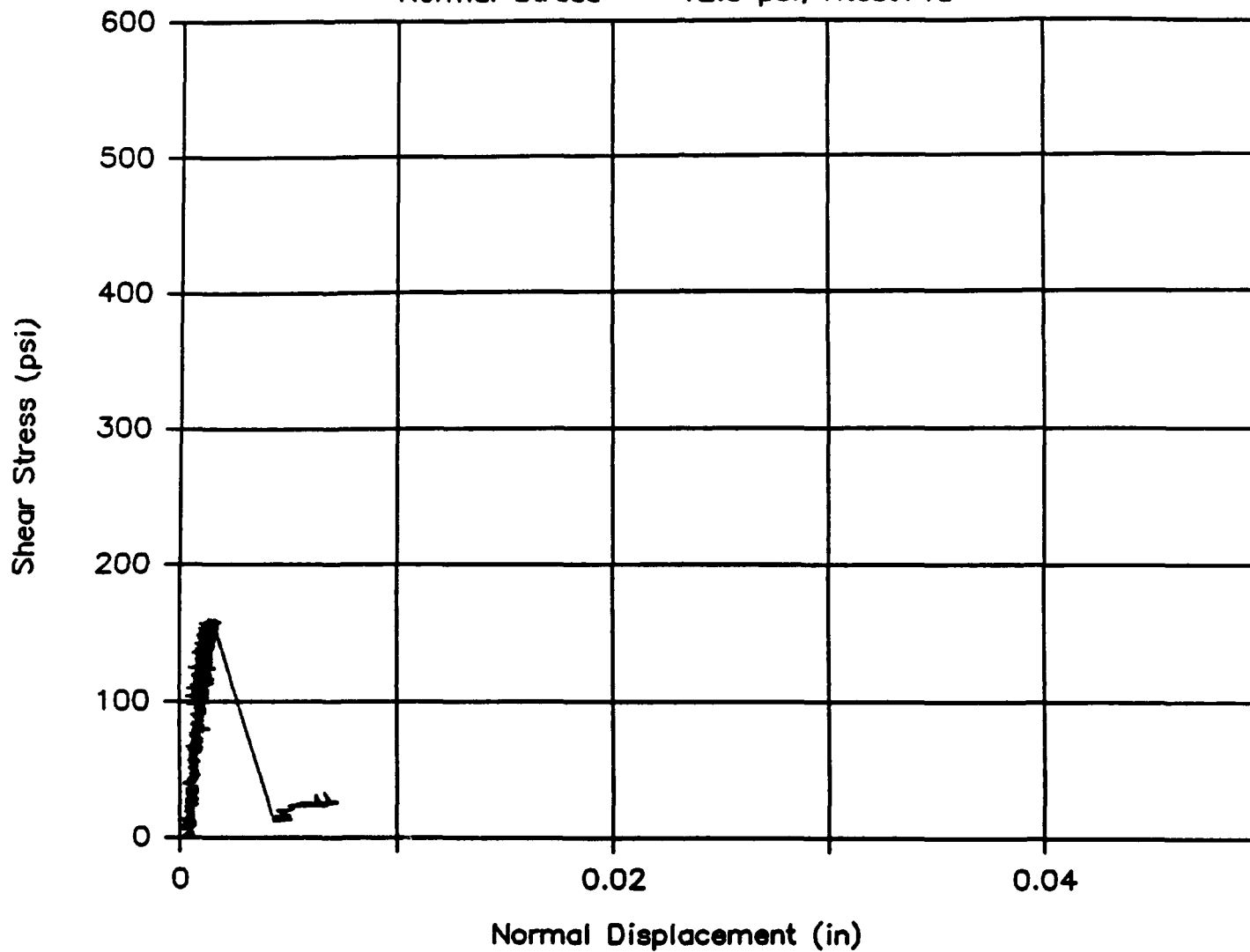
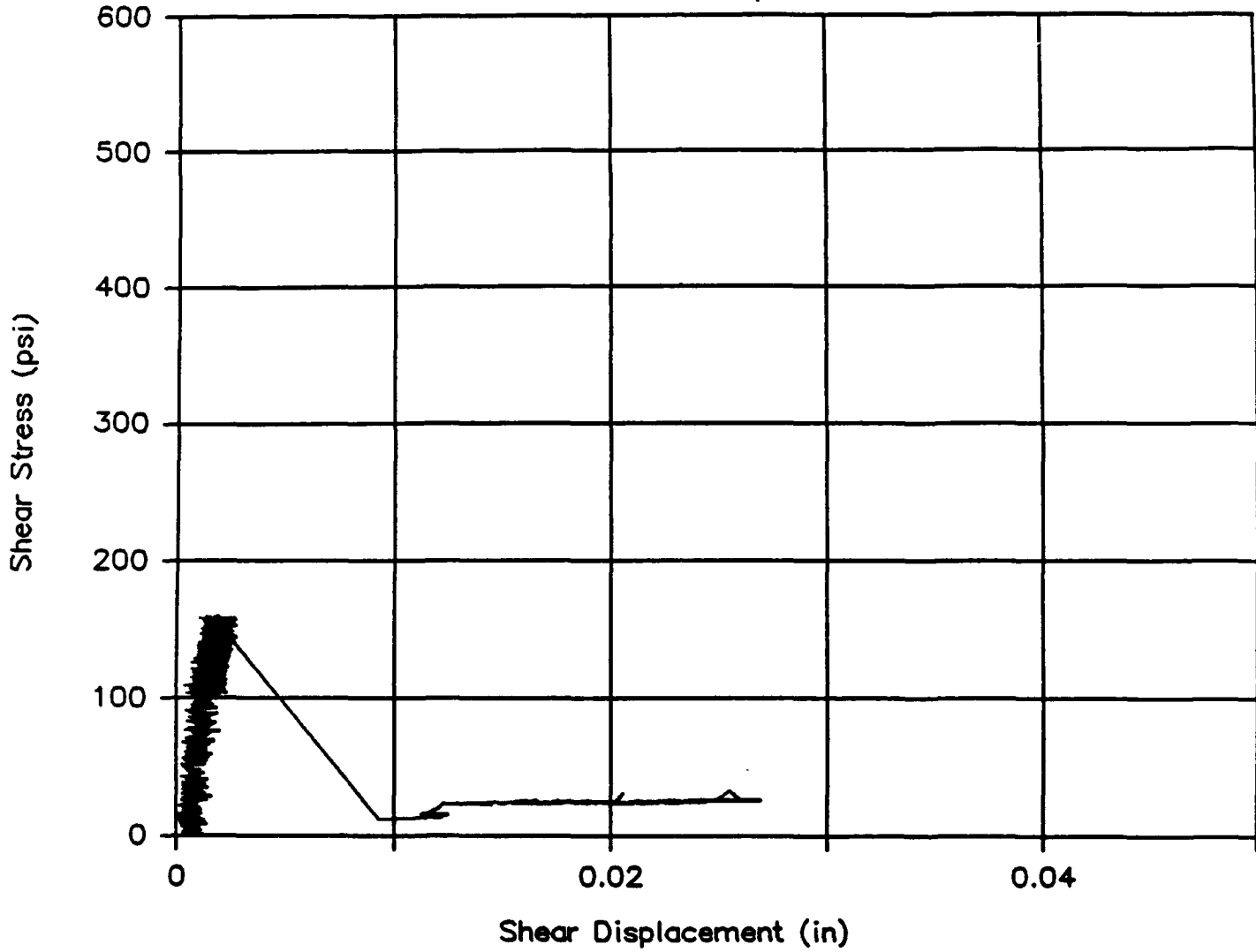


Fig. 11 (a) - (e) Load-displacement response diagrams for test series 14

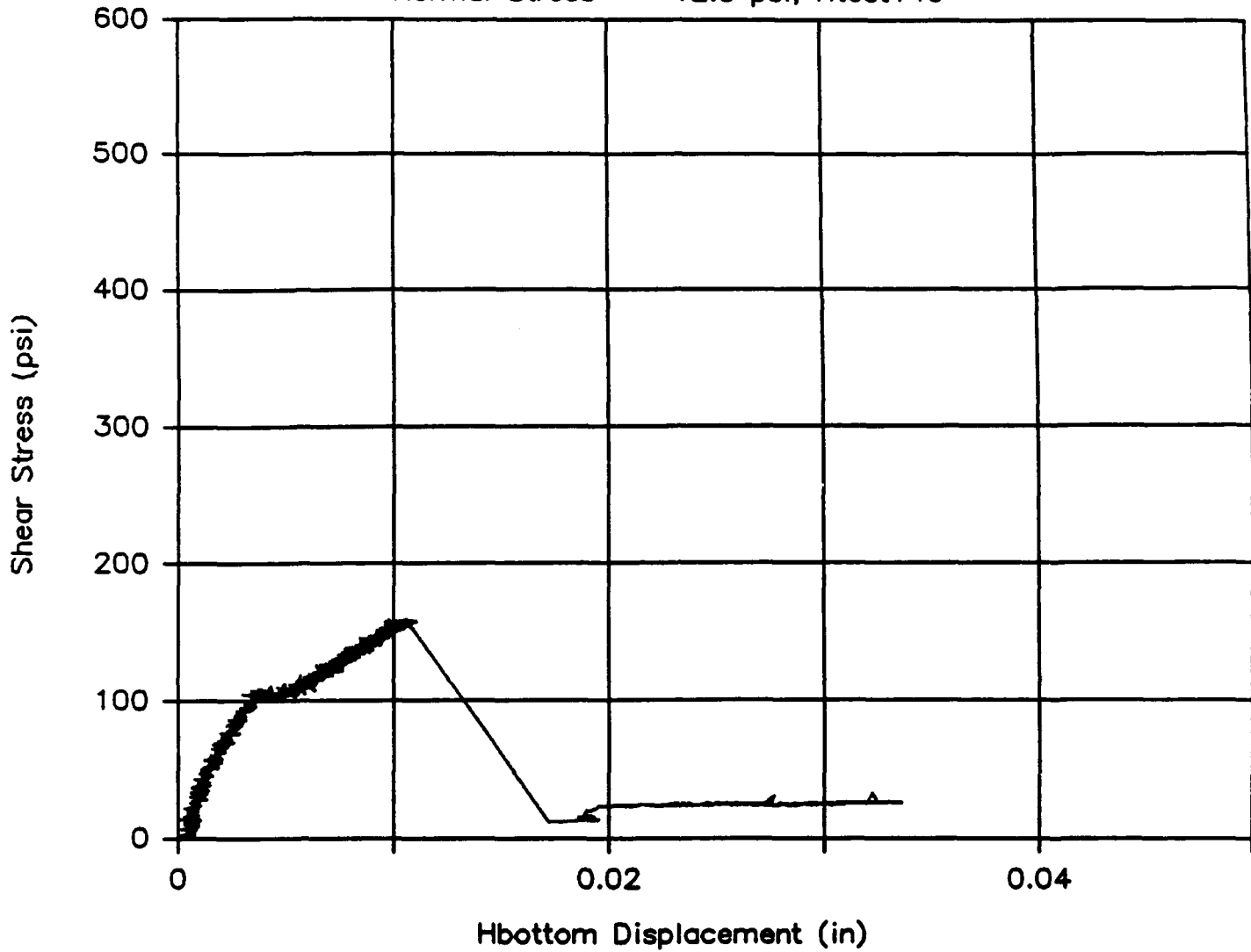
Shear Displacement – Shear Stress

Normal Stress = -12.5 psi, Htest14b



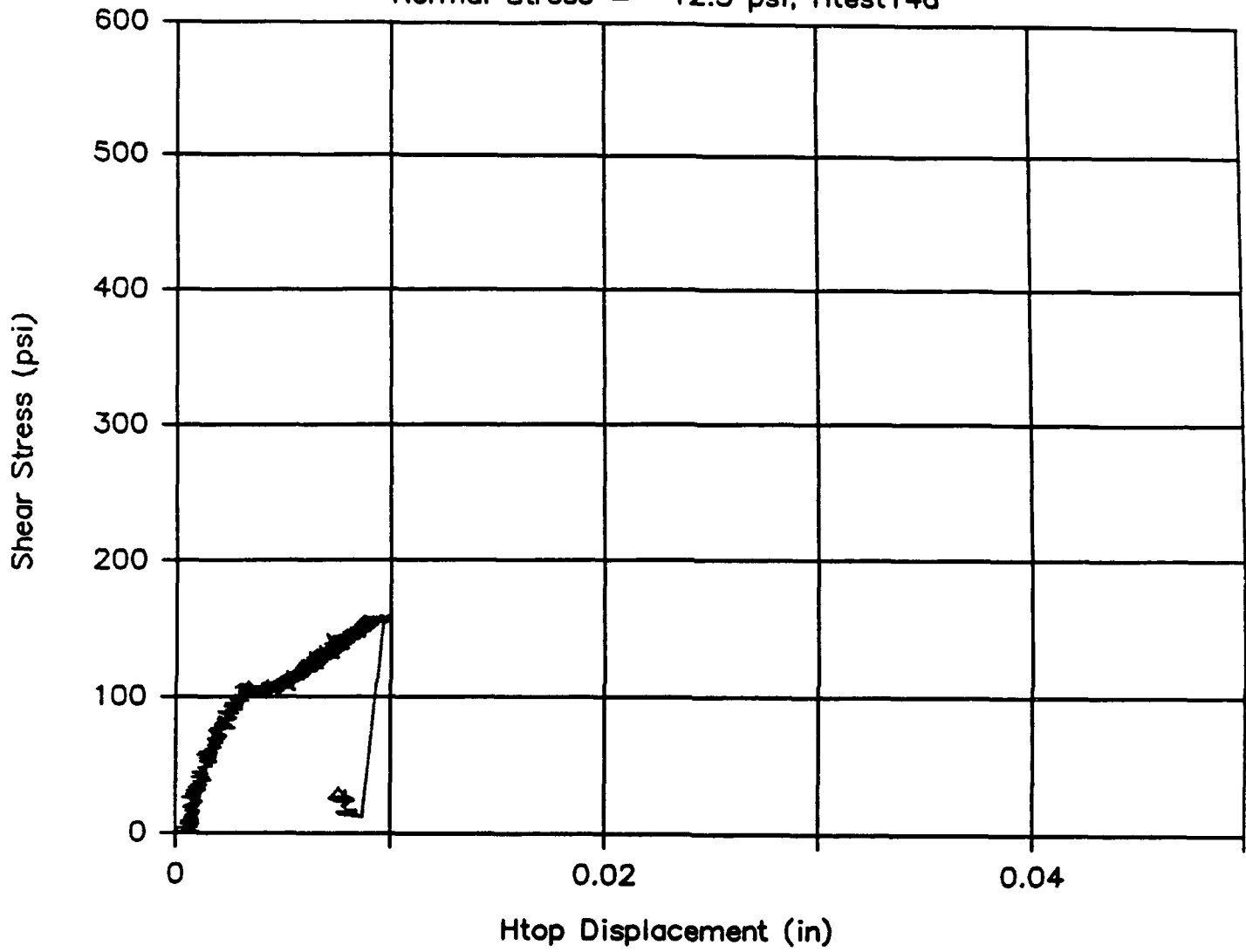
Hbottom Displacement – Shear Stress

Normal Stress = -12.5 psi, Htest14c



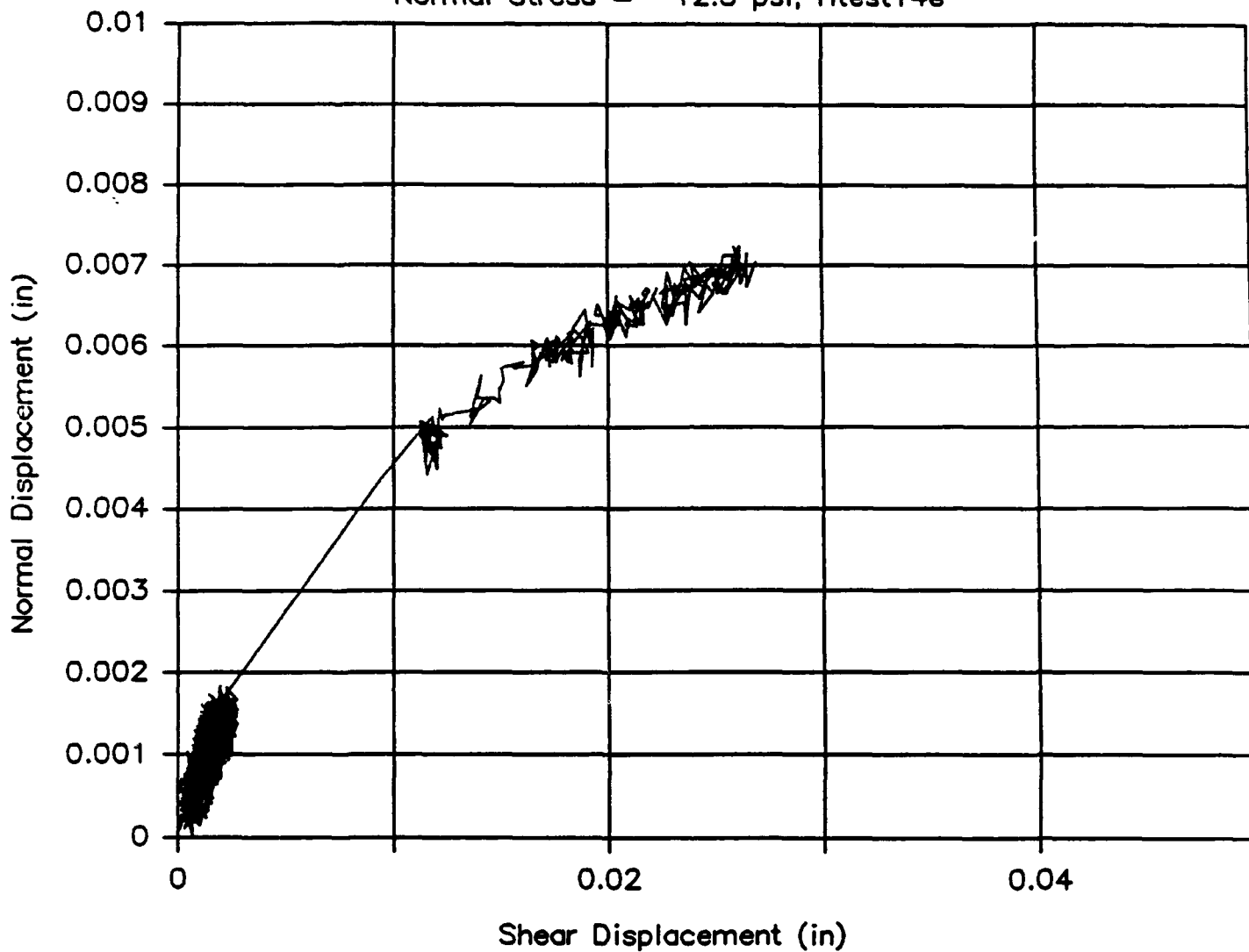
Htop Displacement – Shear Stress

Normal Stress = -12.5 psi, Htest14d



Shear Displacement—Normal Displacement

Normal Stress = -12.5 psi, Htest14e



Normal Displacement – Shear Stress

Normal Stress = -400 psi, Htest15a

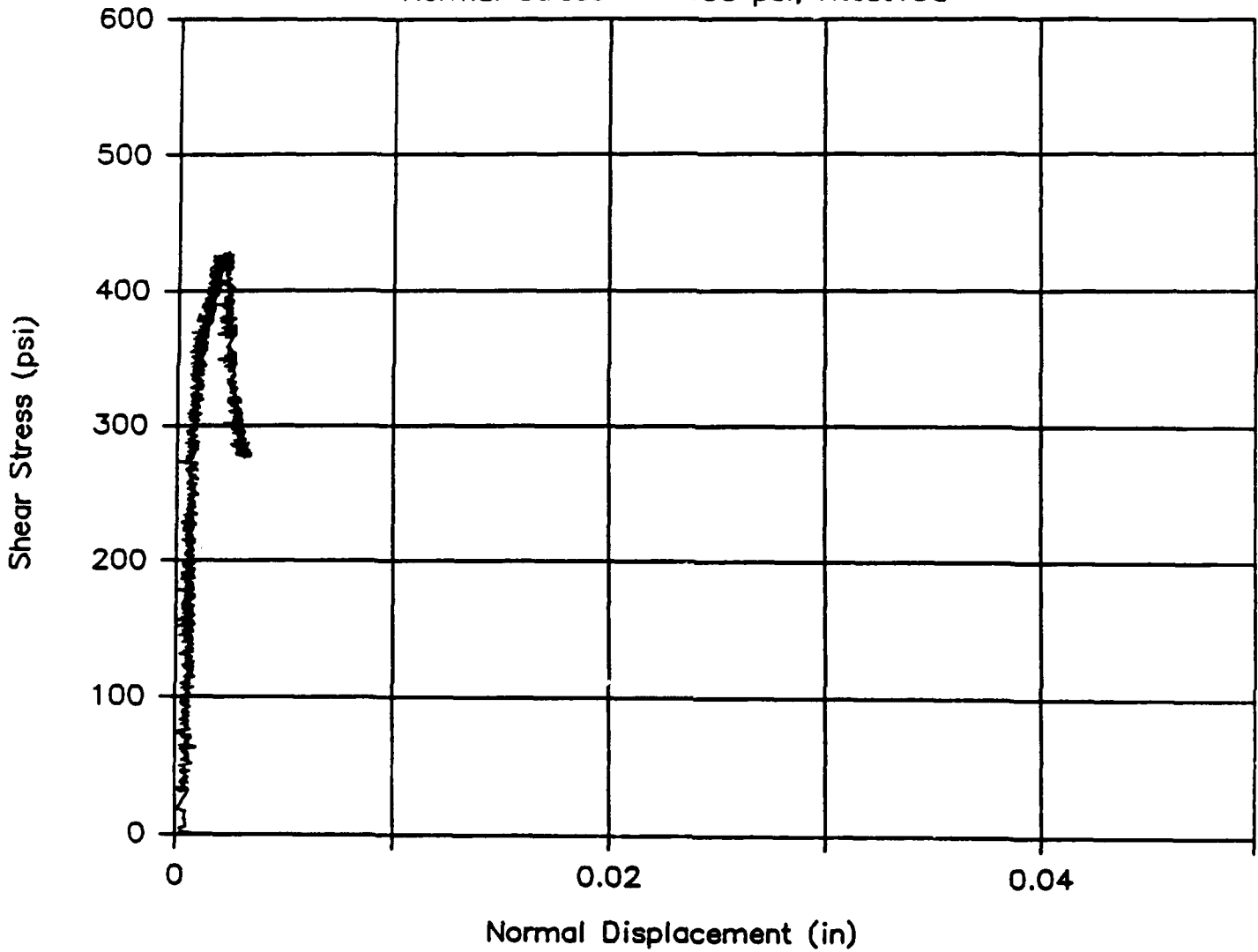
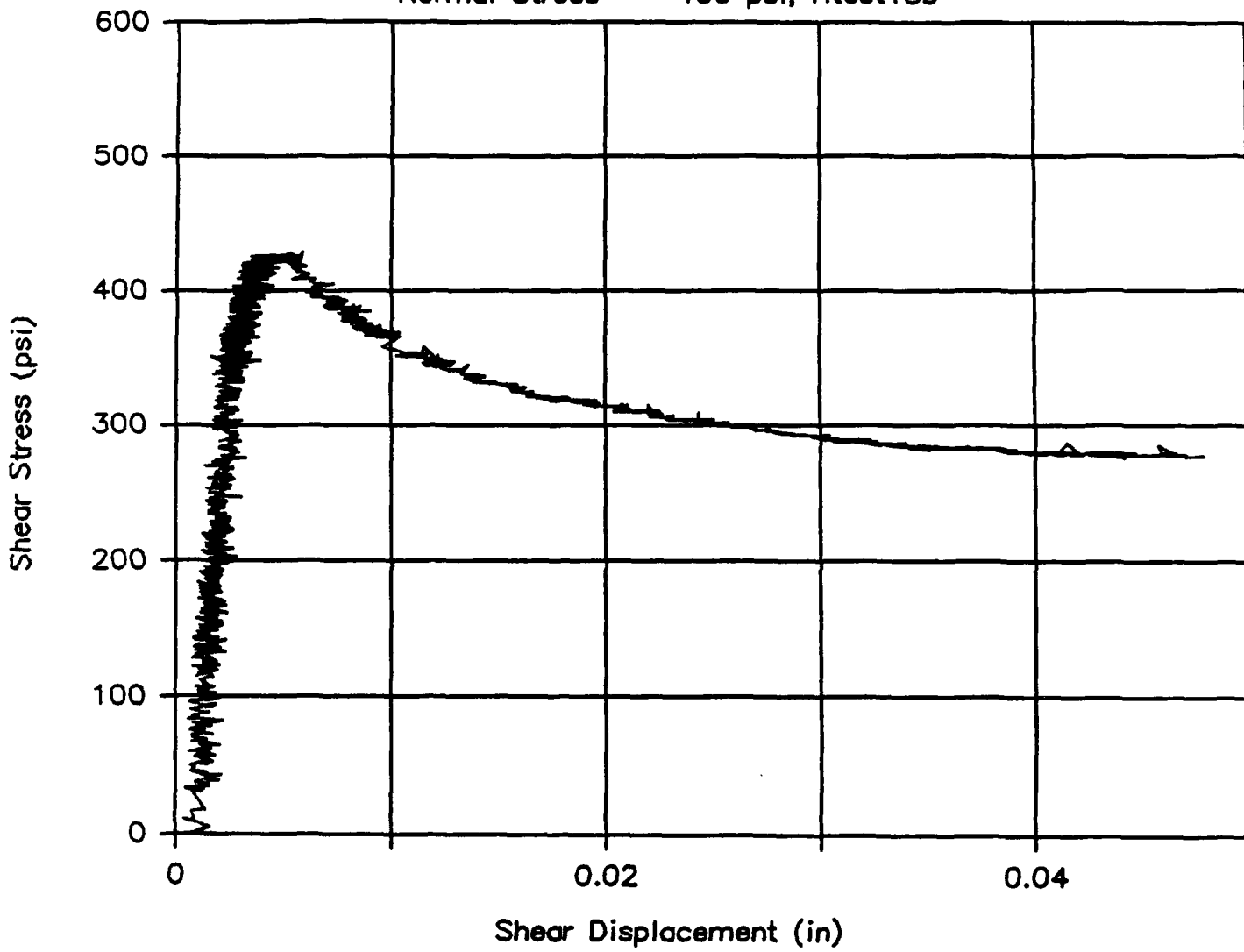


Fig. 12 (a) - (e) Load-displacement response diagrams for test series 15

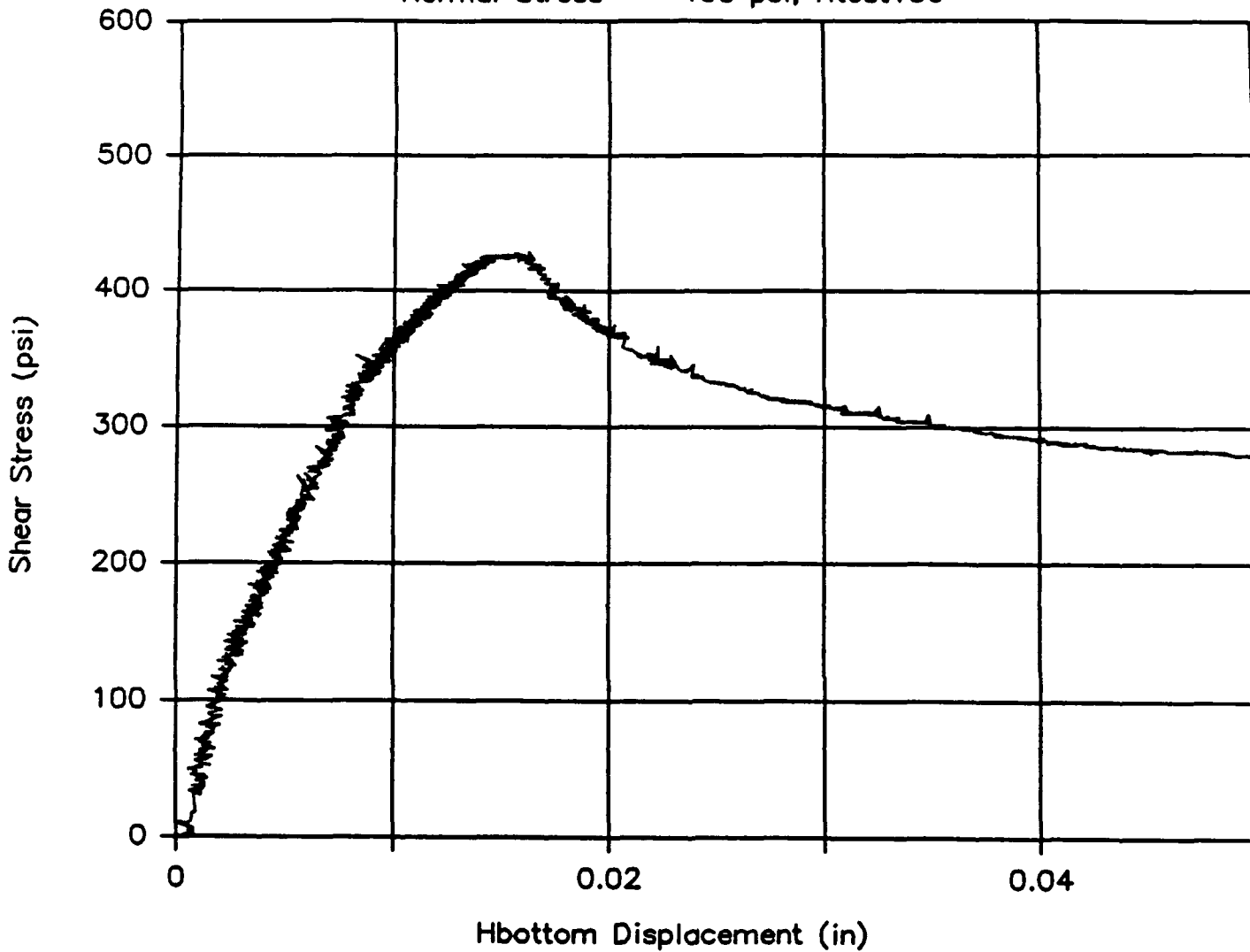
Shear Displacement – Shear Stress

Normal Stress = -400 psi, Htest15b



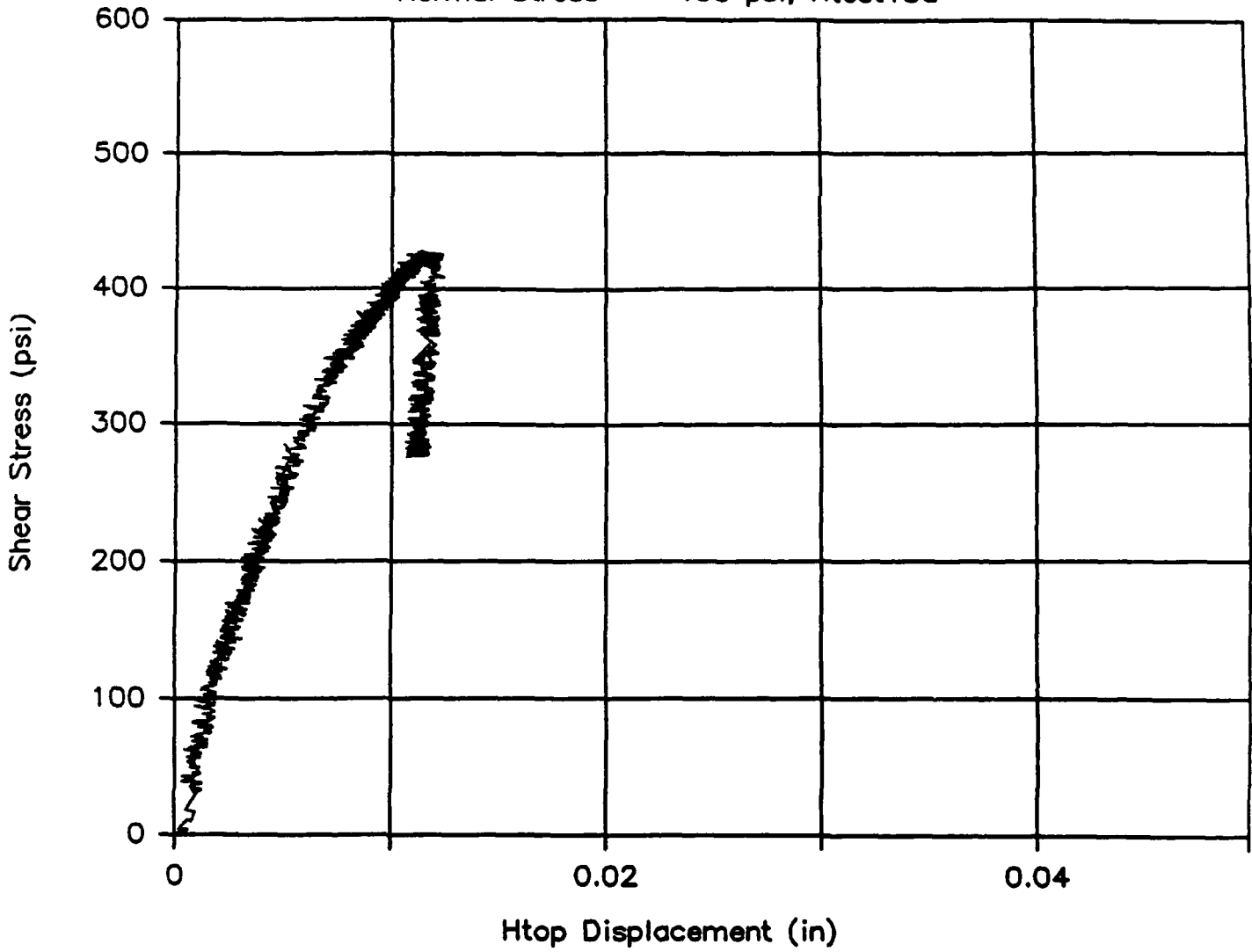
Hbottom Displacement – Shear Stress

Normal Stress = -400 psi, Htest15c



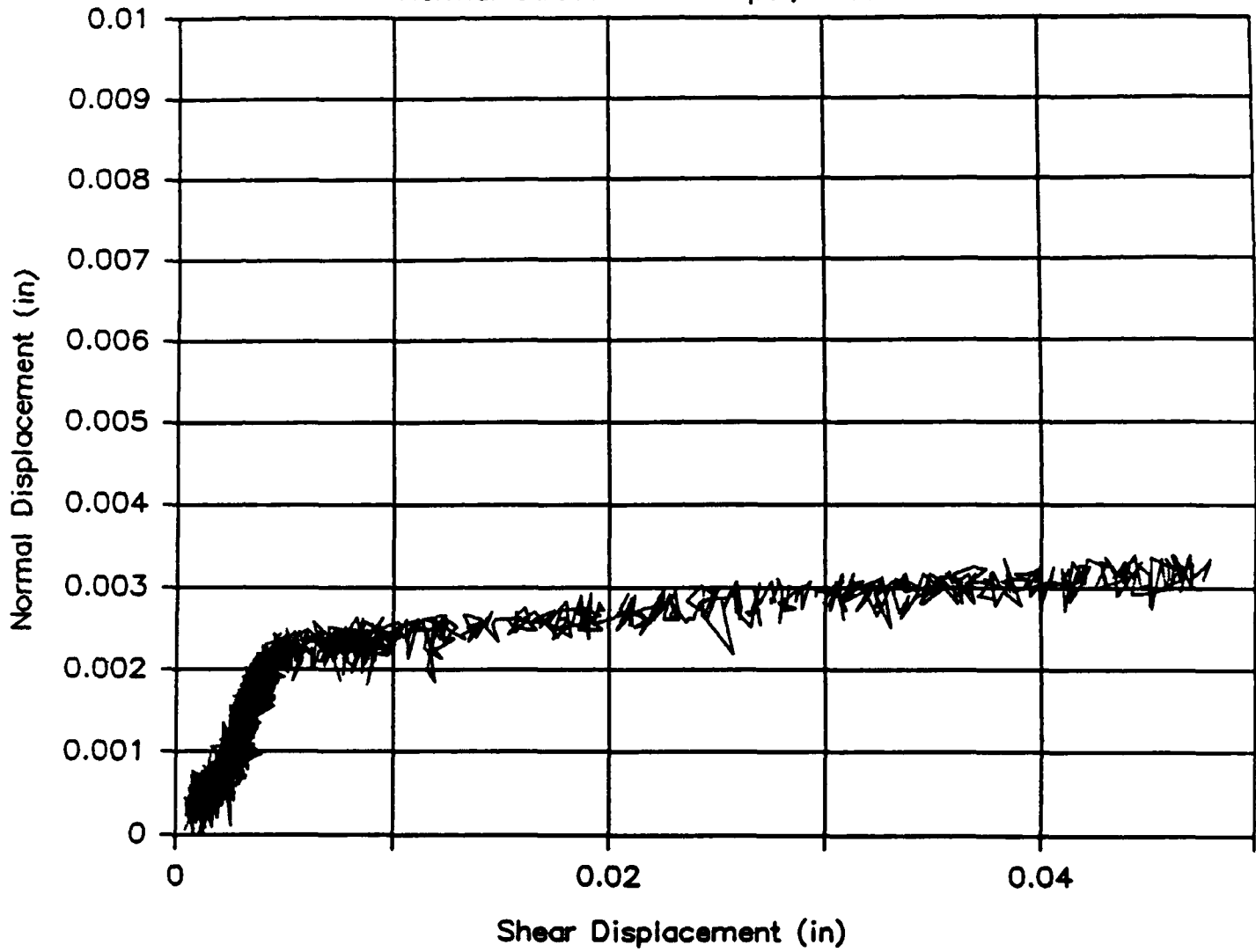
Htop Displacement – Shear Stress

Normal Stress = -400 psi, Htest15d



Shear Displacement—Normal Displacement

Normal Stress = -400 psi, Htest15e



Normal Displacement – Shear Stress

Normal Stress = 0 psi, Htest21a

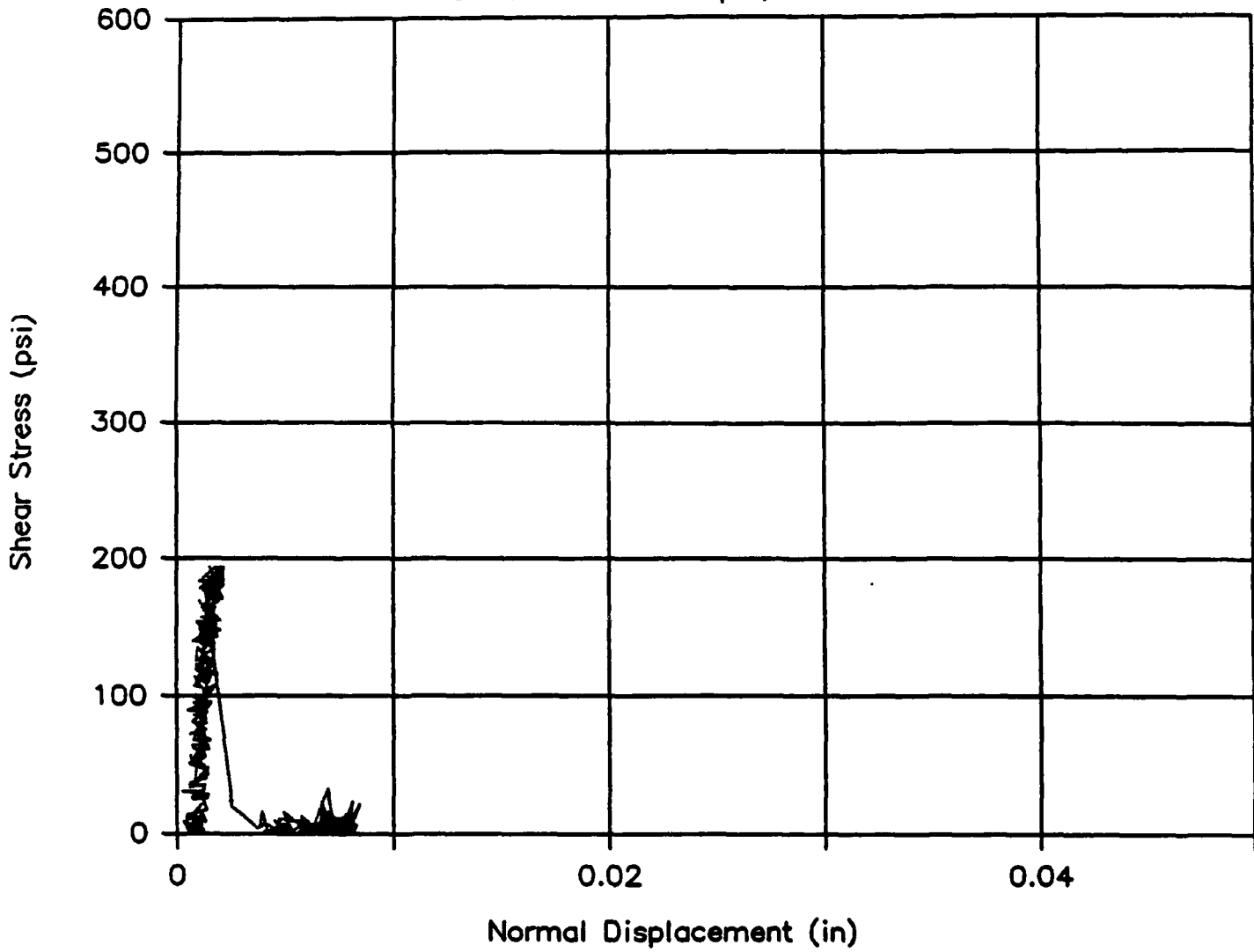
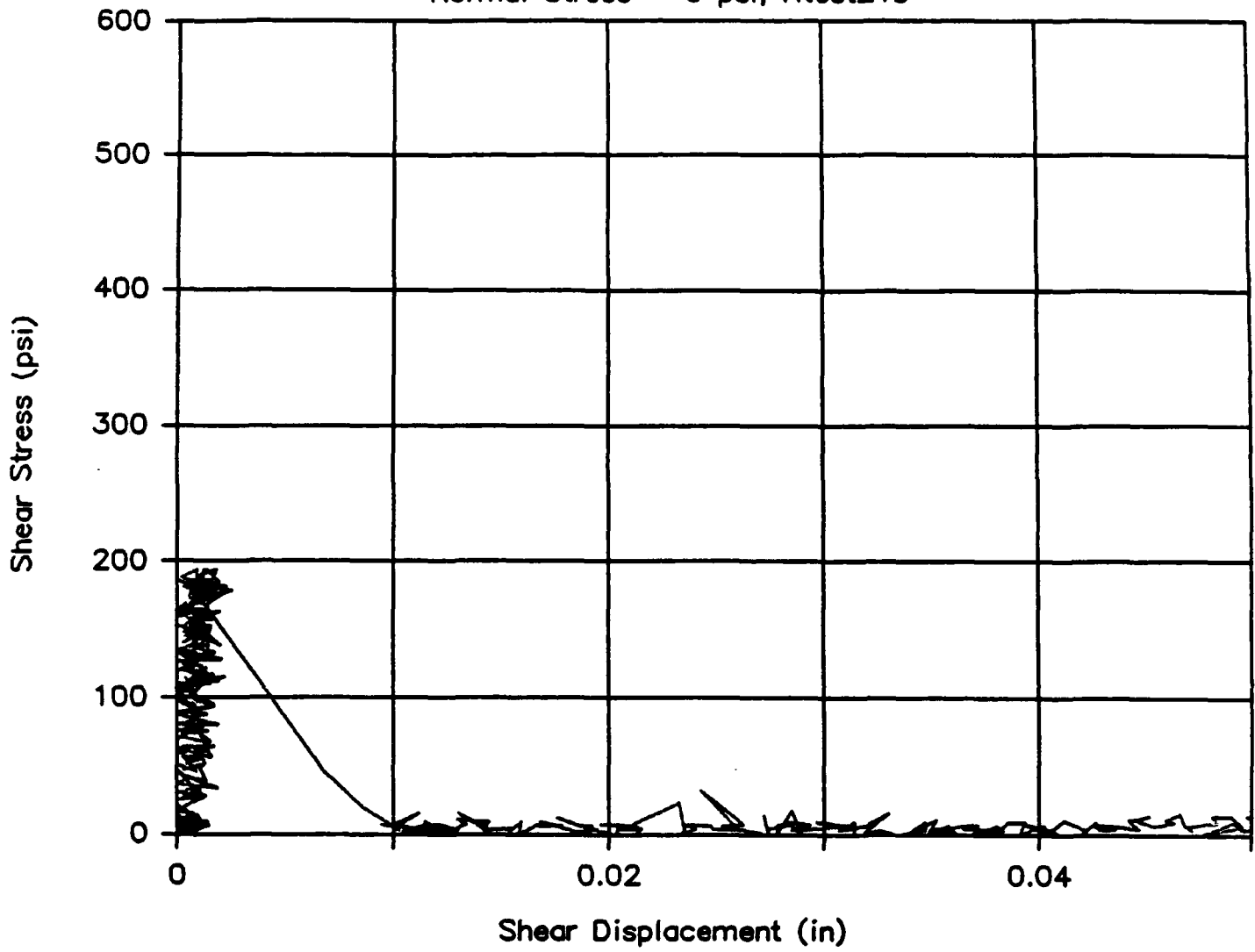


Fig. 13 (a) - (e) Load-displacement response diagrams for test series 21

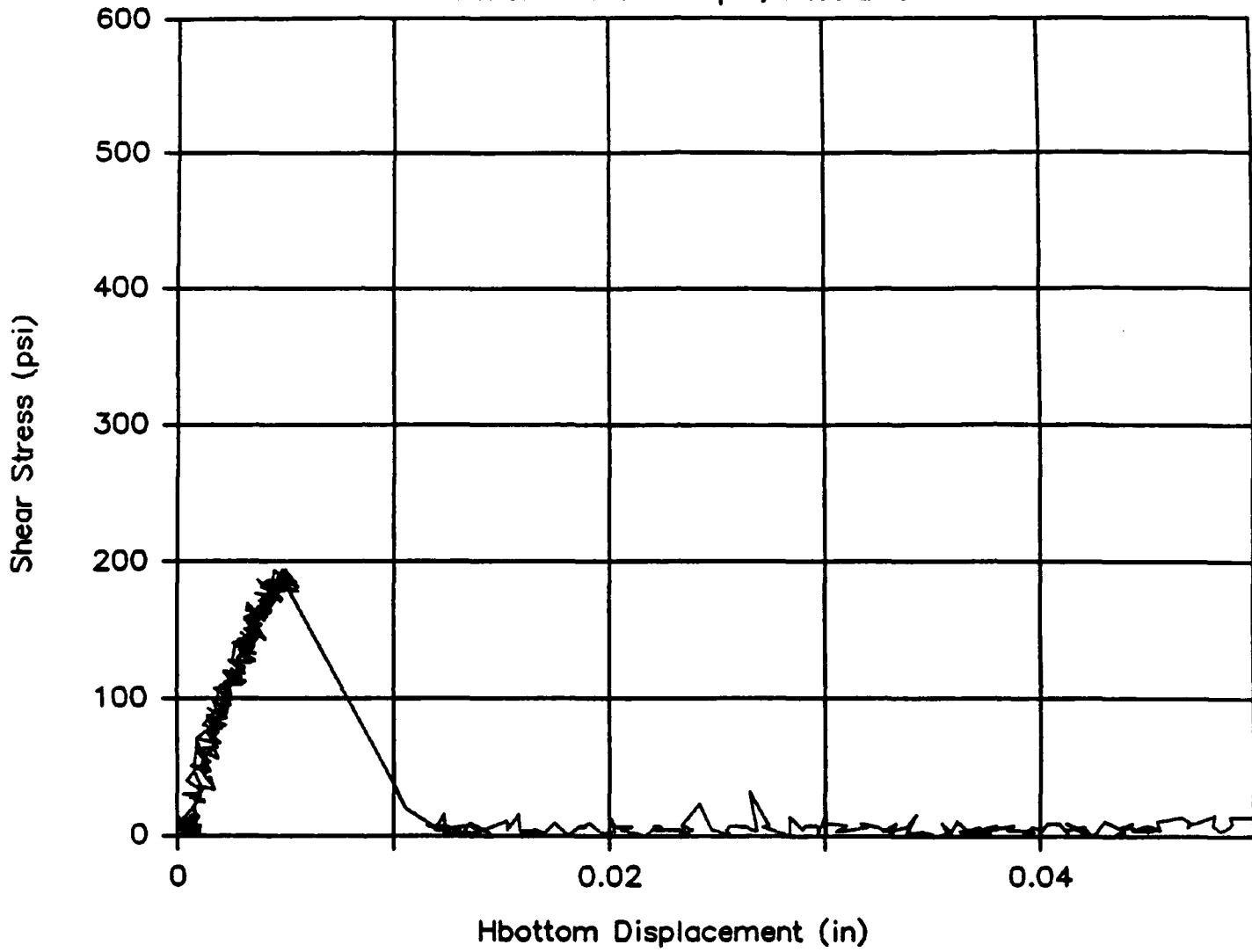
Shear Displacement – Shear Stress

Normal Stress = 0 psi, Htest21b



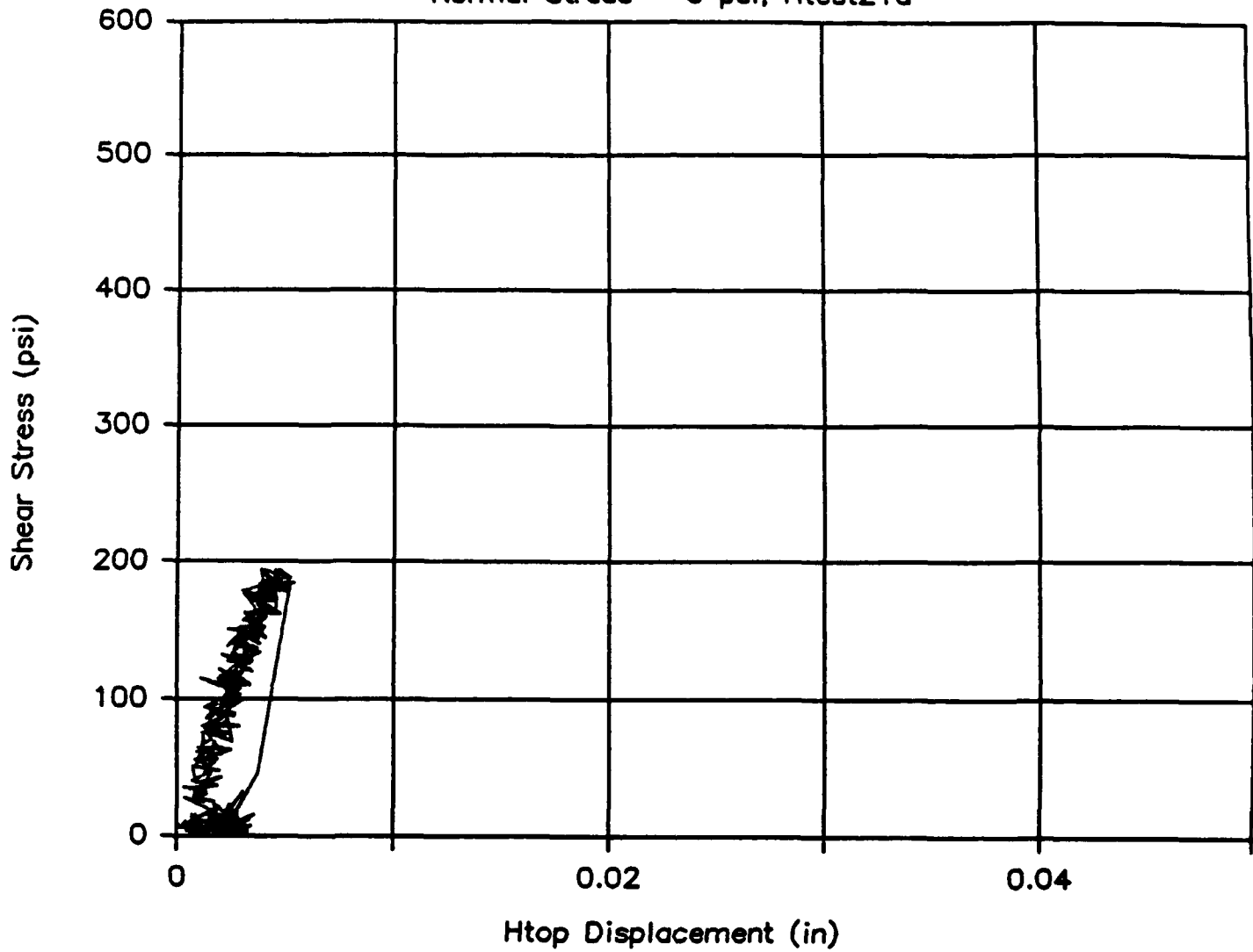
Hbottom Displacement – Shear Stress

Normal Stress = 0 psi, Htest21c



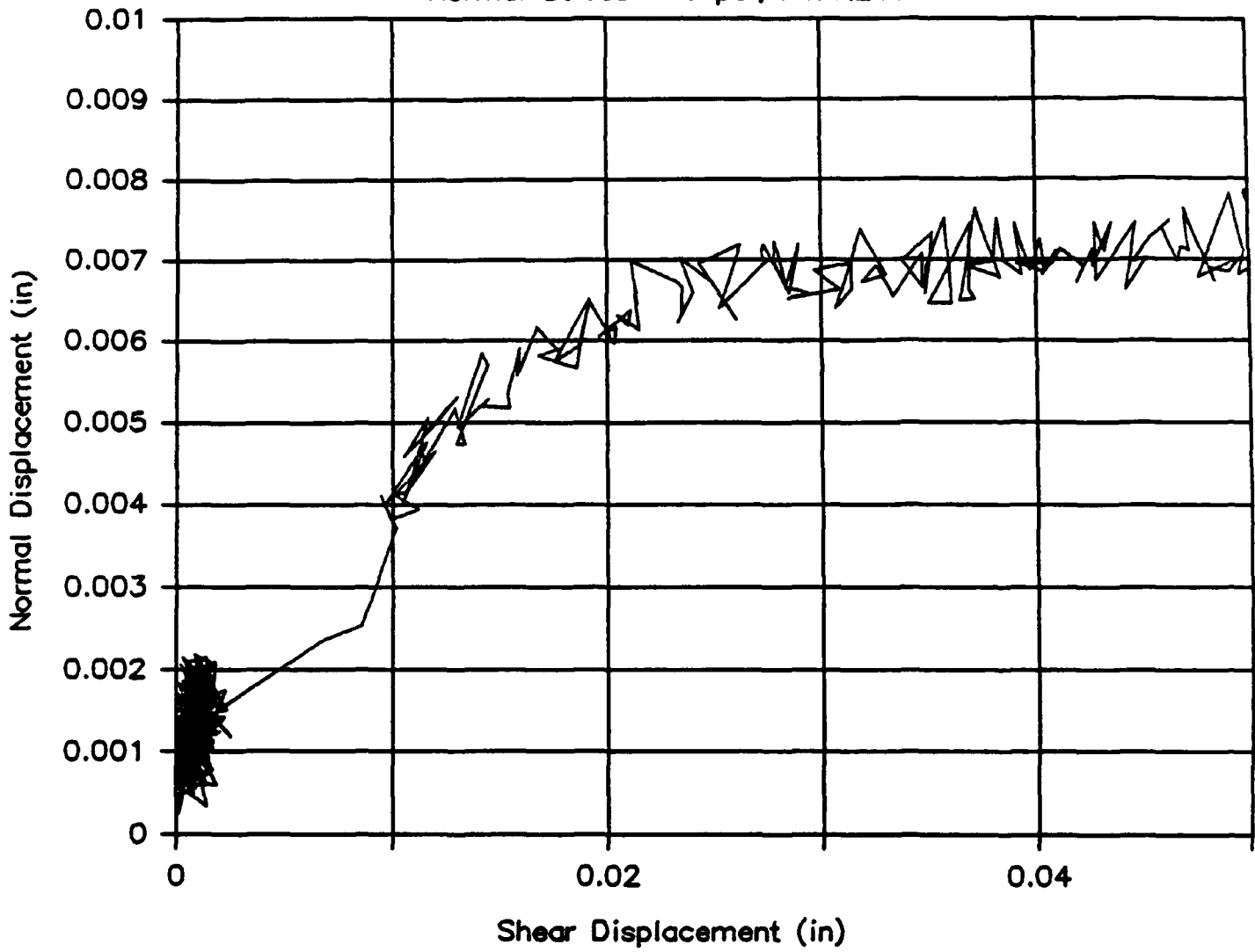
Htop Displacement — Shear Stress

Normal Stress = 0 psi, Htest21d



Shear Displacement—Normal Displacement

Normal Stress = 0 psi, Htest21e



Normal Displacement — Shear Stress

Normal Stress = 0 psi, Htest22a

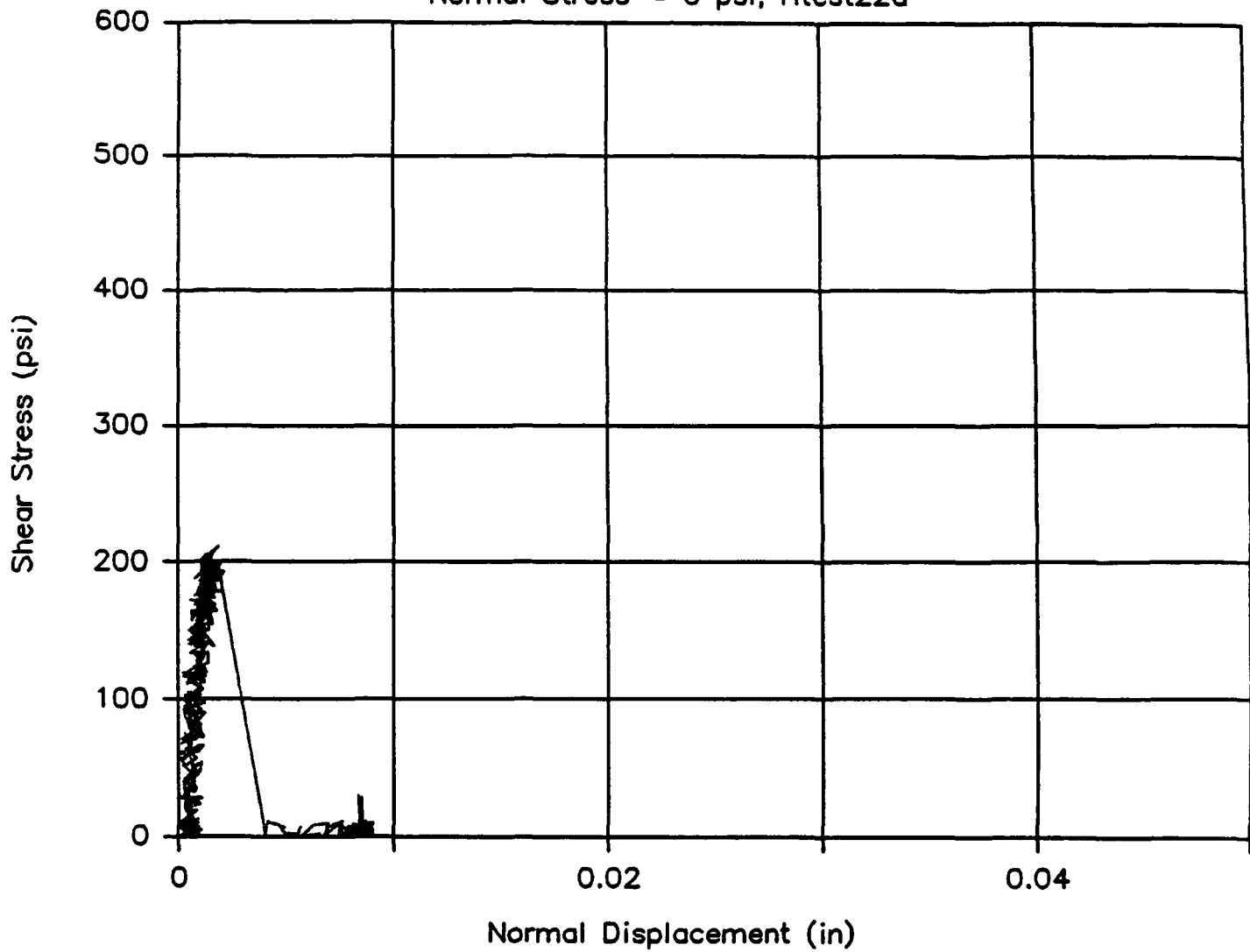
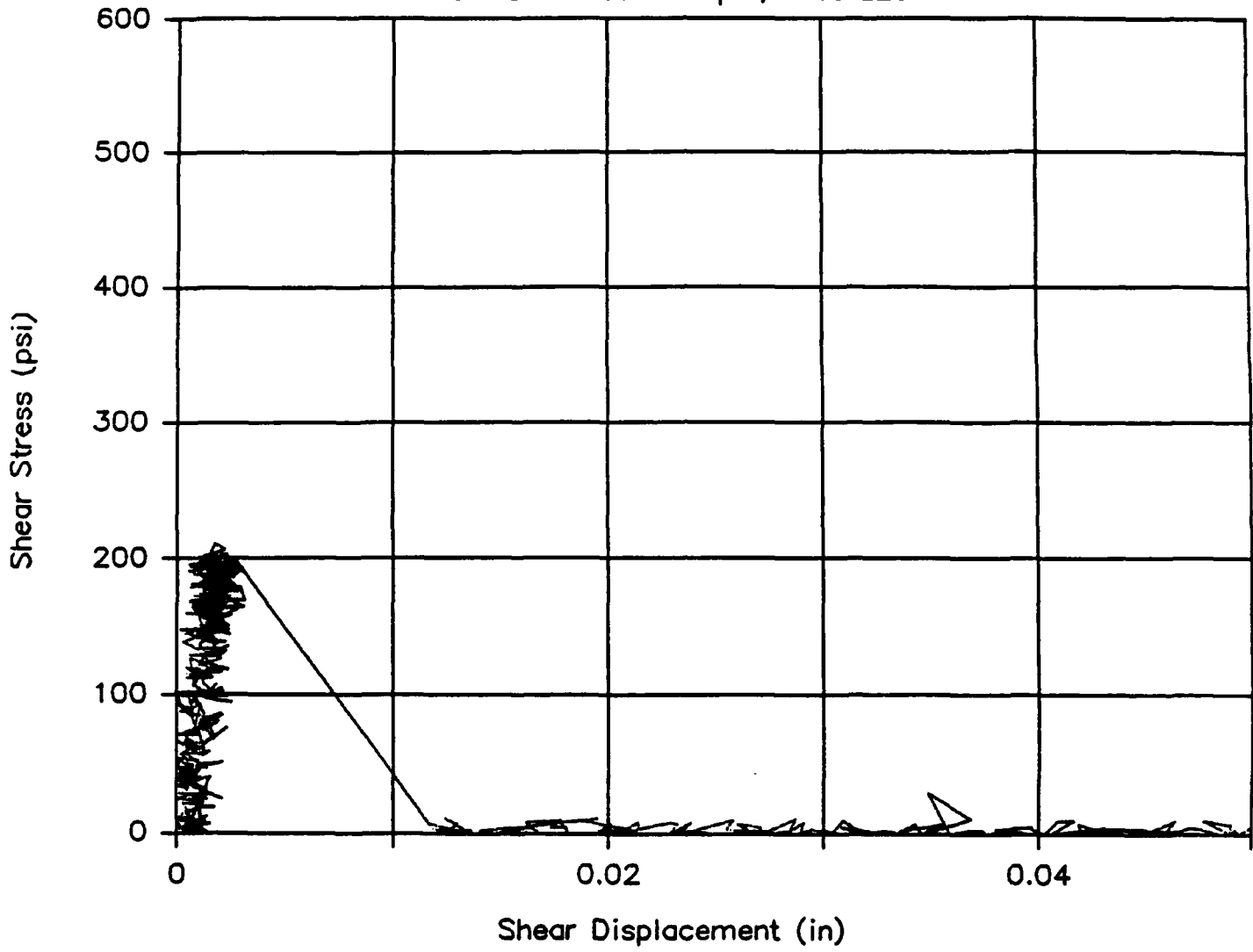


Fig. 14 (a) - (e) Load-displacement response diagrams for test series 22

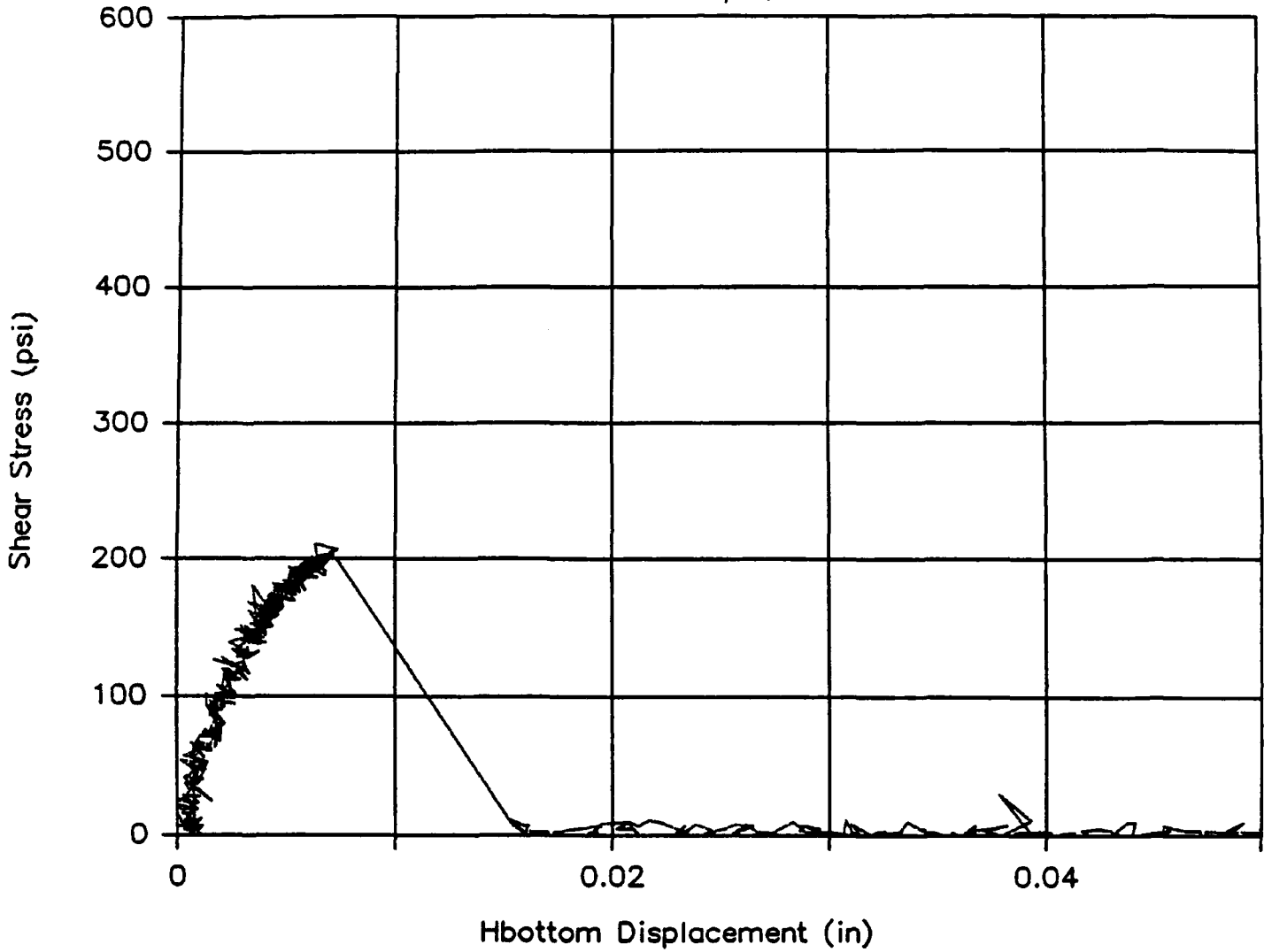
Shear Displacement – Shear Stress

Normal Stress = 0 psi, Htest22b



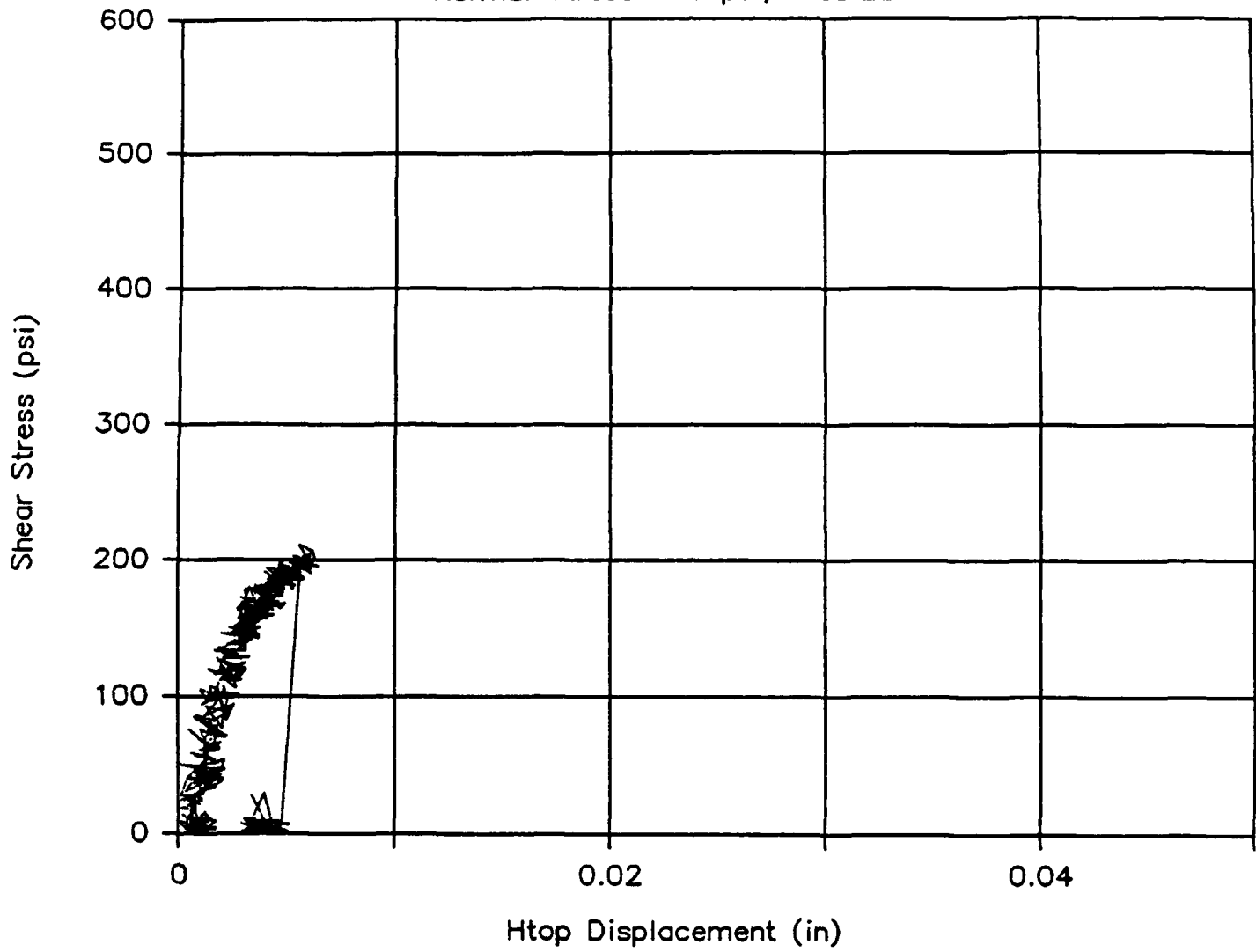
Hbottom Displacement – Shear Stress

Normal Stress = 0 psi, Htest22c



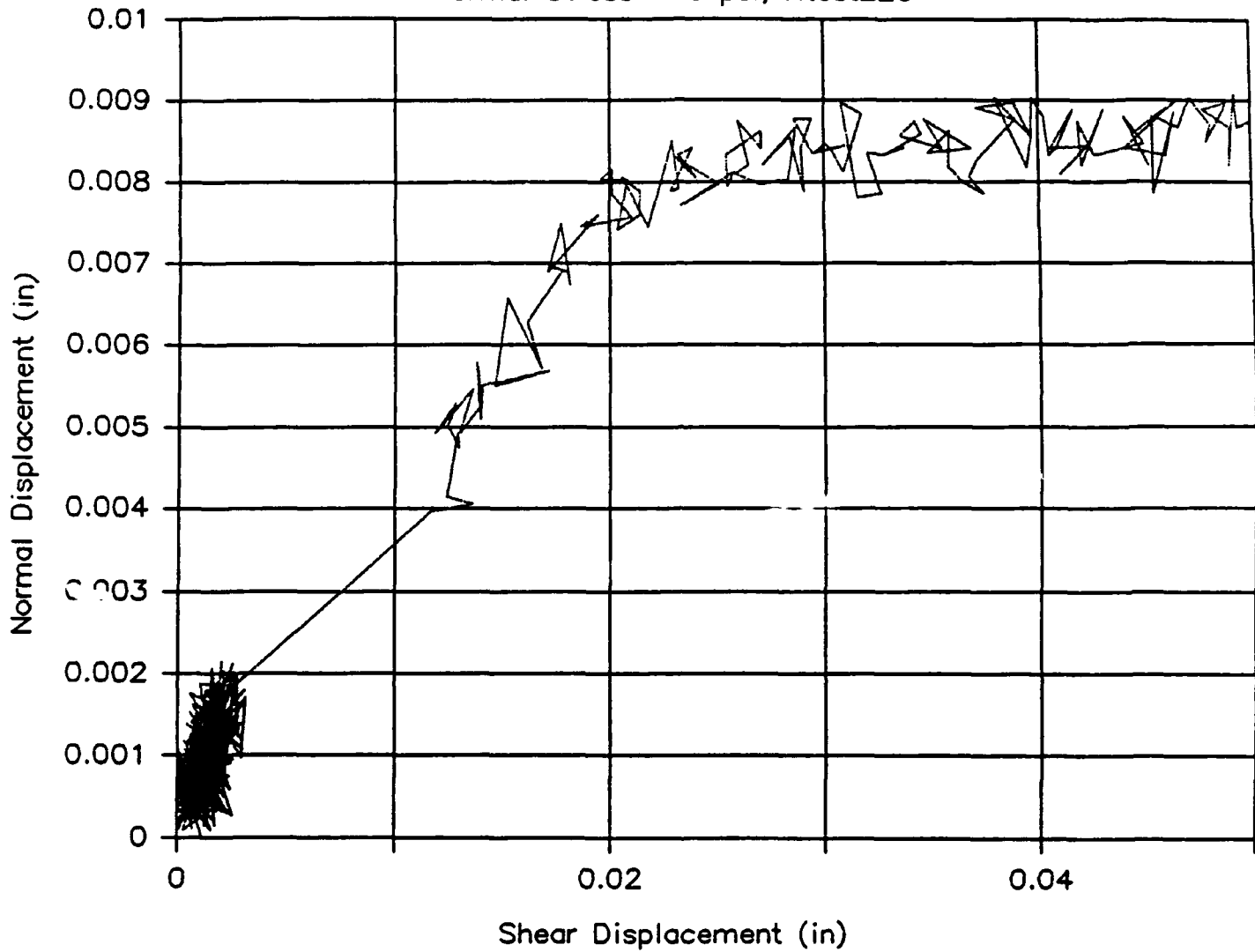
Htop Displacement – Shear Stress

Normal Stress = 0 psi, Htest22d



Shear Displacement—Normal Displacement

Normal Stress = 0 psi, Htest22e



Normal Displacement – Shear Stress

Normal Stress = +25 psi, Htest23a

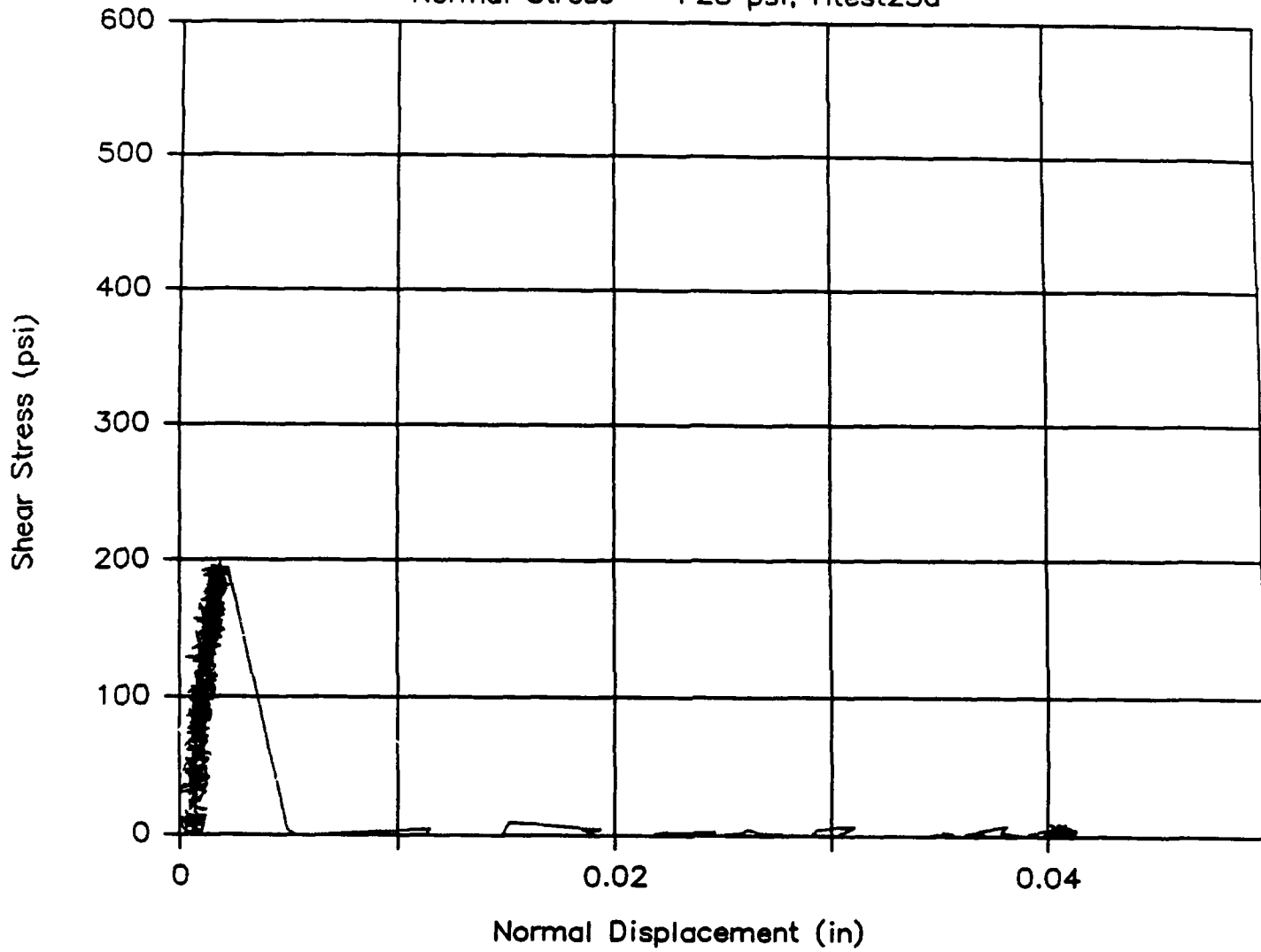
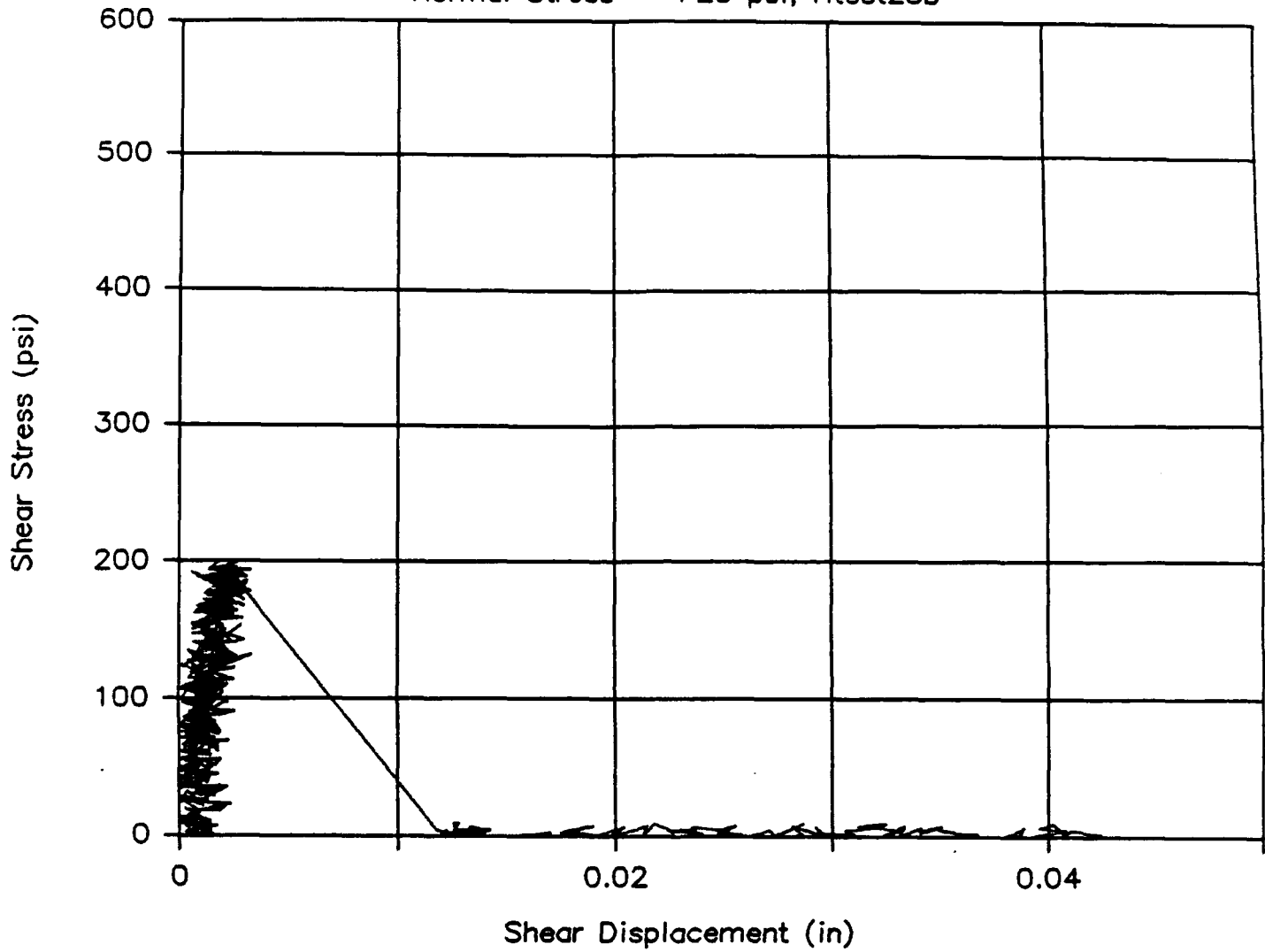


Fig. 15 (a) - (f) Load-displacement response diagrams for test series 23

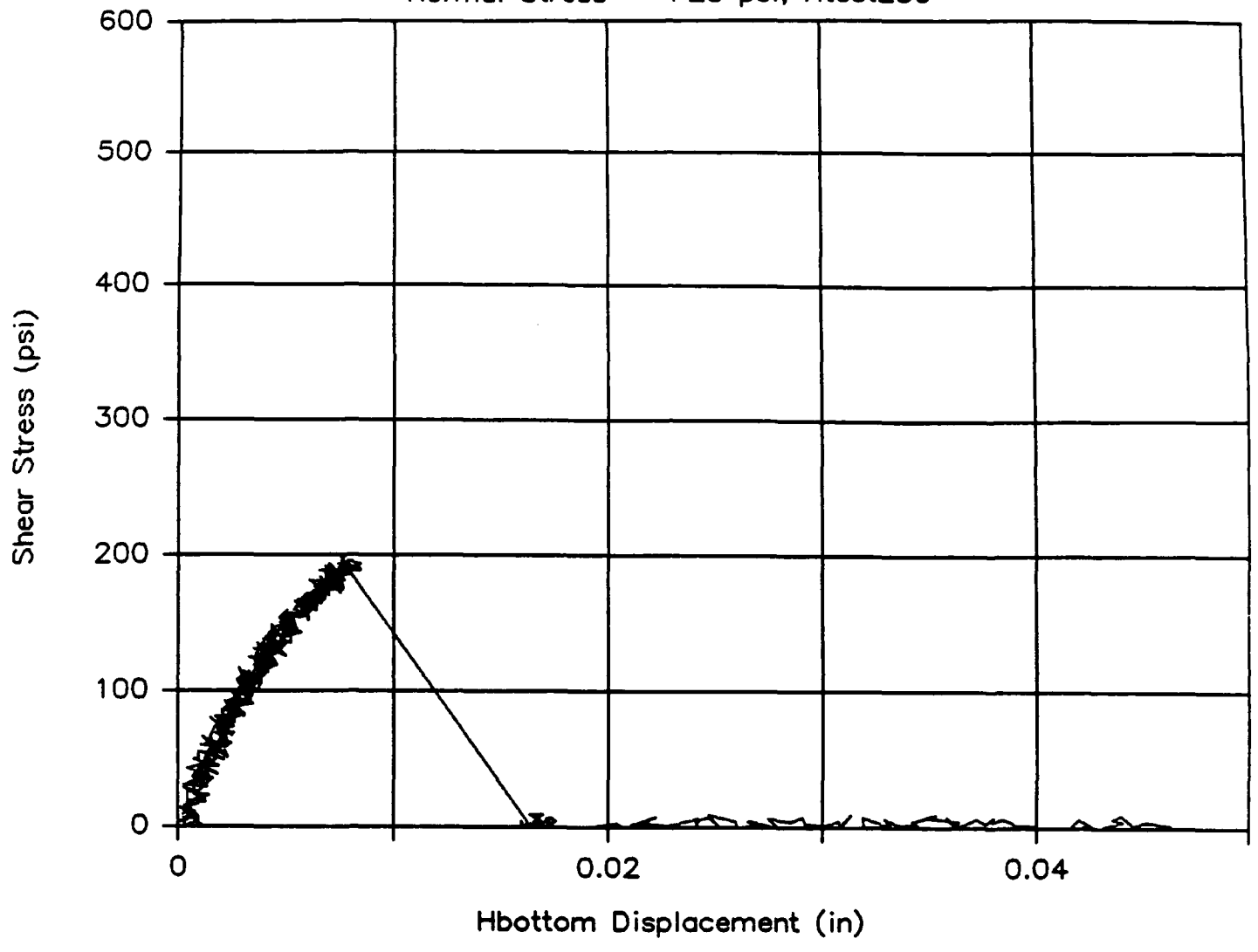
Shear Displacement – Shear Stress

Normal Stress = +25 psi, Htest23b



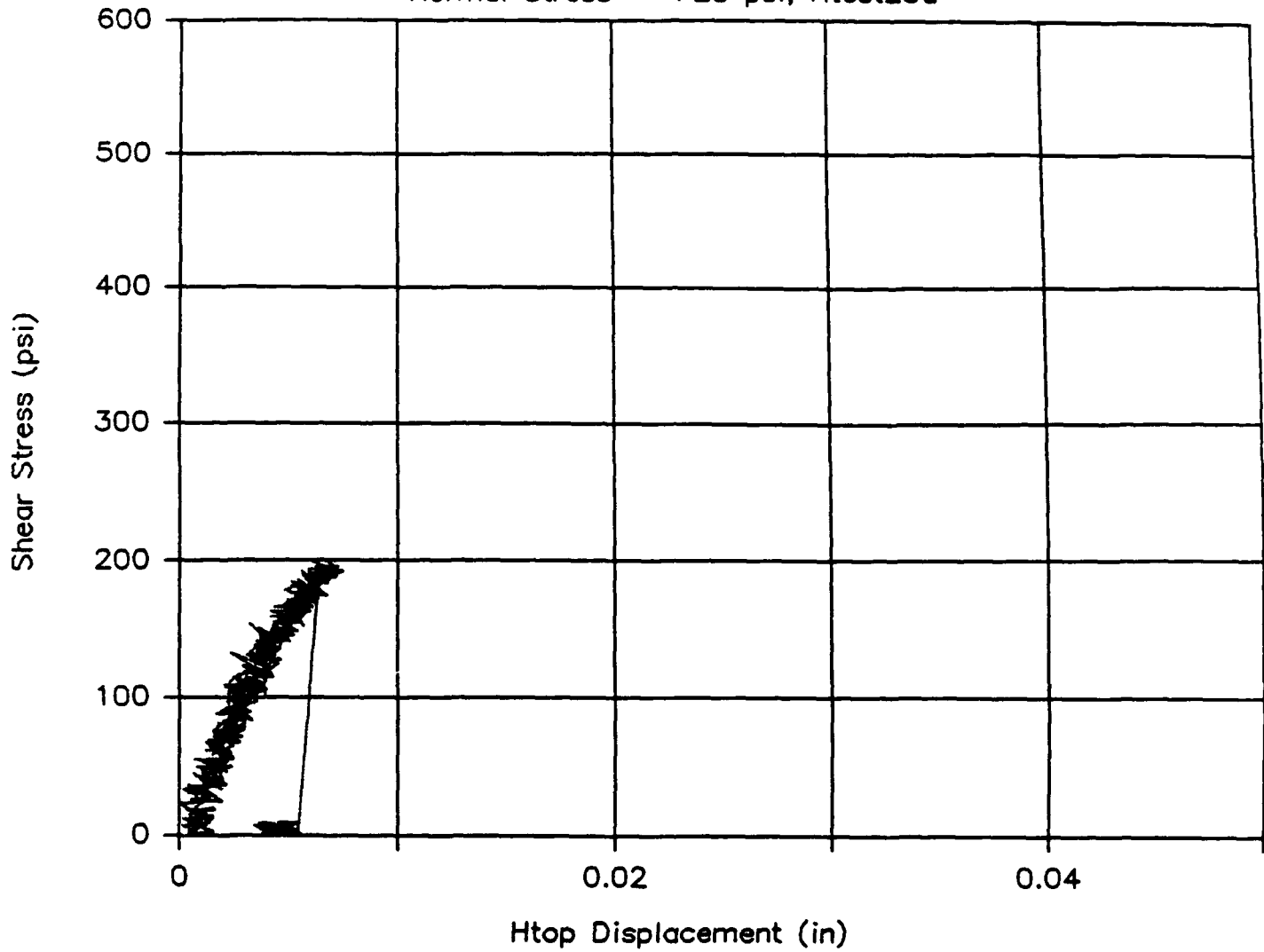
Hbottom Displacement – Shear Stress

Normal Stress = +25 psi, Htest23c



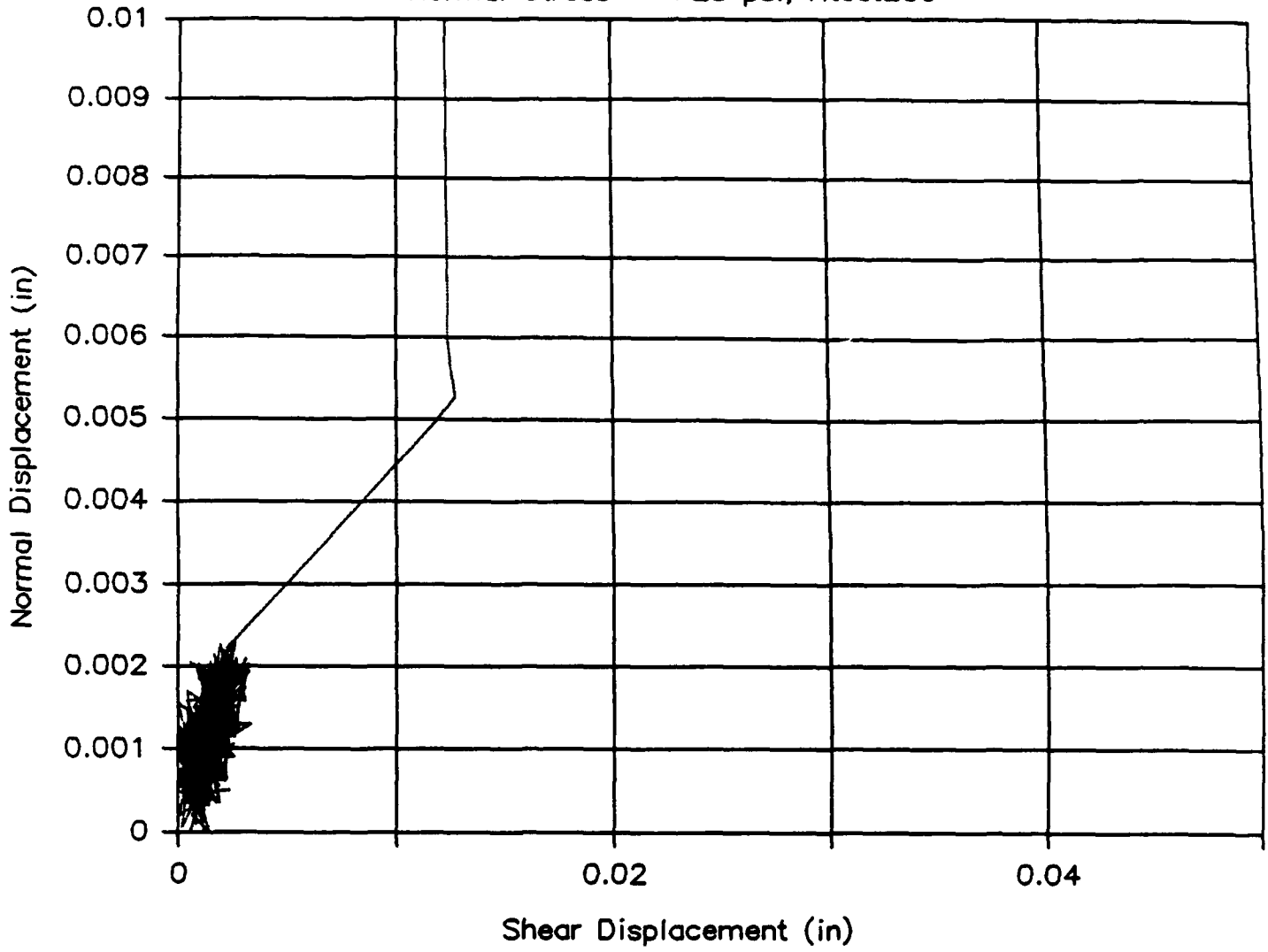
Htop Displacement – Shear Stress

Normal Stress = +25 psi, Htest23d



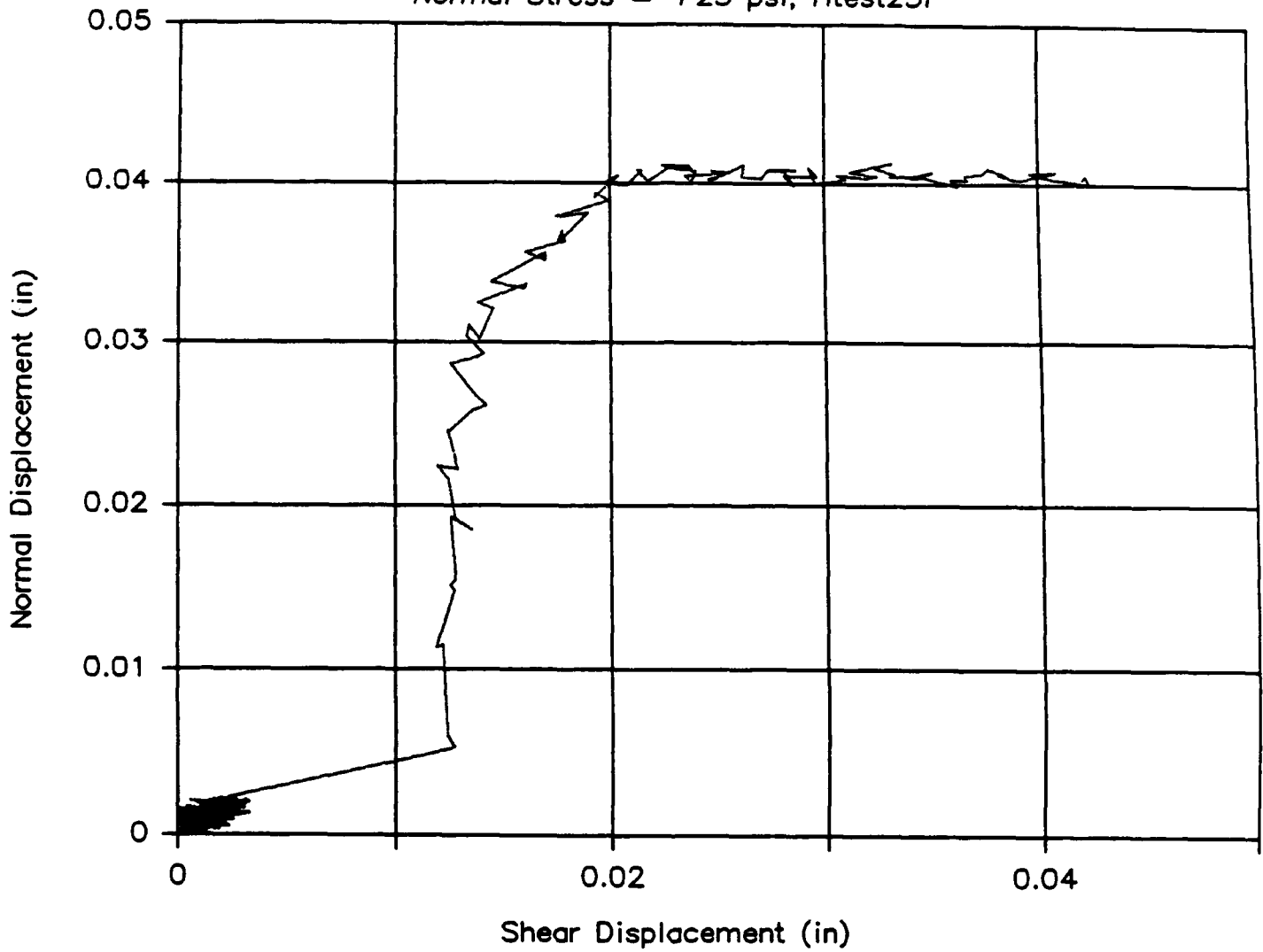
Shear Displacement—Normal Displacement

Normal Stress = +25 psi, Htest23e



Shear Displacement—Normal Displacement

Normal Stress = +25 psi, Htest23f



Normal Displacement – Shear Stress

Normal Stress = +25 psi, Htest24a

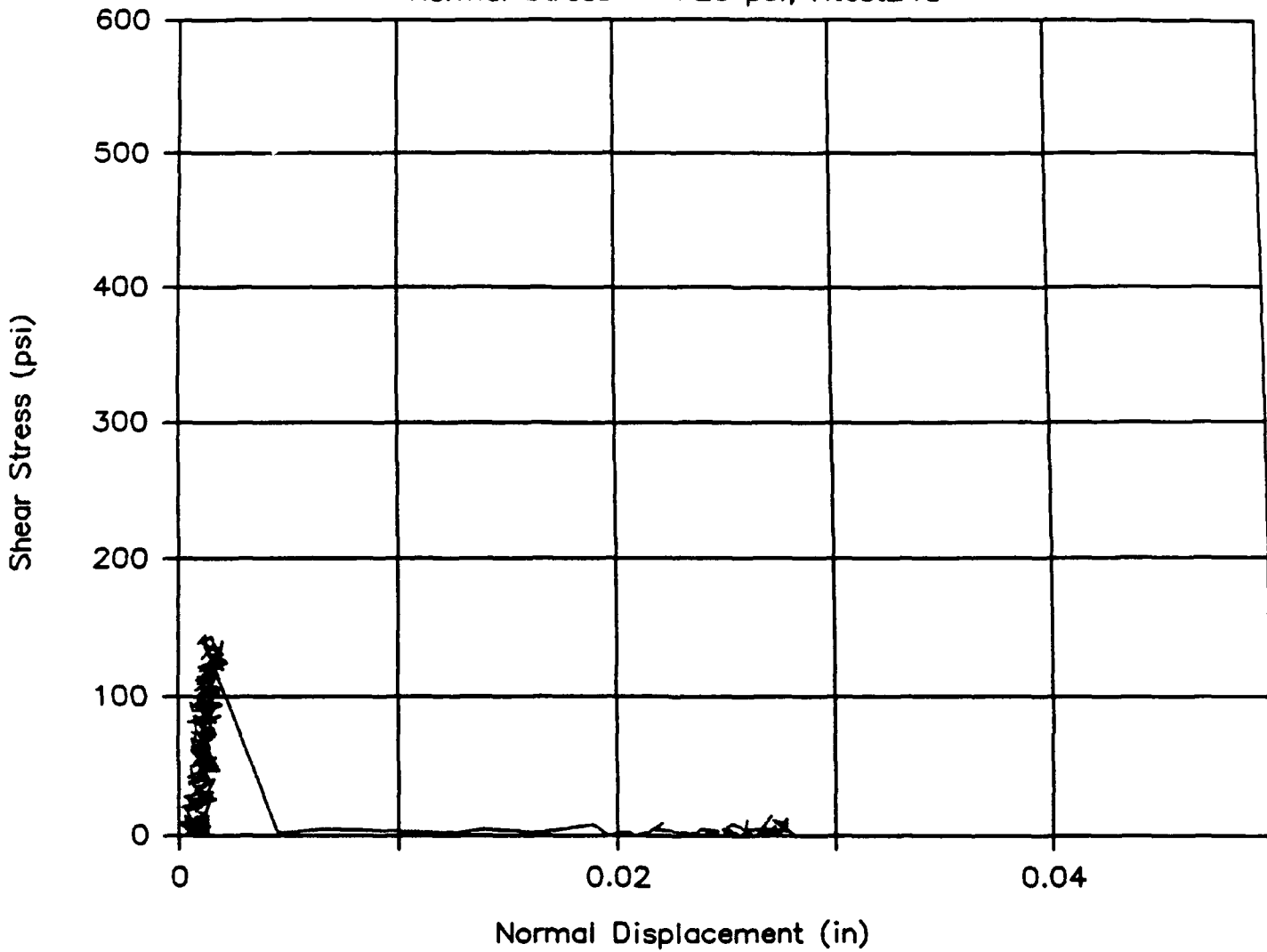
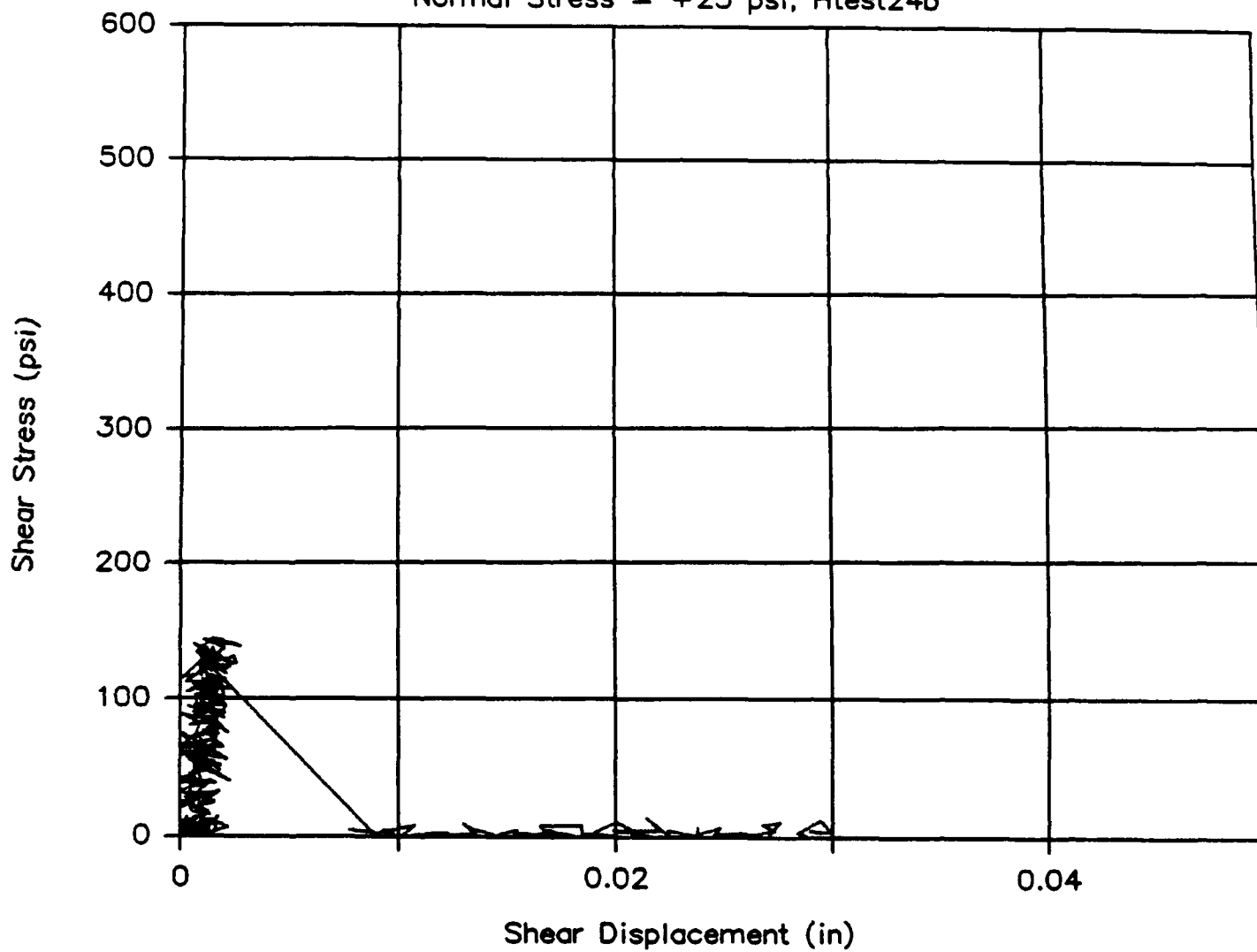


Fig. 16 (a) - (e) Load-displacement response diagrams for test series 24

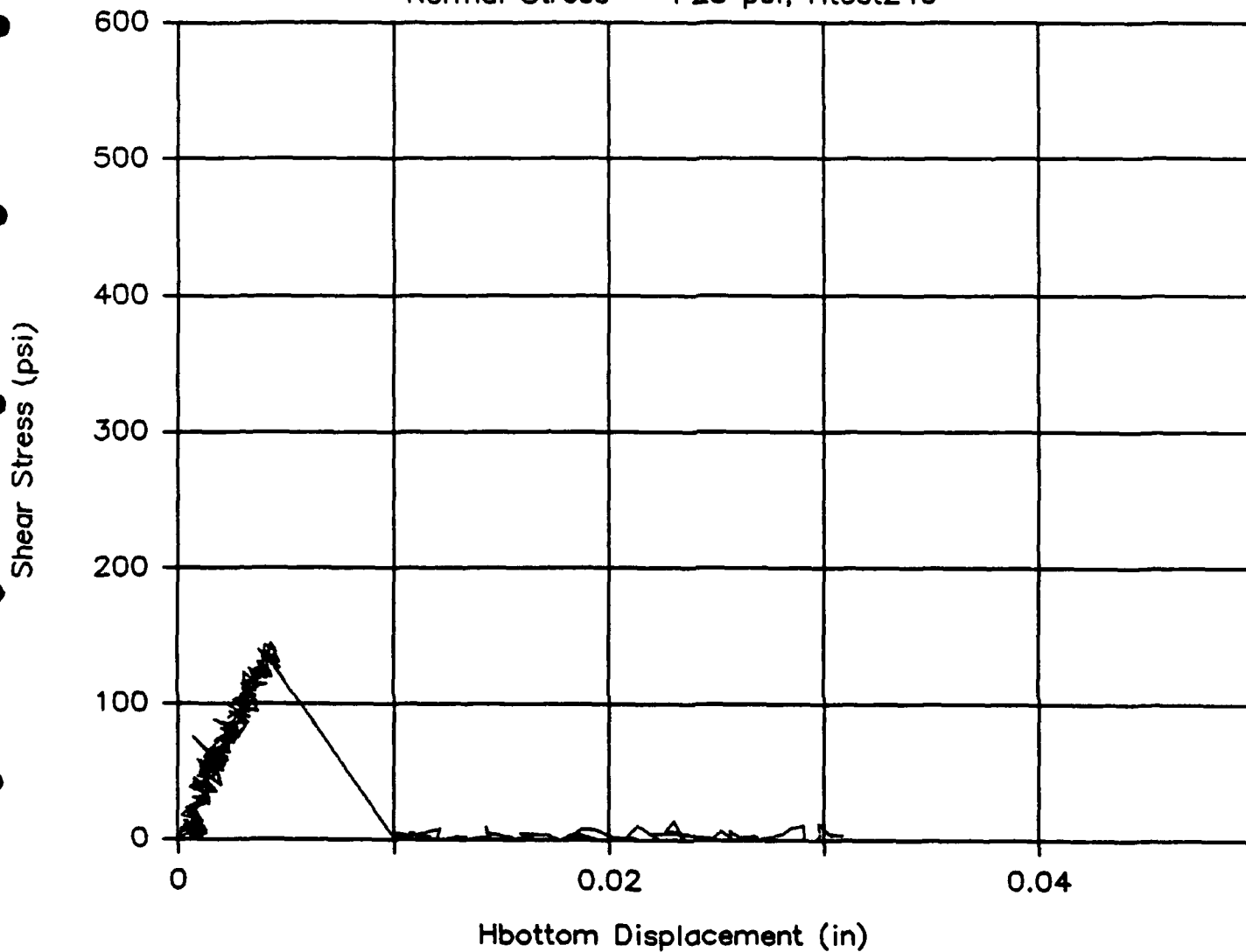
Shear Displacement – Shear Stress

Normal Stress = +25 psi, Htest24b



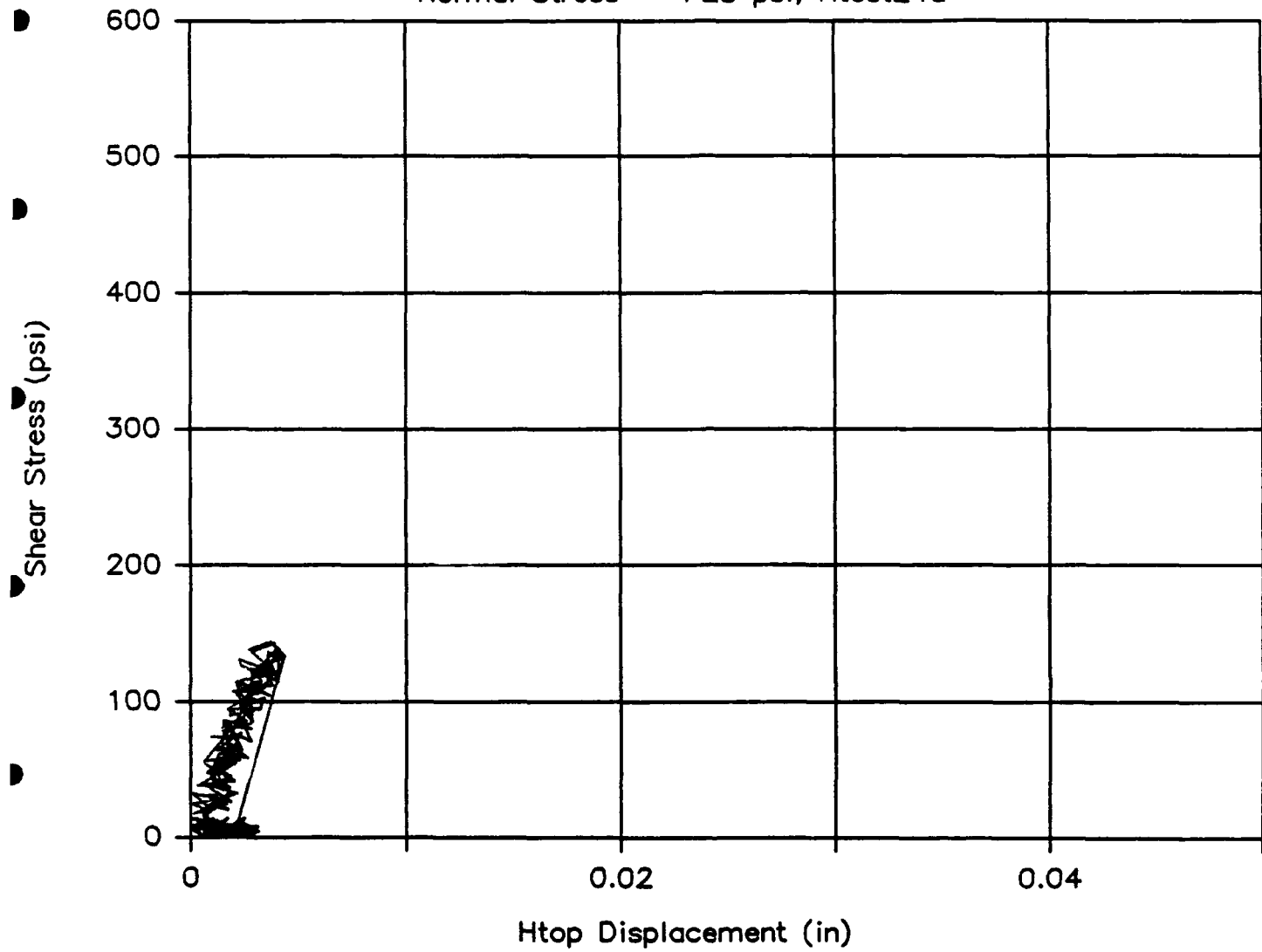
Hbottom Displacement – Shear Stress

Normal Stress = +25 psi, Htest24c



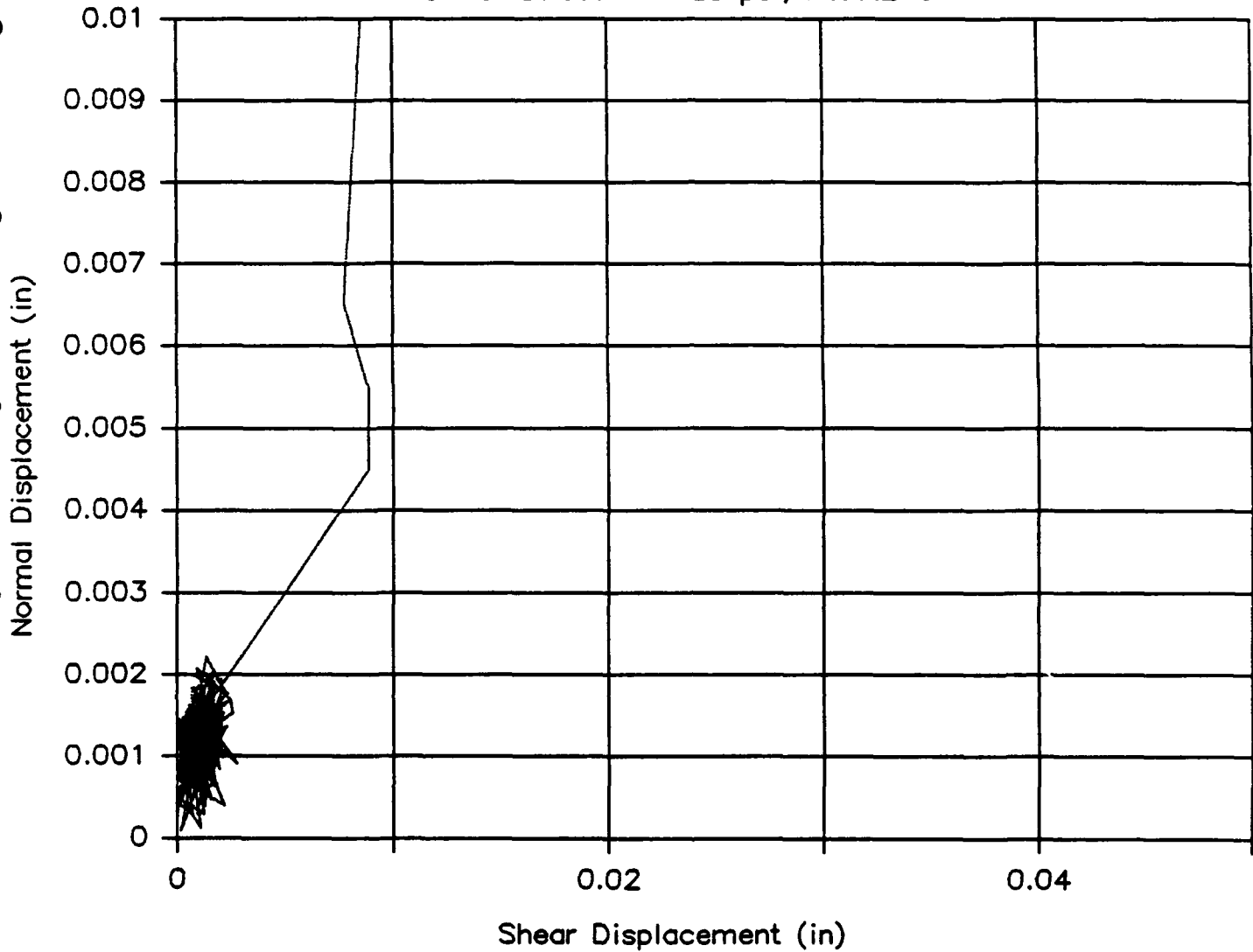
Htop Displacement – Shear Stress

Normal Stress = +25 psi, Htest24d



Shear Displacement—Normal Displacement

Normal Stress = +25 psi, Htest24e



Normal Displacement – Shear Stress

Normal Stress = +50 psi, Htest28a

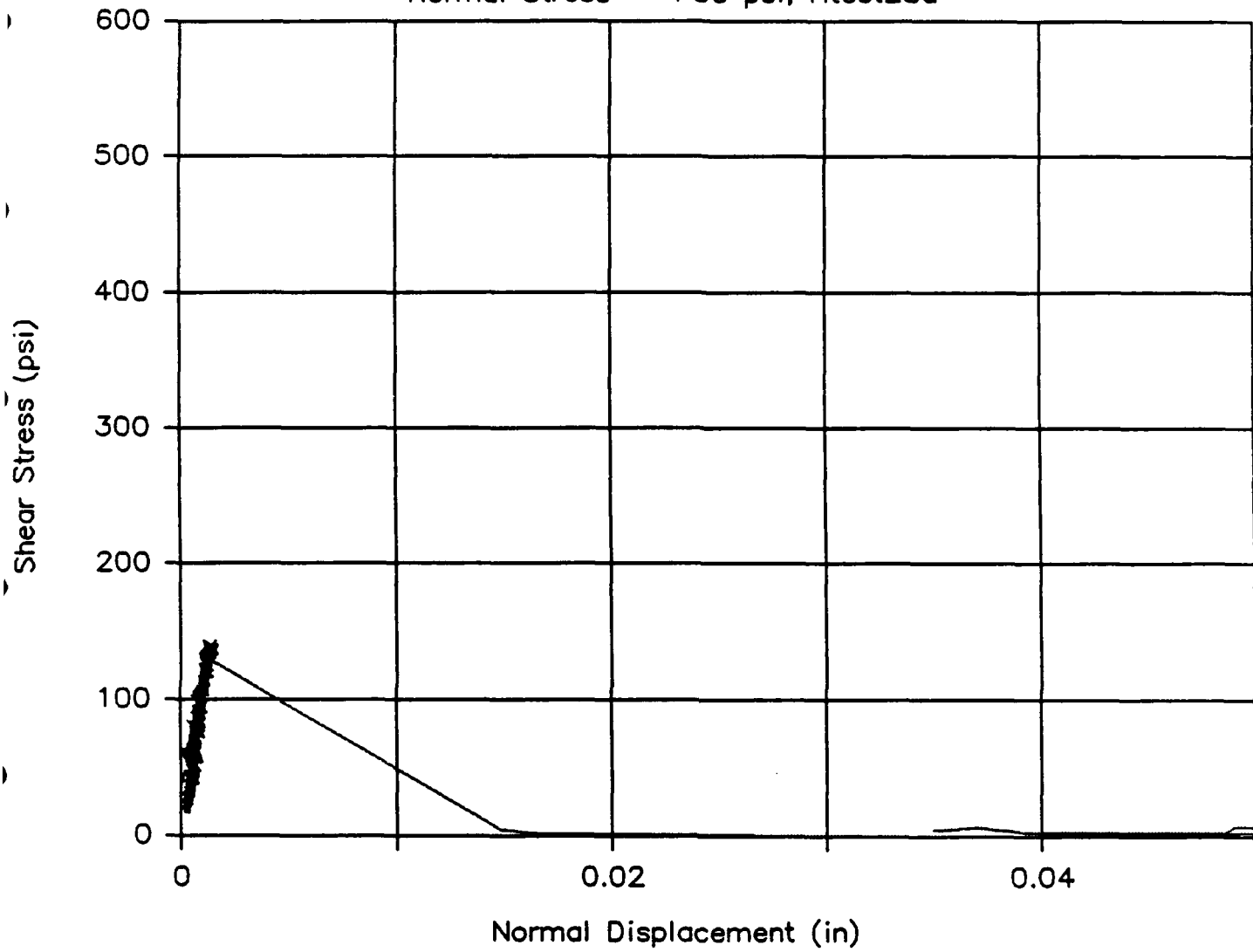
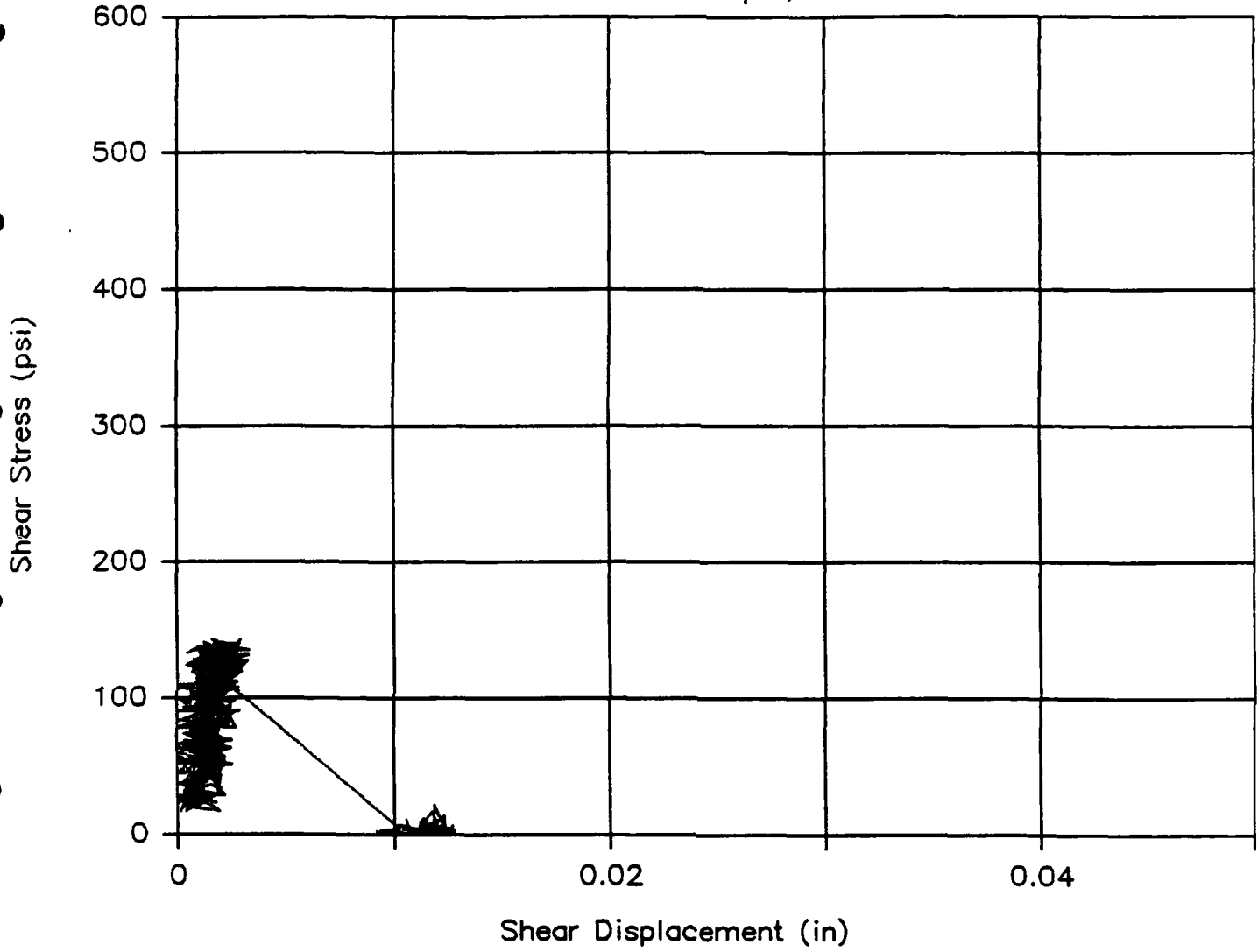


Fig. 17 (a) - (f) Load-displacement response diagrams for test series 28

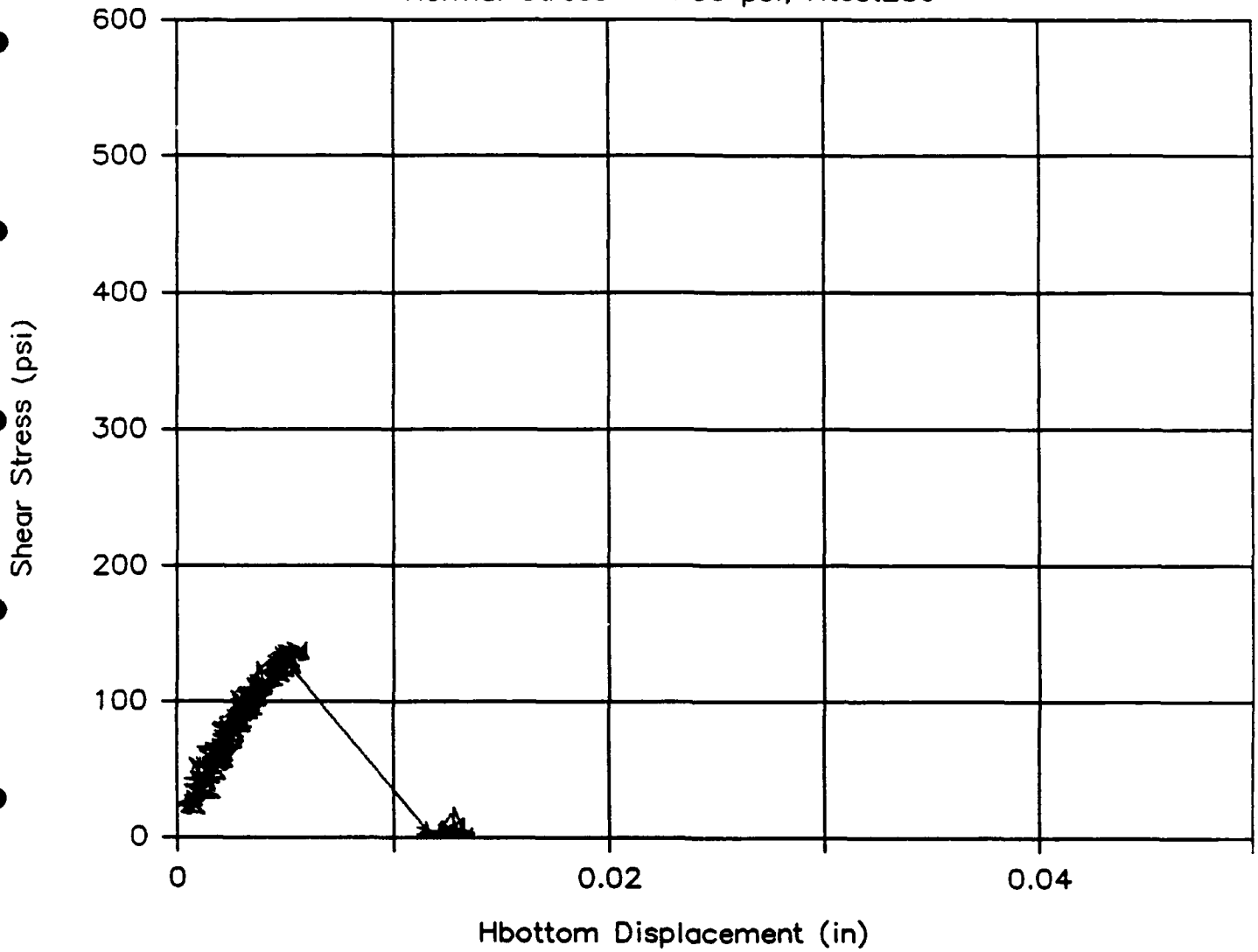
Shear Displacement – Shear Stress

Normal Stress = +50 psi, Htest28b



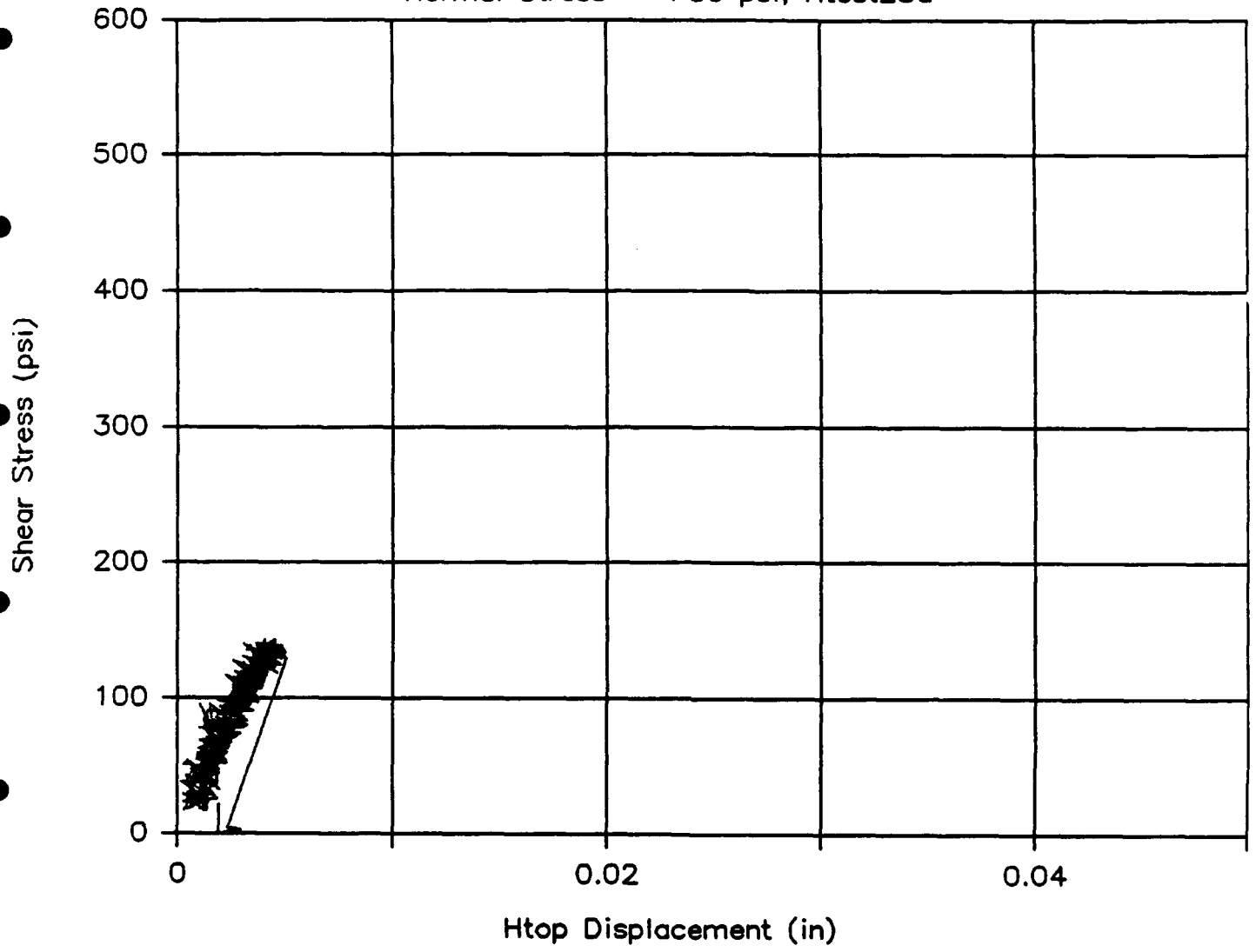
Hbottom Displacement – Shear Stress

Normal Stress = +50 psi, Htest28c



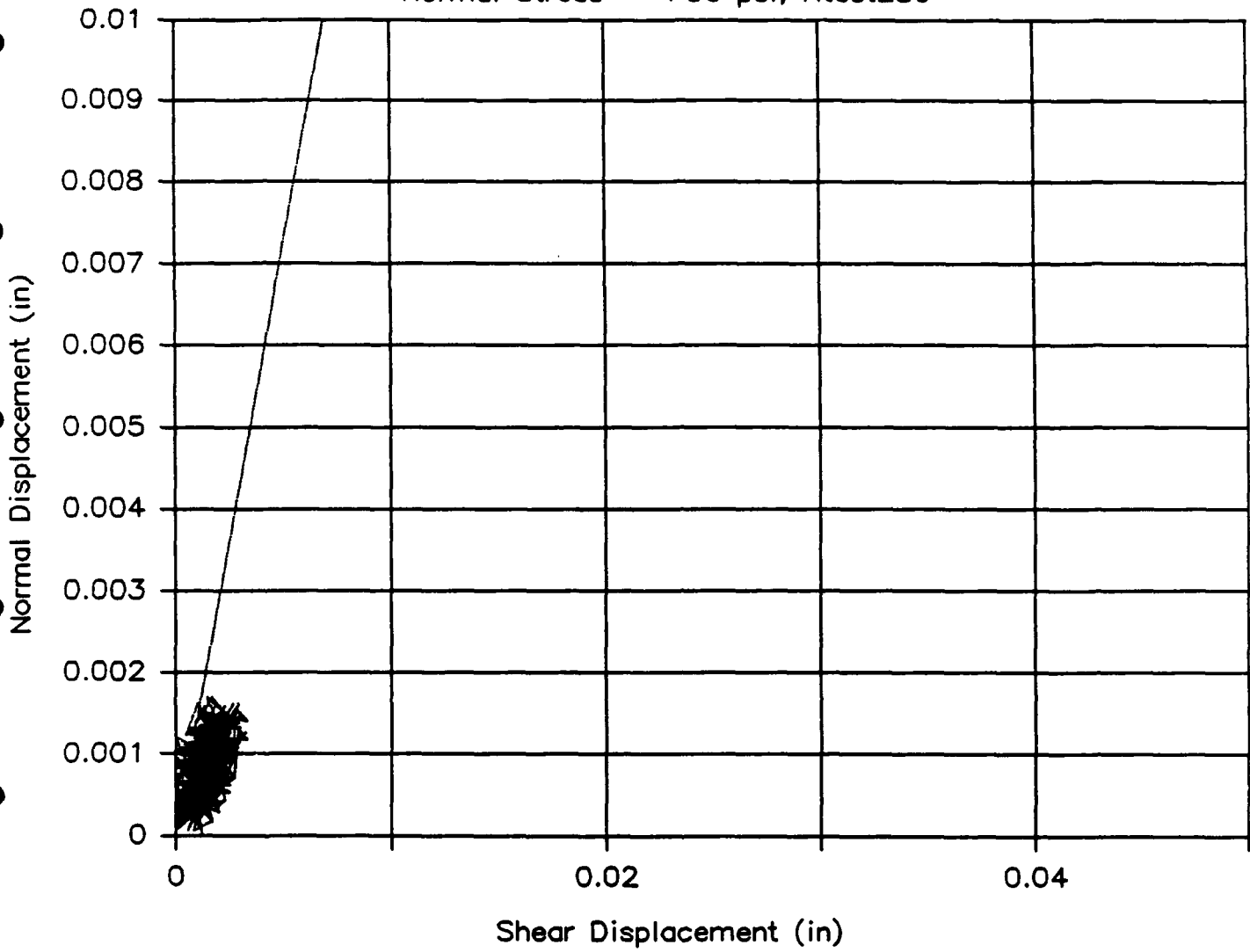
Htop Displacement – Shear Stress

Normal Stress = +50 psi, Htest28d



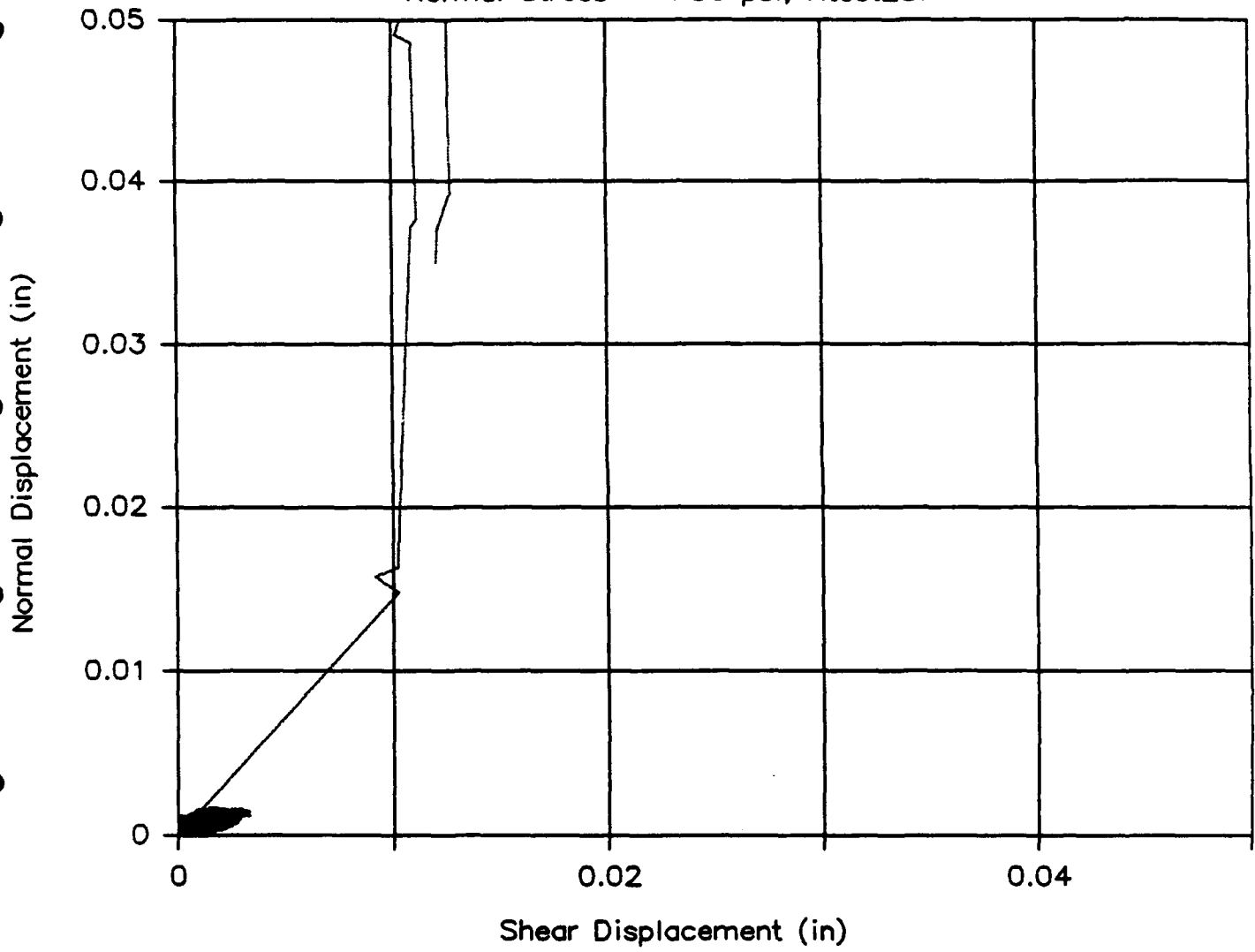
Shear Displacement—Normal Displacement

Normal Stress = +50 psi, Htest28e



Shear Displacement—Normal Displacement

Normal Stress = +50 psi, Htest28f



Normal Displacement – Shear Stress

Normal Stress = +50 psi, Htest29a

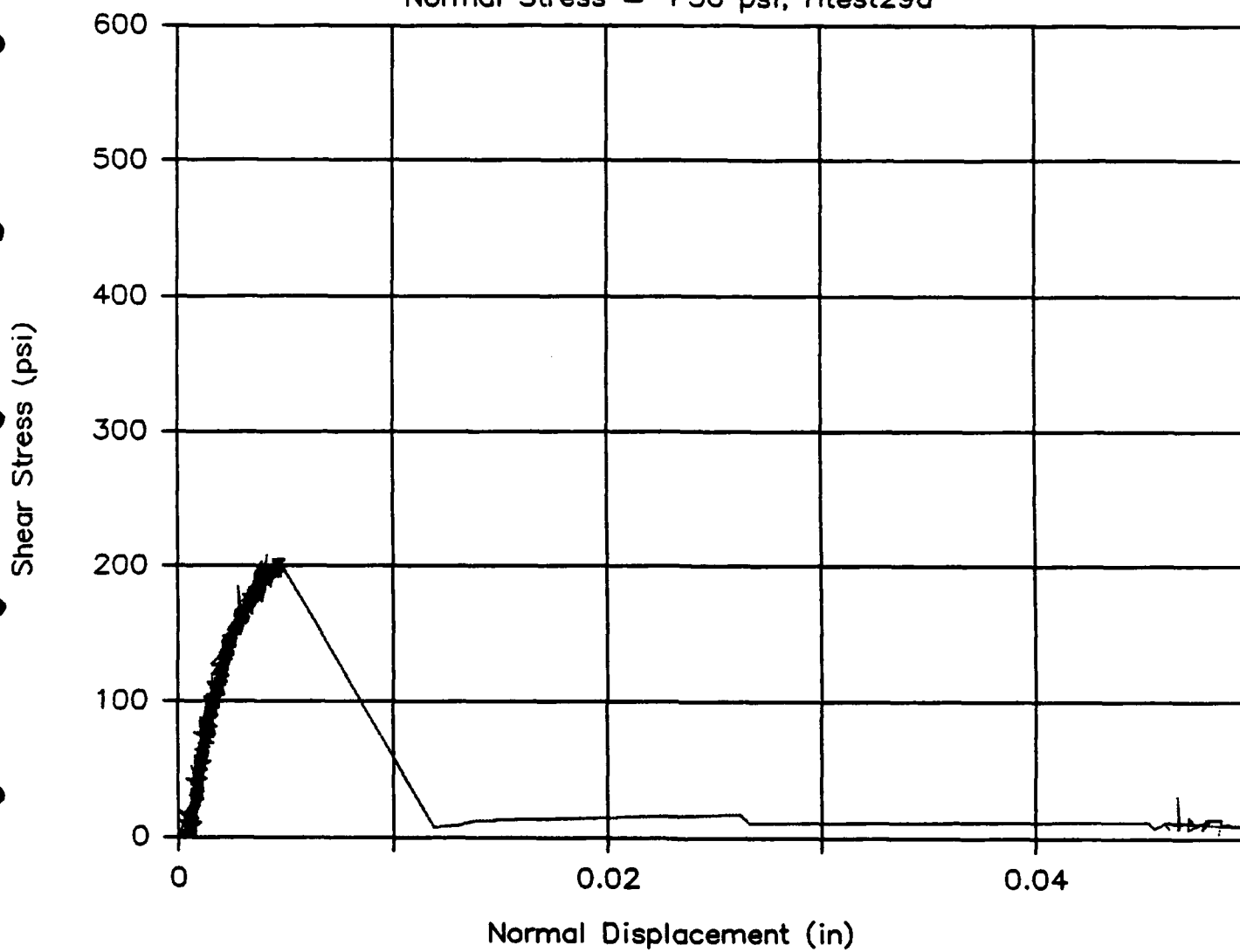
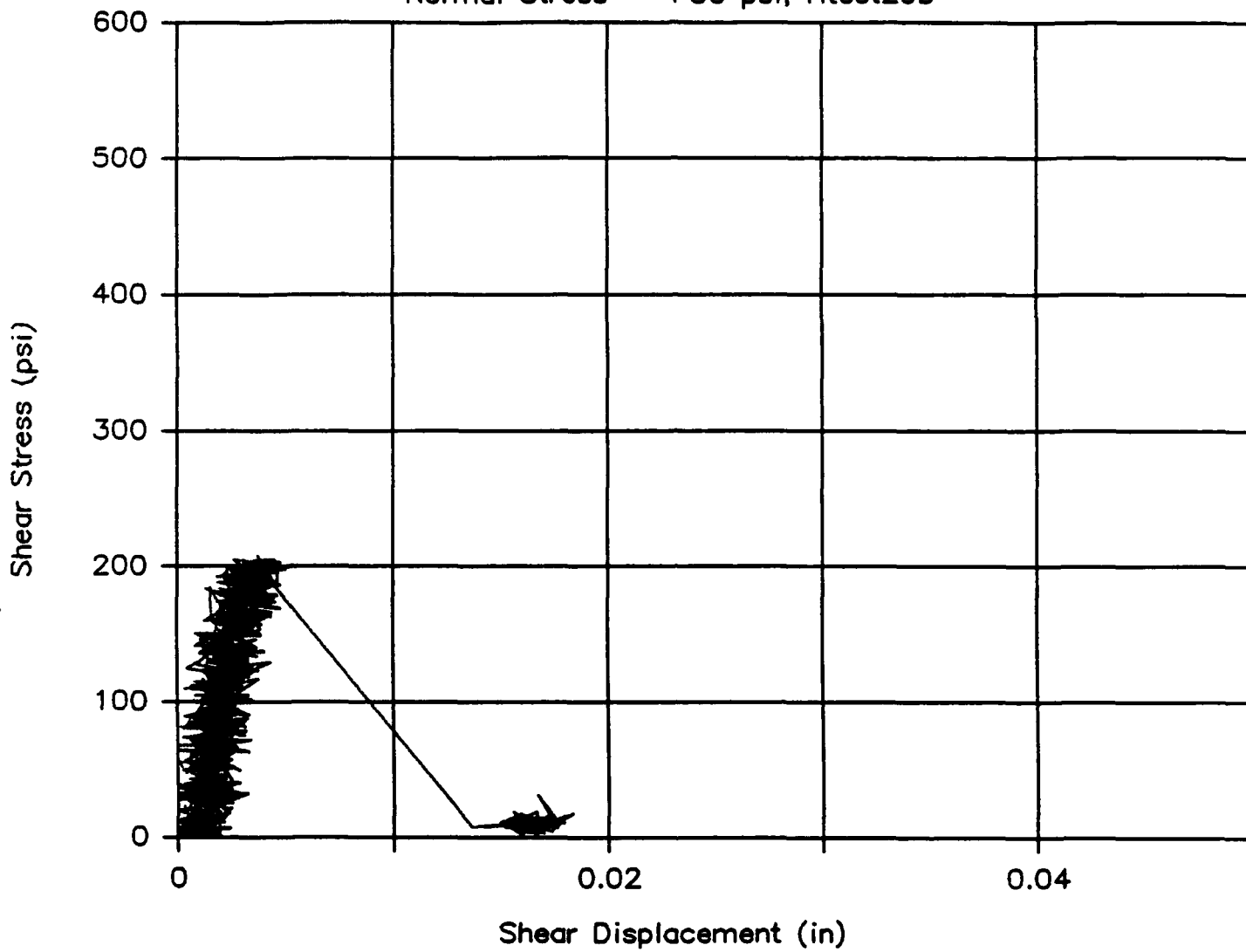


Fig. 18 (a) - (f) Load-displacement response diagrams for test series 29

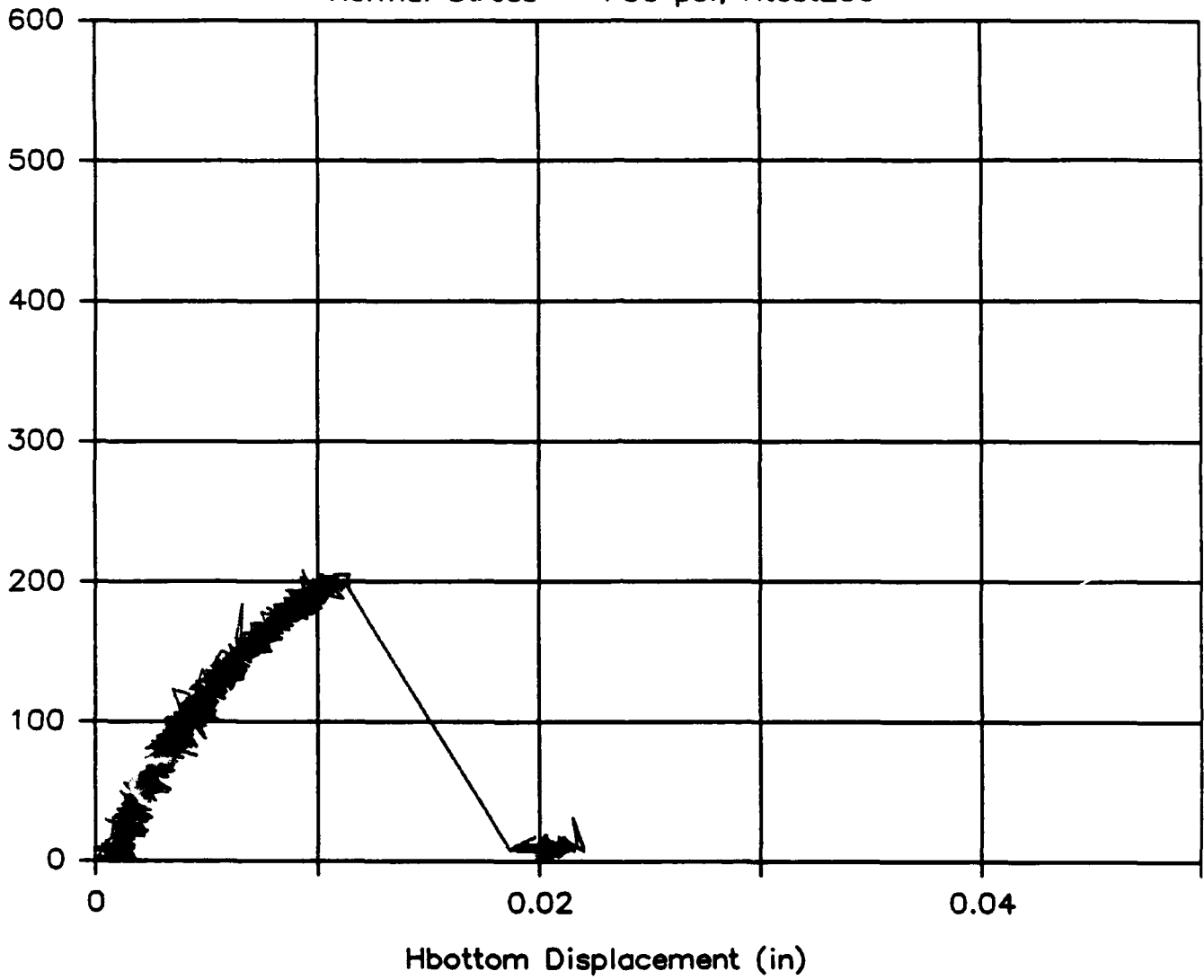
Shear Displacement — Shear Stress

Normal Stress = +50 psi, Htest29b



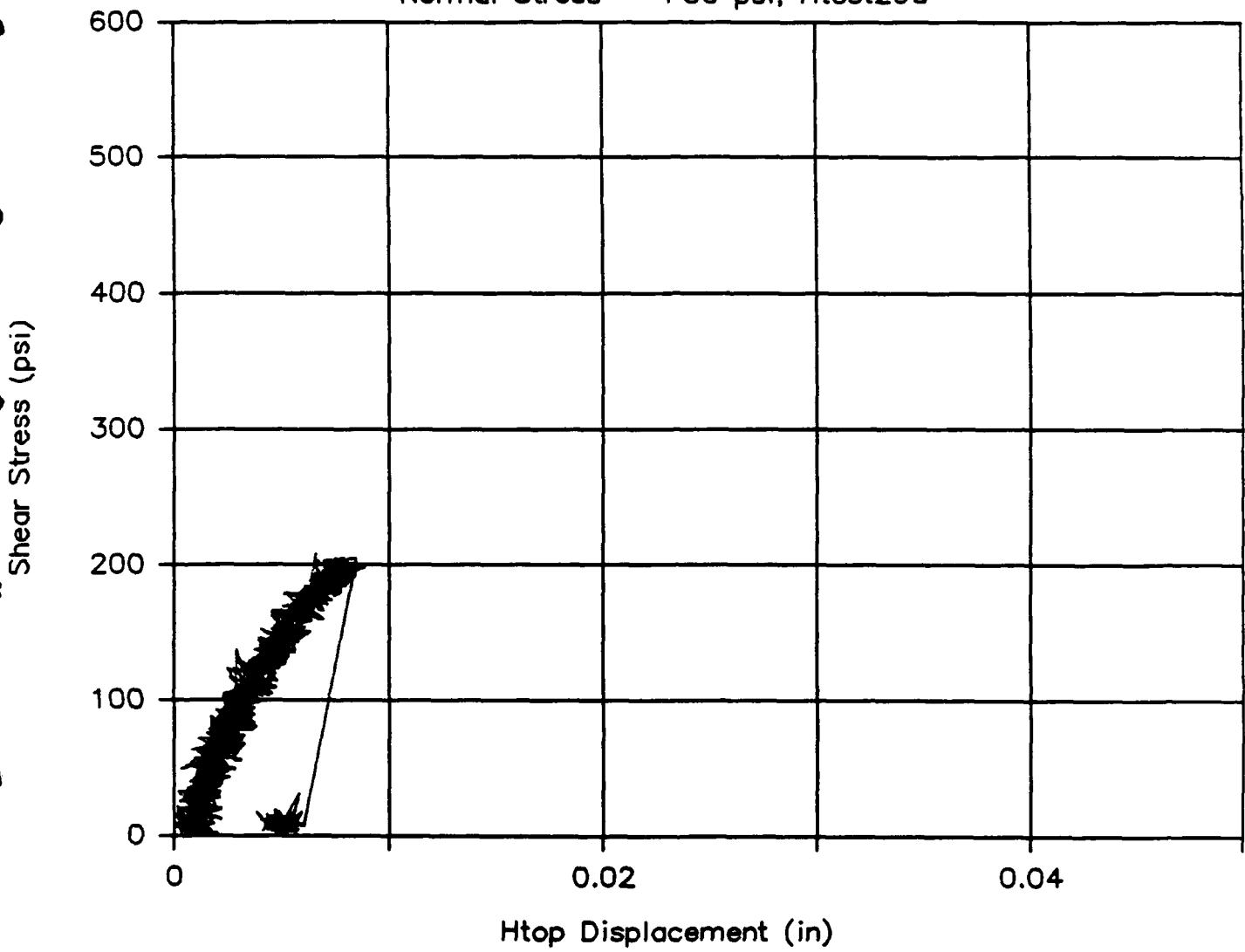
Hbottom Displacement – Shear Stress

Normal Stress = +50 psi, Htest29c



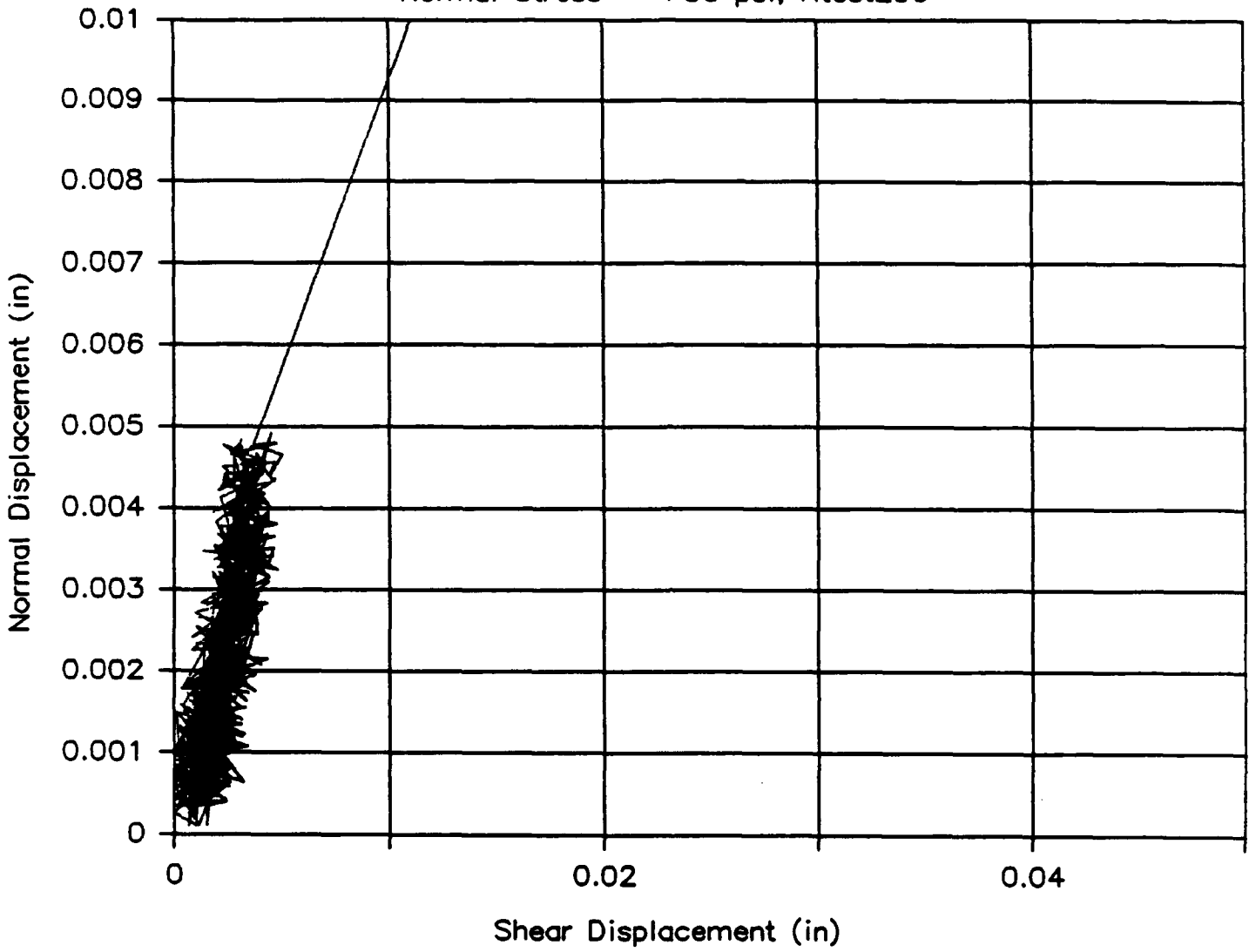
Htop Displacement – Shear Stress

Normal Stress = +50 psi, Htest29d



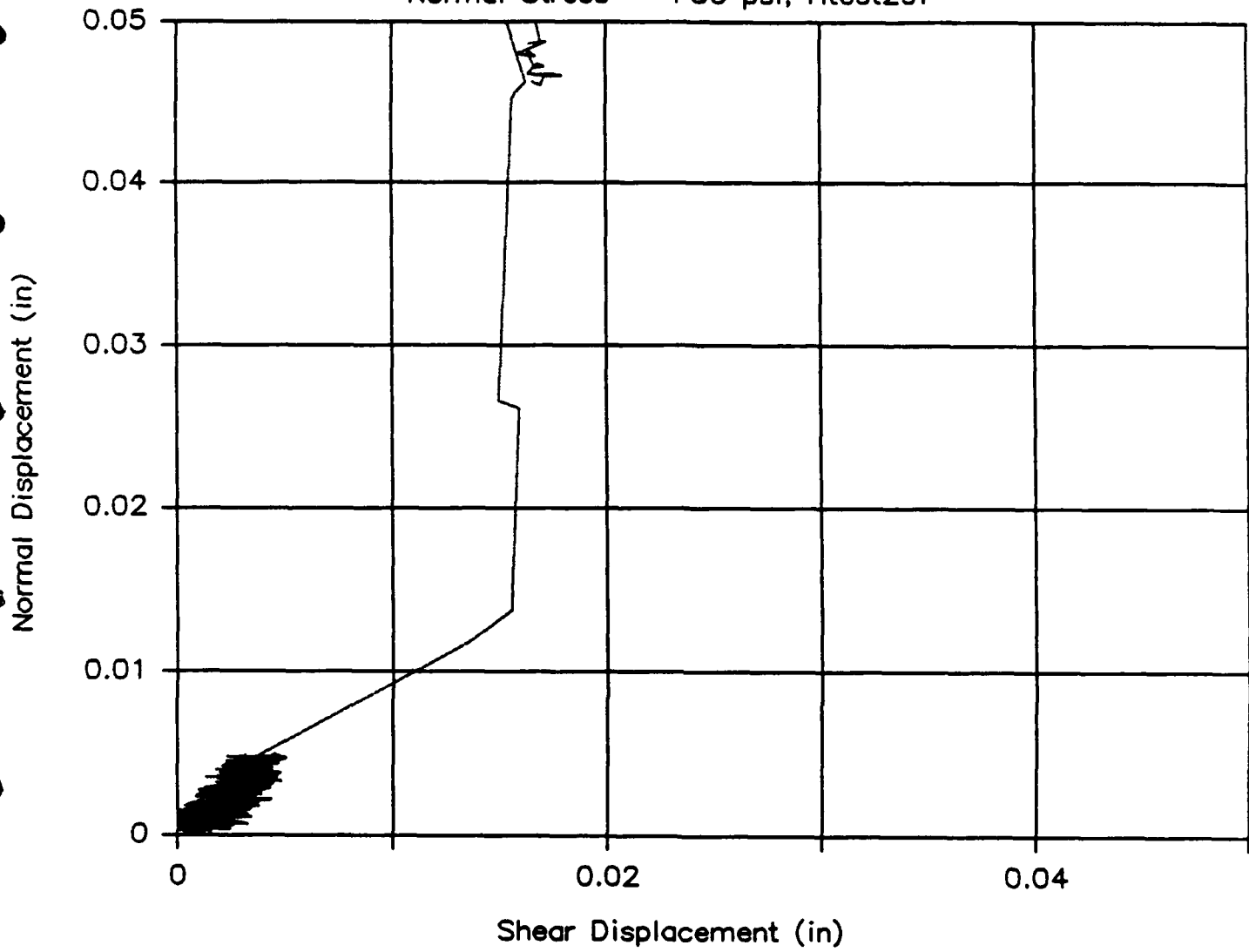
Shear Displacement—Normal Displacement

Normal Stress = +50 psi, Htest29e



Shear Displacement—Normal Displacement

Normal Stress = +50 psi, Htest29f



Normal Displacement – Shear Stress

Normal Stress = +75 psi, Htest30a

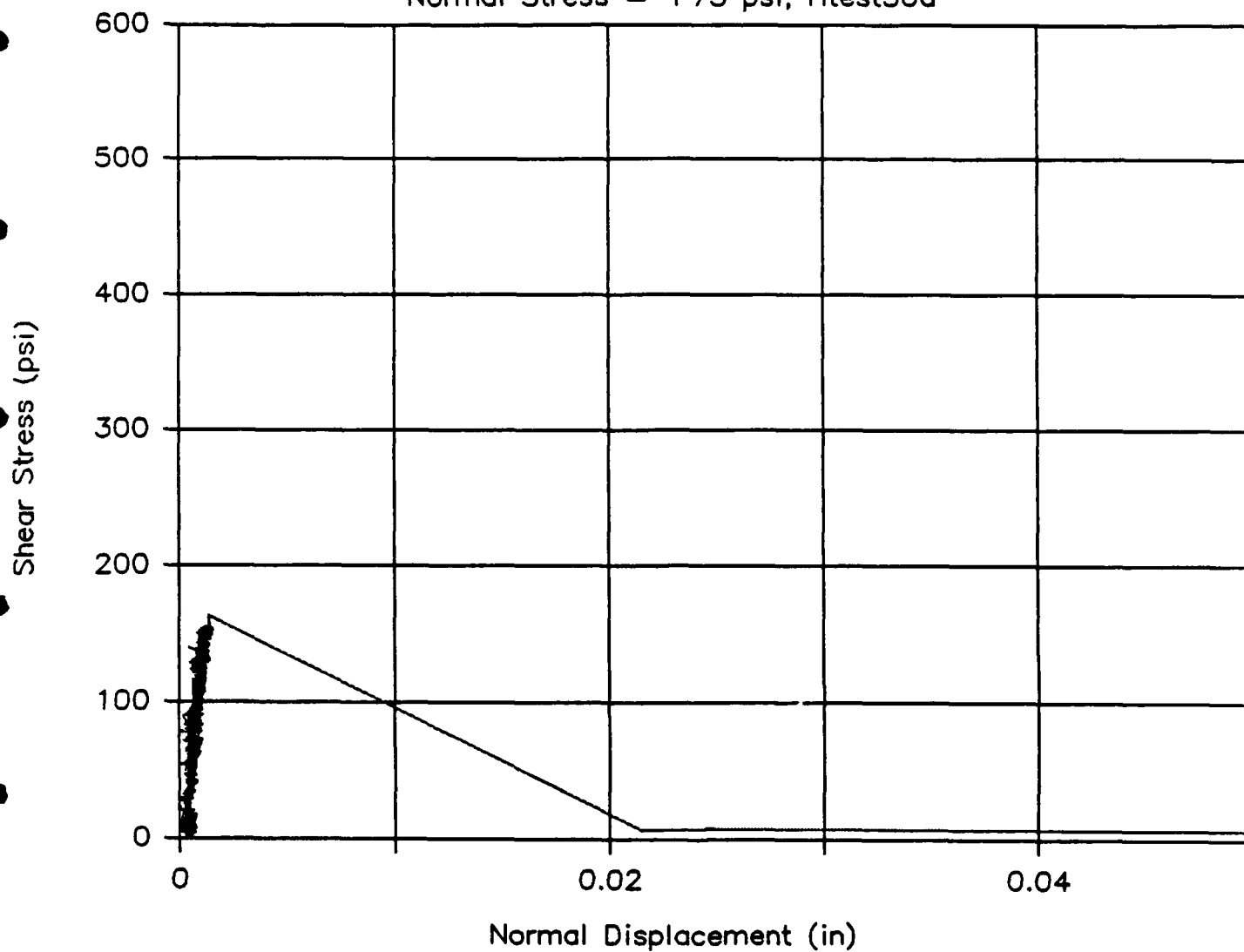
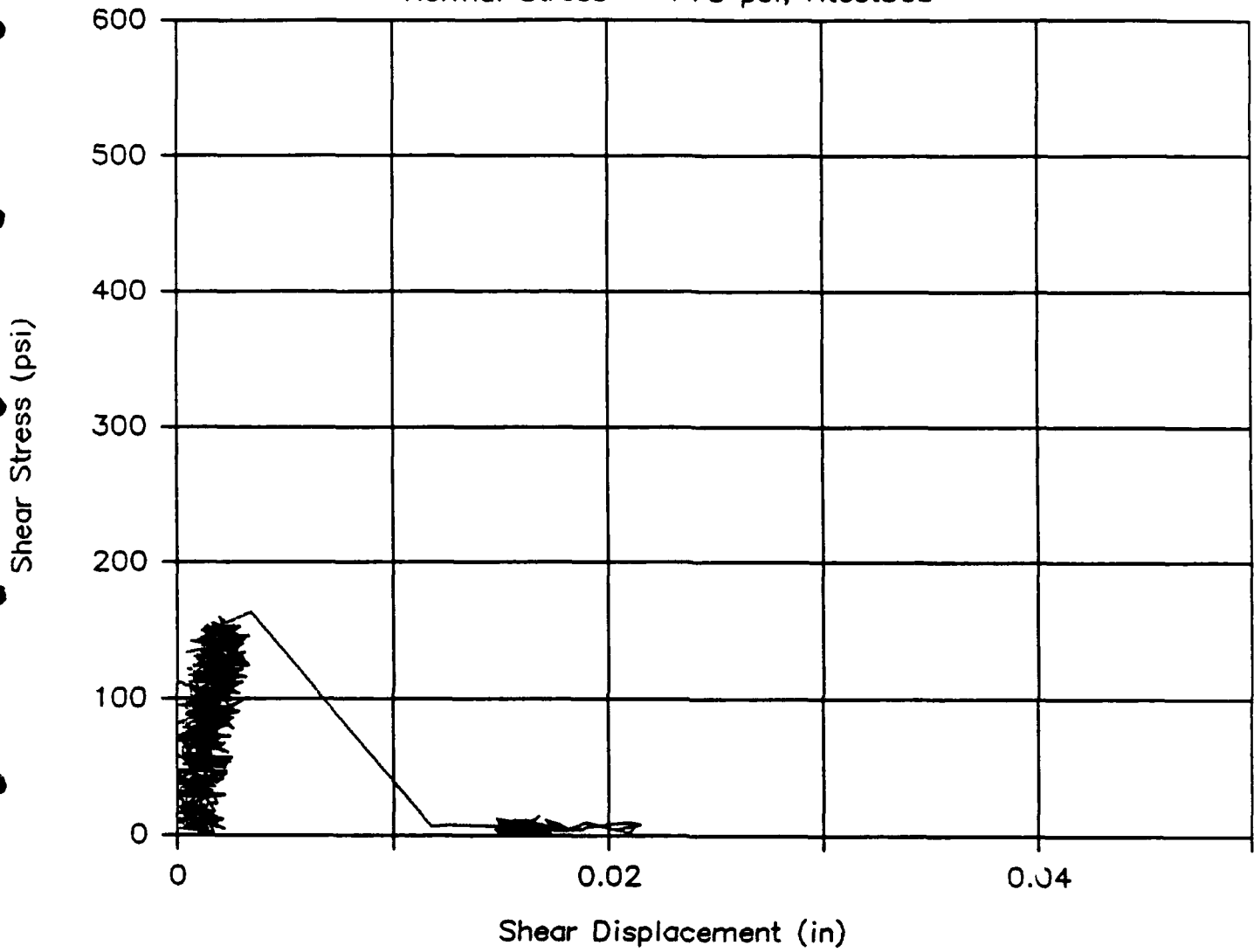


Fig. 19 (a) - (f) Load-displacement response diagrams for test series 30

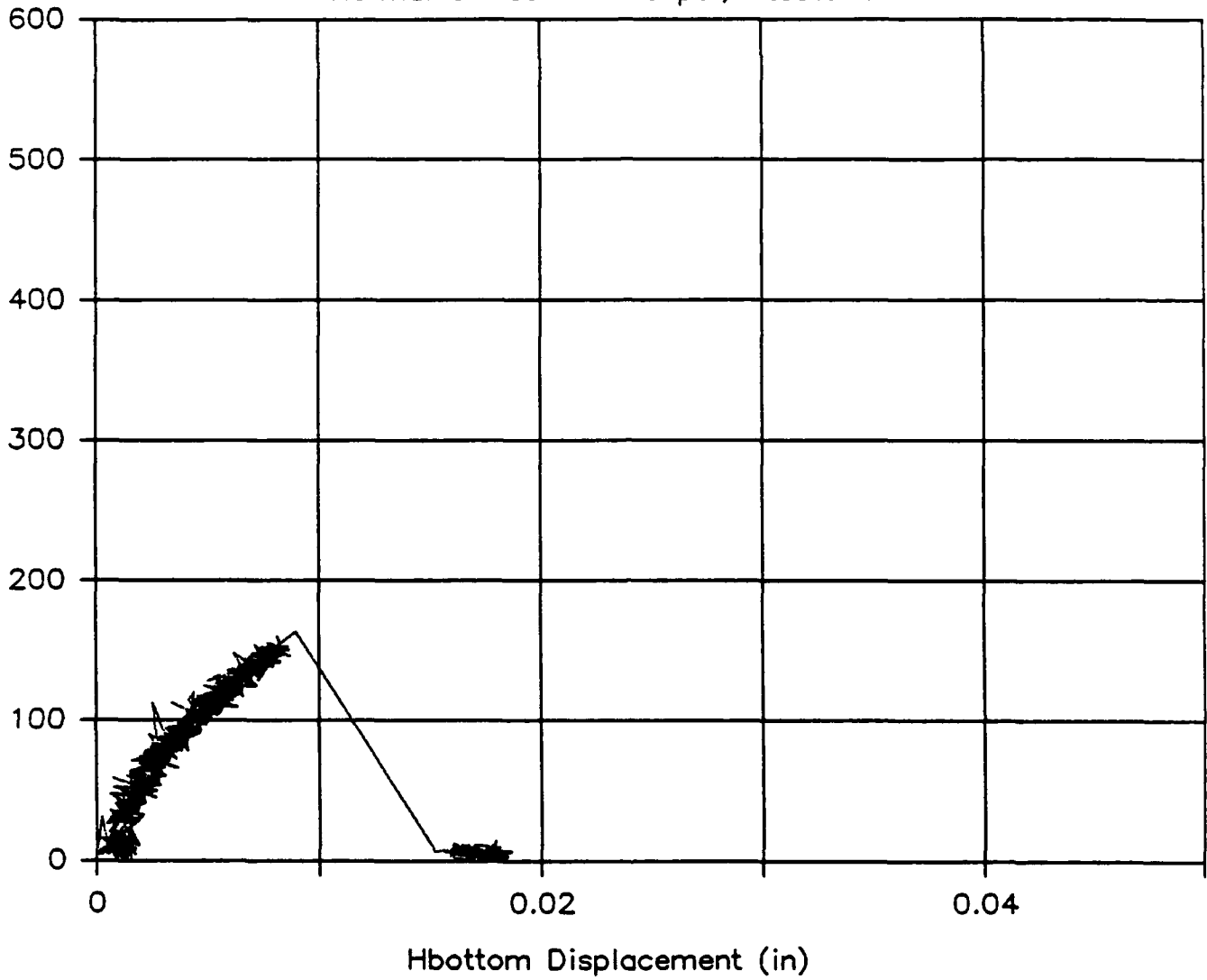
Shear Displacement – Shear Stress

Normal Stress = +75 psi, Htest30b



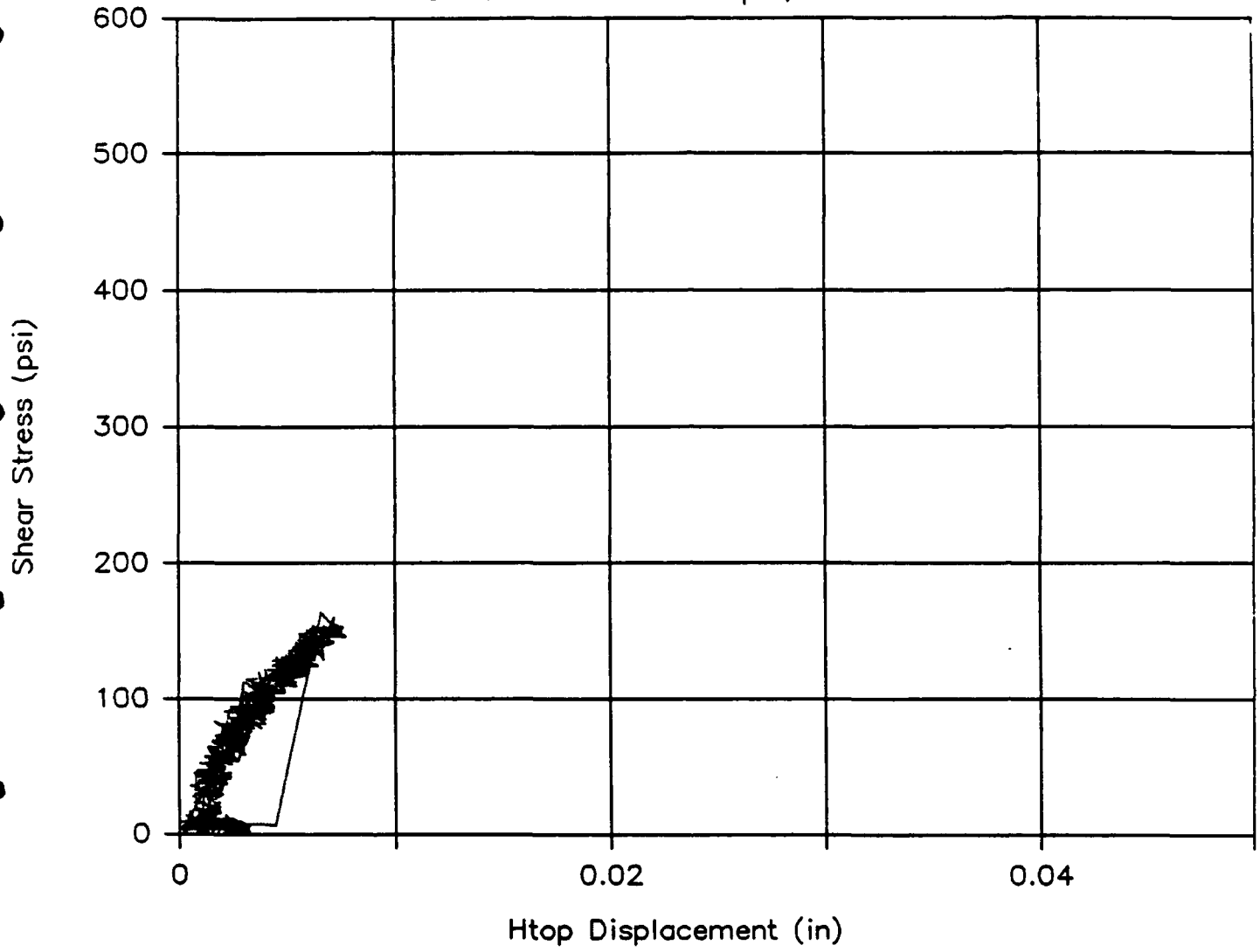
Hbottom Displacement – Shear Stress

Normal Stress = +75 psi, Htest30c



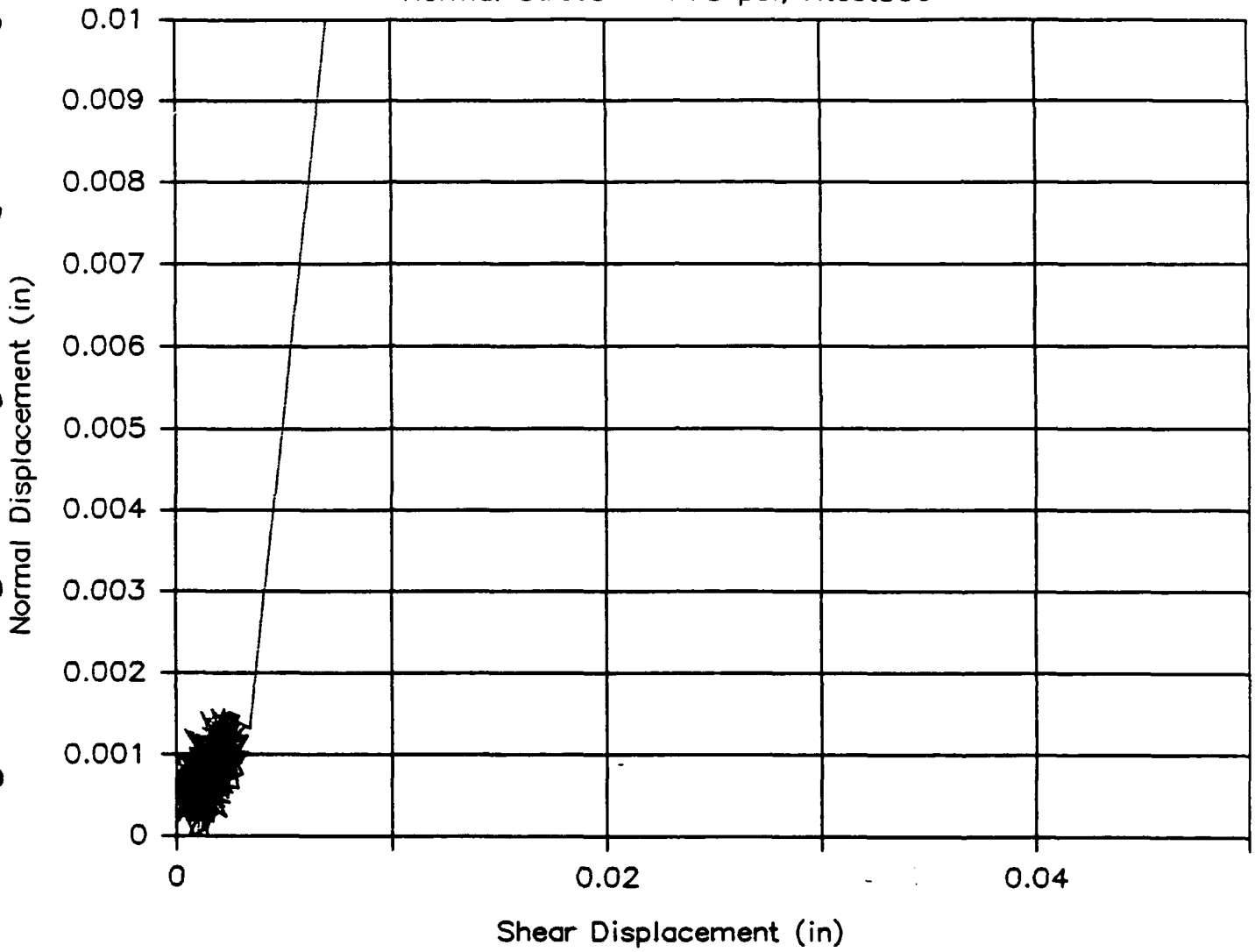
Htop Displacement – Shear Stress

Normal Stress = +75 psi, Htest30d



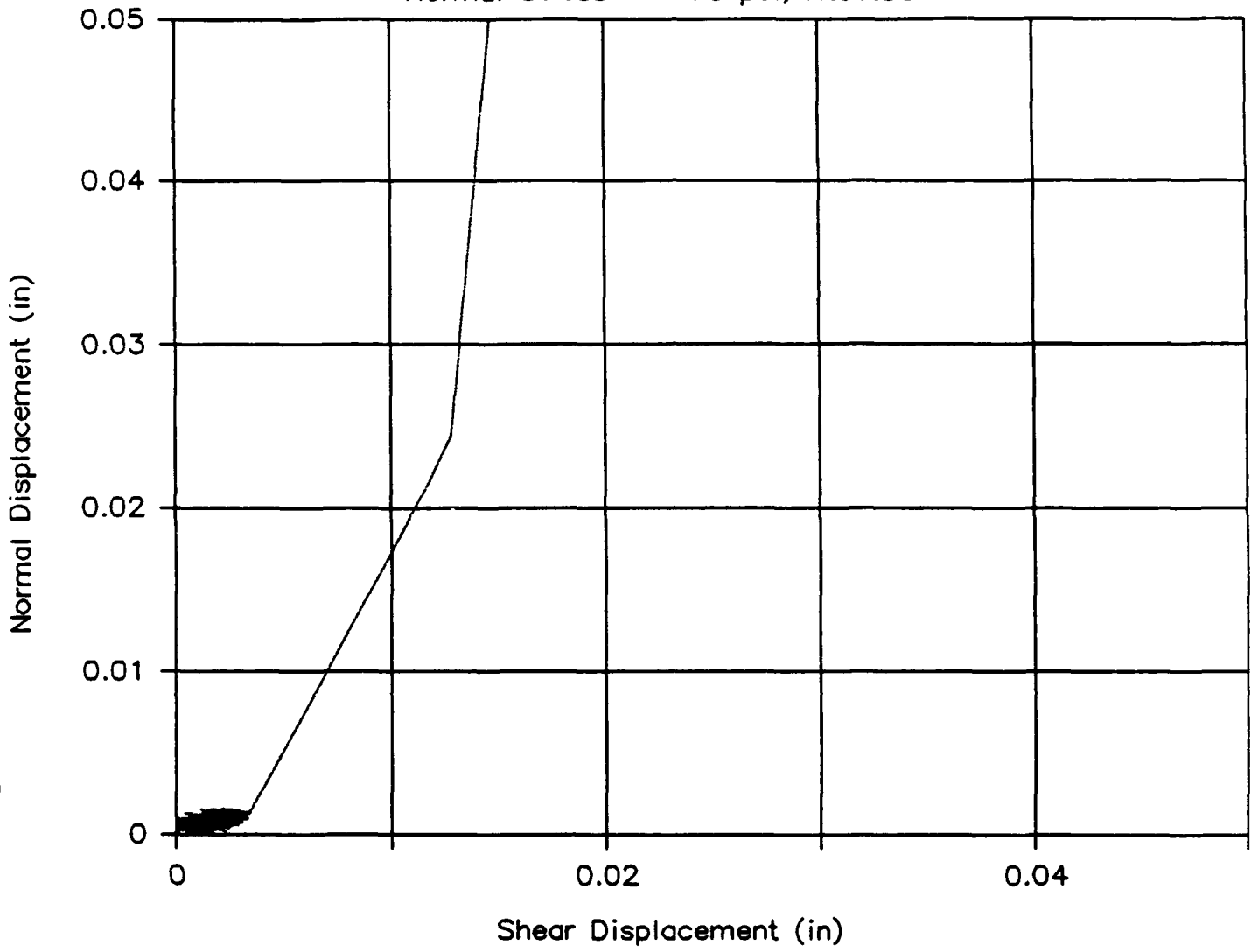
Shear Displacement—Normal Displacement

Normal Stress = +75 psi, Htest30e



Shear Displacement—Normal Displacement

Normal Stress = +75 psi, Htest30f



Normal Displacement - Shear Stress

Normal Stress = +100 psi, Htest31a

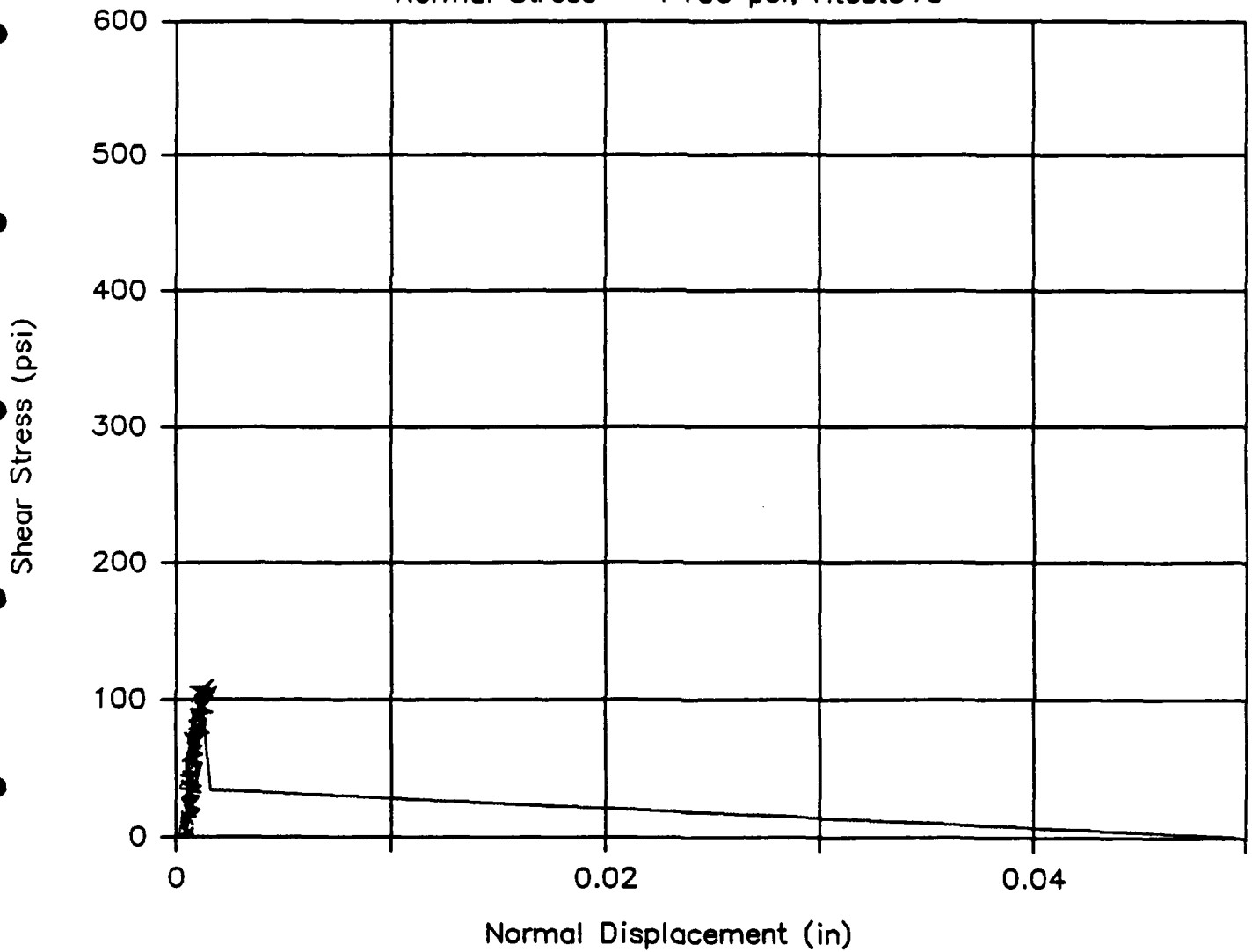
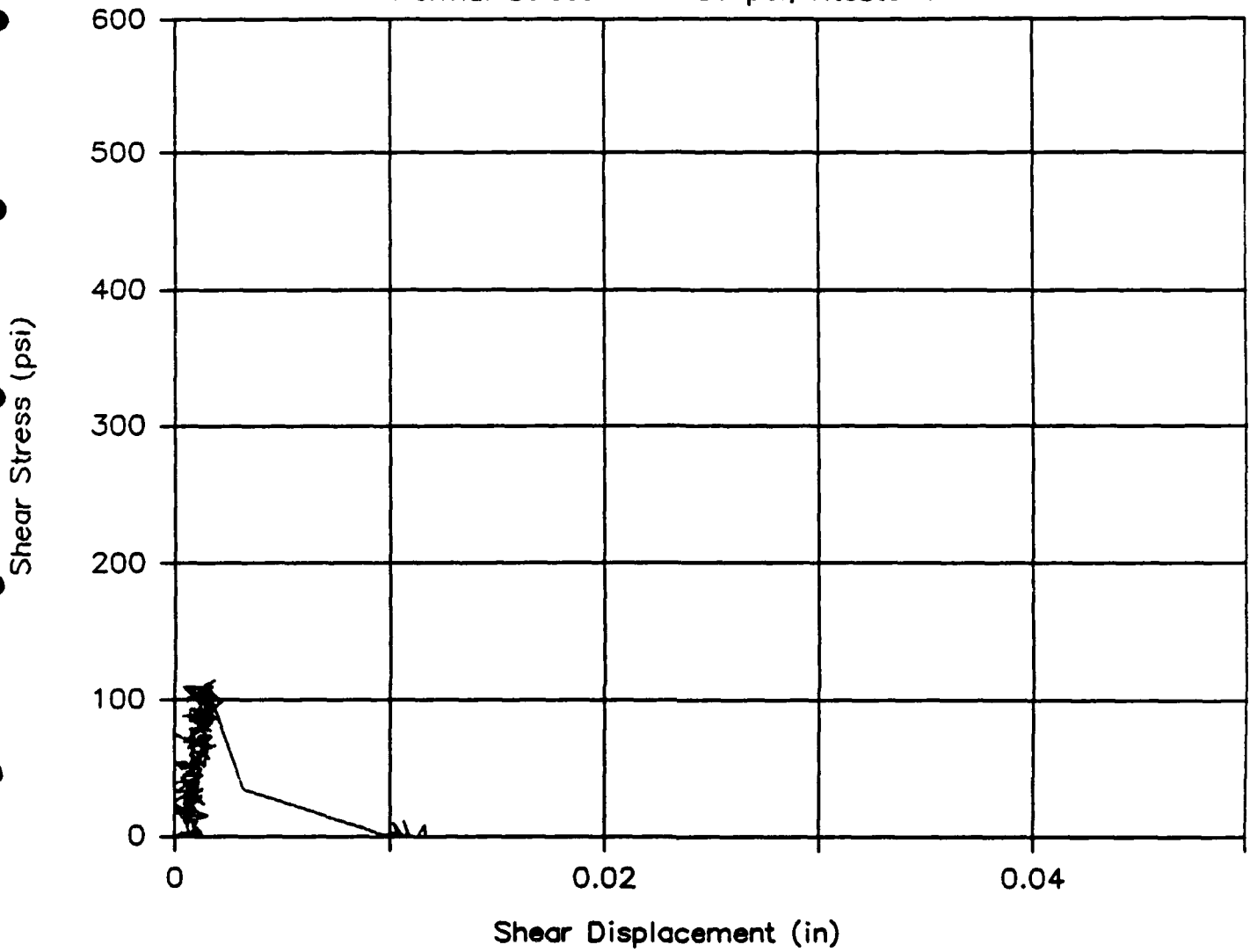


Fig. 20 (a) - (f) Load-displacement response diagrams for test series 31

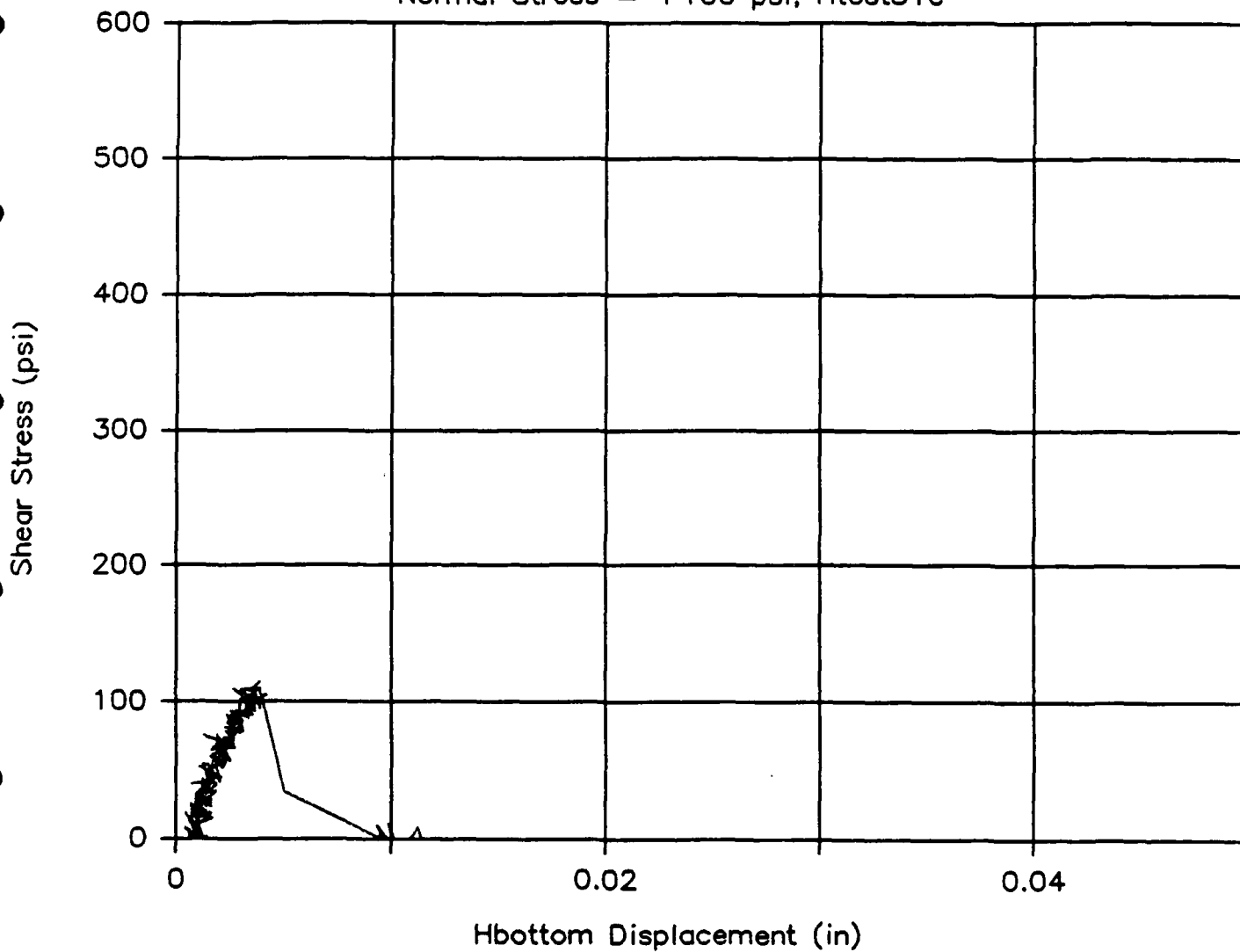
Shear Displacement - Shear Stress

Normal Stress = +100 psi, Htest31b



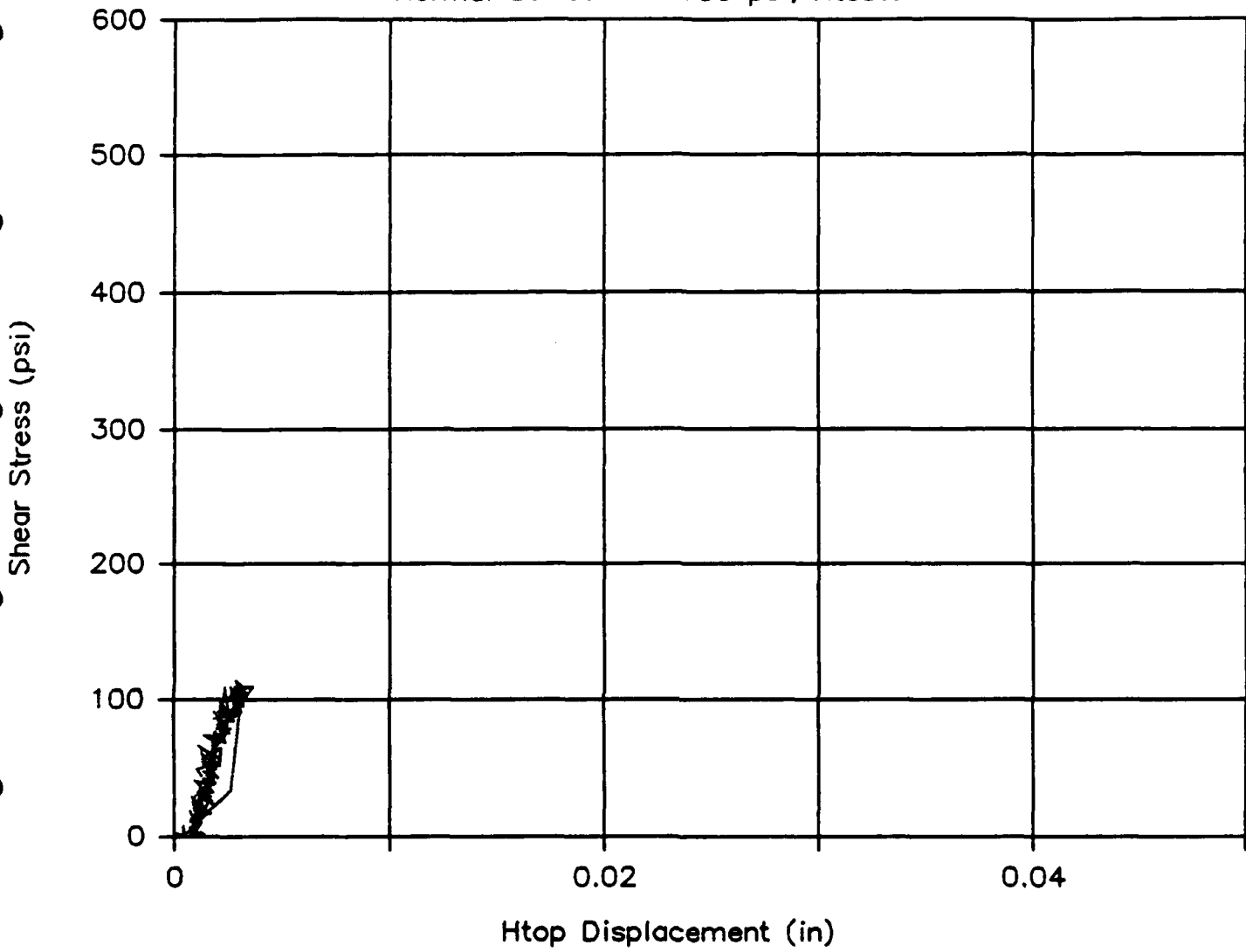
Hbottom Displacement – Shear Stress

Normal Stress = +100 psi, Htest31c



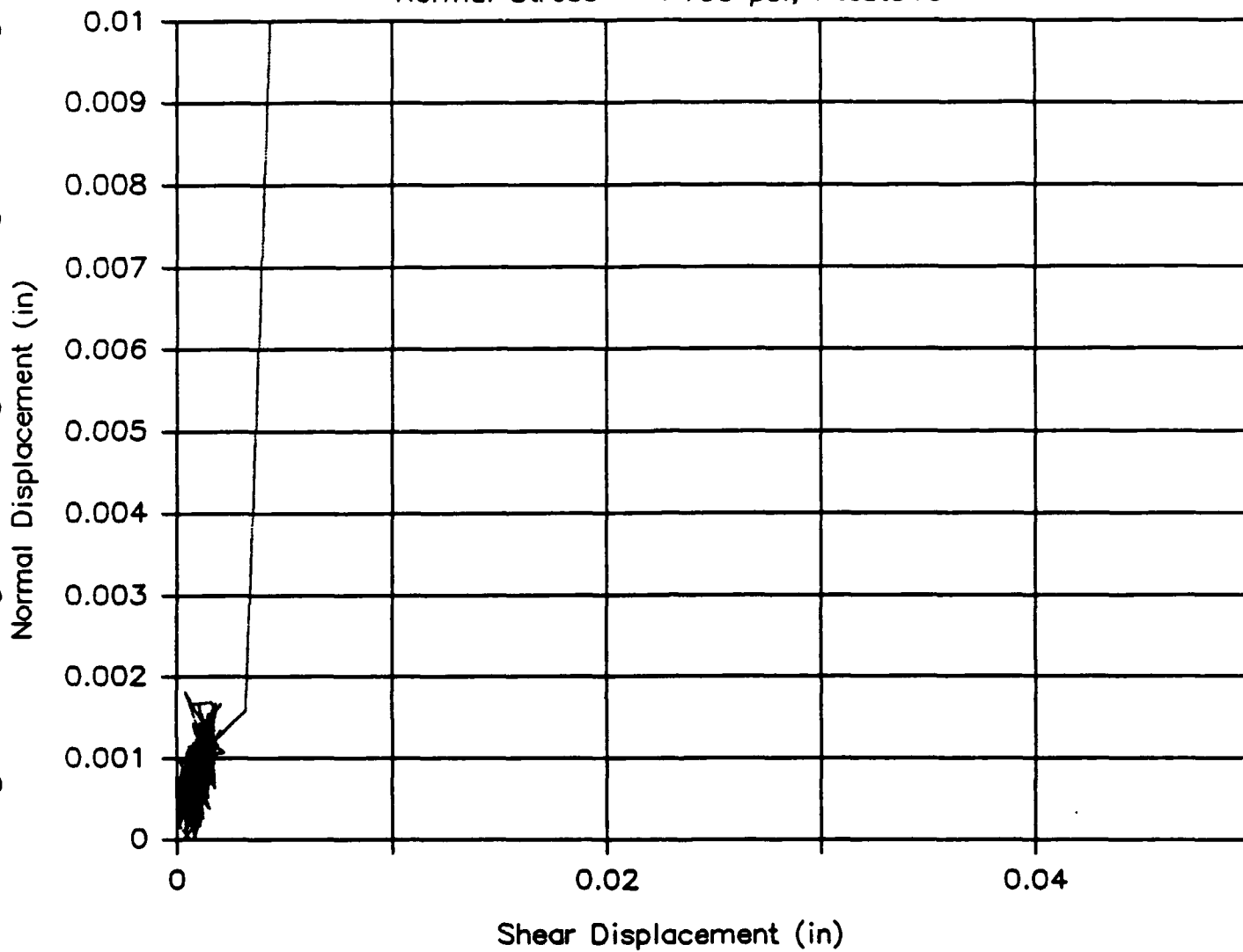
Htop Displacement – Shear Stress

Normal Stress = +100 psi, Htest31d



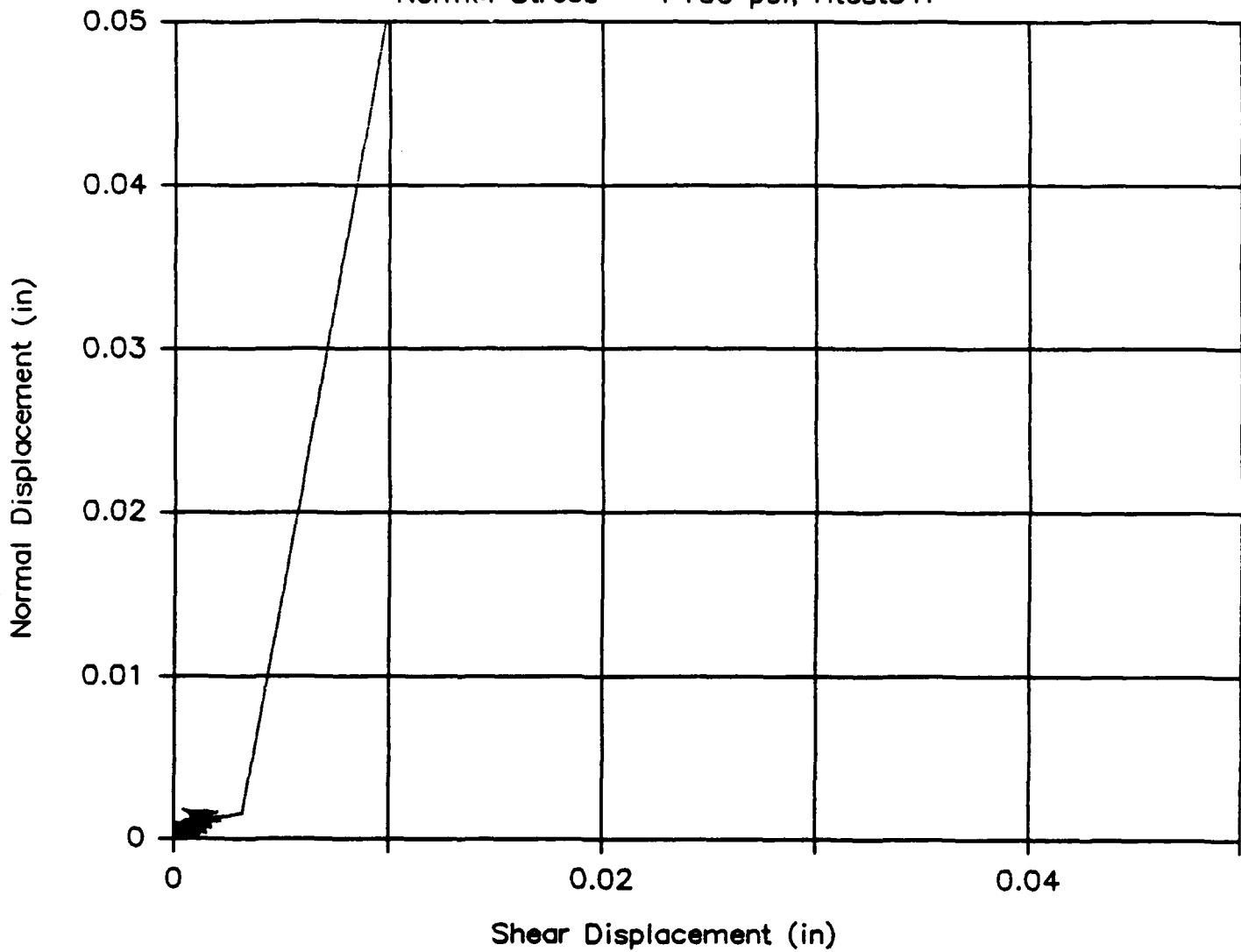
Shear Displacement—Normal Displacement

Normal Stress = +100 psi, Htest31e



Shear Displacement—Normal Displacement

Normal Stress = +100 psi, Htest31f



Normal Stress - Shear Stress

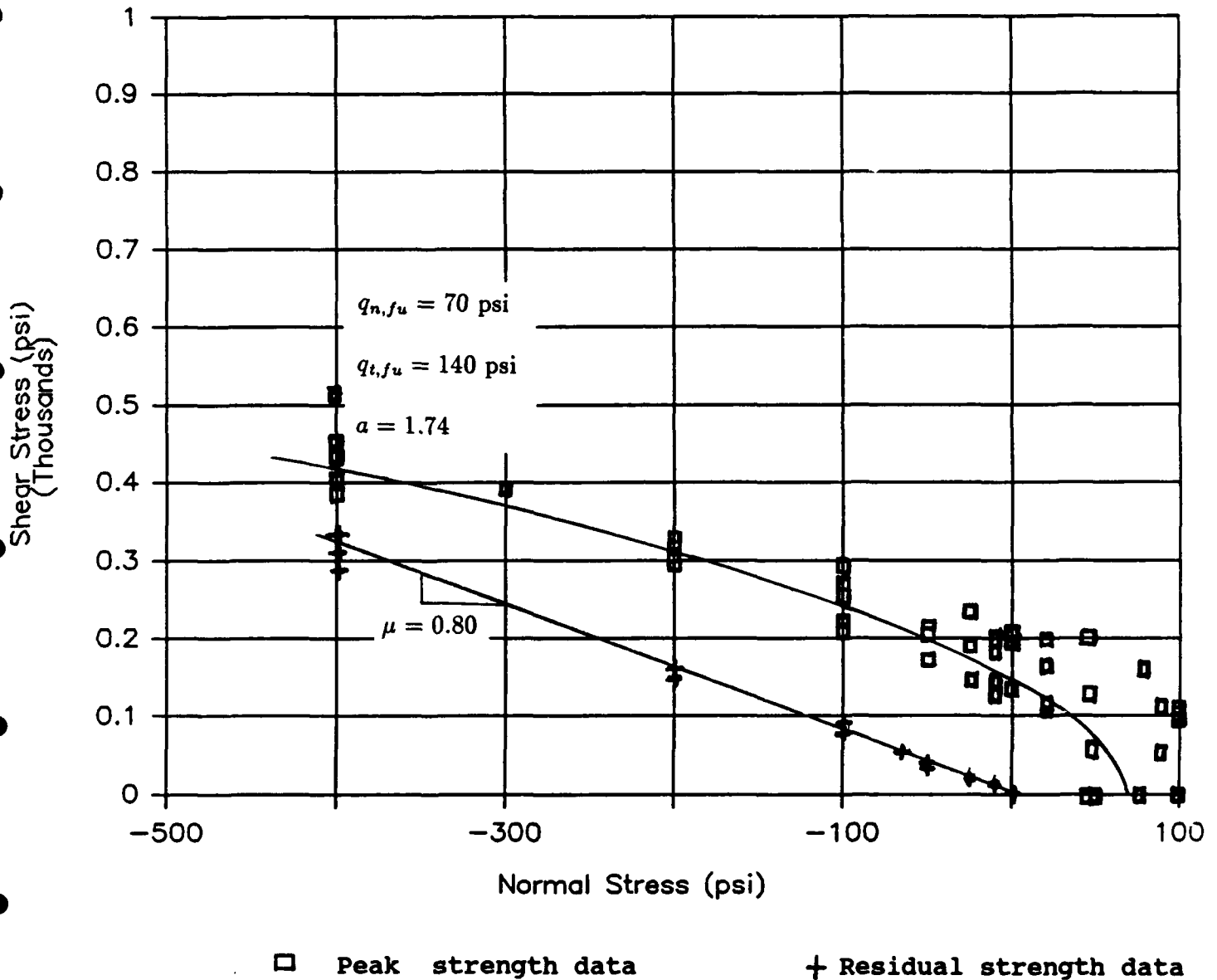


Fig. 21 Ultimate (Peak) and residual strength envelopes for mortar-aggregate (granite) interfaces and calibrated model parameters